Universidade do Minho
Escola de Ciências

Filipe André Peixoto Oliveira

Raman Spectroscopy Studies of Sn_xGe_{1-x} and ZnO:Mn Semiconductor Solid Solutions

July 2018

Filipe André Peixoto Oliveira **Raman Spectroscopy Studies of Sn_xGe_{1-x} and ZnO:Mn Semiconductor Solid Solutions**

UMinho | 2018

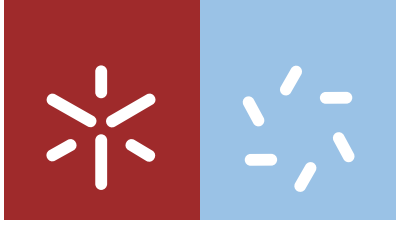

Universidade do Minho
Escola de Ciências

Filipe André Peixoto Oliveira

Raman Spectroscopy Studies of Sn_xGe_{1-x} and ZnO:Mn Semiconductor Solid Solutions

Doctoral Program in Physics (MAP-Fis)

Work developed under the supervision of:
Professor Mikhail I. Vasilevskiy
Professor Maria de Fátima Guimarães Cerqueira
Prof. Dr. habil. Jörg Schutze

July 2018

STATEMENT

AUTHOR:
Filipe André Peixoto Oliveira

TITLE OF THE THESIS:
Raman Spectroscopy Studies of Sn_xGe_{1-x} and ZnO:Mn Semiconductor Solid Solutions

SUPERVISORS:
Professor Mikhail I. Vasilevskiy
Professor Maria de Fátima Guimarães Cerqueira
Prof. Dr. habil. Jörg Schutze

CONCLUSION YEAR:
2018

Ph.D in Physics (MAP-Fis)

Universidade of Minho, 03/07/2018

Signature: Filipe Oliveira

STATEMENT OF INTEGRITY

I hereby declare having conducted my thesis with integrity. I confirm that I have not used plagiarism or any form of falsification of results in the process of the thesis elaboration.
I further declare that I have fully acknowledged the Code of Ethical Conduct of the University of Minho.

University of Minho, 03/07/2018

Full name: Filipe André Peixoto Oliveira

Signature: Filipe Oliveira

Acknowledgments

I would like to express my gratitude to some persons and institutions which the support was essential to the execution of this work.

First of all, I would like to express my special appreciation and thanks to Professor Mikhail Vasilevskiy and Professor Fatima Cerqueira for all the help and support during the Ph.D work but also for all the support in the past 15 years since my first year in the university.

I would also like to express my gratitude to Professor Jőrg Schulze for admitting me and taking care of me in the Institut für Halbleitertechnik (IHT) and Dr. Inga Fisher for all the help while I was in the IHT.

My gratitude is equally extended to all persons and institutions that directly or indirectly help me developing all the necessary work during the Ph.D project, such as Dr. A. Benedetti, Dr. S. Stefanov, Prof. S. Chiussi from the University of Vigo, Dr. Eduardo Alves do Instituto Superior Técnico (ITN) and Prof. Aleksander S. Vasin form the N. I. Lobachevsky University of Nizhny Novgorod (Russia).

Finally, I would like to express my gratitude to the Fundação para a Ciência e a Tecnologia (FCT) for providing me with the very essential fellowship to fulfill my Ph.D project.

Resumo

Título: Estudos de espectrocopia Raman em soluções solidas de semicondutores Sn_xGe_{1-x} e ZnO:Mn

O foco do trabalho apresentado nesta tese é o estudo por espectroscopia Raman de duas promissoras soluções sólidas de semicondutores (SSs), GeSn e ZnO: Mn. Estes dois sistemas são de grande interesse científico devido às suas potenciais aplicações em várias áreas, como a fotónica, optoeletrónica, eletrónica e spintrónica. O sistema GeSn é considerado o melhor candidato para a obtenção de semicondutores de banda proibida directa, compatível com a tecnologia Si CMOS, uma vez que a adição de estanho à rede de Ge deve diminuir a energia da banda de condução no ponto Γ da primeira zona de Brillouin. A solução sólida ZnO:Mn é outro material interessante devido à sua transparência na região visível do espectro eletromagnético, juntamente com a possibilidade de controlo da condutividade elétrica e eventualmente das suas propriedades magnéticas.

Neste trabalho, as amostras em estudo foram produzidas usando duas técnicas de deposição diferentes, nomeadamente, epitaxia de feixe molecular (MBE) para o sistema GeSn (incluindo amostras de referência de germânio puro) e pulverização reativa por magnetrão para o ZnO:Mn (incluindo ZnO não dopado e ZnO dopado de Al). Estas técnicas de crescimento são brevemente explicadas na tese, juntamente com os métodos de caracterização primários utilizados, como Rutherford Backscattering Spectrometry (RBS), Microscopia de Força Atómica (AFM), Microscopia Electrónica de Transmissão (TEM) e Difração de Raios-X (XRD). Adicionalmente foi realizada espectroscopia de rotação de Faraday e medidas de Ressonância Magnética para algumas amostras do sistema ZnO:Mn que apresentaram um comportamento paramagnético à temperatura ambiente.

A espectroscopia Raman é uma técnica poderosa para estudar materiais semicondutores. Esta técnica foi, nesta tese, utilizada para estudar as duas famílias de soluções sólidas, tanto do ponto de vista macro- como microscópico. Esta técnica permite a determinação de frequências de vibração atómicas e permite também analisar a simetria dos cristais, efeitos de desordem nas ligas, estados de superfícies e de interfaces, presença de deformações, impurezas, defeitos, etc. Esta capacidade torna a espectroscopia Raman a técnica de análise a escolher para estudo de

Abstract

This work is focused on Raman spectroscopy studies of two promising semiconductor solid solutions (SSs), GeSn and ZnO:Mn. Both systems are of high scientific interest owing to their potential applications across multiple areas, such as photonics, optoelectronics, electronics and spintronics. The GeSn system is considered the best candidate for direct band gap semiconductor compatible with Si CMOS technology, since the adding of tin is supposed to lower the conduction band energy in the Γ point of the Brillouin zone. The ZnO:Mn solid solution is another interesting material owing to its transparency in the visible range along with controllable electrical conductivity and eventually magnetic properties at room temperature.

In this work, samples of the two materials were grown using two different deposition techniques, namely, molecular beam epitaxy (MBE) for the GeSn system (including reference samples of pure germanium) and magnetron sputtering for the ZnO:Mn one (including undoped and Al-doped ZnO). These growth techniques are briefly explained in the thesis along with the primary characterisation methods used, such as Rutherford Backscattering (RBS), Atomic Force Microscopy (AFM), Transmission Electron Microscopy (TEM), and X-Ray Diffraction (XRD). Additionally, Faraday rotation spectroscopy and Magnetic Resonance measurements were performed for some samples of the ZnO:Mn system that showed a paramagnetic behaviour at room temperature.

Raman spectroscopy, a powerful technique for studying semiconductor materials, was used to study the solid solution materials from both macro- and microscopic points of view. It allows for the determination of atomic vibration frequencies and permits to analyse the crystal symmetry, alloy disorder, the state of surfaces and interfaces, the presence of strain, impurities, defects, *etc*. This capacity makes the Raman spectroscopy a technique of choice in the study of semiconductors. The fundamentals of this technique applied to semiconductors and its features for solid solutions are discussed in detail in the thesis.

A common feature of both alloy systems is the substitutional doping with an element of the same chemical group (Sn/Ge and Mn/Zn). Even though, the solubility limit is not high, ≈ 10% for Mn in ZnO and only ≈ 0.5% for tin in germanium (although it is possible to grow samples with higher content by low-temperature deposition). The difference in atomic radius between the substitutional dopant and host atoms perturbs the length of the bond involving a doping atom and, consequently, its strength for both solid solutions. Yet, there is one important difference between the two systems, related to the atomic mass difference between the dopant and the host. Consequently, a Mn atom inserted into the cationic sublattice of the ZnO crystal originates a local vibrational mode, while the Sn dopant substituting Ge produces a resonant mode overlapping with the continuum of Ge crystal phonons. Consequently, tin-related modes are intrinsically weak in Raman scattering by GeSn SSs.

The Sn doping effect on the Ge lattice vibrations is caused by (i) the atomic mass difference and (ii) a macroscopic strain induced by the elastic force caused by the lattice constant difference between the alloy layer and the substrate. The Raman spectroscopy results are in agreement with those of microscopic modelling performed using the semi-empirical Tersoff potentials and show that the effects (i) and (ii) partially compensate each other for a strained layer, so that the Raman peak is redshifted for relaxed alloys where the stress vanishes, e.g. because of the formation of misfit dislocations.

Raman spectroscopy studies of the ZnO:Mn system, performed with either non-resonant or resonant excitation, revealed several effects: (1) strong enhancement of the LO-phonon band attributed to the “forbidden” Fröhlich-type scattering that becomes dominating under resonance conditions, accompanied by (2) the appearance of multiple LO-phonon peaks, and (3) the presence of a Mn-related mode, seen only off resonance, with the intensity increasing with the Mn content. These effects have been explained theoretically. The intense multi-LO-phonon lines observed in the resonant Raman spectra of all studied ZnO samples are caused by phonon-assisted emission and reabsorption of photons by hot excitons with appropriate energy, which may be called a pseudo-Raman effect. The nature of the Mn-related mode (3) was clarified based on model calculations of the local vibration frequency of Mn atoms beyond the isotope defect approximation.

semicondutores. Os fundamentos desta técnica aplicada a semicondutores e as suas características para soluções sólidas são discutidos em detalhes na tese.

Uma característica comum a ambos os sistemas em estudo é a dopagem com um elemento do mesmo grupo químico (Sn / Ge e Mn / Zn). Muito embora o dopante seja do mesmo grupo o limite de solubilidade não é alto, ≈ 10% para Mn em ZnO e apenas ≈ 0,5% para estanho em germânio (embora seja possível cultivar amostras com maior conteúdo por deposição de baixa temperatura). A diferença de raio atómico entre os átomos dopantes e nativos perturba o comprimento da ligação que envolve um átomo dopante e, consequentemente, a sua força para ambas as soluções sólidas. No entanto, há uma diferença importante entre os dois sistemas, relacionada com a diferença de massa atómica entre o dopante e o hospedeiro. Consequentemente, um átomo de Mn inserido na sub-rede catiónica do cristal de ZnO origina um modo de vibração local, enquanto o dopante de Sn que substitui o átomo de Ge produz um modo de ressonância que se sobrepõe ao contínuo de fonões do cristal de Ge. Consequentemente, os modos relacionados com o estanho são intrinsecamente fracos na dispersão Raman em soluções sólidas de GeSn.

O efeito da dopagem com Sn nas vibrações da estrutura Ge é devido (i) à diferença de massa atómica e (ii) à deformação macroscópica induzida pela força elástica (tensão) devido à diferença da constante de rede entre a camada da liga e o substrato. Os resultados de espectroscopia Raman obtidos estão de acordo com os modelos microscópicos calculados com os potenciais semi-empíricos de Tersoff e mostram que os efeitos (i) e (ii) compensam-se parcialmente numa camada sob tensão, de modo que o pico de Raman correspondente à vibração fundamental Ge-Ge se aproxime da sua posição espetral num cristal de germânio puro. Se a rede cristalina da solução sólida se relaxar, a tensão desaparece, em particular, devido à formação de deslocações na interface e o pico Raman desloca-se para menores números de onda.

Os estudos de espectroscopia Raman do sistema ZnO:Mn, realizados com excitação não ressonante e ressonante, revelaram vários efeitos: (1) elevada intensidade da banda de fonões LO, sob excitação ressonante, atribuída à dispersão do tipo Frőhlich que é proibida nas condições fora de ressonância, acompanhada pelo (2) aparecimento de múltiplos fonões LO nos espectros Raman ressonante e (3) pela presença de um modo relacionado com Mn, visto unicamente em condições de Raman não ressonante, cuja intensidade aumenta com a concentração de Mn. Esses efeitos foram explicados teoricamente. As linhas intensas de multi-fonões LO observadas nos espectros de Raman ressonante, em todas as amostras de ZnO estudadas, são causadas por emissão assistida por fonões e reabsorção de fotões por excitões quentes com energia apropriada. Este efeito pode ser chamado de efeito pseudo-Raman. A natureza do modo relacionado com Mn (3) foi esclarecida com base nos cálculos do modelo da frequência de vibração local dos átomos de Mn na aproximação do defeito isótopo.

Outline of the thesis

The thesis is divided in six chapters and two appendices: I) introduction and objectives, II) sample fabrication and characterization techniques, III) fundamentals of Raman scattering in semiconductors, IV) results on Ge-Sn samples, V) results on ZnO:Mn thin films, VI) conclusions and outlook, Appendix A) Publications, and Appendix B) Faraday effect details.

In **Chapter I,** a resume of the state-of-art of the GeSn solid solutions, ZnO and ZnO:Mn is provided. In the end of the chapter, the objectives of this work are provided.

Chapter II is dedicated to describe samples preparation methods as well as the major characterization techniques. A special emphasis is given to growing technique molecular beam epitaxy (MBE) and characterization technique Faraday rotation effect due being less known.

Chapter III provides an overview of the Raman scattering in semiconductors from a macroscopic and microscopic point of view. The chapter finishes with an overview of the experimental determination of the Raman scattering spectra.

In **Chapter IV**, the experimental results for the GeSn system are presented and discussed. Here multiple results are analysed such as transmission electron microscopy (TEM), X-ray diffraction (XRD), Rutherford backscattering spectrometry (RBS) and atomic force microscopy (AFM). The Raman spectroscopy results are presented and discussed in a dedicated section of the chapter.

Chapter V provides the experimental results and discussion for the ZnO:Mn system (undoped and Mn-, Al- doped). Here multiple results are analysed such as Raman scattering, X-ray diffraction, Faraday rotation effect, optical (transmission) and electric conductivity. The Raman spectroscopy results in non-resonant and resonant mode are presented and discussed in a separate dedicated section of the chapter.

Chapter VI summarizes the results of this work and presents general conclusions.

Appendix A provides a list of publications that resulted from the scientific work produced during the Ph.D.

Appendix B completes the information about the Faraday effect presented in **Chapter II** by providing the theoretical treatment of the effect.

Appendix C shows the deduction of the Raman peak shift owing to strain.

Contents

Acknowledgments ..... **v**

Abstract ..... **vii**

Título e Resumo (Title and Abstrat in Portuguese) ..... **ix**

Outline of the Thesis ..... **xi**

Contents ..... **xiii**

List of Definitions ..... **xix**

List of Acronyms ..... **xxi**

I. Introduction and Objectives **1**

I.1. Semiconductors with Diamond Structure: Si, Ge, α-Sn 5

I.1.1. Electronic Band Structure 6

I.2. $Ge_{1-x}Sn_x$ Solid Solutions 11

I.2.1. Crystal Structure 13

I.2.2. Electronic Properties 15

I.2.3. GeSn and High Mobility 17

I.2.4. GeSn Growth 18

I.2.5. GeSn-on-Si 19

I.2.6. Applications of $Ge_{1-x}Sn_x$ 20

I.3. Low-dimensional Structures of Group IV materials 22

I.4. Zinc Oxide (ZnO) 23

I.5. ZnO:Mn, a Transparent Magnetic Semiconductor 26

I.5.1. Diluted Magnetic Semiconductors 27

I.5.2. Magneto-Optical Response of a DMS 29

I.5.3. ZnO Doped with Transition Metals 35

I.6. Objectives of this Work 36

Bibliography 38

II. Sample Fabrication and Characterization Techniques 45
II.1. Molecular Beam Epitaxy: Requirements and Epitaxial Growth 45
II.1.1. MBE Requirements 46
II.1.2. Epitaxial Growth Processes 47
II.1.3. Nucleation of Epitaxy layers 49
II.1.4. Monolayer Concept 53
II.1.5. Strain Relaxation 55
II.1.6. Lattice Defects in Epitaxy Growth 58
II.2. Molecular Beam Epitaxy: Deposition System 58
II.2.1. MBE System Description and Calibrations 61
II.2.1.1. Load-Lock 62
II.2.1.2. Central Chamber 63
II.2.1.3. MBE Chamber 64
Vacuum System, UHV and RGA 64
Substrate Heater and Support 65
Si Electron Beam Evaporator 67
Ge Effusion Cell 67
Sn Effusion Cell 69
Other Cells 70
Feedback flux control 70
Pyrometer 70
II.2.1.4. Control Unit and Computers 71
II.2.2. MBE Calibration 71
II.2.2.1. Si Flux Calibration 72
II.2.2.2. Ge Flux Calibration 73
II.2.2.3. Sn Flux Calibration 74
II.2.2.4. Substrate Heater Calibration 74
II.2.3. Standard Growth Proceedings 76
II.2.3.1. Si Substrate Cleaning and Surface Preparation 76
II.2.3.2. Si Buffer Layer 80
II.2.3.3. Ge Buffer Layer and Virtual Substrate 81

II.3. Sputtering 83
II.3.1. Sputtering and Reactive Sputtering 85
II.3.2. Microstructure of Sputtered Samples 89
II.3.3. Experimental Growth Conditions for ZnO 89
II.4. Morphological and Structural Characterisation Techniques 91
II.4.1. Atomic Force Microscopy 91
II.4.2. Transmission electron microscopy 94
II.4.3. X-Ray Diffraction 99
II.4.3.1. Bragg-Brentano Geometry 100
II.4.4. Rutherford Backscattering Spectrometry 102
II.5. Faraday Rotation Effect 107
II.5.1. Brief Description of the Faraday Rotation Effect 108
II.5.2. Magneto-Optic Effects in Semiconductors 110
II.5.2.1. Fixed Polarizers 111
II.5.3. Faraday Rotation Setup 113
II.5.4. Measurement of the Faraday Angle in Thin Films 113
Summary 117
Bibliography 118

III. Fundamentals of Raman Scattering in Semiconductors 123
III.1. Inelastic Light Scattering, Momentum and Energy Conservation 125
III.2. Phonons in Semiconductors 130
III.2.1. Phonons in Crystalline Semiconductors 130
III.2.2. Electron-Phonon Interaction Mechanisms 132
III.3. Classical Theoretical Approach of Inelastic Light Scattering by Phonons 134
III.4. Raman Tensor, Symmetry and Selection Rules 137
III.5. Microscopic (Quantum) Theory of One-Phonon Raman Scattering, Resonant Effects 141
III.6. Resonant Raman Scattering 144
III.6.1. Free and Bound Excitions 146
III.6.2. Wavevector Dependence of Exciton–LO-Phonon Interaction 147
III.7. Phonon Modes and Raman Scattering in Solid Solutions 148

III.8. Experimental Determination of Raman Spectra 151
III.8.1. Description and Characteristics of the Raman Setups Used 154
III.8.2. Analysis of Typical Spectra of Semiconductor Crystals 156
Summary 163
Bibliography 164

IV. Results on Ge-Sn samples 167
IV.1. Samples' Description 167
IV.2. Sample Characterization 171
IV.2.1. GeSn Thin Films 172
IV.2.1.1. Morphological Characterization by TEM 172
IV.2.1.2. Morphological and Compositional Characterization by RBS 174
IV.2.1.3. Structural Characterization by XRD 176
IV.2.2. Multilayer GeSn/Si and Ge/Si samples 182
IV.2.2.1. Morphological Characterization by TEM 182
IV.2.2.2 Morphological Characterization by AFM 187
IV.3. Raman Spectroscopy Results 191
IV.3.1. GeSn Thin Films 193
IV.3.1.1. Ge-Ge Mode 196
IV.3.1.2. Ge-Sn Mode 199
IV.3.2. Multilayers GeSn/Si and Ge/Si samples 200
IV.4. Modelling Using Semi-Empirical Potentials: Distribution of Bond Lengths and Angles 204
IV.4.1. Stillinger-Weber Potential 205
IV.4.2. Tersoff Potential 207
IV.4.3. Building Relaxed Ge-Sn Structure 209
IV.4.4. Bond Length Distribution 209
IV.5. Calculated Raman Spectra and Comparison with Experiment 213
Conclusions 218
Bibliography 220

V. Results on ZnO:Mn Thin Films **225**

V.1. Samples Description 225

V.2. Optical, Electrical, Chemical and Structural Characterization Results 228

V.2.1. Optical Characterization 228

V.2.2. Compositional and Structural Characterization 229

V.2.3. Electrical Characterization (Van der Pauw) 231

V.3. Spectroscopy of Faraday rotation 232

V.3.1. Experimental Details 233

V.3.2. Results 233

V.3.2.1. Magnetic Resonance 234

V.3.2.2. Faraday Effect 235

V.4. Non-Resonant Raman Spectroscopy Results 237

V.4.1. Undoped ZnO: Symmetry Analysis 237

V.4.2. Mn- (and Al)- Doped ZnO 241

V.4.2.1. ZnO:Al Samples 242

V.4.2.2. ZnO:Mn Samples 243

V.4.2.3. ZnO:Al:Mn Samples 246

V.5. Theoretical Estimation of the Mn Local Vibration Mode 248

V.6. Resonant Raman Scattering Results: Multi-Phonon Peaks and Phonon-Assisted Absorption/Re-Emission Model 253

Conclusions 262

Bibliography 264

VI. Conclusion **269**

Appendix A. Publications **275**

A1. Most Relevant Publications Related with Group IV Materials 275

A2. Most Relevant Publications Related with ZnO:Mn 278

A3. Other Publications 280

Appendix B. Faraday effect details **281**
B1. Magneto-Optic Effects 281
B1.1. Faraday Rotation Effect 281
B1.2. Kerr Effect 282
B1.3. Magnetic Circular Dichroism 283
B2. Theory of Magneto-Optic Effects in Semiconductors 284
B2.1. Macroscopic Theory 284
B2.1.1. Magnetized Medium 284
B2.1.2. Complex Refractive Index 285
B2.1.3. Faraday Effect 286
B2.2. Microscopic models of Magneto-Optic Effects 287
B2.2.1. Becquerel model 287
B2.2.2. Lorentz model 287
B2.2.3. Drude Model 290
B2.2.4. Interband Transitions 291
B2.2.5. Excitons 294
Bibliography 295

Appendix C. Raman peak shift owing to strain **297**
Bibliography 300

List of Definitions

A small list of definitions is presented here to provide clarity of some terms. Some these terms are can be less know due to there specificity, while others are better know, but frequently suffering from linguistic abuse and being applied broadly.

Alloy – is a homogeneous mixture or solid solution of two or more material where, in general, at least one being a metal. The designation is frequently used with a broader meaning in science materials, without the need of a metal to by present, *e. g.*, SiGe alloys. Alloys are developed with the intent of obtaining significantly new properties in relation to the basis materials.

Solid solution – is a solution in solid-state where one or more solutes are solved in a solvent. Such a mixture can be considered as a solution when the crystal structure of the solvent remains unchanged by addition of the solutes in a single homogeneous phase. The incorporation of the solute materials may be incorporate into the solvent crystal lattice substitutionally, or interstitially. This incorporation affects the properties of the solvent material due to the distorting the crystal lattice and disrupting the physical and electrical homogeneity of the solvent material by the solvent materials. In the end it is expected that the solid solution has properties similar to those of the solvent material.

Doping – is an impurity added in small quantity to a semiconductor with the objective to modify the electric and / or magnetic properties of the material while keeping all the other properties little affected.

Alloy vs Solid solution vs Doping – the difference between alloy and solid solution sometimes can be subtle, but some differences can be pointed: (1) in a solid solution it is expected a significant content of one material (solvent) versus the other materials (solutes), a alloy does not have the same restriction, *e. g.*, SiC or SiGe; (2) consequently a solid solution will keep comparable properties to the solvent material but a alloy can exhibit a substantial differences in proprieties *e. g.*, brass. In doping the levels of “impurities” can reach to a few at. % of the material, *e. g.* Ge doped with Sb

can easily reach 2 %. Even though the solid solutions and doping can have similar levels of added “impurities” the expected effects are different as explained in the previous definitions.

Critical thickness of an epitaxial film – it is the maximum thickness where the growth of an epitaxial single crystal layer is viable. Afterwards, the crystal epitaxy ‘break down’ and the growth is not longer single crystal.

Adatom – the word is a contraction of “absorbed atom”. It is used in crystal growth for arrived atoms lying on the crystal surface, and still not fixed to crystal lattice. It can be thought of as the opposite of a surface vacancy. In general, it is a temporary state thermodynamically unfavourable.

Monolayer (ML) – A monolayer is a single layer of atoms fully completed growth epitaxial. An extended discussion is presented in **section II.1.4**.

Dot – the term is frequently used in association to quantum dots or the formation of self-assemble dots. Again, this term can be considered in a broader or narrow meaning. In this work the term island will be reserved with the intent of a broader meaning and ‘dot’ will be reserved to the expression ‘self-assembled dots’ and in cases where potentially the islands have a rounded shape form.

Wetting layer (WL) – in the growth of epitaxial films with Stranski-Krastanov growth mode, after self-assemble dots formation two zones in the deposited material can be distinguished: the wetting layer and the dots / islands. The wetting layer corresponds to the part of the film with the epitaxial monolayers fully formed. The islands correspond to the incomplete monolayers above the wetting layer. Note that the term island is used here instead of dot or quantum dot or other similar terms.

Critical thickness in Stranski-Krastanov (S-K) growth – it is the thickness where a transition from 2D to 3D epitaxial growth occurs.

Quantum dot (QD) and Quantum well (QW) – these terms are commonly used a broad way, many times applied only based in the shape of the structure and not the in the quantum confinement of the structure properties. In this work, these terms are considered in a more narrow way and in general there use presupposes the existence of quantum confinement.

Ultra Thin Films – term used for thin films in the range of few nanometres, the limit will differ between authors, but in general below 10 nm. Here, it is considerer ultra-thin film all the film with less than 10 ML.

List of acronyms

AFM	Atomic Force Microscopy
BF [-TEM]	Bright Field [Transmission Electron Microscopy mode]
BZ	Brillouin Zone
CB	Conduction Band
DF [-TEM]	Dark Field [Transmission Electron Microscopy mode]
DFT	Density Functional Theory
DMS	Dilute Magnetic Semiconductor
DOS	Density Of States
EBV	Electron Beam Evaporator
EDS	Energy Dispersive Spectrometry
FE	Faraday Rotation Effect
HH	Heavy-Hole
HR-TEM	High Resolution Transmission Electron Microscopy
IC	Integrated Circuit
INS	Inelastic Neutron Scattering
LCL	Left-handed Circularly polarized Light
LH	Light-Holes
MBE	Molecular Beam Epitaxy
MCB	Magnetic Circular Birefringence
MIR	Mid-InfraRed
ML	MonoLayer
MO	Magneto-Optic
MQWs	Multi Quantum Wells
ODP	Optical Deformation Potential
PIXE	Proton Induced X-Ray Emission
QD	Quantum Dot
QMS	Quadrupole Mass Spectrometer
QW	Quantum Well

RBS	Rutherford Backscattering Spectrometry
RCL	Left-handed Circularly polarized Light
RF	Radio-Frequencies
RF-sput	Reactive magnetron sputtering
RKKY	Ruderman–Kittel–Kasuya–Yosida
RRS	Resonance Raman Spectroscopy
SC	Semiconductor
SE	Spectroscopic Ellipsometry
S-K	Stranski-Krastanov [growth mode]
SO	Spin-Orbit [interaction]
SS	Solid Solution
STEM	Scanning Transmission Electron Microscopy
SW	Stillinger-Weber [semi-empirical potential]
UHV	Ultra High Vacuum
VFF	Valence Force Field
TEM	Transmission Electron Microscopy
TM	Transition Metal
TOF-ERDA	Time-Of-Flight Elastic Recoil Detection Analysis
VB	Valence Band
VCA	Virtual Crystal Approximation
XRD	X-Ray Diffraction
XTEM	Cross-Section Electron Microscopy
WL	Wetting Layer

Chapter I

Introduction and Objectives

The study of semiconductor material started in the 19th century, although the term "semiconducting" was used in the previous century by Alessandro Volta (1782) **[I.1]**. The first known study in observing a semiconductor effect was conducted by Michael Faraday in 1833, where he observed that the resistance of silver sulphide decreased with temperature, which was different than the dependence observed in metals **[I.2]**. Other works on semiconductors followed, with Alexander Edmund Becquerel (1839) discovering the photovoltaic effect at a junction between a semiconductor and an electrolyte **[I.3]** and Karl Ferdinand Braun (1874) observed conduction and rectification in metal sulphides probed with a metal point **[I.4]**, only to mention a few.

By 1914, Johan Koenigsberger introduced the division of solid-state materials in to three groups with respect to their conductivity: metals, insulators and semiconductors **[I.1]**. Semiconductors knowledge suffered a great advance with the advent of the quantum theories. One of the first steps was provided by Felix Bloch, that in 1928 presented the theory of electrons in lattices **[I.5]**, later in 1930 Rudolf Peierls presented the concept of forbidden gaps, and in 1931 Alan Wilson developed the band theory of solids based on the idea of empty and filled energy bands (see **Figure I.1**), again, only to mention a few works.

A material to be considered a semiconductor has to fulfil some characteristics: (1) having an electric conductivity value falling between that of a conductor and an insulator; (2) the resistance decreases with the increase of temperature (higher the temperature, more carriers available for conduction), which is a behaviour opposite of a metal, and; (3) conducting properties can be significantly changed by controlled introduction of impurities (doping) into the crystal lattice.

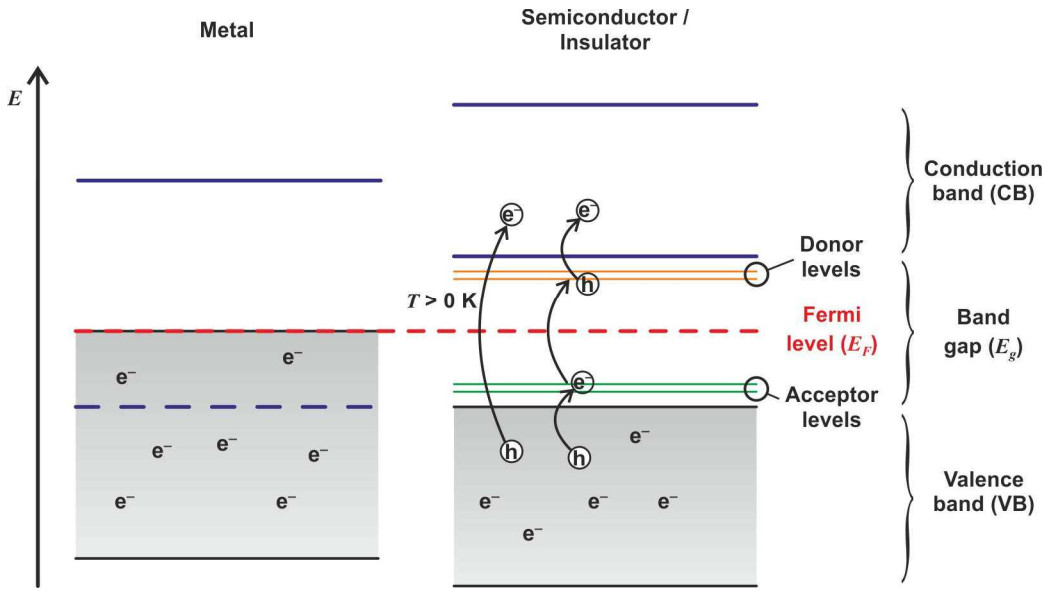

Figure I.1: Illustration of the energy bands of crystalline materials of different kinds of conductivity. The valence band is shown with grey areas and the conduction band is shown delimited by blue lines. In the case of a metal the valence band (VB) is full and is intersected by the conduction band (CB). The energy of the Fermi level (that represents the energy of the highest occupied level at T = 0 K) is inside the CB, resulting in a flow of electrons with very low energy. In the case of a semiconductor or insulator the CB and VB are separated by a gap (bang gap). The energy difference between the top of the VB and the minimum of the CB is the energy gap (E_g). In a semiconductor, E_g can be as low as 0 eV, for example α-Sn, and in general, E_g is inferior to 4 eV although exceptions exist, like diamond. Insulators have higher E_g, for example SiO_2 has E_g = 8.9 eV. The Fermi level is in between the CV and the VB. In a semiconductor as in an insulator, at a temperature of 0 K, the VB is full and the CB is empty, but, for a semiconductor, at higher temperatures some of electrons can pass from the VB to the CB, leaving then holes in the VB. Such processes (indicated by the arrows) can be direct or involve intermediate (*e.g.* defect or impurity) states. The population of holes/electrons in the VB/CB increases with the temperature, consequently a semiconductor has higher conductivity at higher temperatures, in contrast to metals.

Semiconductor material can be doped with impurities to increase the concentration of free electrons or holes. When a crystal is made with two differently-doped regions, a semiconductor junction is created. The behaviour of charge carriers, electrons and holes, at these junctions is the basis of build electronic devices: diodes, transistors and the numerous variants of these two. These electronic devices are the basis of the actual electronics and microelectronics. The microelectronics, in particular its computational sector, is playing a more and more important role in the human

development. A big part of this success owes to the use of silicon, because it offers the best cost/benefit ratio and it is unlikely that any other material can substitute silicon in the mainstream of electronic industry in the near future **[I.6]**.

Silicon (Si) and Germanium (Ge) from the Group IV were the first semiconductors to be intensively exploited commercially, and play a key role in microelectronics. Unfortunately, Group IV semiconductors do not display a direct band gap, which precludes their use as active layers in light-emitting diodes and lasers. The alternatives are alloys of III-V compound such as gallium arsenide (GaAs) and indium phosphide (InP), but although they are interesting materials for micro- and opto-electronics, they are very expensive for mass production. The same restriction applies also to II-VI materials some of which (such as CdTe) could be an alternative to the III-V's, in addition elements like Cd are problematic from the environmental point of view. Because of this, the idea of designing a Group IV (ideally, Si) based material with acceptable optoelectronic properties was always inspiring researchers, physicists and materials scientists.

After the success with IV-IV materials, such as Ge_xSi_{1-x}, Si_xC_{1-x} and Ge-on-Si, researchers try to explore IV-IV systems capable to display direct band gap. In the 1980's, it was suggested that an alloy of germanium and tin (Sn) could be a candidate to achieve direct band gap.

The number of applications for semiconductors is increasing and with new needs emerging. Recently two area of high interest are transparent semiconductors and semiconductors with magnetic capabilities. The transparent semiconductors are useful for applications such as displays and image sensors, while the second type is useful for opto-magnetic devices and spintronic devices. ZnO of group II-VI is one of the most promising candidates for both areas.

The following sections provide an introduction to group IV materials, present the state of the art of the group IV-IV materials developed with the aim to produce direct band gap semiconductors and also the state of art concerning ZnO and doped ZnO with magnetic properties. Finally the objectives of this work are presented.

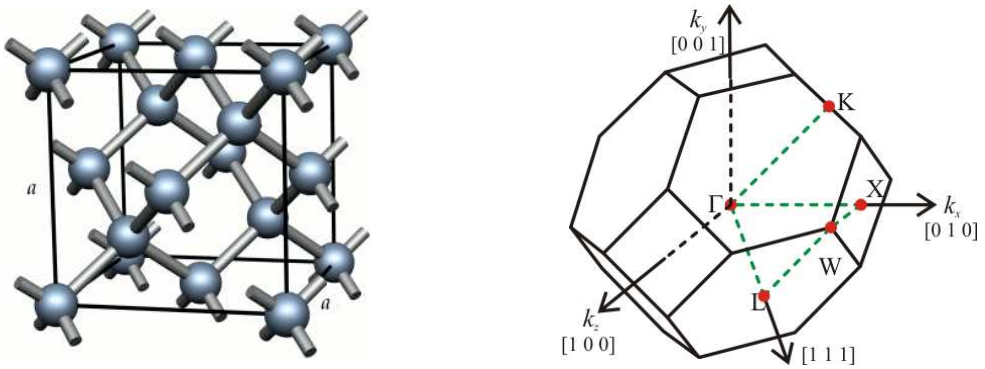

a) **b)**

Figure I.2: a) Illustration of the diamond structure, typical of the Group IV elements like C (diamond), Si, Ge and α-Sn. The underlying lattice is face-centred cubic and there is a two-atom basis. [I.7] b) Illustration of the corresponding first Brillouin zone - the same shape for all Group IV elements. [I.8]

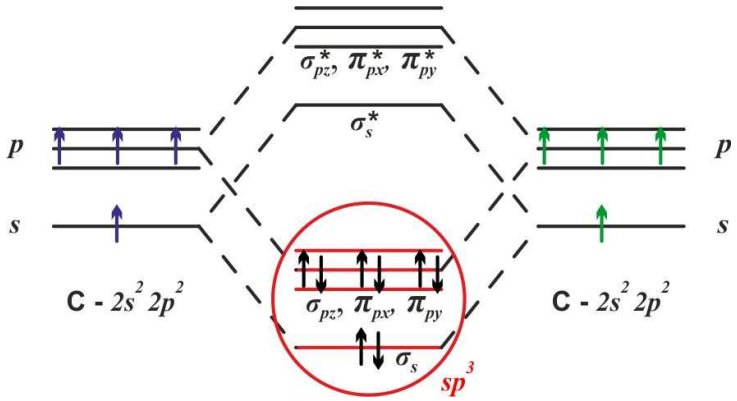

Figure I.3: Schematics of the formation of sp^3 hybrid bonding states in diamond. The scheme is similar for all diamond cubic structures of other group IV materials.

Table I.1: Some electronic and structural properties of Group IV (C, Si, Ge, Sn) and III-V (GaAs, InP) semiconductors for comparison. All of them have a diamond-cubic or zinc blende structure (III-V materials).

	C*	Si*	Ge*	α-Sn	$Ge_{1-x}Sn_x$	GaAs*	InP*
E_g (eV)	5.46 - 5.6	1.12	0.661	0.0/-0.4+ (1)	0 ~ 0.5$	1.424	1.344
E_Γ(eV)	7.3 - 7.4	4.2	0.8				
μ_e ($cm^2V^{-1}s^{-1}$)	≤2200	≤1400	≤3900	$\leq 1.2 \cdot 10^{5}$#	≤20000§	≤8500	≤5400
μ_h ($cm^2V^{-1}s^{-1}$)	≤1800	≤450	≤1900	$\leq 1 \cdot 10^{4}$#	≤10000§	≤400	≤200
a (Å)	3.567	5.431	5.658	6.489	5.658~6.0&	5.653	5.869

* Ioffe web site and references in there **[I.9]**; + α-Sn exist for temperatures below 13.2 ºC **[I.10]**; #**[I.11]**; $ **[I.12]**; § Expected values with band engineering **[I.13]**; & **[I.14]**.

[1] α-Sn is a zero-gap semiconductor. This negative band gap, -0,4 eV, means that Γ_7^- band being located lower in energy than the Γ_8^+ band. See the last paragraph of **Section I.2.1**.

I.1. Semiconductors with Diamond Structure: Si, Ge, α-Sn

The elements C (diamond), Si, Ge and Sn (α phase) all crystallise in what is known as the diamond or diamond-cubic structure. This structure can be visualised as two overlapped face-centred-cubic lattices, *i. e.*, as a face-centred-cubic (fcc) Bravais lattice with a two-atom basis as show in **Figure I.2a**. The first Brilloiun zone for this structure is the truncated octahedron shown in **Figure I.2b**. In this structure, each atom has tetragonal symmetry, with four bonds to its four nearest neighbours. Taking carbon ($2s^2 2p^2$) as an example, the atoms form bonding and anti-bonding states for both *s* and *p* orbitals (see **Figure I.3)**; the lowest four states from each atom mix to form sp^3 hybrid orbitals. As there are two atoms per primitive cell, each with four electrons, the lower sp^3 states, which overlap to form a band, are completely filled. Thus, diamond is not metallic, as the occupied and unoccupied electron states are separated by a considerable energy gap. **[I.8]**

It is interesting to examine what happens, in terms of electronic and structural properties, as one descends Group IV of the periodic table (C, Si, Ge, Sn), as also for some alloys. **Table I.1** shows the energy gap, E_g, separating the filled sp^3 hybrid band from the unoccupied (conduction) band derived from the anti-bonding orbitals, and the lattice parameter a (the edge of the conventional cubic cell as shown in **Figure I.2a**). It is important to note that the band gap decreases as the separation of the atoms increases. Indeed, α-Sn is a semiconductor of gap zero (or semi-metal) and β-Sn is a metal (body-centered tetragonal lattice structure) **[I.8]**. The reason for this variation is illustrated in **Figure I.4**, which shows the variation of the tight-binding bands with interatomic distance. The larger atomic spacing in Sn corresponds to the portion of the diagram where the upper and lower bands overlap, so that Sn is a metal. As the atomic spacing decreases, the gap between the band derived from the sp^3 bonding states and that derived from the anti-bonding states opens up, resulting in an energy gap between full and empty states. **[I.8]**

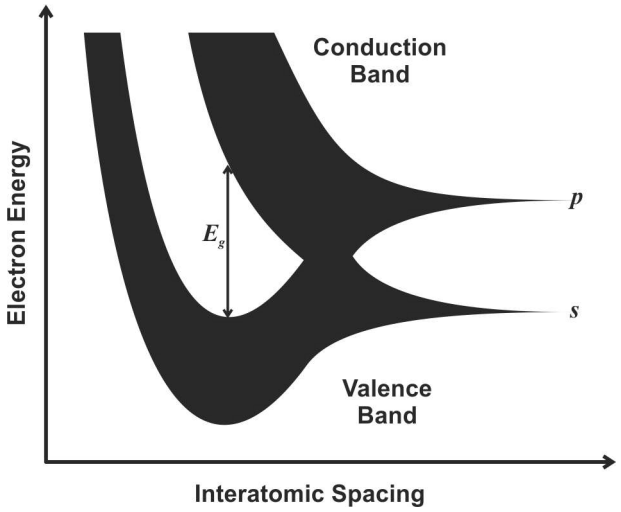

Figure I.4: Schematic of band formation in the Group IV elements. The larger atomic spacing in Sn corresponds to the portion where the upper and lower bands overlaps, so that Sn is a metal; as the atomic spacing decreases, the gap between the band derived from the sp^3 bonding states and that derived from the antibonding states opens up, resulting in a energy gap between full and empty states. Figure adapted from [I.8]

I.1.1. Electronic Band Structure

All Group IV elements, *i.e.* C, Si, Ge, Sn, Pb, are well known, and all of them, with exception of Ge, were part of the first Mendeleev's Periodic Table in 1869. It was indeed Mendeleev who predicted the existence of germanium. All these elements are now widely used in integrated circuits (ICs), Si and Ge as elemental semiconductors and C (SiC) and Pb (PbSe, PbS, ...) mostly as part of semiconductor alloy compounds. Sn and Pb are also used as a solder.

Figure I.5, **I.6** and **I.7** shows the electronic band structure of Si, Ge and α-Sn, respectively, in detail. A more recent calculated band structure for these materials can be found in **Ref. [1.15]**. The band structure of Si and Ge is very similar (**Figure I.5** and **I.6**). For both, the energy maximum of the valence band (VB) is located in the centre of the Brillouin zone (Γ point, $\vec{k}$ = 0). The VB consists of three bands, degenerate in the Γ point, namely, the heavy-hole (HH) band, the light-holes (LH) and a third band resulting from spin-orbit (SO) interaction. This degeneracy is partially removed by the spin-orbit interaction that shifts the SO band to lower energies. Concerning the conduction band, in silicon, is characterized by six equivalent minima along the family of the <100> directions, near the X point of the Brillouin zone, causing a six-fold degeneracy of this band. For silicon the energy gap (indirect one) is E_g = 1.12 eV at

room temperature and $E_g(0)$ = 1.17 eV at 0 K. In the case of Ge, the absolute minimum of the conduction band is located at the border point (L) of the first Brillouin zone along the <111> directions. Eight-fold degeneracy takes place giving rise to 8 equivalent valleys in the conduction band. Germanium presents an energy gap (also indirect) of E_g = 0.66 eV at room temperature and $E_g(0)$ = 0.74 eV at 0 K.

Thus, Si and Ge are indirect band gap semiconductors and α-Sn has a direct gap. Although germanium has a higher electron mobility (see **Table I.1**), which can result in faster devices, it is not the material of choice for microelectronics since it has several drawbacks when compared to silicon. In comparison with germanium, silicon has several advantages: 1) it can work at higher temperatures (~100 ^{o}C instead of ~50 ^{o}C for Ge; actual integrated circuits (ICs) require at least 80 ^{o}C); 2) it is easy to grow high quality insulators on silicon (SiO_2); 3) the greater band gap of Si results in a smaller electrical leakage; and 4) silicon is easier to process and much cheaper. Silicon is the semiconductor with the best ratio properties/cost for mass production of ICs, even when compared with the high performance of III-V semiconductors.

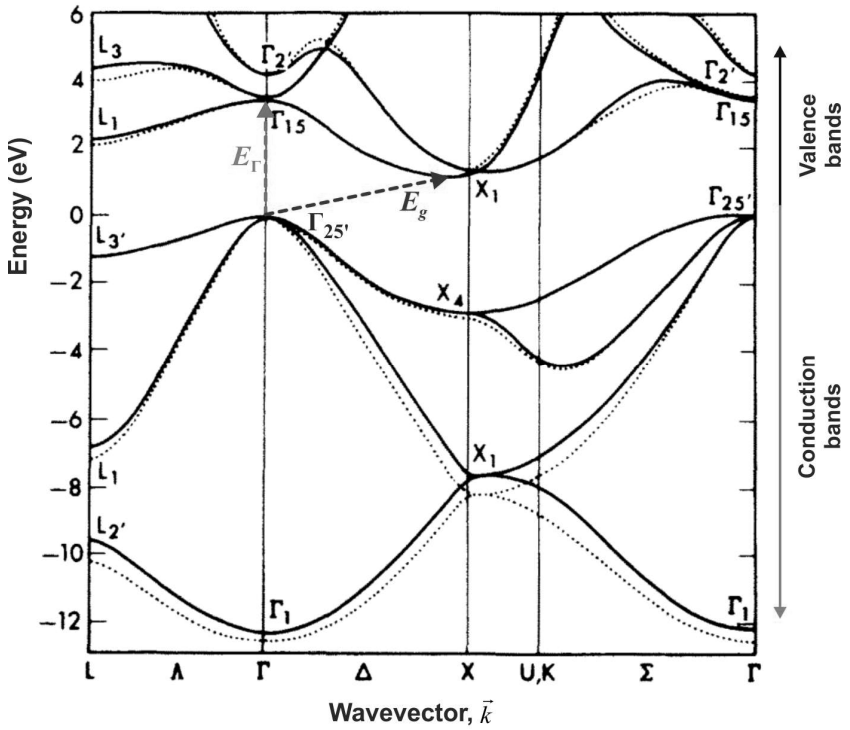

Figure I.5: Electronic band structure for Si obtained by pseudopotencial calculations. Two results are present: non-local pseudopotential (solid line) and local pseudopotential (dashed line). E_g and E_Γ are the energy gap and the energy gap at Γ point (k = 0), respectively. Figure adapted from [I.16]

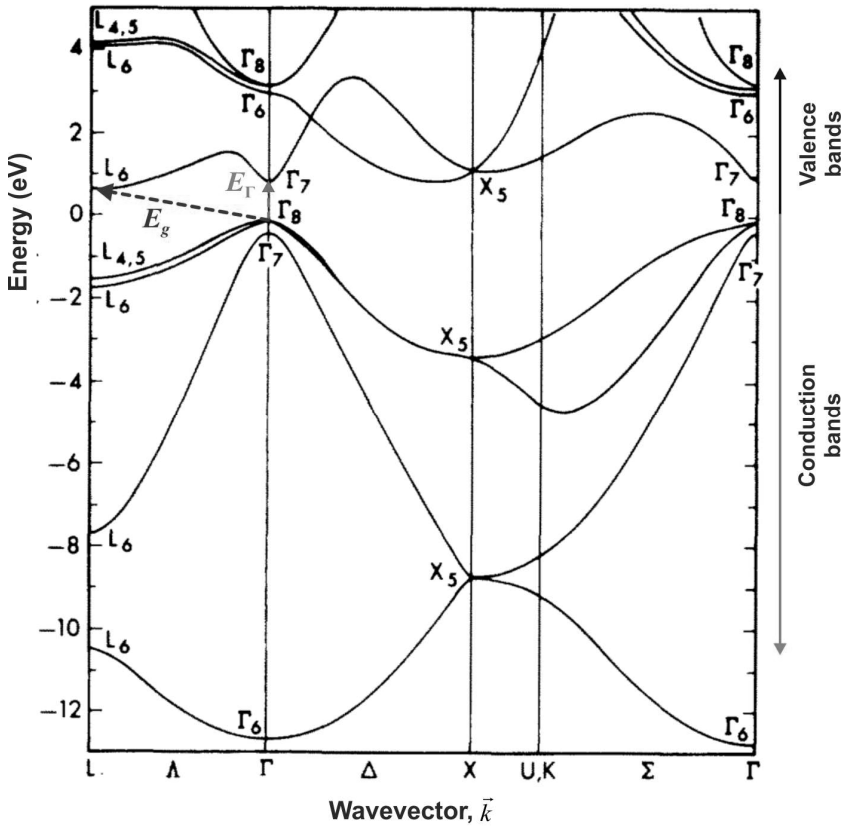

Figure I.6: Electronic band structure for Ge by non-local pseudopotential calculations. E_g and E_Γ are the energy gap and the energy gap at Γ point (k = 0), respectively. Figure adapted from [I.16]

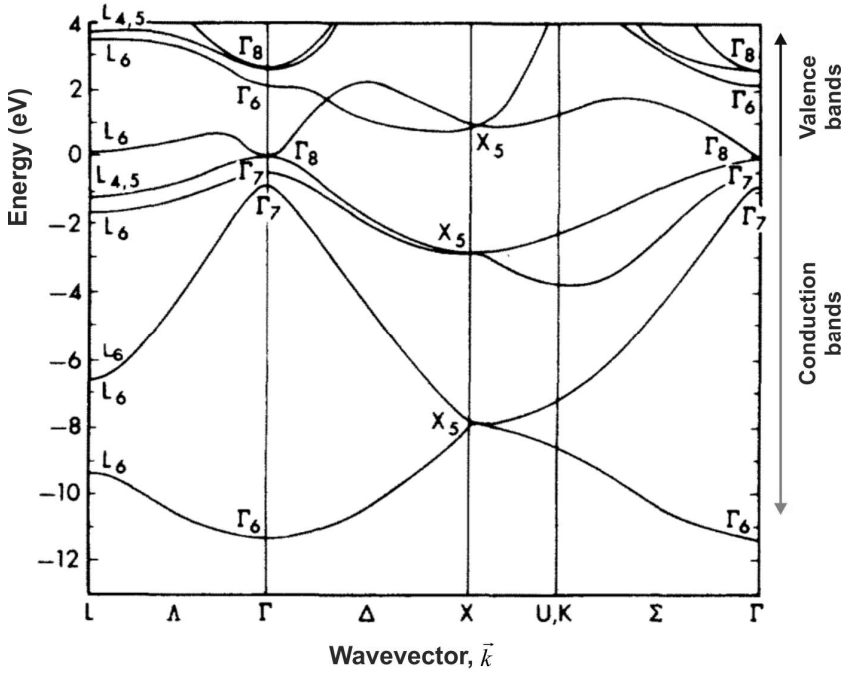

Figure I.7: Electronic band structure for α-Sn by non-local pseudopotential calculations. α-Sn one of the few known semiconductors with zero energy gap. Figure adapted from [I.16]

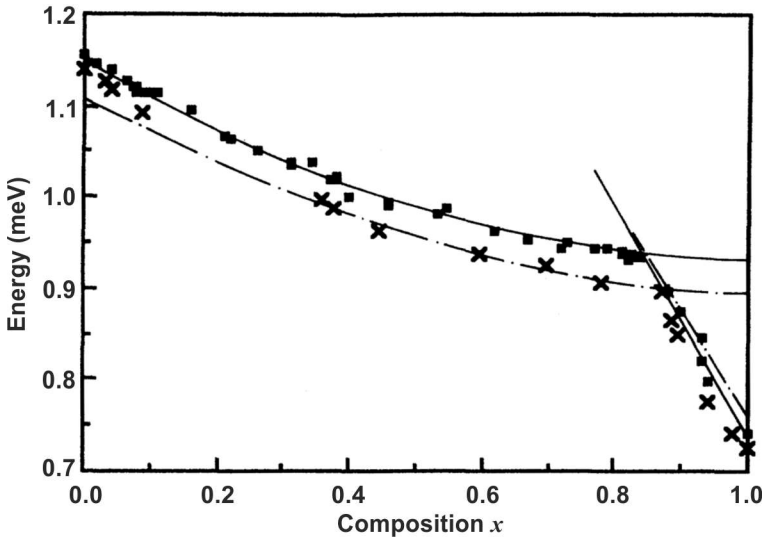

Figure I.8: Energy band gap as function of the composition x for $Si_{1-x}Ge_x$ alloys, determined from low temperature photoluminescence spectra (full squares) and respective fit (solid curve) [I.17] and crosses are experimental points [I.18]. The dotted line corresponds to the analytical expression given in Ref. [I.19].

With the necessity of devices with higher figures of merit, researchers began to develop new growth methods and new alloys based on Si, namely Ge_xSi_{1-x} and Ge-on-Si structures. Interesting is also the possibility of growing unstressed Ge-on-Si substrates allowing cheaper Ge microelectronics (see **Section II.2.3.**). In particular, the well-studied Ge_xSi_{1-x} system is a nearly ideal semiconductor alloy, in which the lattice constant and interband optical transition energies are essentially linear functions of x **[I.10]**. Si and Ge, although having similar electron affinities (distance between the vacuum level and the bottom of the conduction band), have very different band gap energies, namely, the Ge gap is almost half of that of Si. When combined into a $Si_{1-x}Ge_x$ alloy, it is possible to adjust the conduction and valence bands between the two limits according to the contents of the constituents. **Figure I.8** shows the energy values of the energy gap for the $Si_{1-x}Ge_x$ alloy as a function of x, going from the value of bulk Si (1.12eV) to the bulk Ge (0.66 eV) as x increases from 0 to 1. The gap is Si-type with a conduction band minimum lying at some point along the [100] direction for $x < 0.85$ and is Ge-type, with the minimum in the L point for $x > 0.85$. The dependence of the energy gap is parabolic in the first case and linear in the second case.

As already mentioned, the electronic structure of SiGe alloys, for low Ge concentration is similar to the Si band structure, having an indirect gap, with the

minimum energy in the X point of the Brillouin zone, while for high Ge concentrations it becomes similar to the Ge bands, also with an indirect gap and the conduction band minimum located in the L point of the Brillouin zone. The band structure for the SiGe alloy is described in detail in references **[I.20, I.21]**. Recent calculations of the Si, Ge and SiGe alloy electron structures were performed by K. Zellat *et al.* **[I.22]**.

In our days one of the most important requests for cheap electronics is the compatibility with silicon wafers and CMOS technology. All these materials are interesting to use in integrated circuits, but because all these Group IV elements and IV-IV alloys have an indirect band structure, they can not be used as active layers in light emitting diodes and lasers. Some works in the beginning of the 1980's suggested that it could be possible to produce a IV-IV compound with direct band gap using Ge and Sn. Goodman in 1982 **[I.23]** was one of the first suggesting this. At that date, the production of epitaxial and stable films of α-Sn was already known.

There are two commonly known phases of tin, α and β. α-Sn has a diamond-cubic structure and only exist for temperatures below 13,2 ^{o}C, while β-Sn has a body centred tetragonal structure. The transition from α phase to β phase represents a looseness of ~17% of the volume **[I.10]**. β-Sn is known as a metal and α-Sn is a semiconductor.

The band structure of α-Sn (**Figure I.7**) is qualitatively different from those of the other group IV elements (C, Si, Ge) **[I.24]**. The *s*-like Γ_7^- conduction band edge is situated, in energy, below the *p*-like Γ_8^+ valence band edge, causing an inversion of the curvature of the Γ_8^+ light-hole band (see **Figure I.6** and **I.7**). Consequently, α-Sn is a zero-gap semiconductor with its lowest conduction band and its highest valence band being degenerated at the Γ-point (symmetry Γ_8^+). A second conduction band with L_6^+ minima follows at a slightly higher energy. Two further valence bands with Γ_7^- and Γ_7^+ symmetry, respectively, are situated below the Γ_8^+ valence band. Although α-Sn is a zero-gap semiconductor, historically, the band gap is measured between the Γ_7^- and Γ_8^+ bands (as is measured in other diamond structure semiconductors of group IV), resulting in a negative value, -0.4 eV, due to the Γ_7^- band being located lower in energy than the Γ_8^+ band.

I.2. $Ge_{1-x}Sn_x$ Solid Solutions

Germanium has already been demonstrated to be a promising material for optoelectronic devices, such as photo-detectors and modulators **[I.25]**. However, as mentioned above, Ge also is an indirect band gap semiconductor (even though there is a direct band gap at ≈ 0.8 eV), which makes Ge-based light sources very inefficient and limits their practical use. Fortunately, the direct band gap is only 0.14 eV higher than the indirect one (see **Figure I.6** and **Table I.1**), suggesting that with band-structure engineering germanium has the potential to become a direct band gap material and an efficient light emitter. This makes Ge the most interesting group IV material for the light emitting process. However, achieving direct band gap in Ge and improving the Ge light emitting efficiency are still huge challenges. Three methods have been proposed to tune the Ge band structure to achieve a direct band gap material, namely:

- Heavy *n*-type doping of Ge: Ge is capable of behaving like a direct band gap material if heavy *n*-type doped: the excess of electrons in the conduction band first fill the indirect L band and then fill the direct Γ band of Ge **[I.26]**;

- Biaxial tensile strain of Ge: Fischetti and Laux in **[I.27]** predicted that with about 1.75% biaxial tensile strain Ge becomes a direct band gap material. Tensile strain in Ge is not only beneficial for optical devices (as can be seen in **Figure I.9**), but also good for electrical devices. Under in-plane biaxial tensile strain, the charge mobility is greatly increased. Although tensile strained Ge has many advantages, the way how to achieve high-quality tensile strained Ge is a challenge;

- $Ge_{1-x}Sn_x$ solid solutions: Many theoretical studies have predicted that a GeSn alloy can become a direct band gap material **[I.10, I.14]**. However, the Sn content to achieve a direct bandgap is poorly defined: predictions vary from 6% to 22%, depending on the theoretical model **[I.14]**. GeSn have many other interesting properties, such as tunable lattice constant and also the, predicted, high mobility of electrons **[I.13]**.

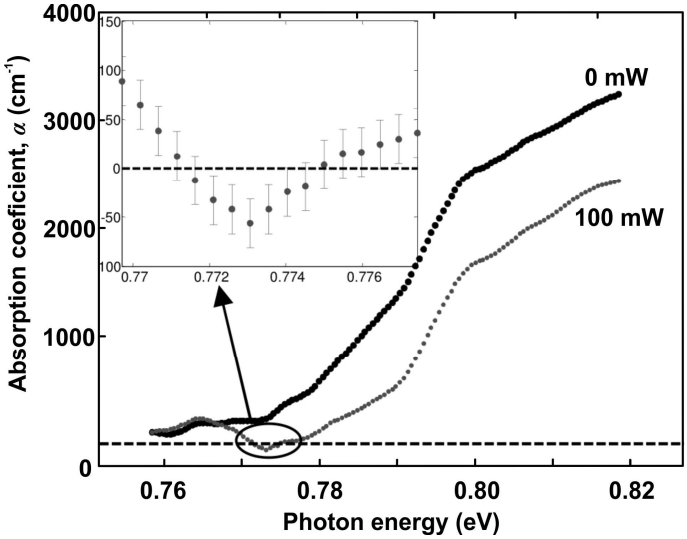

Figure I.9: Absorption spectra of the n^+-Ge mesa sample under 0 and 100mW optical pumping. Negative absorption coefficients corresponding to the onset of optical gain are observed in the wavelength range of 1600-1608 μm, as show in the inset. Figure adapted from [I.28]

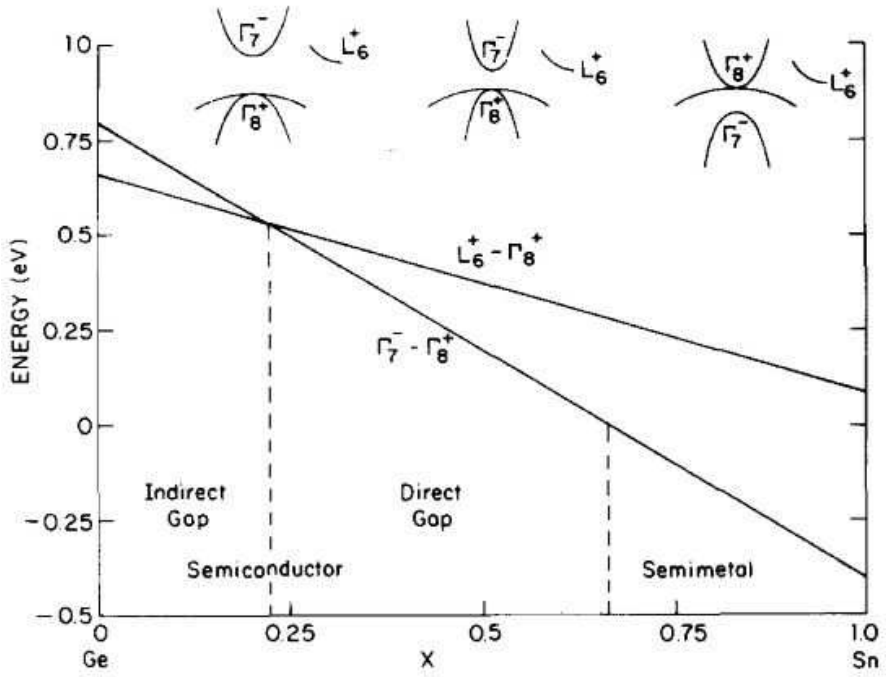

Figure I.10: Variation of energy differences ($\Gamma_7^- - \Gamma_8^+$) and ($\Gamma_6^+ - \Gamma_8^+$) in the alloy system $Ge_{1-x}Sn_x$. For *x* = 0, the smallest band gap ($\Gamma_6^+ - \Gamma_8^+$) is indirect, with a value of about 0.65 eV at room temperature; the direct gap ($\Gamma_7^- - \Gamma_8^+$) is approximately 0.8 eV. For *x* = 1, the indirect gap ($\Gamma_6^+ - \Gamma_8^+$) is ≈ 0.1 eV, and the direct gap ($\Gamma_7^- - \Gamma_8^+$) of ≈ -0.4 eV (the minus sign means inverted band structure). [I.12]

From these three methods, GeSn solid solutions are the most promising candidates for laser emission, having also potentialities for several other applications. GeSn has already been studied for more than half a century. In 1954, Ewald **[I.30]** reported that although α-Sn was only stable for temperatures below 13 ^{o}C, he observed a "high degree of stability at elevated temperatures of germanium-doped grey tin". Up until the 1980's, the majority of the studies ware concentrated on doping germanium (and silicon) with tin.

Oguz *et al* in 1983 **[I.12]** reported, maybe, the first attempt to predict the crossover from indirect to direct band gap of the GeSn system by using a simple linear interpolation between the band structure of the Ge (semiconductor) and of the α-Sn (zero gap semiconductor). The Oguz results indicates the existence of a composition range, for the $Ge_{1-x}Sn_x$ system, that results in a direct band gap semiconductor with E_g ranging from 0.55 eV to zero (see **Figure I.10**). The major problem with Sn incorporation into the Ge lattice is the large (17%) lattice mismatch between these two elements and also the instability of the diamond-cubic structure of α-Sn above 13.2 ^{o}C **[I.30, I.31]**. Accordingly, the thermodynamic solubility of Sn in Ge is less than 0.5 at.%, while that of Ge in Sn is zero **[I.28, I.31]**. As a result the $Ge_{1-x}Sn_x$ system with high concentration of tin is highly instable and cannot be produced in bulk form, then, GeSn can only be produced as metastable thin films.

The main idea of the GeSn solid solution is to create a material similar to crystalline Ge, where the Sn atoms will substitute atoms of Ge in the structure, moving down the energy of the conduction band at the Γ point faster than at the L points while maintaining a similar band structure. GeSn is seen as an alternative to III-V and II-VI compounds in which the carrier mobilities are limited by polar scattering **[I.12]**.

I.2.1. Crystal Structure

The knowledge of the GeSn crystal structure is essential for understanding the material properties. Techniques such as Rutherford backscattering spectrometry (RBS), Raman spectroscopy, ellipsometry, electron microscopy, X-ray diffraction (XRD) and others help to determine the structure.

In **Refs. [I.10, I.31]**, Bauer *et al* used RBS, random and aligned (known as channelling), to determine the quality of epitaxial growth GeSn and evaluate the Sn substitutionality in the lattice. They concluded that both Sn and Ge channel well α-particles despite the large difference in lattice constant with the Si(100) substrate and that the entire Sn contents occupy homogeneously the substitutional tetrahedral sites of the crystal structure of germanium.

In **Refs. [I.14, I.31]**, Kouvetakis, Menendez and Chizmeshya characterized the local bonding environment in the GeSn lattice by Raman spectroscopy. The material showed a strong peak corresponding to Ge-Ge longitudinal optical phonon mode, which was downshifted with respect to pure Ge. The vibrational frequency of the Ge-Ge mode decreases monotonically with increasing Sn concentration owing to the combined effects of mass substitution and elongation of the average Ge-Ge bond distances. They also identified a band corresponding to Ge-Sn vibrations, but they were not able to detect any peaks for Sn-Sn vibrations (in fact, the latter are not easy to observe, even though a broad Raman band located approximately at 190 cm^{-1} has been observed and attributed to Sn-Sn bonds in several works **[I.32, I.33]**). These works provide evidence for the presence of tetrahedral GeSn coordination and support the formation of a random solid solution with the diamond-cubic structure, and also mean that Sn atoms were isolated. Ellipsometric studies also provide evidence for a Ge-like band structure that is substantially redshifted compared with that of elemental Ge (see **Figure I.11**).

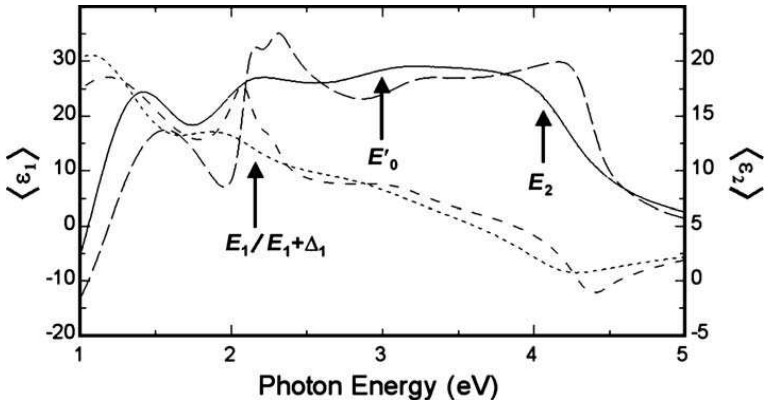

Figure I.11: Real, ε_1 (solid line), and imaginary, ε_2 (dotted line), parts of pseudodielectric function for $Ge_{0.84}Sn_{0.16}$ compared with that of pure Ge (ε_1, long dashed line; ε_2, short dashed line). $E_1/E_1+\Delta_1$, E_0', and E_2 critical points can be compared between both materials. [I.14]

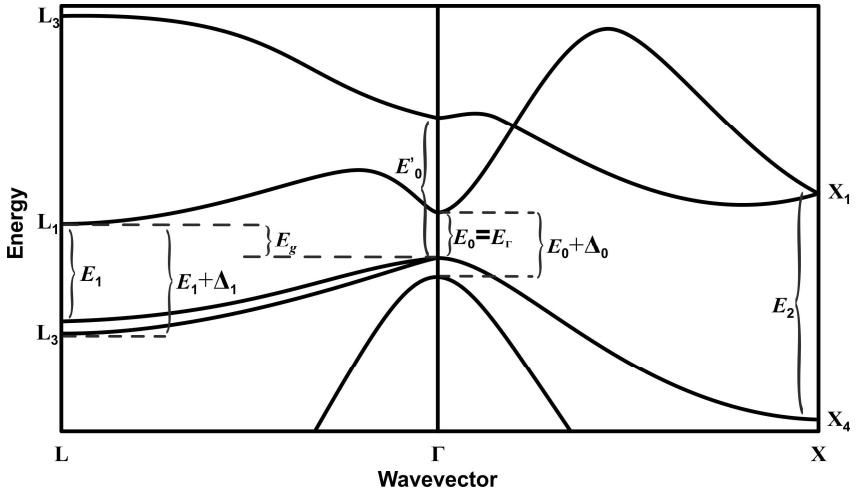

Figure I.12: Ge-like band structure in the vicinity of the fundamental gap. The diagram shows the Van Hove critical points and the indirect gap. Figure adapted from [I.14]

I.2.2. Electronic Properties

In addition to their attractive structural properties and their potential as templates, $Ge_{1-x}Sn_x$ solid solutions possess intriguing electronic properties. Many of the most important properties can be obtained by optical measurements.

The optical response of semiconductors shows several characteristic features at transition energies E_i that can be associated with critical points (van Hove singularities) in the joint valence-conduction density of electronic states **[I.34]**. In most alloys and solid solution semiconductors the energies $E_i(x)$ of the critical point features are found to have a smooth compositional dependence that can be well described by a quadratic polynomial of the form:

$$E_i(x) = E_i^A x + E_i^B(1-x) - b_i x(1-x)$$

where A and B refer to the two crystalline semiconductor systems being alloyed. The coefficient b_i is called the bowing parameter. Knowledge of the bowing parameter is very important for applications, particularly when the transition in question corresponds to the lowest-energy gap.

Figure I.12 shows a Ge-like band structure with the indication of the most important critical points. In **Refs. [I.14, I.35]**, ellipsometry and photoreflectance experiments were applied to study several samples with different concentrations of Sn

and compared with several simulations shown in **Refs. [I.36 – I.38]**. The results for E_0, E_1 and $E_1 + \Delta_1$ critical points can be seen in **Figure I.13** and **Figure I.14**. The study of these critical points accompanied by band structure calculations help to better predict the indirect-to-direct band gap crossover (see **Figure I.15**). Using absorption measurements, He and Atwater **[I.36]**, and Pérez Ladrón de Guevara *et al*. **[I.39]** determined the crossover concentration of x_c ≈ 0.1. On the theoretical side, the crossover of $Ge_{1-x}Sn_x$ from an indirect to a direct band gap material as a function of Sn content has been predicted to occur for a value of x between 0.06 and 0.1 for the unstrained material **[I.14, I.36, I.39 – I.42]**. For pseudomorphic $Ge_{1-x}Sn_x$, considerably higher values have been predicted, x_c ≈ 0.17 **[I.43]** or x_c ≈ 0.19 **[I.42]**.

Recently, a lot of experimental progress **[I.44 – I.47]** has been made towards producing GeSn solid solutions with Sn concentrations above the thermodynamic solubility of Sn in Ge, which is less than 0.5 at. % **[I.30, I.31]**, and direct band-gap behaviour was observed in the partially relaxed alloy $Ge_{0.874}Sn_{0.126}$ on Si **[I.48].**

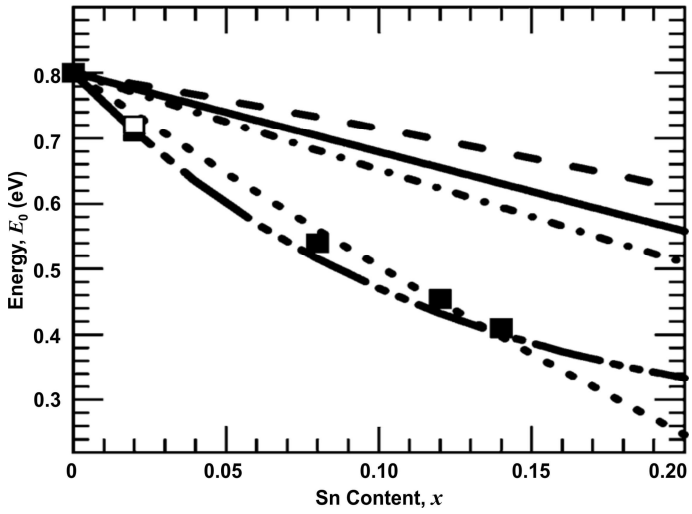

Figure I.13: Compositional dependence of the direct gap, E_0, in $Ge_{1-x}Sn_x$ alloys at room temperature. The solid squares indicate band gaps obtained from ellipsometry; the empty square represents a photoreflectance result. The top dashed line represents virtual crystal approximation (VCA) pseudopotential calculation results [I.37]. The solid line is a linear interpolation between Ge and α-Sn (see Figure I.10). The dashed-dotted line is a VCA calculation within a tight-binding formalism [I.36]. The dotted line is a fit with a quadratic polynomial equation, and the dashed/double-dotted line is obtained using the compositional-dependent bowing proposed by Chibane *et al.* [I.38]. Figure adapted from [I.14, I.35]

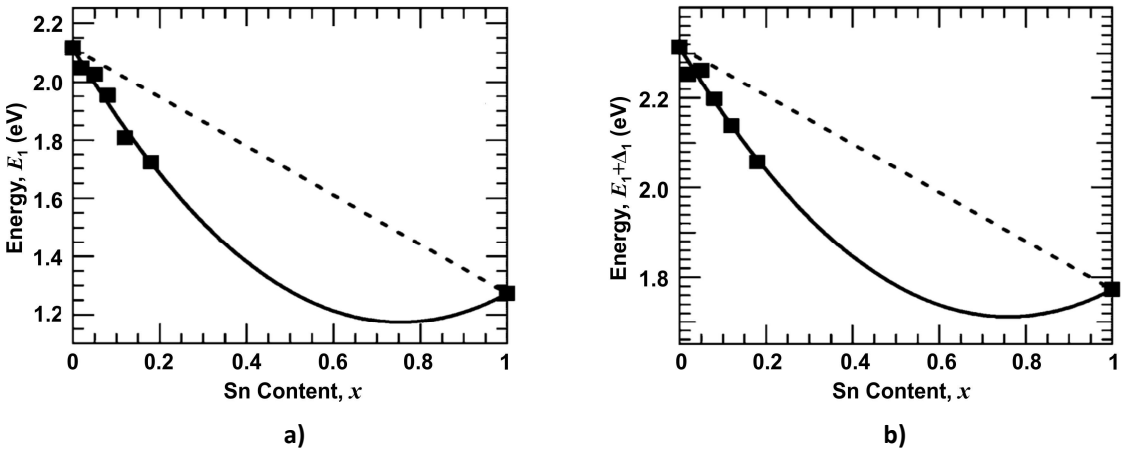

Figure I.14: Compositional dependence of the E_1 (a) and $E_1+\Delta_1$ (b) transition energies in $Ge_{1-x}Sn_x$ solid solution. Figure adapted from [I.14, I.35]

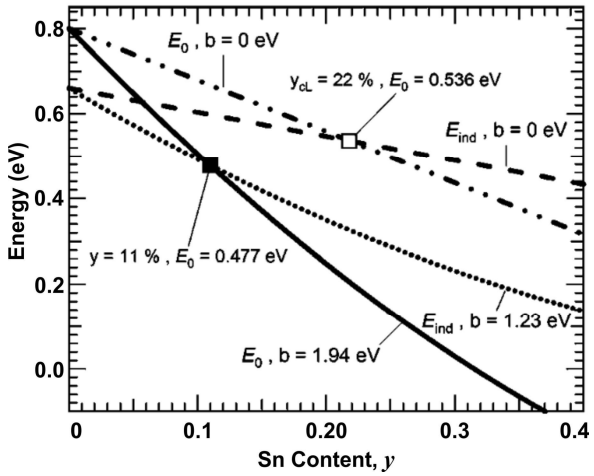

Figure I.15: Predicted compositional dependencies of the direct and indirect band gap energies in $Ge_{1-y}Sn_y$ solid solutions. The dashed-double-dotted and dashed lines represent linear interpolations between Ge and α-Sn (see Figure I.10). The solid line is experimental result for the direct gap. The dotted line represents the indirect gap computed with the bowing parameter, b_{ind} = 1.23 eV. Figure adapted from [I.35]

I.2.3. GeSn and High Mobility

Recently silicon microfabrication technology has reached a stage in increasing processing speed where the heat generated during the switching of transistors is beginning to limit the speed. Therefore it is attractive to consider higher mobility semiconductors.

The experimentally measured **[I.49]** large temperature dependence of mobilities in diamond and zinc-blende structure semiconductors indicates that phonon scattering

dominates the carrier mobility. Since both the electronic structure and the electron-phonon couplings in these semiconductors are well understood, several first principles' calculations of the mobilities for a number of semiconductors (Ge, Si, GaAs, SiGe alloys, etc) have been successful. Based on those previous results, Cohen and Sau showed that adding Sn can improve the carrier mobility **[I.13]**. They modelled bilayers of biaxial strained GeSn with buffer layers of GeSn to obtain direct gap GeSn and with high mobility. They reached mobilities of 20000 $cm^2V^{-1}s^{-1}$ for electrons and 10000 $cm^2V^{-1}s^{-1}$ for holes, which are two times more that would be expected for biaxial-strained Ge. The same authors in **Ref. [I.50]** concluded that this material could reach carrier mobilities as high as 10^5 $cm^2V^{-1}s^{-1}$.

I.2.4. GeSn Growth

The synthesis of germanium-tin alloys requires conditions of non-equilibrium and then growing $Ge_{1-x}Sn_x$ solid solutions are limited to thin films. Nevertheless, significant efforts have been devoted to the growth of $Ge_{1-x}Sn_x$ solid solutions. The required conditions of growth and the necessary quality of the material for micro-electronic applications are limited to two growth methods: molecular beam epitaxy (MBE) and (ultra high vacuum) chemical vapour deposition (CVD) **[I.14, I.30, I.31]**.

Molecular beam epitaxy is a physical deposition technique based on the evaporation or sublimation of ultrapure elements under ultra-high vacuum in order to create a pure, pollution-free film. One or more thermal beams of atoms or molecules react on the surface of a single-crystal wafer, which serves as a lattice for the formation of an epitaxial film. **Chapter II.2** provides an extensive description of a MBE system employed to grow part of the samples used in this study.

Chemical vapour deposition is a chemical process used to produce high-purity, high-performance solid materials. In CVD process, the substrate is exposed to one or more volatile precursors, which react and/or decompose on the substrate surface to produce the desired deposit. Frequently, secondary volatile products are also produced, which are removed by gas flow through the reaction chamber.

I.2.5. GeSn-on-Si

One important factor for the integration of GeSn in integrated circuits, optoelectronics or even photonic integrated circuits, is the growth of epitaxial germanium-tin on silicon. CMOS compatibility is important to guarantee low cost in mass production. It is necessary to remember that GeSn solid solutions have a much larger lattice constant than Si. Moreover, the lattice constant of Ge is 4 % larger that of Si and this poses a problem when Ge needs to be grown on a silicon substrate. The strain resulting from the lattice mismatch builds up with film thickness and causes dislocation defects. Despite these challenges, excellent progress has been made towards Ge-on-Si detectors **[I.51 – I.53]** with speeds even higher than III-V detectors. Example of this are the p-i-n detectors of 49 GHz **[I.51]** developed by the Institute for Semiconductor Engineering (IHT, Stuttgart University) and the avalanche detector of 340 GHz developed by Intel **[I.53]**.

In what concerns alloy layers on silicon, Bauer *et al* **[I.10]** grew samples of GeSn-on-Si(100) and analysed them by cross-section electron microscopy (XTEM) (see **Figure I.16)**. The XTEM studies revealed thick single-crystal layers with low concentration of threading defects. The images in the (100) projection showed occasional threading dislocations and {111} stacking faults sometimes extending through to the uppermost surface. They estimated the density of these defects as ~10^7/cm^2, a value well within the levels considered acceptable for device applications The predominant defects accommodating the large misfit are Lomer edge dislocations at the interface which are parallel to the interface plane.

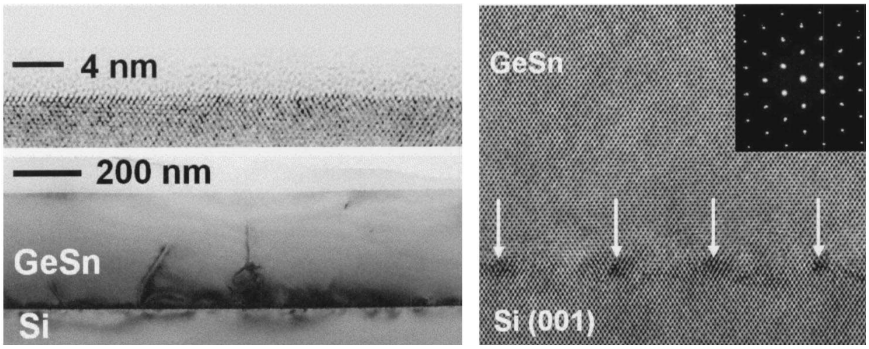

Figure I.16: Cross-sectional electron micrographs of $Ge_{0.94}Sn_{0.06}$. Left top panel shows atomically flat film surface morphology, left bottom panel shows the exceptional uniformity of the film thickness. Right panel is a high-resolution electron micrograph of the interface region showing virtually perfect epitaxial growth. Arrows indicate the location of misfit dislocations. [I.31]

I.2.6. Applications of $Ge_{1-x}Sn_x$

GeSn solid solutions are an interesting family of materials due to their predicted properties, namely, high carrier mobility, direct band gap crossover, large lattice constant, and good absorption for lower energies in relation to pure Ge. These characteristics provide, at least, five potential applications: lasers, photodetectors, buffer layers, photonic modulators and faster electronic circuits.

The direct consequence of direct band gap crossover is the possibility to use GeSn as active layers for LEDs and lasers. Since the direct band gap is related with the Sn concentration, it can be used to produce active layers with different emission wavelength. This allows the wavelength-division multiplexing (WDM) capacity without use frequency shifters that would bring several other difficulties unnecessarily.

In photonic integrated circuits, Ge is mostly used for photon detection because it can absorb in all important fibre-optic telecommunication wavelengths (780, 980, 1310 and 1550 nm), and high quality Ge-on-Si is possible. Although simple p-i-n detector is able to work with speeds higher than 49 GHz **[I.51]**, there is a demand for higher speeds and higher responsivities. The introduction of small quantities of tin in these detectors can improve the absorption and, consequently, the responsivity. For example, in **[I.54]**, a 0.5 at % concentration of Sn was used, and it was capable to improve the responsivity three times for 1550 nm, the most important wavelength in telecommunications (**Figure I.17**). Because the band gap of this material can be tuned down to very small energies (≈ 0.2 eV without segregation of Sn) with the concentration of Sn, GeSn is also a good candidate to produce new near-to far-infrared photodetectors.

Lattice constant of the $Ge_{1-x}Sn_x$ solid solutions it is also dependent of x. Varying x it can be adjusted to grow other materials on GeSn, *i.e.*, using GeSn as buffer layers. Examples of this are the GeSnSi-on-GeSn-on-Si (see **Figure I.18**), and GaAs-on-GeSn-on-Si (see **Figure I.19**) heterostructures. This can provide large and low cost virtual substrates of material that in general are expensive and only exist in small dimensions substrates like GaAs.

As it has been discussed previously, one of the interesting properties of GeSn is the potential for high carrier mobility. High mobility channels are indispensable to

continue MOSFET technology improvements. In **Ref. [I.55]**, the authors try to use a new architecture for Ge p-MOSFET using GeSn as source/drain materials as uniaxial compressive stressors for Ge channels, taking advantage of the Ge/GeSn lattice mismatch. High mobility also provided the potentiality to have faster integrated circuits, and can be used in faster modulators for photonic integrated circuits.

Recent years have seen increased efforts in the search for all-group-IV light emitters. While progress on solely Ge-based light emitters has been made **[I.56]**, a large amount of research has been devoted to investigating $Ge_{1-x}Sn_x$ solid solutions as a candidate for a Group-IV direct band gap material for both light sources and detectors **[I.14, I.44 – I.48, I.57 – I.59]**. For instance, lasing has been observed in the partially relaxed direct-bandgap alloy $Ge_{0.874}Sn_{0.126}$ on Si **[I.48]**.

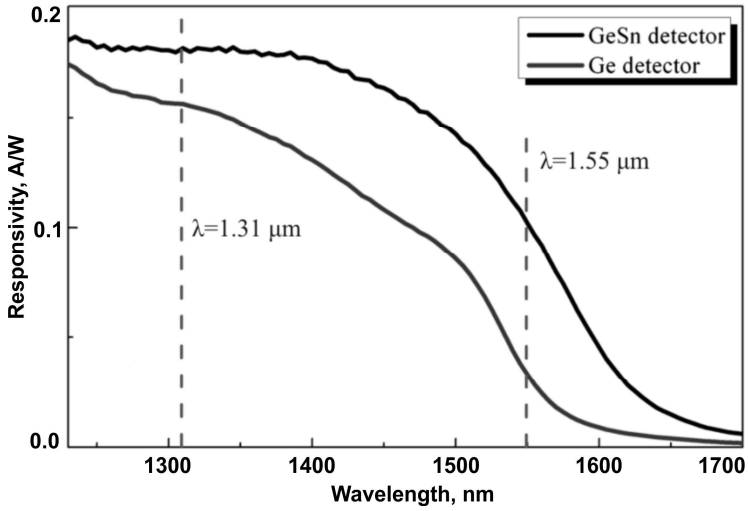

Figure I.17: Optical responsivity from a GeSn p-i-n photodetector and a similar one of Ge without Sn. Dashed lines denote two important wavelengths used in telecommunications. [I.54]

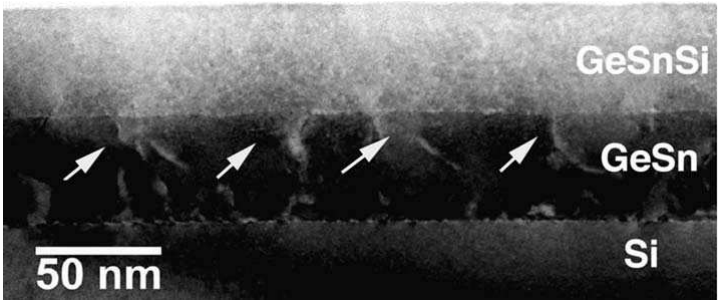

Figure I.18: XTEM of a highly mismatched GeSiSn/GeSn/Si heterostructure. The top layer is defect free and displays a flat surface. The defects are concentrated in the buffer layer. Defects originating at the GeSiSn/GeSn interface appear to be absorbed by the softer GeSn buffer layer (arrows). [I.14]

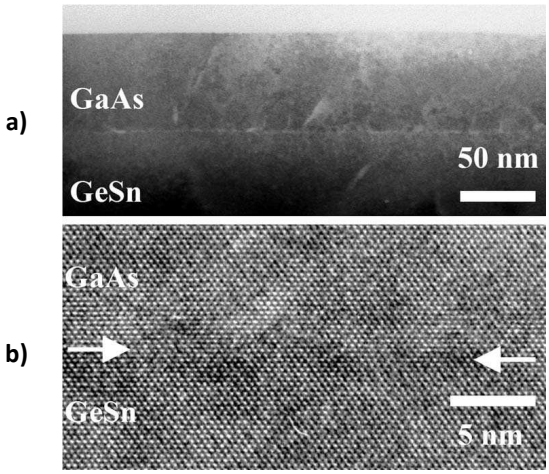

Figure I.19: XTEM micrographs of the GaAs/GeSn interface: a) bright-field image, b) GaAs/GeSn interface region (arrows indicate interface). [I.14]

I.3. Low-Dimensional Structures of Group IV Materials

An alternative approach to the problem of obtaining direct band gap in Group IV materials consists in employing quantum confinement. The epitaxial growth of self-assembled Ge quantum dots (QDs) on Si has been studied for several decades **[I.60, I.61]**. When depositing a few monolayers (MLs) of Ge on a Si substrate, the lattice mismatch between Ge and Si results in the growth of Ge QDs by the well-known Stranski-Krastanov (S-K) mechanism **[I.62]** (see **Section II.1**). The size and distribution of the Ge dots are strongly influenced by the growth parameters used. When multiple layers of Ge dots are grown, each QD layer is capped by a silicon layer that forms a spacer between two adjacent Ge dot layers. This Si cap also modifies dot properties such as material composition, dot geometry and strain **[I.63**, **I.64]**. The carrier confinement inside the Ge QD embedded in a Si matrix influences the optical properties of the structure **[I.65]** and makes Ge self-assembled dots particularly interesting for optoelectronic device applications such as photodetectors.

While the above approaches were concerned with growth of bulk GeSn, several approaches have been tried to produce Sn or $Ge_{1-x}Sn_x$ nanostructures, namely: Sn dots were grown on Ge **[I.66]**, $Ge_{1-x}Sn_x$ dots were grown on thin SiO_2 layers on top of Si (111) substrates **[I.67]** and Sn nanostructures were also embedded into a Si or Ge matrix by annealing of SiSn or GeSn films **[I.68]**. So far, none of these approaches have lead to direct bandgap nanostructures that were embedded within Si or Ge devices.

I.4. Zinc Oxide (ZnO)

The interest reborn on Zinc Oxide (ZnO) in the last decade was due to the possibility of using it for a number of device applications and goes back to the principles of century when the first published works in the structural, optical and electrical characteristics were published **[I.69 – I.72]**. Since then, this transparent semiconductor became attractive to the scientific community. Indeed, the renewed interest in ZnO was mainly due to the development (in the 1990s- focused on the production of GaN for device applications) of semiconductor thin film growth by vapour phase epitaxy (*i.e.* MOVCD and MOVPE) and by molecular beam epitaxy (MBE). Since GaN is a semiconductor with characteristics similar to ZnO, the ZnO community has strengthened the interest in this semiconductor oxide which presented itself as a potential alternative to GaN, with lower production costs, allowing analogous ZnO-based devices to be competitive market **[I.73]**. However, ZnO is intrinsically *n*-type doped, and it has not yet been possible to obtain *p*-type ZnO in a controlled and reproducible way. Nowadays, this is one of the most investigated subjects in what concerns this material together with a deepening of the knowledge of its physical properties and different processing methodologies.

ZnO is a semiconductor with a direct energy gap (E_g) of ≈3.37 eV at room temperature **[I.74]**. This material can crystallize in the cubic structures or in the modified hexagonal structure of wurtzite, depending on the growth temperature and pressure. This last one, belonging to the space group $P6_3mc$ ($C^4 6v$), corresponds to the crystalline structure more stable at atmospheric pressure and has the following lattice constant: a_0 = 3.2496 Å and c_0 = 5.2042 Å **[I.75]**.

In the wurtzite phase the anion is coordinated by four cations forming a tetrahedron, and vice versa. In this type of coordination, covalent bonds are favoured by sp^3 hybridization (see **Figure I.20**). The structure has a polar direction (*c*-axis) and can be described as two sublattices with compact hexagonal packaging (hcp) displaced along the vertical axis, as seen in **Figure I.21**. The unit cell includes two molecules of ZnO, *i.e.* four ions.

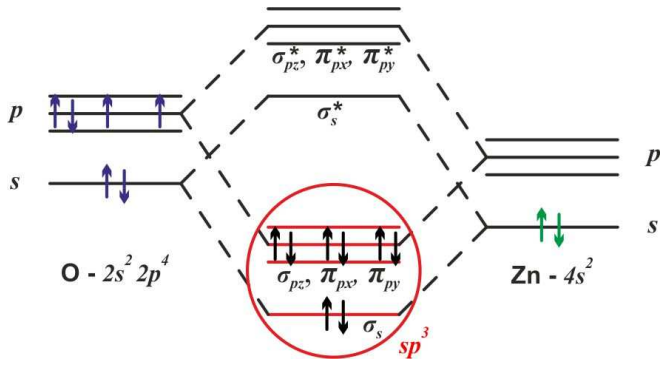

Figure 20: Schematics of the formation of sp^3 hybrid bonding states in ZnO.

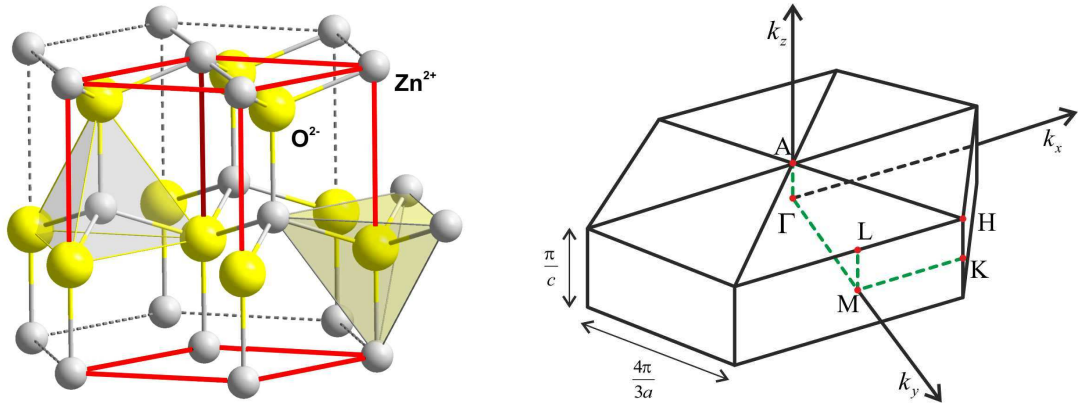

a) **b)**

Figure I.21: a) Illustration of the wurtzite ZnO structure; [I.7] b) The first Brillouin zone for the ZnO.

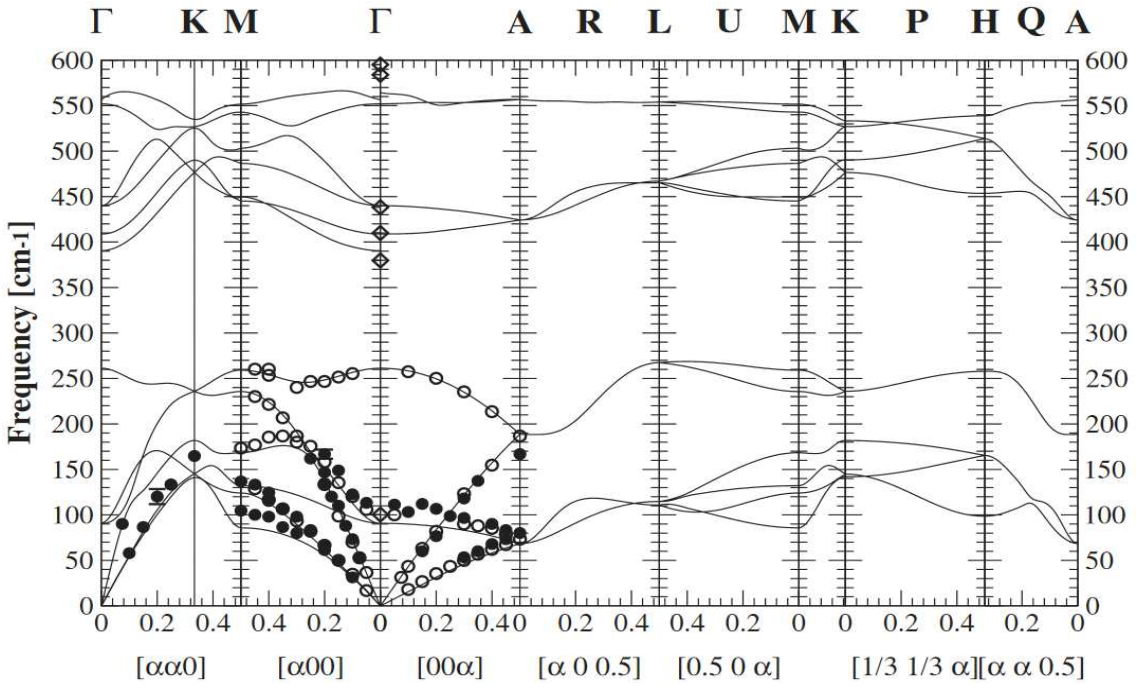

Figure I.22: Calculated ZnO band structure. The solid and open circles represent inelastic neutron data at room temperature from Refs. [I.76] and [I.77], respectively, and the open diamonds represent Raman data for natural ZnO at 6 K from Ref. [I.78]. Figure adapted from [I.79]

The wurtzite structure is similar to zinc-blende, but with a hexagonal distortion. This distortion produces a crystal field energy that splits and mixes the Γ_8 and the Γ_7 states. **Figure I.22** illustrates the electronic band structure for ZnO calculated using *ab initio* density functional theory (DFT) method. Since the valence band maximum and the conduction band minimum occur at the Γ point ($\vec{k}$ =0) of the 1st Brillouin zone, this is a direct gap semiconductor. **Figure I.23** shows the splitting of the valence band by crystalline field effect and spin-orbit interaction. The valence band built mostly from the p-orbitals of oxygen (Γ_1 and Γ_5 symmetries) splits into three bands (A, B and C in the figure). The lowest energy conduction band, constructed mainly from states 4s of Zn has symmetry Γ_7. **Table I.2** shows some of the most relevant properties of ZnO, a semiconductor material on which is focused all the work presented in **Chapter V** of this dissertation. The vibrational properties of wurtzite structure crystals such as ZnO are discussed in **Chapter III**.

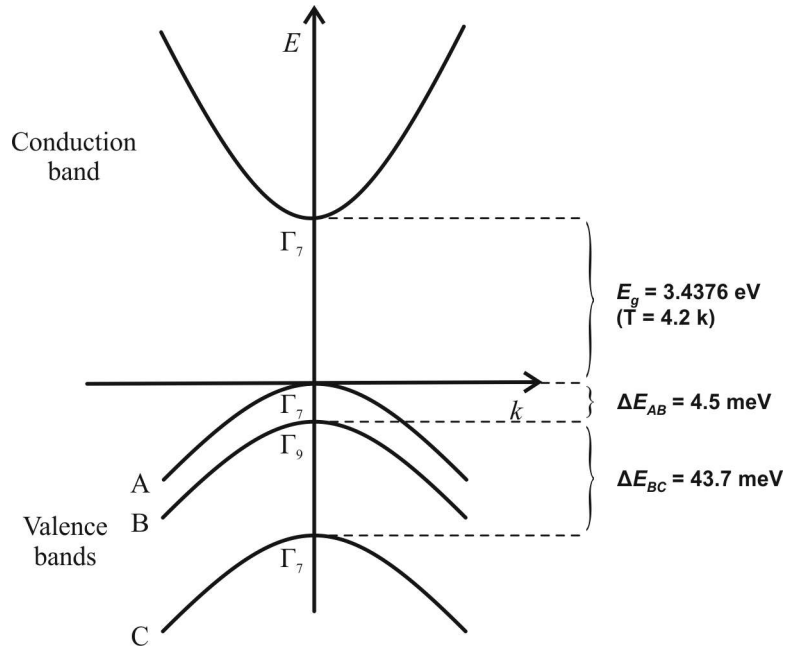

Figure I.23: Scheme illustrating the band structure of ZnO, with the splitting of the valence band by crystalline field effect and spin-orbit coupling [I.79, I.80].

Table I.2: Some properties of ZnO in the wurtzite phase. [I.79]

Properties	**Value**
Stable phase (300 K)	Wurtzite
Lattice constant	a_0 = 3.2495 Å c_0 = 5.2059 Å a_0/c_0 = 1.602 (ideal hexagonal: 1.633)
Density	5.606 g/cm^3
Melting point	1975^{o}C
Thermal conductivity	0.6 to 1.4 W cm^{-1} K^{-1}
Thermal expansion coefficient (300K)	$\Delta a/a_0$: 4.31x10^{-6} $\Delta c/c_0$: 2.31x10^{-6}
Dielectric constant	8.656
Refraction index	E // c = 2.008 E ⊥ c =2.029
Energy gap (E_g)	3.37 eV (RT) 3.4376 eV (T = 4.2 K)
Bound exciton energy	60 meV
Intrinsic carrier concentration	>10^6 cm^{-3} (maximum *n-type* > 10^{20} cm^{-3} ; *p-type* > 10^{17} cm^{-3})
Electron effective mass (m/m$_0$)	0.24
Hole effective mass (m/m$_0$)	0.59
Electron mobility (300K)	200 cm^2/V s
Hole mobility (300K)	5-50 cm^2/V s

I.5. ZnO:Mn, a Transparent Magnetic Semiconductor

In the last few decades researchers studied the possibilities of controlling the intrinsic electron spin in solid state media. In 1985, Johnson and Silsbee **[I.81]** observed the spin-polarized electron injection from a ferromagnetic metal to a normal metal and, since then, the development of devices capable of using the advantages of spin control is being explored. Nowadays, the research field that studies the spin of the electrons and its associated magnetic moment, in addition to its electric charge, in solid-state devices, is known as spintronics. The most known applications of spintronics are the read heads used in computer hard drives and, to a smaller extent, in magnetoresistive random-access memory (MRAM) devices. Yet, one of the biggest aspirations for spintronics applications lies in the field of quantum computing.

The control of the spin is done by using the magnetic properties of the material. Then, in order for the spintronics components to be easily integrated into the traditional electronics, it is advantageous to use of semiconductors with magnetic properties is desirable. To archive strong magnetic properties, semiconductors can be

doped with transition metals, such as Co, Mn, Fe, Ni, etc. The result is a Dilute Magnetic Semiconductor (DMS). An example of such material is $Cd_{1-x}Mn_xTe$ (or CdTe:Mn) which has a large Faraday effect (see **Chapter II** and **Appendix B**). However, this material is opaque for visible light. As stated above, in this work the focus is on ZnO:Mn which is transparent in the visible range thanks to its large band gap. Still, in the following section it will be provided a brief overview of other DMSs.

I.5.1. Diluted Magnetic Semiconductors

The magneto-optical response of dilute magnetic semiconductors can be understood by recalling the hybridization of *d*-electron states of transition metal ions with the *sp*-band electron (*sp-d* exchange interaction). These interactions can cause large Zeeman splitting and magneto-optic (MO) effects. In dilute magnetic semiconductor materials, both the charge and spin of the electrons can be used for device operations. Doping of semiconductors with transition metal (TM) elements offers a viable means of tuning the optical band gap of the material and achieving the ferromagnetism.

Dietl *et al.* in **[I.82]** predicted room temperature ferromagnetism in a range of *p*-doped semiconductors including ZnO containing 5% of manganese (see **Figure I.24**). The prediction was made for the *p* doped material because the interaction between magnetic *d* electrons in the manganese atoms and the oxygen *p* electrons in the valence band was known to be much stronger than their interaction with the *s* electrons in the conduction band. As in the case of GaAs:Mn, which also is of the *p* type, it is necessary to have unequal filling of the magnetically split valence band to stabilize ferromagnetism. The mechanism of coupling (indirect exchange interaction) between localized core spins of the Mn atoms mediated by the valence band electrons is known as Ruderman–Kittel–Kasuya–Yosida (RKKY) model. Within this model, the spin-spin interaction parameter oscillates (and also decreases) with the distance.[2]

[2] Concerning GaAs:Mn, there are experimental results that contradict the RKKY model predictions.

More precisely, this model includes a sum of Friedel oscillations with the Fermi wavevectors of the different types of free carriers that mediate the spin-spin coupling, such as light and heavy holes in a heavily *p*-doped semiconductor. Moreover, the spin splitting leads to the occurrence of various contributions to the RKKY coupling which are characterized by different distance dependencies and various characteristic lengths. Consequently, the effective magnetic field created by all other atomic spins, acting on a particular spin $\vec{S}_j$, equal to $\vec{B}_i = \sum_{j \neq i} \hat{J}_{ij} \vec{S}_j$ with $\hat{J}_{ij}$ denoting the exchange integrals, may have random directions and magnitudes in a system of randomly distributed spins and, therefore, no magnetization exist. Such a state of a diluted magnetic is called spin glass. However, there are statistical-mechanical arguments in favour of an ordered ground state even for a system of spins that occupy random positions in the lattice and coupled via interactions that oscillate in space **[I.83]**. It means that there should be spin alignment necessary for the ferromagnetism below a certain critical temperature (similar to usual ferromagnetics it can be called Curie temperature). With this theoretical background and based on the first-principle calculations of the exchange parameters first performed by Dietl *et al.*, numerous experimental works have been dedicated to the search of ferromagnetism in diluted magnetics semiconductors. To the best of our knowledge, no convincing and reproducible room temperature ferromagnetism in any of the materials shown in **Figure I.24** has been presented so far. Moreover, theoretical arguments have been presented in support of absence of ferromagnetism in DMSs **[I.84]** and the authors of this article consider incorrect the results of T. Dietl *et al.* **[I.82]**. Even though, many works dedicated to DMSs are published every year, so the impossibility of room tempearure ferromanetism in these materials has not completely been accepted by the scientific community so far. In particular, defect- or surface-related magnetism still could be possible **[I.84, I.101]**.

ZnO based DMSs have some advantages over others because of the large band gap and, consequently, high transparency to the visible and near infrared light, large exciton binding energy and, consequently, the existence of excitons even at room

temperature, and a large interband transition oscillator strength. When doped with transition metal ions, particularly Mn, ZnO is a potential candidate for high Curie temperature magnetism. These features make ZnO:Mn a good candidate for the fabrication of various optoelectronic and possibly also magneto-optical devices.

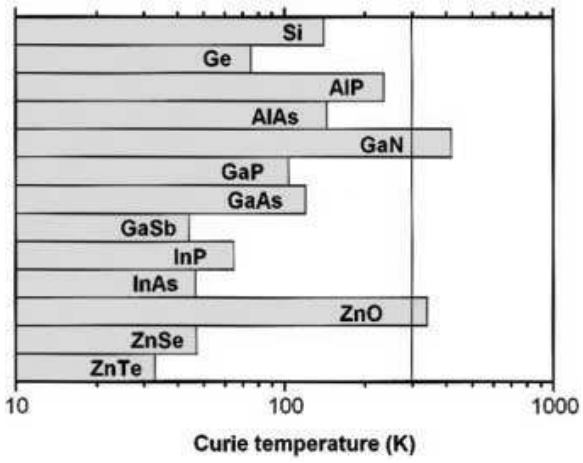

Figure I.24: Theoretical predictions of the Curie temperature, T_C, for various p-type semiconductors (3.4x10^{20} holes per cm^3) containing 5% of Mn. [I.82]

I.5.2. Magneto-Optical Response of a DMS

The first theoretical description concerning the magneto-optical response of the DMS material of a wurtzite structure was developed by M. Arciszewska and M. Nawrocki **[I.85]** who proposed a complete set of band parameters and exchange integrals for CdSe:Mn ($Cd_{1-x}Mn_xSe$). When compared with the cubic phase, the wurtzite structure brings more complexity to the description because it has a more complicated valence band structure due the crystal field splitting and spin-orbit (SO) interaction anisotropy, which implies the analyses of a larger number of parameters.

The results of the work **[I.85]** can be applied to the case of ZnO:Mn **[I.86]**. The theoretical description of the magnetic-optical response requires the consideration of the complete Hamiltonian including the exchange interaction between localized Mn^{2+} ions and band electrons mentioned above. The resulting Hamiltonian is a simple sum of the wurtzite crystal Hamiltonian, H_{wur} **[I.87 – I.92]**, and an exchange term H_{ex}:

$$H = H_{wur} + H_{ex}. \qquad \{I.2\}$$

Still certain changes of the original wurtzite Hamiltonian may be expected due to the presence of substitution manganese ions in the crystal.

The exchange term is usually expressed in the Heisenberg form[3]:

$$H_{ex} = \sum_i J\left(\vec{r} - \vec{R}_i\right)\hat{\mathrm{S}}_i \cdot \hat{\sigma}\,, \qquad \textbf{\{I.3\}}$$

where $\hat{\mathrm{S}}_i$ and $\hat{\sigma}$ are the spin vector operators of the manganese ion localized at the site $\vec{R}_i$ and of the band electron, respectively, and $J\left(\vec{r} - \vec{R}_i\right)$ is the electron-ion exchange coupling constant. The exchange term can be simplified by using the mean field approximation[4] and the virtual crystal model:

$$H_{ex} = x\left\langle \hat{S}_z \right\rangle \sum_{\vec{R}} J\left(\vec{r} - \vec{R}\right)\hat{\sigma}_z \qquad \textbf{\{I.3\}}$$

where x denotes the manganese content, $\langle S_z \rangle$ is the thermal average of the Mn^{2+} spin component along the external magnetic field and $\vec{R}$ is the cation lattice vector. One can notice that, according to **{I.3}**, the entire exchange contribution vanishes in the absence of an external magnetic field ($\langle S_z \rangle = 0$).

By virtue of H_{ex}, the conduction band splits into two sub-bands corresponding to the two spin orientations of the electron **[I.85]**. The splitting energy denoted as $2A$ is:

$$2A = N_0 \alpha\, x\langle S_x \rangle \qquad \textbf{\{I.4\}}$$

with

$$\alpha = \langle s | \hat{J} | s \rangle \qquad \textbf{\{I.5\}}$$

where N_0 is the number of unit cells per unit volume and α is the exchange integral for the *s*-like conduction band electrons ($\hat{J}$ is the exchange operator).

---

[3] The Heisenberg model is a statistical mechanical model used in the study of critical phenomena and phase transitions in magnetic systems, in which the spins of the magnetic systems are treated quantum mechanically.

[4] The mean field theory studies the behaviour of large and complex stochastic models by studying a simpler model. The models consider a large number of small individual components which interact with each other. The effect of all the other individuals on any given individual is approximated by a single averaged effect, thus reducing a many-body problem to a one-body problem.

The influence of the presence of manganese ions on the valence band electronic states is more complicated. First, the exchange splitting of the electronic states here occurs similar to the conduction band. Secondly, the *p-d* exchange interaction affects the electron wave functions, leading to a change in the coefficients describing the mixing of wave functions with opposite spin directions for the sub-bands' splitting in the effective magnetic field introduced by the magnetic ions **[I.85].** The upper three valence bands (A, B and C, see **Figure I.23**) are split by the combined effects of the anisotropic crystal field and the spin-orbit interaction and are twofold spin degenerate **[I.85]**. The energies of these A, B, C bands can be expressed in terms of three band parameters, namely, the crystal field splitting constant, Δ_1, and the two spin-orbit coupling constants, Δ_2 and Δ_3 **[I.89]**. Neglecting the spin-orbital coupling constant anisotropy, i.e. setting $\Delta_2 = \Delta_3$ the energies became:

$$E_A = \Delta_1 + \Delta_2, \qquad \{I.5a\}$$

$$E_{B,C} = \frac{\Delta_1 - \Delta_2}{2} + \sqrt{\left(\frac{\Delta_1 - \Delta_2}{2}\right)^2 + 2\Delta_2^2}\,. \qquad \{I.5b\}$$

The corresponding wave functions are:

A: $\left|+\frac{3}{2}\right\rangle = \left|1,\uparrow\right\rangle$ $\left|-\frac{3}{2}\right\rangle = \left|-1,\downarrow\right\rangle$ **{I.6a}**

B: $\left|+\frac{1}{2}\right\rangle = \sqrt{1-b^2}\left|1,\downarrow\right\rangle + b\left|0,\uparrow\right\rangle$ $\left|-\frac{1}{2}\right\rangle = -\sqrt{1-b^2}\left|-1,\uparrow\right\rangle + b\left|0,\downarrow\right\rangle$ **{I.6b}**

C: $\left|+\frac{1}{2}\right\rangle = b\left|1,\downarrow\right\rangle - \sqrt{1-b^2}\left|0,\uparrow\right\rangle$ $\left|-\frac{1}{2}\right\rangle = b\left|-1,\uparrow\right\rangle + \sqrt{1-b^2}\left|0,\downarrow\right\rangle$ **{I.6c}**

where $\uparrow$ and $\downarrow$ denote the spin functions with spin vector parallel and anti-parallel to the z-axis, and the mixing parameter, b, is given by:

$$b^2 = \frac{1}{2}\left[1 - \frac{\Delta_1 - \Delta_2}{2\sqrt{\left(\frac{\Delta_1 - \Delta_2}{2}\right)^2 + 2\Delta_2^2}}\right]. \qquad \{I.7\}$$

For pure ZnO, the crystal field splitting constant, Δ_1, and the spin-orbit coupling constant were measured as Δ_1 = 0.043 eV, Δ_2 = 0.005 eV **[I.93, I.94]**, and consequently b^2 = 0.031.

The eingenvalues of the complete Hamiltonian **{I.2}** are given by:

$$E_A^{\pm} = \Delta_1 + \Delta_2 \pm B, \qquad \textbf{\{I.10a\}}$$

$$E_B^{\pm} = \frac{\Delta_1 - \Delta_2}{2} + E_{\mp}, \qquad \textbf{\{I.10b\}}$$

$$E_C^{\pm} = \frac{\Delta_1 - \Delta_2}{2} - E_{\mp}, \qquad \textbf{\{I.10c\}}$$

$$E_{\mp} = \sqrt{\left(\frac{\Delta_1 - \Delta_2}{2} \mp B\right)^2 + 2\Delta_2^2}, \qquad \textbf{\{I.10d\}}$$

$$B = 1/2\, N_0 \beta x \langle S_z \rangle, \qquad \textbf{\{I.10e\}}$$

where β is the exchange integral for the valence band electrons, similar to **{I.5}** but with p-orbitals, $N_0\beta \approx -(1.2-1.3)$ eV **[I.85].**

It can be examined the cases where the crystal field splitting constant, Δ_1, the spin-orbit coupling constant Δ_2, and mixing parameter, b, can be approximated by zero, in order to help a better understanding of the system. If the crystal field splitting constant Δ_1 is set to zero, then it results in a zinc-blend structure ($B = 0$):

$$E_A = E_B = \Delta_2 \qquad \textbf{\{I.11a\}}$$

$$E_C = -2\Delta_2 \qquad \textbf{\{I.11b\}}$$

with a mixing parameter of b^2 = 2/3. Consequently, the intensity ratio of the σ transitions from the heave and light holes is 3:1 and the intensity from Γ_7 state is 2/3 that of the heavy holes. These results are well known for cubic semiconductors.

With the "effective magnetic field" term **{I.10e}** added, the energies become:

$$E_A^{\pm} = \Delta_2 \pm B, \qquad \textbf{\{I.12a\}}$$

$$E_B^{\pm} = -\frac{\Delta_2}{2} + \sqrt{\frac{9}{4}\Delta_2^2 + B^2 \pm \Delta_2 B}, \qquad \textbf{\{I.12b\}}$$

$$E_C^{\pm} = -\frac{\Delta_2}{2} - \sqrt{\frac{9}{4}\Delta_2^2 + B^2 \pm \Delta_2 B}. \qquad \textbf{\{I.12c\}}$$

These equations remind the Zeeman splitting of atomic terms with angular momentum 3/2 (states A and B) and 1/2 (state C).

In the case that the spin-orbit coupling constant Δ_2 is small enough that can be neglected, the resulting energies are:

$$E_A^{\pm} = E_B^{\mp} = \Delta_1 \pm B\,, \qquad \textbf{\{I.13a\}}$$

$$E_C^{\pm} = \pm B\,. \qquad \textbf{\{I.13b\}}$$

The observed splitting between A and B valence band is 4.5 meV (see **Figure I.23**), then the crystal-field splitting plays an important role in quenching the orbital angular momentum **[I.85]**. If the spin-orbit coupling is neglected (Δ_2 = 0), the energies of the A and B states are coincident, when the magnetic field is reversed. This has the effect that the magnetic circular dichroism of the A and B states cancel exactly **[I.93]**. The mixing parameter *b* is also important. If the mixing parameter is set to zero, b = 0, the intensities of the A and B states are equal, and C is now a pure m_l = 0 state (m_l denotes the orbital momentum projection). Thus, there are no transitions between the C band and the conduction band, leading to the emission or absorption of circular polarized light. In the absence of the spin-orbit coupling, the spin index is conserved in an electric dipole transition. This is shown in **Figure I.25** where A and B bands almost coincide and the Zeeman splitting (see **Figure I.26**) is purely due to spin.

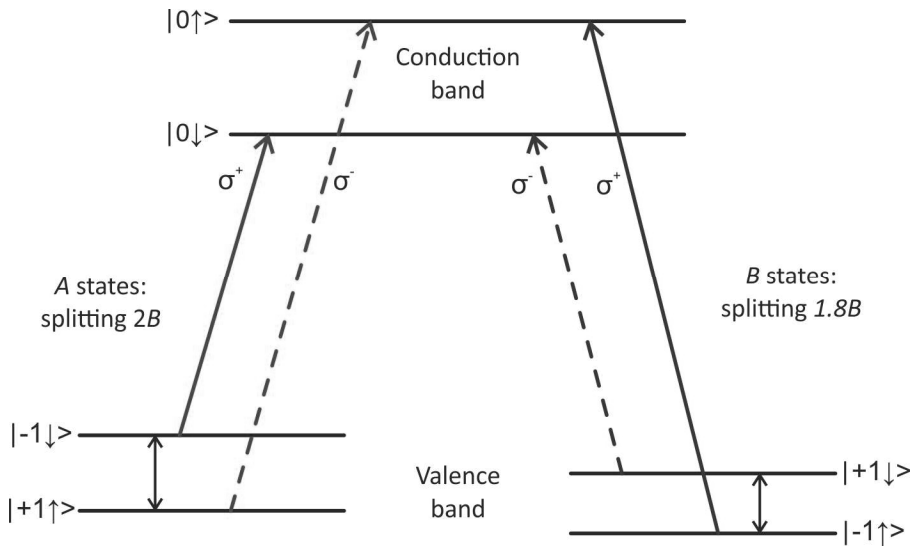

Figure I.25: Schematic demonstration of the relevant transitions for magneto-optical response in ZnO:Mn. The centre of the *A* and *B* levels differ by 4.5 meV. [I.86, I.94]

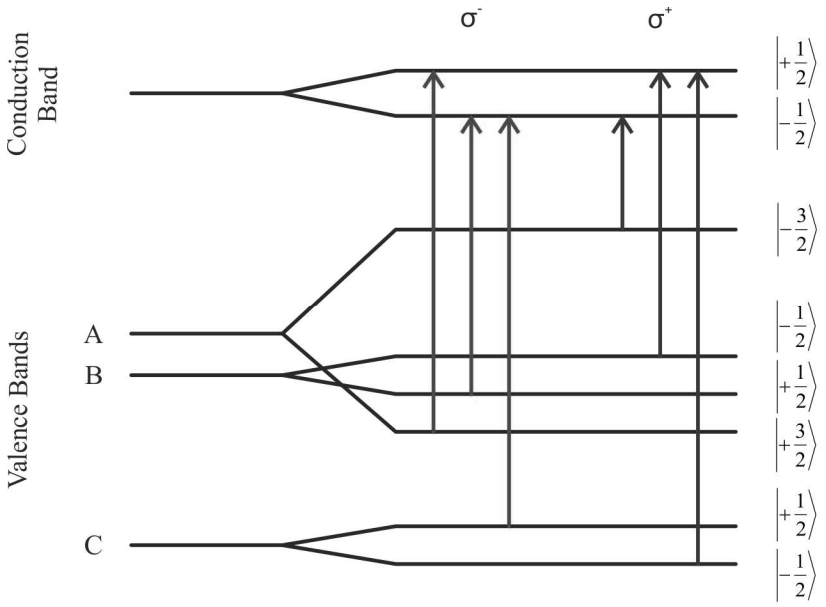

Figure I.26: Scheme of the Zeeman splitting and transitions corresponding to the absorption of σ^+ and σ^- photon in the Γ point in the ZnO doped with Mn.

It is interesting to note that the magnetic response of the ZnO valence band should be very anisotropic because the energies, as given in **Equation {I.13}**, were derived for the average magnetic moment of the localized spins directed along the hexagonal axis. If it were in the orthogonal direction, the A and B states would mix and the magnetism would be reduced. This effect should be important if the valence band is partially occupied **[I.86]**.

In general, two types of transitions can occur in a direct band gap semiconductor: band to band transitions and transitions involving exciton states. Because of the large exciton binding energy, larger than the crystal field splitting Δ_1 and the negligible spin-orbital splitting Δ_2, the excitons from the A, B, and C bands will lie below the smallest direct band gap, E_g^A. As stated above, C-excitons are expected to couple only to linear-polarized light, while A and B excitons couple to σ- polarized photons. It is the lowest energy exciton involving an A band hole that is observed most strongly.

It has been suggested **[I.95]** that the large Faraday rotation below the absorption edge in DMSs is a combined effect of inter-band transitions, bound excitons and intrinsic transitions related to the Mn^{2+} ions. The resulting spectral dependence is rather complex, as will be seen in **Chapter V**.

I.5.3. ZnO Doped with Transition Metals

Neal *el at* **[I.96]** made an extensive magneto-optic study of ZnO doped with transition metals Co, Mn, V, and Ti, founding that significant magnetic circular dichroism occur at the ZnO band edge at room temperature. **Figure I.27a** shows the magnetic circular dichroism of $Zn_{0.98}Mn_{0.02}O$ at 10 K and 300 K. At 10 K, there are characteristic Mn features at ≈ 3 eV from *d-d* transitions on the Mn **[I.97]**. It is also possible that there are minority phases of Mn_2O_3 or Mn_3O_4 **[I.98]**, which have band gaps near the energy where the absorption is observed. Ando *et al.* **[1.93]** showed that there were magneto-optic features at the band edge. The spectra for Mn in this region are rather similar to those for Co (see **Figure I.27a** and **I.27b**). There is a sharp dip at low temperatures that is replaced by a peak at 300 K. In this case, there also is an indication of absorption involving an impurity band at ≈ 3.1 eV at low temperatures. The low and room temperature data were taken at the same value of the magnetic field indicating that the magnetic circular dichroism changes shape as a function of temperature (see **Figure I.27**).

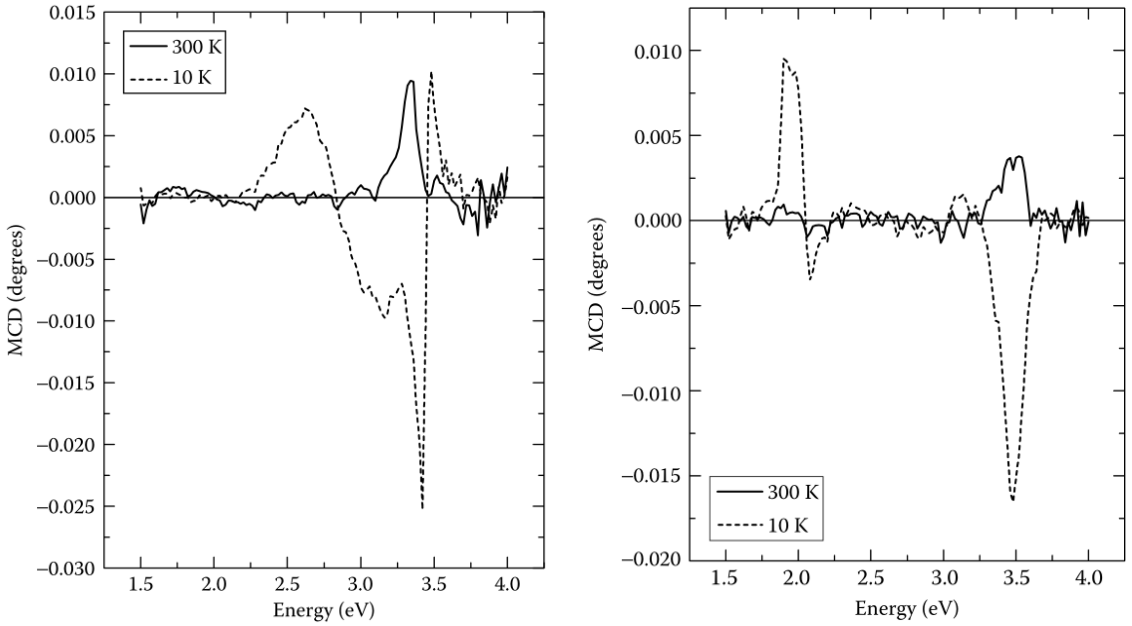

Figure I.27: Magnetic circular dichroism spectra for: a) 2% Mn and b) 2% Co, in ZnO grown by PLD in 10 mtorr of O_2 on C-cut sapphire taken at 10 K and at room temperature (300 K) with the same magnetic field intensity. [I.86, I.96]

1.6. Objectives of This Work

This PhD thesis is focused on Raman spectroscopy studies of two promising semiconductor solid solutions, GeSn and ZnO:Mn, although the author also dedicated considerable efforts and time to their growth and characterisation using a broad range of other techniques. Both studied systems are of high scientific and practical interest owing to their potential applications across multiple areas within the field of modern electronics and photonics.

Silicon, the second most abundant element in the Earth's crust and virtually the ideal material for semiconductor electronics, is not quite suitable for optoelectronics because of its indirect band gap. The GeSn system is considered the best candidate for direct band gap semiconductor compatible with Si CMOS technology, since the adding of tin is supposed to lower the conduction band energy in the Γ point. Therefore GeSn is considered the group IV material with the highest potential to produce laser emission. Theoretical studies **[I.14, I.36, I.39, I.42]** predicted its emission in the mid-infrared (MIR) range, a region lacking efficient lasers, with the emission wavelength controlled by Sn concentration. Furthermore, MIR detectors based on GeSn layers grown on Si substrates were recently developed and their emission has been demonstrated **[I.14, I.44 – I.48, I.57 – I.59]**. Unfortunately, the high density of defects in the GeSn layer results in a rather poor efficiency of the optoelectronic devices demonstrated so far. The present research work has been aimed at better understanding of the lattice dynamics of this solid solution material, in particular, grown on silicon substrates.

Zinc Oxide, a wide band gap semiconductor studied back in the 60-s of the last century, attracted again researchers' attention in the last decades. This is for several reasons: (1) it has a suitable band gap **[I.74, I.99]** for applications with the need of a semiconductor transparent in the visible range; (2) its direct band gap is appropriate for laser emission in the near UV region **[I.100]**; (3) manganese-doped zinc oxide, ZnO:Mn is a diluted magnetic material and if it can be made ferromagnetic under some conditions it will be interesting for spintronics; and (4) it is a cheaper, less dangerous and easier-to-grow material than others with similar properties. Thus, the ZnO:Mn

solid solution is a very interesting material owing to its transparency in the visible range along with the controllable electrical conductivity and predicted ferromagnetic properties at room temperature. Yet, the experimentally observed magnetic properties of this material are a matter of contradiction and one issue is the position that manganese atoms occupy in the ZnO crystal lattice.

The Raman spectroscopy is a powerful non-destructive technique for studying semiconductor materials, sensitive to both vibrational and electronic degrees of freedom. It allows for the determination of atomic vibration frequencies and permits to analyse the crystal symmetry, alloy disorder, electronic resonances, the presence of strain, impurities, defects, *etc*. This capacity makes the Raman spectroscopy a technique of choice in the study of semiconductors through their characteristic lattice modes.

Studies of the lattice dynamics of the two semiconductor solid solutions have been the main goal of this PhD work. A common feature of both alloy systems is the substitutional doping with an element of the same chemical group (Sn/Ge and Mn/Zn), even though it had not been clearly confirmed in the literature for the latter system. On the other hand, there is one important difference between the two systems, related to the atomic mass difference between the dopant and the host. Because of this, a Mn atom inserted into the cationic sublattice of the ZnO crystal originates a local vibrational mode, while the Sn dopant substituting Ge produces a resonant mode overlapping with the continuum of germanium crystal phonons. This promises interesting comparisons between the two systems.

In the course of this project, experimental results obtained by measuring Raman spectra of carefully characterised samples of the two solid solutions have been analysed in the framework of appropriate theoretical models. Their development (such as calculation of the local vibration mode frequency within and beyond the isotope defect model and numerical alloy lattice dynamics calculations using semi-empirical atomic potentials) and their application to these two particular systems has been an important task in this work. The understanding of the lattice dynamics of the studied solid solutions is expected to contribute to the technological development of these materials.

Bibliography

[I.1] G. Busch. *Early history of the physics and chemistry of semiconductors – from doubts to fact in a hundred years*. Eur. J. Phys. **10**, 254, (1989).

[I.2] F. Laeri, F. Schüth, U. Simon, and M. Wark. *Host-Guest-Systems Based on Nanoporous Crystals*. Wiley, Weinheim, USA, 435, (2003).

[I.3] Z. A. Smith, and K. D. Taylor. *Renewable and Alternative Energy Sources: A Reference Handbook.* ABC-CLIO Inc., Santa Barbara, USA, 157, (2008).

[I.4] T. K. Sarkar, R. Mailloux, A. A. Oliner, M. Salazar-Palma, and D. L. Sengupta. *The History of Wireless*. Wiley, Hoboken, USA, (2006).

[I.5] L. Hoddeson, E. Braun, J. Teichmann, and S. Weart. *Out of the Crystal Maze: Chapters in the History of Solid State Physics*. Oxford University Press, New York, USA, (1992).

[I.6] Lorenzo Pavesi, and David J. Lockwood. *Silicon Photonics.* Springer, Germany, 53, (2004).

[I.7] Public domain images. Avaibable at www.wikipedia.com, (June, 2017).

[I.8] John Singleton. *Band Theory and Electron Properties of Solids.* Oxford University Press, Oxford Master Series in Condensed Matter Physics, 36, (2010).

[I.9] http://www.ioffe.ru/SVA/NSM/Semicond/ (March, 7, 2011)

[I.10] Matthew R. Bauer, John Tolle, Corey Bungay, Andrew V. G. Chizmesshya, David J. Smith, José Menéndez, and John Kouvetakis. *Tunable band structure in diamond-cubic tin-germanium alloys grown on silicon substrates.* Solid State Communications **127**, 355, (2003).

[I.11] Otfrid Madelung. *Semiconductors: Data* Handbook. 3nd Edition, Springer, 59 (2004).

[I.12] S. Oguz, William Paul, T. F. Deutsch, B-Y. Tsaur, and D. V. Murphy. *Synthesis of metastable, semiconducting Ge-Sn alloys by pulsed UV laser crystallization.* Applied Physics Letters **43**, 848, (1983).

[I.13] Marvin L. Cohen, and Jay Deep Sal. *Proposal for a high mobility Ge-Sn alloy system*. AIP Conference Proceedings **893**, 189, (2007).

[I.14] J. Kouvetakis, J. Menendez, and A.V.G. Chizmeshya. *Tin-based group IV semiconductors: new platforms for opto- and microelectronics on silicon.* Annual Review of Materials Research **36**, 497, (2006)

[I.15] Pairot Moontragoon, Zoran Ikonić, and Paul Harrison. *Band structure calculations of Si-Ge-Sn alloys: achieving direct band gap materials.* Semiconductor Science and Technology **22**, 742, (2007).

[I.16] James R. Chelikowsky and Marvin L. Cohen. *Nonlocal pseudopotential calculations for the electronic structure of eleven diamond and zinc-blende semiconductors*. Phys. Rev. **B 14**, 556, (1976).

[I.17] J. Weber, and M. I. Alonso. *Near-band-gap photoluminescence of Si-Ge alloys*. Phys. Rev. **B 40**, 5683, (1989).

[I.18] R. Braunstein, A. R. Moore, and F. Herman. *Intrinsic Optical Absorption in Germanium-Silicon Alloys.* Phys. Rev. **109**, 695, (1958).

[I.19] S. Krishnamurthy, A. Sher, and A. –B. Chen. *Generalized Brooks' formula and the electron mobility in Si_xGe_{1-x} alloys*. Appl. Phys. Lett. **47**, 160, (1985).

[I.20] M. V. Fischetti, and S. E. Laux. *Band structure, deformation potentials, and carrier mobility in strained Si, Ge, and SiGe alloys*. J. Appl. Phys. **80**, 2234, (1996).

[I.21] D. Stroud, and H. Ehrenreich. *Band Structure of SiGe: Coherent-Potential Approximation.* Phys. Rev. B **2**, 3197, (1970).

[I.22] K. Zellat, B. Soudini, N. Sekkal, and S. M. Ait Cheikh. *Computational Investigation of Electronic and Optical Properties of Si, Ge and $Si_{1-x}Ge_x$ Alloys Using the FP-LMTO Method Augmented by a Plane-Wave Basis*. American Journal of Condensed Matter Physics **2**, 1, (2012).

[I.23] C. H. L. Goodman. *Direct-gap group IV semiconductors based on tin*. Solid-State and Electron Devices, IEE Proceedings **I 129**, 189, (1982).

[I.24] Steven Groves, and William Paul. *Band Structure of Gray Tin*. Physical Review Letters **11**, 194, (1963).

[I.25] Yijie Huo. *Strained Ge and GeSn band engineering for Si photonic integrated circuits*. Ph.D dissertation, Stanford University, Department of Ellectrical Engineering, (2010).

[I.26] J. Liu, X. Sun, D. Pan, X. Wang, L. C. Kimerling, T. L. Koch, and J. Michel. *Tensile-strained, n-type Ge as a gain medium for monolithic laser integration on Si*. Optics Express **15**, 11272, (2007).

[I.27] M.V. Fischetti, and S.E. Laux. *Band structure, deformation potentials, and carrier mobility in strained Si, Ge, and SiGe alloys.* Journal of Applied Physics **80**, 2234, (1996).

[I.28] Xiaochen Sun, Jifeng Liu, Lionel C. Kimerling, and Jurgen Michel. *A Ge-on-Si Laser for Electronic-Photonic Integration*. Optical Society of America, CLEO/QELS2009 – Laser and electro-optics 2009 and Quantum electronics and Laser Science Conference, (2009).

[I.29] A. W. Ewald. *Germanium-Stabilized Gray Tin*. Journal of Applied Physics **25**, 1436, (1954).

[I.30] O. Gurdal, P. Desjardins, J. R. A. Carlsson, N. Taylor, H. H. Radamson, J.-E. Sundgren, and J. E. Greene. *Low-temperature growth and critical epitaxial thicknesses of fully strained metastable $Ge_{1-x}Sn_x$ ($x \delta 0.26$) alloys on Ge(001) 2x1*. Journal of Applied Physics **83**, 162, (1998).

[I.31] M. Bauer, J. Taraci, J. Tolle, A. V. G. Chizmeshya, S. Zollner, David J. Smith, J. Menendez, Changwu Hu, and J. Kouvetakis. *Ge-Sn semiconductors for band-gap and lattice engineering*. Applied Physics Letters **81**, 2992, (2002).

[I.32] J.-H. Fournier-Lupien, S. Mukherjee, S. Wirths, E. Pippel, N. Hayazawa, G. Mussler, J.M. Hartmann, P. Desjardins, D. Buca, and O. Moutanabbir. *Strain and composition effects on Raman vibrational modes of silicon-germanium-tin ternary alloys.* Appl. Phys Lett. **103**, 263103, (2013).

[I.33] C. Chang , H. Li, T.P. Chen, W.K. Tseng, H. Chen, C. T. Ko, C. Y. Hsie, M. J. Che, and G.Su. *The strain dependence of $Ge_{1-x}Sn_x$ (x=0.083) Raman shift.* Thin Solid Films **593**, 40, (2015).

[I.34] Marvin L. Cohen, and James R. Chelikowsky. *Electronic Structure and Optical Properties of Semiconductors.* Springer, (1989).

[I.35] Vijay R. D'Costa, Candi S. Cook, A. G. Birdwell, Chris L. Littler, Michael Cononico, Stefan Zollner, John Kouvetakis, and José Menéndez. *Optical critical points of thin-film $Ge_{1-y}Sn_y$ alloys: A comparative $Ge_{1-y}Sn_y/Ge_{1-x}Si_x$ study.* Physical Review B **73**, 125207 (2006).

[I.36] Gang He, and Harry A. Atwater. *Interband Transitions in Sn_xGe_{1-x} Alloys*. Physical Review Letters **79**, 1937, (1997).

[I.37] Regina Ragan, and Harry A. Atwater. *Measurement of the direct energy gap of coherently strained $Sn_xGe_{1-x}/Ge(001)$ heterostructures*. Applied Physics Letters **77**, 3418, (2000).

[I.38] Y. Chibane, B. Bouhafs, and M. Ferhat. *Unusual structural and electronic properties of Sn_xGe_{1-x} alloys*. Physica Status Solidi (b) **240**, 116, (2003).

[I.39] H. Pérez Ladrón de Guevara, A. G. Rodríguez, H. Navarro-Contreas, and M. A. Vidal. *Determination of the optical gap of Ge1-xSnx alloys with 0<x<0.14*. Applied Physics Letters **84**, 4532, (2004).

[I.40] H. Lin, R. Chen, W. Lu, Y. Huo, T. I. Kamins, and J. S. Harris, Appl. *Investigation of the direct band gaps in $Ge_{1-x}Sn_x$ alloys with strain control by photoreflectance spectroscopy*. Phys. Lett. **100**, 102109, (2012).

[I.41] S. Gupta, B. Magyari-Köpe, Y. Nishi, and K. C. Saraswat. *Achieving direct band gap in germanium through integration of Sn alloying and external strain*. J. Appl. Phys. **113**, 073707, (2013).

[I.42] L Jiang, J D Gallagher, C L Senaratne, T Aoki, J Mathews, J Kouvetakis and J Menéndez, Semicond. Sci. Technol. **29**, 115028, (2014)

[I.43] A. A. Tonkikh, C. Eisenschmidt, V. G. Talalaev, N. D. Zakharov, J. Schilling, G. Schmidt, and P. Werner. *Pseudomorphic GeSn/Ge(001) quantum wells: Examining indirect band gap bowing*. Appl. Phys. Lett. **103**, 032106, (2013).

[I.44] H. H. Tseng, K. Y. Wu, H. Li, V. Mashanov, H. H. Cheng, G. Sun, and R. A. Soref. *Mid-infrared electroluminescence from a $Ge/Ge_{0.922}Sn_{0.078}/Ge$ double heterostructure p-i-n diode on a Si substrate.* Appl. Phys. Lett. **102**, 182106, (2013).

[I.45] O. Nakatsuka, Y. Shimura, W. Takeuchi, N. Taoka, and S. Zaima. *Development of epitaxial growth technology for $Ge_{1-x}Sn_x$ alloy and study of its properties for Ge nanoelectronics*. Solid State Electronics **83**, 82, (2013).

[I.46] B. Vincent, F. Gencarelli, H. Bender, C. Merckling, B. Douhard, D. H. Petersen, O. Hansen, H. H. Henrichsen, J. Meersschaut, W. Vandervorst, M. Heyns, R. Loo, and M. Caymax. *Undoped and in-situ B doped GeSn epitaxial growth on Ge by atmospheric pressure-chemical vapor deposition.* Appl. Phys. Lett. **99**, 152103, (2011).

[I.47] S. Wirths, Z. Ikonic, A. T. Tiedemann, B. Holländer, T. Stoica, G. Mussler, U. Breuer, J. M. Hartmann, A. Benedetti, S. Chiussi, D. Grützmacher, S. Mantl, and D. Buca. *Tensely strained GeSn alloys as optical gain media*. Applied Physics Letters **103**, 192110, (2013).

[I.48] S. Wirths, R. Geiger, N. von den Driesch, G. Mussler, T. Stoica, S. Mantl, Z. Ikonic, M. Luysberg, S. Chiussi, J. M. Hartmann, H. Sigg, J. Faist, D. Buca, and D. Grützmacher. *Lasing in direct-bandgap GeSn alloy grown on Si.* Nat. Photonics **9**, 88, (2015).

[I.49] M. B. Princ. *Drift Mobilities in Semiconductors*. *I. Germanium.* Physical Review **92**, 681, (1953).

[I.50] J. D. Sau, and M. L. Cohen. *Possibility of increased mobility in Ge-Sn alloy system*. Physical Review **B 75**, 045208, (2007).

[I.51] S. Klinger, M. Berroth, M. Kaschel, M. Oehme, and E. Kasper. *Ge-on-Si p-i-n Photodiodes with a 3-dB Bandwith of 49 GHz*. IEEE Photonics Technology Letters **21**, 920, (2009).

[I.52] Tao Tin, Rami Cohen, Mike M. Morse, Gadi Sarid, Yoel Chetrit, Doron Rubin, and Mario J. Paniccia. *31GHz Ge n-i-p waveguide photodetectors on Silicon-on-Insulator substrate*. Optics Express **15**, 13965, (2007).

[I.53] Yimin Kang, Han-Din Liu, Mike Morse, Mario J. Paniccia, Moshe Zadka, Stas Litski, Gadi Sarid, Alexandre Pauchard, Ying-Hao Kuo, Hui-Wen Chen, Wissem Sfar Zaoui, John E. Bowers, Andreas Beling, Dion C. Mclntosh, Xiaoguang Zheng, and Joe C. Campbell. *Monolithic germanium/silicon avalanche photodiodes with 340 GHz gain-bandwith product*. Nature Photonics **3**, 59, (2009).

[I.54] J. Werner, M. Oehme, M. Schmid, M. Kaschel, A. Schirmer, E. Kasper, and J. Schulze. *Germanium-tin p-i-n photodetectors integrated on silicon grown by molecular beam epitaxy*. Applied Physics Letters **98**, 061108, (2011).

[I.55] B. Vincent, Y. Shimura, S. Takeuchi, T. Nishimura, G. Eneman, A. Firrincieli, J. Demeulemeester, A. Vantomme, T. Clatysse, O. Nakatsuka, S. Zaima, J. Dekoster, M. Caymax, and R. Loo. *Characterization of GeSn materials for future Ge pMOSFETs source/drain stressors*. Microelectronic Engineering **88**, 342, (2011).

[I.56] J. Liu, L. C. Kimerling, and J. Michel. *Monolithic Ge-on-Si lasers for large-scale electronic–photonic integration.* Semicond. Sci. Technol. **27**, 094006, (2012).

[I.57] M. Oehme, M. Schmid, M. Kaschel, M. Gollhofer, D. Widmann, E. Kasper, and J. Schulze. *GeSn p-i-n detectors integrated on Si with up to 4% Sn.* Appl. Phys. Lett. **101**, 141110, (2012).

[I.58] M. Rojas-Lópes, H. Navarro-Contreras, P. Desjardins, O. Gurdal, N. Taylor, J. R. A. Carlsson, and J. E. Greene. *Raman scattering from fully strained $Ge_{1-x}Sn_x$ (x≥0.22) alloys grown on Ge(001)2×1 by low-temperature molecular beam epitaxy.* J. Appl. Phys. **84**, 2219 (1998).

[I.59] P. Desjardins, T. Spila, O. Gürdal, N. Taylor, and J. E. Greene. *Hybrid surface roughening modes during low-temperature heteroepitaxy: Growth of fully-strained metastable $Ge_{1-x}Sn_x$ alloys on Ge(001)2×1.* Phys. Rev. **B 60**, 15993, (1999).

[I.60] Y.-W. Mo, D. E. Savage, B. S. Swartzentruber, and M. G. Lagally. *Kinetic pathway in Stranski-Krastanov growth of Ge on Si(001).* Phys. Rev. Lett. **65**, 1020, (1990).

[I.61] D. J. Eaglesham, and M. Cerullo. *Dislocation-free Stranski-Krastanow growth of Ge on Si(100).* Phys. Rev. Lett. **64**, 1943 (1990).

[I.62] I. N. Stranski, and Krastanow, Sitzungsber. *Theory of orientation separation of ionic crystals.* Wien. Akad. Wiss Math.-Nat. Kl, IIB **146**, 797 (1938).

[I.63] J. Stangl, V. Holý, and G. Bauer. *Structural properties of self-organized semiconductor nanostructures.* Rev. Mod. Phys. **76**, 725, (2004).

[I.64] M. Brehm, M. Grydlik, H. Groiss, F. Hackl, F. Schäffler, T. Fromherz, and G. Bauer. *The influence of a Si cap on self-organized SiGe islands and the underlying wetting layer*. J. Appl. Phys. **109**, 123505, (2011).

[I.65] K. L. Wang, Dongho Cha, Jianlin Liu, and C. Chen. *Ge/Si Self-Assembled Quantum Dots and Their Optoelectronic Device Applications.* Proc. IEEE **95**, 1866, (2007).

[I.66] W. Dondl, P. Schittenhelm, and G. Abstreiter. *Self-assembled growth of Sn on Ge (001)*. Thin Solid Films **294,** 308, (1997).

[I.67] Y. Nakamura, A. Masada, S.-P. Cho, N. Tanaka, and M. Ichikawa. *Epitaxial growth of ultrahigh density $Ge_{1-x}Sn_x$ quantum dots on Si (111) substrates by codeposition of Ge and Sn on ultrathin SiO2 films.* J. Appl. Phys. **102**, 124302, (2007).

[I.68] R. Ragan, K. S. Min, and H. A. Atwater. *Direct energy gap group IV semiconductor alloys and quantum dot arrays in Sn_xGe_{1-x}/Ge and Sn_xSi_{1-x}/Si alloy systems.* Mater. Sci. Eng. B **87**, 204, (2001).

[I.69] M.A. Reshchikov, H. Morkoç, B. Nemeth, J. Nause, J. Xie, B. Hertog, and A. Osinsky. *Luminescence properties of defects in ZnO.* Physica B: Condensed Matter **401**, 358 (2007)

[I.70] Edited by H. Morkoç, and U. Ozgur. *Zinc Oxide Fundamentals, Materials and Device Technology*. Wiley-VCH, Germany, (2007).

[I.71] U. Ozgur, D. Hofstetter, and H. Morkoç. *ZnO Devices and Applications: A Review of Current Status and Future Prospects.* Proceedings of the IEEE **98**, 1255, (2010).

[I.72] U. Ozgur, Y.I. Alivov, C. Liu, A. Teke, M.A. Reshchikov, S. Dogan, V. Avrutin, S.J. Cho, and H. Morkoç. *A comprehensive review of ZnO materials and devices.* Journal of Applied Physics **98**, 041301, (2005).

[I.73] S. Pearton. *GaN and ZnO-based Materials and Devices*. Springer Series in Materials Science, USA. (2012).

[I.74] Claus Klingshirn, J. Fallert, H. Zhou, J. Sartor, C. Thiele, F. Maier-Flaig, D. Schneider, and H. Kalt. *65 years of ZnO research – old and very recent results.* Phys. Status Solidi **B 247**, 1424, (2010).

[I.75] H. Karzel, W. Potzel, M. Kofferlein, W. Schiessl, M. Steiner, U. Hiller, G.M. Kalvius, D.W. Mitchell, T.P. Das, P. Blaha, K. Schwarz, and M.P. Pasternak. *Lattice dynamics and hyperfine interactions in ZnO and ZnSe at high external pressures.* Physical Review **B 53**, 11425, (1996).

[I.76] A. W. Hewat. *Lattice dynamics of ZnO and BeO.* Solid State Commun. **8**, 187, (1970).

[I.77] K. Thoma, B. Dorner, G. Duesing, and W. Wegener. *Lattice dynamics of ZnO.* Solid State Commun. **15**, 1111, (1974).

[I.78] J. Serrano, F. Widulle, A. H. Romero, A. Rubio, R. Lauck, and M. Cardona. *Dependence of phonon widths on pressure and isotopic mass: ZnO*. Phys. Stat. Sol. **(b) 235**, 260, (2003).

[I.79] B.K. Meyer, H. Alves, D.M. Hofmann, W. Kriegseis, D. Forster, F. Bertram, J. Christen, A. Hoffmann, M. Strassburg, M. Dworzak, U. Haboeck, and A.V. Rodina. *Bound exciton and donor–acceptor pair recombinations in ZnO.* Physica Status Solidi (b): Basic Solid State Physics **241**, 231, (2004).

[I.80] Edited by S. Sugano, and K. Kojima. *Magneto-Optics.* Springer, Solid State Science **128**, Germany, 211-244, (2000).

[I.81] M. Johnson, and R. H. Silsbee. *Interfacial charge-spin coupling: Injection and detection of spin magnetization in metals.* Physical Review Letters **55**, 1790, (1985).

[I.82] T. Dietl, H. Ohno, F. Matsukura, J. Cibert, and D. Ferrand. *Zener Model Description of Ferromagnetism in Zinc-Blende Magnetic Semiconductors*. Science **287**, 1019, (2000).

[I.83] J. Ziman. *Models of disorder*. Cambridge University Press, UK, (1979)

[I.84] A. Zunger, S. Lany, and H. Raebiger. *The quest for dilute ferromagnetism in semiconductors: Guides and misguides by theory.* Physics **3**, 53, (2010).

[I.85] M. Arciszewska, and M. Nawrocki. *Determination of the band structure parameters of $Cd_{0.95}Mn_{0.05}Se$ from magnetoabsorption measurements.* Nawrocki. J. Phys. Chem. Solids **47**, 309, (1986).

[I.86] Edited by Y. B. Xu, and S. M. Thompson. *Spintronic Materials and Technology*. Taylor & Francis, Series in Materials Science and Engineering, Boca Raton, USA, 1-33, (2007).

[I.87] J. J. Hopfield. *Fine structure in the optical absorption edge of anisotropic crystals.* J. Phys. Chem. Solids **15**, 97, (1960).

[I.88] S. L. Adler. *Theory of the Valence Band Splittings at k=0 in Zinc-Blende and Wurtzite Structures.* Phys. Rev. **126**, 118 (1962)

[I.89] G. E. Pikus. *A new method of calculationg the energy spectrum of carriers in semiconductoirs. II. Account of spin-orbit interaction.* Zh. Eksp. Teor. Fiz. **41**, 1507, (1961); [Sov. Phys. – JETP 14, 1075, (1962)].

[I.90] E. Cutsche and E. Jahne. Spin-Orbit Splitting of the Valence Band of Wurtzite Type Crystals Phys. Status Solidi **19**, 823, (1967).

[I.91] A. V. Komarov, S. M. Ryabchenko, Yu. G. Semenov, B. D. Shanina, and N. I. Vitrikhovskii. *Giant spin splitting of excitonic states in the hexagonal crystal CdSe: Mn.* Zh. Eksp. Teor. Fiz. **79**, 1554, (1980); [Sov. Phys. – JETP 52, 783, (1980).

[I.92] S. I. Chubarev. *Magneto-optical investigation of CdS crystals doped with Mn.* Zh. Eksp. Teor. Fiz. **80**, 1174, (1981); [Sov. Phys. – JETP 53, 601, (1981).

[I.93] K. Ando, H. Saito, Z. Jin, T. Fukumura, M. Kawasaki, Y. Matsumoto, and H. Koinuma. *Magneto-optical properties of ZnO-based diluted magnetic semiconductors.* J. Appl. Phys. **89**, 7284, (2001).

[I.94] D. C. Reynolds, D. C. Look, B. Jogai, C. W. Litton, G. Cantwell, and W. C. Harsch. *Valence-band ordering in ZnO.* Phys. Rev **B 60**, 2340, (1999).

[I.95] P. I. Nikitin, and A. I. Savchuk. *The Faraday effecting semi-magnetic semiconductors*, Soviet Physics Uspekhi **33**, 975, (1990).

[I.96] J. R. Neal, A. J. Behan, R. M. Ibrahim, H. J. Blythe, M. Ziese, A. M. Fox, and G. A. Gehring. *Room-Temperature Magneto-Optics of Ferromagnetic Transition-Metal-Doped ZnO Thin Films.* Phys. Rev. Lett. **96**, 197208, (2006).

[I.97] Zheng-Wu Jin, Y.-Z. Yoo, T. Sekiguchi, T. Chikyow, H. Ofuchi, H. Fujioka, M. Oshima, and H. Koinuma. *Blue and ultraviolet cathodoluminescence from Mn-doped epitaxial ZnO thin films.* Appl. Phys. Lett. **83**, 39, (2003).

[I.98] C.D. Kundalia, S.B. Ogale, S.E. Lofland, S. Dhar, C.J. Metting, S.R. Shinde, Z. Ma, B. Varughese, K.V. Ramanujachary, L. Salamanca-Riba, and T. Venkatesan. *On the origin of high-temperature ferromagnetism in the low-temperature-processed Mn–Zn–O system On the origin of high-temperature ferromagnetism in the low-temperature-processed Mn–Zn–O system.* Nat. Mater. **3**, 709, (2004).

[I.99] A. Portavoce, S. Bertaina, O. Abbes, L. Chow, and V. Le Thanh. *About Ge(Mn) diluted magnetic semiconductor*. Materials Letters **119**, 68 (2014)

[I.100] D. C. Reynolds, K. D. C. Loo, and B. Jogai. *Optically pumped ultraviolet lasing from ZnO*. Solid State Commun. **99**, 873, (1996).

[I.101] Hguyen Hoa Hong, Joe Sakai, and Virginie Brizé. *Observation of ferromagtism at room temperature in ZnO thin films.* J. Physcs: Condensed Matter 19, 036219, (2007).

Chapter II

Sample Fabrication and Characterization Techniques

This chapter is devoted to the techniques used for the growth of the samples (thin films, mono- and multi-layers) and for their characterization. The first three sections are devoted to the two growth methods used, namely molecular beam epitaxy (MBE) and reactive magnetron sputtering (RF-sput). Concerning the MBE growth, a more sophisticate and less common technique, details of the crystal growth are described, including the means necessary for achieving epitaxial growth of layers and the specific method used in this work. The later sections are devoted to the characterization techniques, where the description of the techniques and methods used to analyse the grown samples is provided.

II.1. Molecular Beam Epitaxy: Requirements and Epitaxial Growth

Molecular beam epitaxy (MBE) is one of the best epitaxy growth techniques for semiconductor structures with high quality and single-monolayer-precision control of surfaces and interfaces. Few other techniques allow similar performance. Ultra-high-vacuum chemical vapour deposition (UH-CVD) and atomic layer deposition (ALD) are two of them. The main advantage of MBE over other techniques is the complete and independent control over different atomic sources used in the growth and also the substrate temperature. Consequently, MBE has a fairly predictable behaviour in terms of output parameters, such as layer thickness and composition, due to the lack of a chemical reaction occurring prior to the adatoms' arrival to the substrate.

This first, **section II.1,** is dedicated to a theoretical aspect of the MBE growth, with the description of the growth conditions needed and how the epitaxial atomic growth occurs. In **section II.2**, the MBE machine used is described, as well the basic growth proceeding used.

II.1.1. MBE Requirements

Molecular beam epitaxy growth needs to have certain conditions fulfilled to provide the desired epitaxial growth conditions. MBE involves the generation of fluxes of atomic or molecular species (molecular beam) and their interaction with the substrate to form a single crystal deposit (epitaxy), under ultra-high vacuum (UHV) conditions. **[II.1]**

The atomic (or molecular) elements are in general radiatively heated in crucibles to temperatures such that their vapour pressures are sufficiently high to generate the atomic/molecular beam flux. To obtain these beams of atoms, the conditions need to be such that negligible interaction occurs between atoms/molecules and with residual vacuum species, except at the growing surface **[II.1]**. Due to the precise nature of the technique, close control over the fluxes are used via control loops either directly, using flux monitoring, or indirectly, by measuring the source temperature. The sources are coupled with physical shutters to interrupt the fluxes to the substrate that allows the precise control over growth thickness, composition and doping.

Semiconductors are highly sensitive to impurity species and atomic/molecular purity of the sources and vacuum environment is essential. Ultra-high vacuum conditions are essential to be established and maintained during growth (see **Table II.1**). Heating assemblies need thorough degassing to minimize impurity generation which occurs either by thermal evaporation / decomposition of heated structures or as volatile reaction products.

The MBE growth requirements can be summarised as **[II.1]**:

1) Ultra-high vacuum conditions;
2) Generation of atomic / molecular beams fluxes;
3) Growth temperatures in general far below the melting point;
4) Clean surfaces without adsorption layers from residual and carrier gases or reaction products apart from the intentional dopant material.

Table II.1: List of vacuum ranges and respective density of molecules and mean free path. Medium vacuum range can be reached with a primary vacuum pump, for high vacuum, it is necessary to add a secondary pump, and for ultra-high vacuum, it is necessary to bake the chamber for desorption of trace gases.

Vacuum range	Pressure (mbar)	Molecules / m^3	Mean free path
Atmospheric pressure	1013	2.7×10^{25}	68 nm
Low vacuum	300 – 1	$10^{25} – 10^{22}$	0.1 – 100 µm
Medium vacuum	$1 – 10^{-3}$	$10^{22} – 10^{19}$	0.1 – 100 mm
High vacuum	$10^{-3} – 10^{-7}$	$10^{19} – 10^{15}$	$0.1 – 10^{3}$ m
Ultra-high vacuum	$10^{-7} – 10^{-12}$	$10^{15} – 10^{10}$	$1 – 10^{5}$ km

II.1.2. Epitaxial Growth Processes

Molecular beam epitaxy is a physical growth process that is realized on the substrate surface. The most important processes that occur at the surface are **[II.2]**:

1) adsorption of the atoms or molecules impinging on the substrate surface;
2) surface migration and dissociation of the adsorbed molecules;
3) incorporation of the constituent atoms into the crystal lattice of the substrate or the epilayer already grown;
4) thermal desorption of the species not incorporated into the crystal lattice.

These growth processes are schematically illustrated in **Figure II.1**. The crystal surface is divided in crystal sites where the adatoms arriving to the surface may interact. Each crystal site is a small part of the crystal surface characterized by its individual chemical activity **[II.4]**. A site may be created by a dangling bond, vacancy, step edge, *etc*. **[II.5]**. The surface processes occurring during MBE growth are characterized by a set of relevant kinetic parameters that describe them quantitatively.

The atoms arriving at the substrate surface will have an energy distribution according to the temperature of their source of origin. After arrival at the substrate surface the adatom can re-evaporate immediately or exchange energy with the atoms of the substrate until they are in thermodynamic equilibrium. The adatoms still have a finite probability of acquiring sufficient energy to overcome the attractive forces and leave the substrate.

There are two types of adsorption: 1) physical adsorption, or physisorption, and 2) chymical adsorption, or chemisorption. In the first one, physisorption, attractive forces of Van der Waals type are the only responsible to hold the atom and no electron transfer occurs between the adsorbate and the adsorbent. In the second one, chemisorption, electron transfer occurs (chemical reaction,) between the adsorbate and the adsorbent, *i. e.*, a chemical bond is formed. In general, adsorption energies for physical adsorption are smaller than for chemical adsorption. **[II.4]**

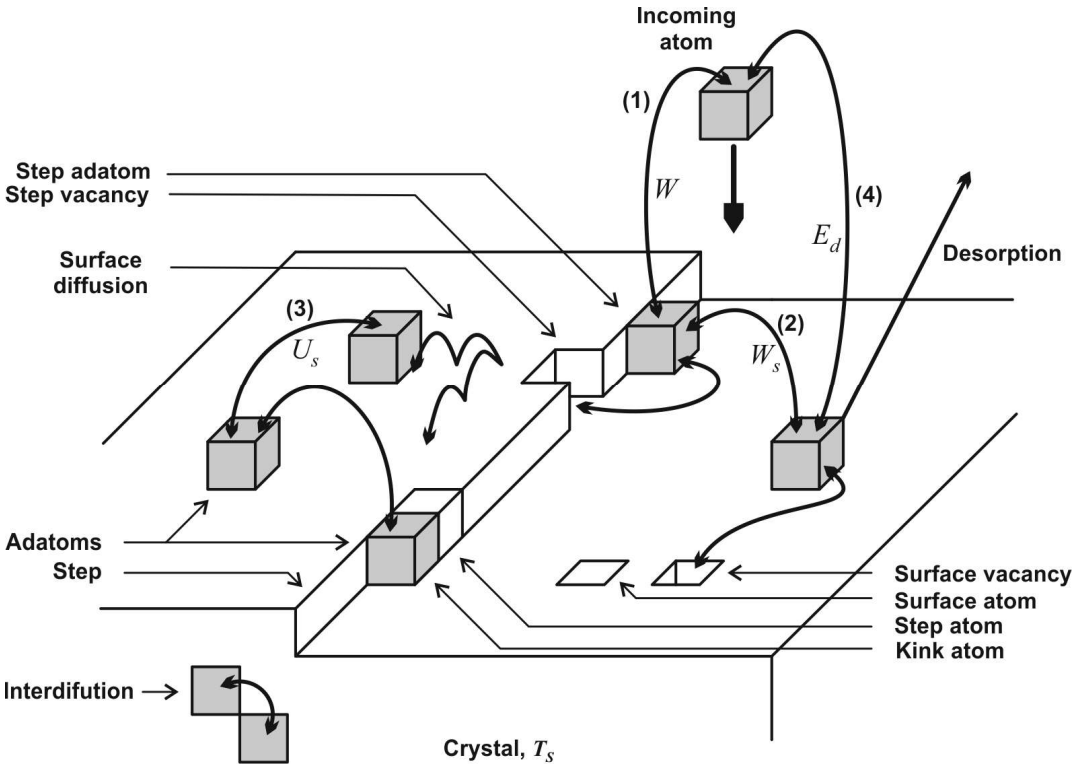

Figure II.1: Schematic illustration of the surface processes occurring during film growth by MBE. The crystal grows by repeated addition of an atom from the vapour to a kink position on a step (1). The adjoining energy gain is the binding energy, W, of the crystal. The most frequent path from the vapour to a step kink is via adsorption on the surface (2) with energy gain, E_d, migration (3) of the adatom and capture by the step (4) with energy gain, W_S, for the jump from an adatom position to the kink position. The energy barrier for the migration process (3) is given by the diffusion barrier, U_S. Figure adapted from [II.1, II.3, II.4]

II.1.3. Nucleation of Epitaxy layers

Epitaxial growth is widely used for producing single crystal layers of semiconductors for research proposes and semiconductor devices production. Epitaxial growth means the growth of crystals of one material on the crystal face of another (heteroepitaxy), for example, Ge on Si substrates; or on the same (homoepitaxy) material, for example, Si doped on Si substrates for devices fabrication.

For the majority of the epitaxial growth, the crystallographic orientation relationship between the substrate and the deposited layer is determined by the crystal plane of the deposit layer being parallel to the crystal plane of the substrate. For the common situation of the substrate surface being flat and parallel to a set of crystal planes, the relationship is simple. For more complex substrate surfaces, such as one containing various vicinal microfacets, the relationship can be complex. The complete epitaxial relationship is determined by the way in which the contacting crystal planes of the substrate and deposited layers are aligned with each other, usually by particular crystal directions or zones axes in the two planes being parallel. Also in the majority of cases, if the substrate is a single crystal, then the deposited layers will also grow as a single crystal under appropriate growth conditions **[II.6]**. When an atom reaches the substrate surface it can behave in different ways (see **Figure II.1)**, mainly determined by the growth temperature, the kinds of atoms and type of substrate (material and orientation). Yet, it will typically have enough time to attain an appropriate site to be incorporated correctly into the growing layer.

The epitaxial growth process of thin films is similar to the one of bulk crystals **[II.7]**, the main difference is the influence of the substrate at the initial growth stages **[II.8]**. The substrate influence comes from the misfit and thermal stress, from the defects appearing at the crystal-film interface and from the chemical interactions between the film and the substrate including segregation of the substrate elements towards the film surface **[II.7, II.8]**. The crystalline thin film can grow in several modes depending on the kind of material (atoms) involved and the growth conditions: the lattice misfit between the substrate and the film, the supersaturation (the flux) of the crystallizing phase, the growth temperature and the adhesion energy are key factors here. **Figure II.2** shows five of the most common modes of crystal epitaxial growth: (a) the Frank-van der Merwe mode; (b) the step flow mode; (c) the Stranski-Krastanov mode; (d) the Volmer-Weber mode and (e) the columnar growth mode.

In the Frank-van der Merwe mode (see **Figure II.2a**), the atoms are more strongly bound to the substrate when compared to the other modes. The first atoms to condense form a complete monolayer on the surface, which becomes covered with a somewhat less tightly bound second layer. Provided that the decrease in binding strength is monotonic toward the value for a bulk crystal of the deposited substance (deposit), the layer growth mode will be obtained. This growth mode is always present in homoepitaxy, where the growth is thermodynamic stable. But it is also possible to occur in the case of heteroepitaxy, as it is suggested in the samples of Ge/Si multi-layers reported in **Chapter IV**. In homoepitaxy, the growth at thermodynamic stable situations occurs according to Franck-van der Merve or step flow mode.

The step flow mode (see **Figure II.2b**) is similar to the Frank-van der Merwe mode, but in this case, the particular atomic orientation of the substrate surface with a tilted cut with respect to a crystal plane with low Miller indices (so called vicinal surface) introduces atomic steps that provided low energy sites for adatoms' joining and consequent growth of the monolayer. A kinetic model was provided by Lev Balykov and Axel Voigt in **Ref. [II.12]**. An example would be the homoepitaxy growth on a Si (110) substrate.

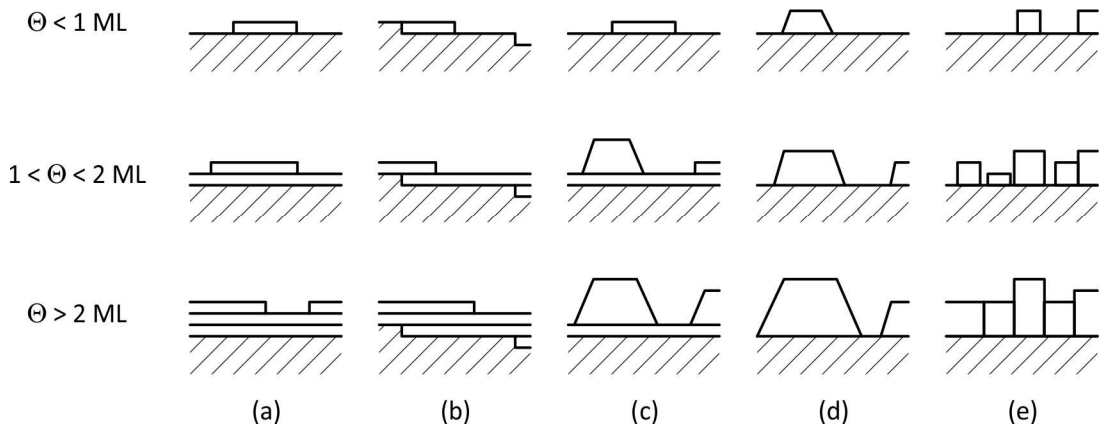

Figure II.2: Illustration of the five most frequent epitaxial film growth modes on flat surfaces of single crystal substrates. (a) growth layer-by-layer or Frank-van der Merwe growth (FM); (b) growth in step flow (SF); (c) growth with layers plus islands formation or Stranski-Krastanov growth (SK); (d) growth with islands formation or Volmer-Weber growth (VW); (e) columnar growth (CG). Θ denotes coverage in monolayers (ML). [II.4, II.9-II.11]

In the Volmer-Weber (see **Figure II.2d**), or island growth mode, small clusters are nucleated directly on the substrate surface and then grow into islands of the condensed phase. This happens when the atoms, or molecules, of the deposit are more strongly bound to each other than to the substrate. **[II.8]**

The Stranski-Krastanov (S-K) mode (see **Figure II.2c** is an "intermediate" case between the Frank-van der Merwe and Volmer-Weber modes, where a continuously growing layer coexists with some "islands" (nuclei of the forthcoming layer). In the Stranski-Krastanov mode, the epitaxial layers start by forming the first few monolayers, atomic layer by atomic layer, until the subsequent layer growth becomes unfavourable and islands are formed on top of this intermediate layer **[II.8]**. This morphologic transition in epitaxial growth is some times referred as a transition from two dimensional (2D) to three dimensional (3D) growth, and the thickness of transition, is known as a critical thickness. The completed atomic monolayers form the wetting layer and the incomplete ones can give rise to differently shaped crystalline features that can become self-assembled dots. (see **Figure II.2c**). There are many possible reasons for this growth mode to occur and almost all the factors that will disturb the monotonic decrease in binding energy characteristic for layer-by-layer growth may be the cause **[II.11]**. The Stranski-Krastanov growth mode occurs especially when the interface energy is high (allowing for initial layer-by-layer growth) and the strain energy of the film is also high (making reduction of the strain energy by island formation favourable) **[II.8]**. A common example in group IV materials is the self-assemble dots of Ge on Si layers / substrates.

In the Stranski-Krastanov mode as well as in the Volmer-Weber mode, when the film becomes thicker, the islands tend to merge and to fill the whole substrate surface. It forms a connected structure, in which the density of the film is a continuous function of the position, but the film can have variations in its thickness and also can have structural defects at the interfaces where adjacent islands merge.

The columnar growth mode (see **Figure II.2e**) also shows some similarities with the Stranski-Krastanov and Volmer-Weber modes, but in contrast to both of these, the film with columnar growth mode usually thickens without the merger of columns. As a result, columns usually remain separated throughout the growth process of the film **[II.7]**. This growth mode occurs when low atomic mobility over the substrate surface

leads to the formation of highly defective atomic columns of the deposited material on this surface **[II.13]**.

A simple analysis of the growth method can be done with resource to thermodynamic considerations, without the need of discrete crystallographic nature of the over layer, by assuming to be liquid like **[II.14]**. The Gibbs free energy is minimized for equilibrium growth conditions and a relation can be formulated from the fraction of the surface covered by the adatoms, ε, the relative Gibbs free energy density of substrate-vacuum interface (G_{S-V}), the deposited layer-vacuum interface (G_{D-V}), and the substrate-deposit layer interface (G_{S-D}) **[II.14,II.15]**:

$$G_{Total} = G_{S-V}(1-\varepsilon) + (G_{S-D} + G_{D-V})\varepsilon \qquad \textbf{\{II.1\}}$$

For $(G_{S-D} + G_{D-V}) < G_{S-V}$, the adatoms tend to spread out over the surface since the atoms are more strongly bound to the substrate than to each other, resulting in the Frank-van der Merwe epitaxial growth mode. For $(G_{S-D} + G_{D-V}) > G_{S-V}$, the opposite happens resulting in the Volmer-Weber mode.

For the Stranski-Krastanov mode, the relation $(G_{S-D} + G_{D-V}) < G_{S-V}$ is valid for the very first layers. However as the number of layers increase, the strain changes the growth morphology due to the mismatch in the lattice constants between two subsequent layers. The lattice mismatch is given by:

$$f = \frac{|a_D - a_S|}{a_S} \qquad \textbf{\{II.2\}}$$

where a_D and a_S are the lattice constants of the deposited material and of the substrate material, respectively. However, the Stranski-Krastanov growth mode not only depends on the mismatch between lattice constants but also on the thermodynamic situation, deposition rates, layer thickness, among some. For example, when a few monolayers of Ge are deposited on Si, the Stranski-Krastanov growth mode can occur. It is known that the critical thickness of the wetting layer, at which the onset of dot formation can be observed, increases when the growth temperature is decreased **[II.16]**. Depending on the thickness and the substrate temperature, the Stranski-Krastanov growth mode may not happen, as happens in the Ge/Si quantum wells samples presented in **Chapter IV**. As already mentioned, the lattice mismatch is also of high importance, has it will be shown later in **Chapter IV**.

II.1.4. Monolayer Concept

In epitaxy growth method, it is common growth layers with thickness of a few atoms. Each layer of deposited atoms is frequently called a monolayer (ML). One ML is defined, according to **Ref. [II.17]**, as corresponding to one adsorbate atom or molecule for each 1x1 unit cell of the ideal non-reconstructed surface. **Figure II.3** illustrates the monolayer coverage of a substrate. When the epitaxial growth starts, if the lattice mismatch between both materials (deposited and substrate) is low or moderated, in general, a pseudomorphic growth can be assumed, *i. e.*, the new material will assume the same lattice as the substrate crystal and the same lattice constant in the directions parallel to the surface.

The growth of precise ultra-thin layers with only a few monolayers represents an enormous challenge. Typical MBE atomic fluxes are too high (≈ 1Å/s) for a precise control of the deposition time. In order to increase time precision, the fluxes are reduced (< 0.1 Å/s) to increase time deposition in laboratory experiments.

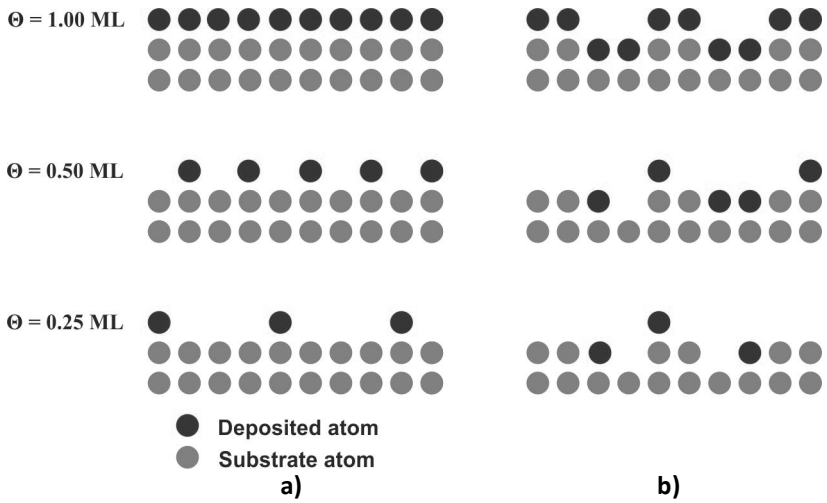

Figure II.3: Monolayer coverage of a substrate: a) with perfect surface; b) and with an imperfect surface. Θ denotes coverage in monolayers (ML)

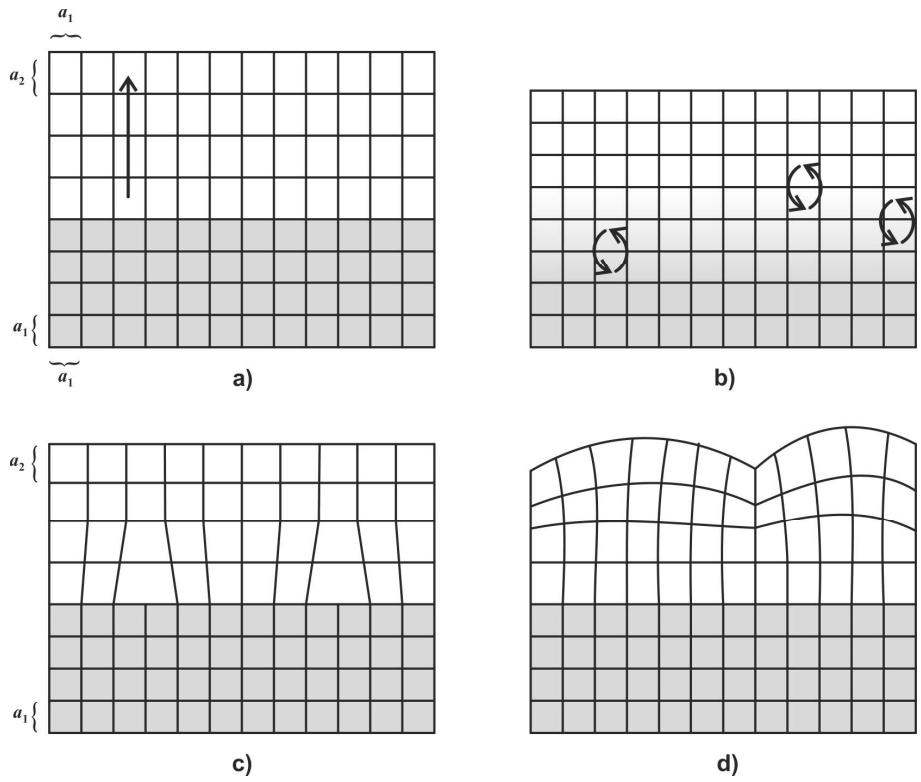

Figure II.4: Illustration of the strain relaxations: a) elastic distortion, b) interdiffusion, c) misfit dislocation, and d) surface roughening. [II.18]

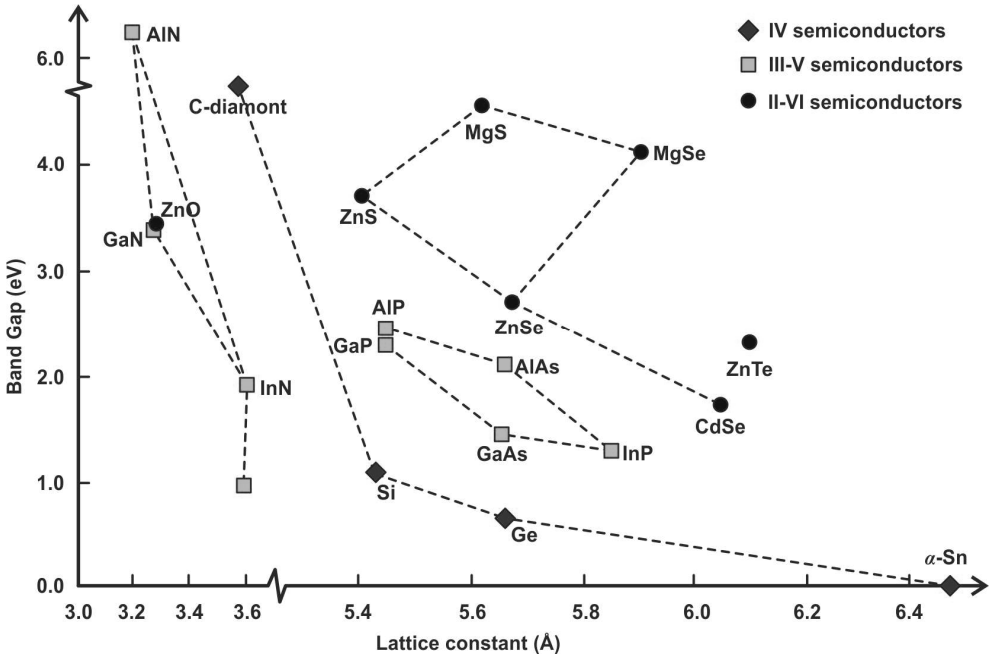

Figure II.5: Graphic illustration of the lattice constant of several semiconductors versus the band gap energy. The dashed lines indicated the possibility of for solid solutions between the materials connected and / or possibility of epitaxial growth of one on the other.

II.1.5. Strain Relaxation

The strain in a hetero-epitaxial structure can be induced by differences in the lattice constants or by differences in the thermal expansion coefficient of the materials. In samples made of group IV elements, the dominating strain factor is the difference in the lattice constant. The induced stain results in an increase of energy. The release of the strain can occur by elastic distortion, interdiffusion (or intermixing), misfit dislocation and surface roughening (see **Figure II.4**).

In the case of elastic distortion, a pseudomorphic growth occurs and the deposited material suffers compression in the parallel plane to the surface and distension in the perpendicular direction to the surface (see **Figure II.4a**). A more detail explanation can be found in **Ref. [II.18]**. This distortion is almost always present in hetero-epitaxial structures due to the mismatch between lattice constants, like Ge on Si, or GeSn on Ge, but in rare cases the mismatch can be close to zero as in the system AlAs/GaAs or GaAs/Ge[5] **[II.19-II.20]** (see **Figure II.5**). The reduction of the elastic distortion will happen with the increase of the layer thickness due to the increase of dislocations and other lattice defects. Carefully develop growth recipes can be used to obtain low strain films (see Ge virtual substrates in **Section II.2.3.3**).

Interdiffusion or intermixing is the diffusion of the adatoms into the substrate (see **Figure II.4b**). In general, the interdiffusion is always present during the growth process even when low solubility elements are present. However the intensity of this diffusion is highly dependent of factors like growth temperature, kind of element involved in the growth, growth rates, among others. The authors of **Ref. [II.21]** reported a study of the growth of quantum wells of Sn in Ge at temperatures as low as 160 ^{o}C, showing that, despite the 17% mismatch in lattice constant **[II.22 – II.23]** between the elements, the low solubility of Sn in Ge **[II.22 – II.23]** and the low growth temperature the intermixing of the Sn and Ge layers indeed takes place.

[5] GaAs on Ge is being researched as a cheap solution over GaAs wafer substrates, due to the compatibility between structures and small mismatch between both lattice constants.

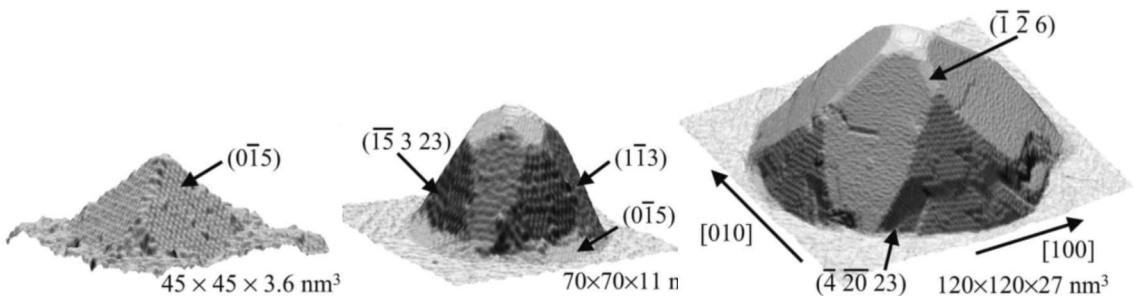

Figure II.6: Typical Ge islands grown on Si obtained by scanning tunnel microscopy, of different shapes a) pyramid, b) dome and c) superdome. [II.24]

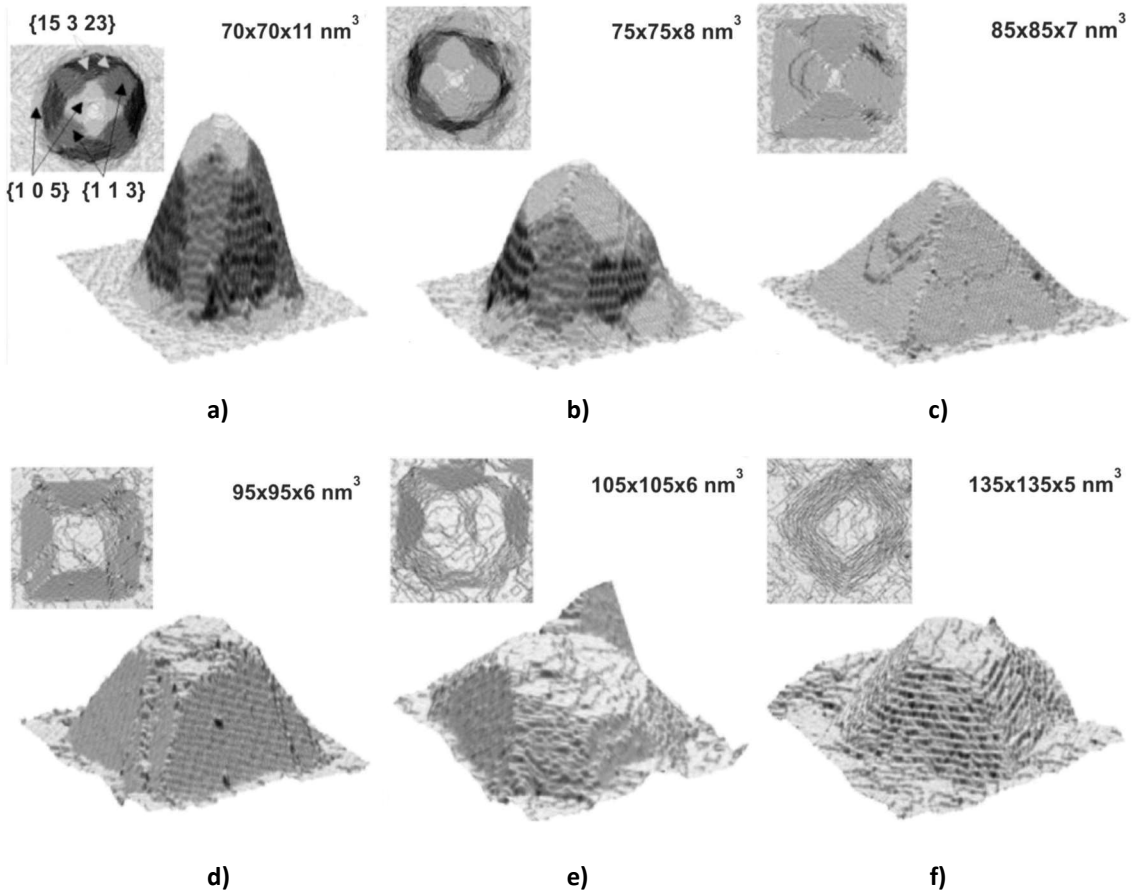

Figure II.7: Typical Ge island shapes obtained by scanning tunnel microscopy during Si capping of Ge domes grown on Si (001): a) and b) domes; c) pyramids; d), e) and f) pre-pyramids. The Si coverages are 0, 1, 2, 4, 8, and 16 ML's for panels a) to f). [II.25]

A misfit dislocation forms when an edge dislocation causes a distortion of the lattice (see **Figure II.4c**). The result is a line of 'holes' of atoms along one of the main lattice directions. The introduction of these dislocations into the grown structure removes strain of the crystal. The dislocations start to form at a critical thickness of a grown layer and there are some developed models in the literature that permit to determine this critical thickness **[II.18]**.

The surface roughening (see **Figure II.4d**) occurs in the Volmer-Weber and Stranski-Krastanov growth modes. The growth conditions play an important role, since the kinetic energy of the adatoms is of main important. For example, in the well know case of Ge on Si(100) in the first few monolayers, the Ge start growing in a pseudomorphic way until ≈ 3 ML (depending of the temperature **[II.16]**), however, as the strain built, due to the lattice mismatch of 4 %, the next adatoms that reach the surface begin to form islands instead of a new layer. However, if the temperature is low, below ~375 ^{o}C, the formation of island may never start and instead additional layers will be formed (see quantum well samples of Ge/Si in **Chapter IV**). This behaviour is due to kinetic limitations in the form of low surface diffusion lengths.

Still having in considering the Ge/Si system, when the temperature is high enough, the adatoms have enough energy to move along the surface to their desired place (thermodynamic favourable). The formation of islands starts by being free of dislocations and shaped as trapezoids, domes or elongated prisms or pyramids (see **Figure II.6**). The two later elongated types are also known as "hut clusters". Tomitori *et al*. **[II.18]** found that the substrate temperature and layer thickness are critical in determining the shape of the islands. The relaxation by forming dislocations follows different scenarios depending on the substrate temperature. It is common to add a passivation layer (or cap layer) to preserve the islands (some of which can become dots). This layer is also responsible for the interaction with the islands and for the change of the shape of the dots (by material intermixing), thus leadings to new surface shapes (see **Figure II.7**).

II.1.6. Lattice Defects in Epitaxy Growth

Epitaxial thin films grown by MBE are precise in compositing and thickness, but they are not atomically perfect, it is common for epitaxial films to have large number of lattice defects, such as: point defects, dislocations, stacking faults, twins, antiphase domain boundaries, misfit dislocations and copy dislocations of the substrate. Special care is needed to avoid / reduce the formation of these defects during growth. Details about these defects in epitaxial layers can be found in **Refs. [III.1, III.8]**.

The fabrication of layers with low defects density is essential for production of optoelectronic devices. The defects can be detected directly by transmission electron microscopy (and its variants). Dislocations are the easiest to observe. The presence of defects can result in broadening of the peaks in Raman scattering spectroscopy measurements and X-ray diffraction.

II.2. Molecular Beam Epitaxy: Deposition System

Molecular Beam Epitaxy (MBE) is probably the best technique for growing semiconductor hetero-structures with high quality and single-monolayer-precision control of surfaces and interfaces. The essence of the method consists in heating a compact source of atoms and molecules in vacuum, covered with a diaphragm with a small opening (effusion cell). The evaporation leads to the formation of an atomic or molecular beam that propagates almost in straight line and can be directed to a substrate. The latter is kept at a lower temperature, so that the atoms or molecules condense on its surface. The temperature of the substrate is still high enough to ensure enough surface mobility of the adsorbed particles, so that they can organize into a periodic layer whose symmetry is “inspired” by the structure of the underlying (usually crystalline) material. To achieve a successful layer-by-layer growth, it is important that the rate of arriving atoms, from the molecular beams, to the growing surface needs to be low enough to provide sufficient time for the adatoms to fix to the lattice (see **Figure II.1**).

Epitaxial growth has to be performed in ultra-high-vacuum (UHV) conditions, in a clean chamber (without pollutants/contaminations[6]) and on a clean substrate surface. These essential conditions make epitaxial growth techniques quite expensive. However, the importance of UHV conditions is not connected only with the effect of the increase of the mean free path of molecular gases used in the deposition process inside the chamber, but also is crucial for the time needed for the monolayer formation. Higher vacuum means less atmospheric particles [inside the chamber] and consequently less flux of contaminants arriving to the growing surface crystal.

During sources refilling and maintenance, the interior of the chamber is exposed to the external atmosphere and the interior becomes coated with an adsorption layer of atmospheric gases, including H_2O, O_2, CO_2, N_2, etc. Water is the main obstacle to achieve UHV, since the polarity of the water molecules leads to a strong adhesion to the walls inside the chamber. Desorption of the water molecules is very slow, preventing the UHV, even when the chamber is open for short periods. Without the proper techniques to reach UHV, the vacuum is held at roughly ≈ 10^{-7} mbar.

Table II.2: Technical differences between the MBE system I (MBE-I) and the MBE system I (MBE-II).

	MBE-I	**MBE-II**
Load-Lock	1 wafer	Up to 25 wafers
Central Chamber	No	Yes
Substrate Storage	No	Yes
Handler	Manual	Semi-automatic
Electro Gun Sources	Si and Ge	Si
Sublimation Cells	Sn and Sb	Ge, Sn, B, Sb
Other Cells	-	C
Ref. Si and Ge Flux	~ 0.4 Å/s	~ 1.0 Å/s
Max. Substrate Temperature	~850 °C	~ 1000 °C
Substrate Roatation	No	Yes

[6] Epitaxial techniques, like MBE, are reserved only to crystals that need to be grown in quasi-equilibrium conditions. The individual materials (for deposition or chamber parts) need to be extensively studied before being allowed inside the chamber in order to avoid the contamination of the whole chamber. If undesired contamination occurs, the recovery can potentially become economically impracticable.

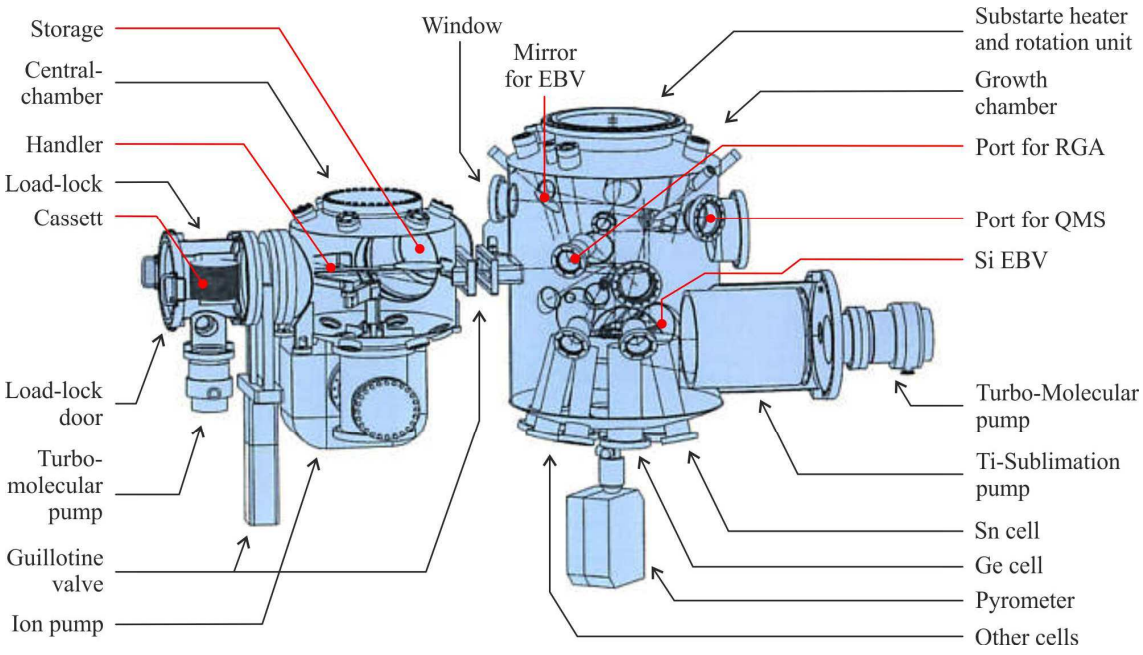

Figure II.8: Illustration of the chambers of the used MBE system II: load-lock, central chamber and growing chamber. Majority, but not all, of the individual components are indicated. Figure adapted from [II.26].

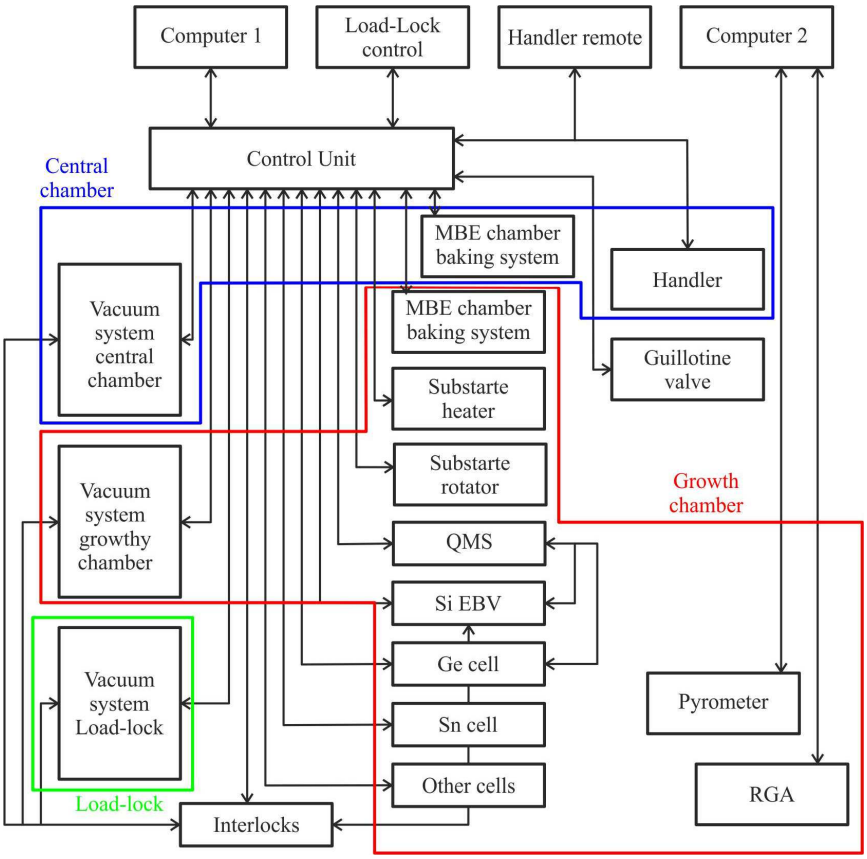

Figure II.9: Diagram showing the connection between the different parts of the MBE system II.

II.2.1. MBE System Description and Calibrations

The *Institut für Halbleitertechnik* (IHT) at the University of Stuttgart is specialized in the growth of group IV semiconductors by MBE with the objective of developing semiconductor devices compatible with Si substrates. Two MBE systems were used to grow group IV samples (MBE system I and MBE system II). Due to the similarity of both systems, this section only provides a description of the IHT MBE system II. The description of this last system was chosen because it was the one used to grow the samples with higher complexity. **Table II.2** provides a short list of differences between both systems. The calibration and the standard growth proceedings used to clean the substrates and to grow buffer layers are also described.

The used MBE system II (MBE-II) is composed of five parts: 1) load-lock, 2) central chamber, 3) MBE chamber, 4) control unit and 5) computers. **Figure II.8** shows an illustration of the chambers (parts 1, 2 and 3) and in **Figure II.9** a diagram where the relation between the different parts of the system can be seen.

The used MBE-II machine allows to handle substrate wafers up to 6” and up to 25 wafers each time, although typically 4” wafers are used and only 2 to 3 wafers are handled each time. This is because the usual long growth run times (between 2 and 4h) limit the production to 3 samples per day. The load-lock, the central chamber and the MBE chamber are connected in series as show in **Figure II.8**. Guillotine valves are used between chambers to maintain the desired UHV conditions in the central and MBE chambers. Each chamber has an independent vacuum system and each one can run independently of the vacuum state of the other chambers. A robotic handler located in the central chamber is responsible for the transportation of the substrates and samples between the load-lock, the central chamber and the MBE chamber. During the operation of the handler, only one of the guillotine valves can be open, thus avoiding contamination between load-lock and growth chamber. The whole system is fully computer controlled electronically.

II.2.1.1 Load-Lock

The load-lock is used to introduce the substrates in and remove the samples out of the machine. It is the only chamber that allows a contact with the exterior in normal conditions. Thanks to it, the UHV conditions are permanently kept in the other two chambers. The substrates / samples are introduced /removed using a standard cassette with capacity to 25 wafers of 6". Smaller substrates can be used with the help of adapters as seen in **Figure II.10**. Contrary to the other two chambers, the vacuum in the load-lock chamber is not maintained at UHV levels, but it is crucial for keeping the UHV conditions in the other two chambers. Using this load-lock chamber, the substrates and samples can be easily loaded/unloaded without breaking the UHV levels in the deposition chamber, keeping then the vacuum conditions for epilayer growth. The load-lock is a minimalistic small chamber with a relatively high pumping rate. The load-lock vacuum system is composed by a scroll pump connected to a turbomolecular pump. A pressure gauge, connected to the control unit, is used to measure the pressure. To load the substrate from the load-lock to the central chamber, the guillotine valve that connects these two chambers must be open. This valve opens only if the pressure in the load-lock reaches 6.5×10^{-6} mbar or lower pressure, in order to keep the UHV conditions in the central chamber when the guillotine valve between but chambers is opened. This pressure is typically achieved some 15 – 20 minutes after the vacuum system has been connected to the load-lock. A low variation of the Central chamber pressure happened because of the volume difference between both chambers.

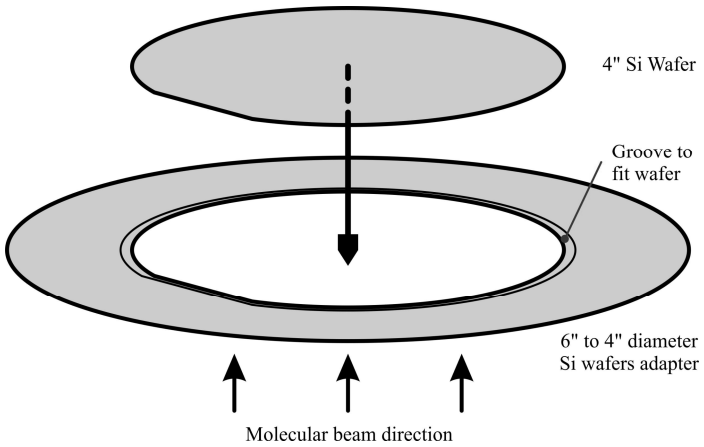

Figure II.10: Adaptor for standard 4" (100mm) diameter Si wafers. The grove helps to hold the wafer in position. The adapter has an internal diameter smaller than the wafer in all its perimeter, preventing the molecular beam flux to escape between the wafer and adapter and consequently coating and damaging the substrate heater.

II.2.1.2. Central Chamber

The central chamber is located between the load-lock and the MBE chamber and it has two purposes: 1) store temporarily multiple substrates and samples allowing a faster work flow, and 2) act as a vacuum buffer chamber between the vacuum in the load-lock and MBE chamber, reducing the eventual contamination of the of the MBE chamber. Furthermore, the temporary storage of substrates in this chamber contributes to their degasification, therefore when they are loaded to the MBE chamber, it does not influence greatly the vacuum level. Like the load-lock, the central chamber has the capacity to store 25 substrates/samples of 6" size. The central chamber has a constant vacuum pressure of $\approx 10^{-9}$ mbar sustained by an ion pump.

To reach UVH, the chamber needs to be baked. For this baking proceeding, the chamber has permanently build heater resistors along the outer side of the chamber. In order to reduce the heat losses during the proceeding, the chamber has an outer isolation shell. Equally all the chamber ports have a resister coupled. The Baking process is controlled by the control unit.

The central chamber holds the handler responsible for transferring the substrates and samples between the three chambers. The handler is connected to the control unit and is controlled electronically (by computer or by remote control). The control unit only allows the opening of the guillotine valves for transfers when the pressure in the chambers and the substrate temperature (in the case of the MBE chamber) are adequate. The handler executes two types of transferences: 1) between central chamber and the load-lock, and 2) between MBE chamber and central chamber. In the first case, the substrate is transferred from the load-lock to the central chamber, and picks the already produced sample from the central chamber to the load-lock. This is repeated as many times as necessary. In the second case, the handler transfers the sample from the MBE chamber to the central chamber and picks the next substrate to introduce in the MBE chamber.

II.2.1.3 MBE Chamber

The MBE chamber is the biggest of the three chambers and is the growth chamber, *i.e.* the samples/layers are grown there. It is composed of: 1) a vacuum system, 2) a substrate heater and support, 3) a Si electron beam evaporator (EBV), 4) effusion cells for Ge, Sn, B and Sb, 5) a Si and Ge feedback control (quadrupole mass spectrometer – QMS), 6) a residual gas analyser (RGA), 7) a pyrometer, 8) baking system (see **Figure II.11**). The distance between the sources and the substrate is ≈ 50 cm. For this particular MBE chamber this is the distance to obtain a uniform deposition throughout a 6" wafer with rotation.

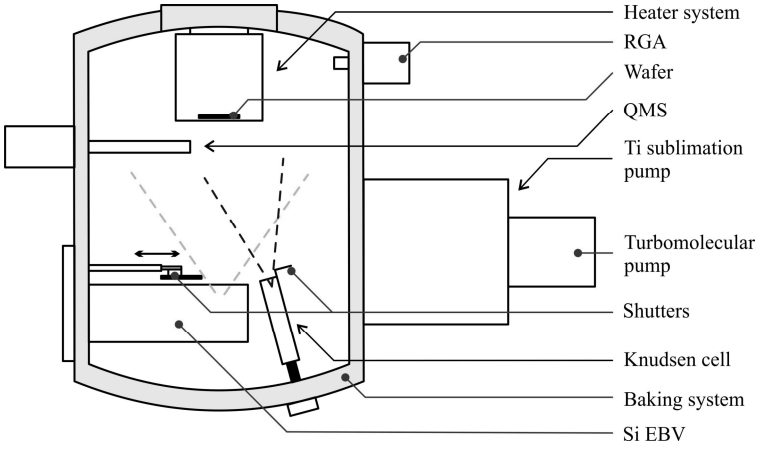

Figure II.11: Diagram of the MBE-II chamber . RGA – Residual gas analyser; QMS – Quadrupole mass spectrometer (feedback control for the Ge effusion cell and Si EBV); EBV – Electron beam evaporator.

Vacuum System, UHV and RGA

The UHV inside the MBE chamber is sustained by using three pumps connected in series, from inside to outside, a titanium sublimation pump refrigerated by a continuous flux of liquid nitrogen, an oil free magnetically levitated turbomolecular pump, water cooled and a scroll pump. However, the sublimation pump is only turned on during the depositions.

The base vacuum pressure (obtained without the sublimation pump) inside the MBE chamber is better than 10^{-10} mbar (value limit by the pressure gauge). During any stage of the samples growth the vacuum pressure is typically better than 10^{-9} mbar. However, during the increase of the Si e-gun power and substrate heater temperature, the pressure can increase momentarily to values close to 10^{-8} mbar. This happens because of the high heat generated that increases desorption of the material from the surface of these two systems.

Like the central chamber, the MBE chamber is also equipped with a baking system (heater and thermal container) capable to heat the whole chamber to ≈ 200 ^{o}C. To reach the UHV regime, the chamber is baked for a continuous period of 48 hour. After this baking process, individually, each molecular source and substrate heather is turned on for degasification of all parts. This process is of higher importance for the Si e-gun, in which high quantities of porous/amorphous Si usually accumulates on the e-gun shields behaving as traps for gases (see **Figure II.15**). The baking step is essential to reach vacuum pressures better that ≈ 6.5x10^{-6} mbar.

The residual gas of the chamber is constantly monitored using a residual gas analyser (RGA) system, which is able to detect the most common molecules present in the atmospheric (see **Table II.2**). Furthermore, helium is used to detect leaks in the chamber and in the case of CO and N_2, isotopes are detected to distinguish between both molecules.

Table II.2: Molecular masses detected by the residual gas analyser for the MBE chamber. u – unified atomic mass unit.

Molecule:	**He**	**CH_4**	**H_2O**	**Ne**	**CO & N_2**	**CO**	**N_2**	**O_2**	**Ar**	**CO_2**	**kr**
Detection at (u):	2	16	18	20	28	29	30	32	40	44	84

Substrate Heater and Support

The substrate support system is located on the top part of the MBE chamber, with the sample growth occurring in the bottom side of the substrate. The system is composed of a substrate support with spin rotation capacity, an electric connection with the exterior for high voltage application (for substrate bias voltage, not used for samples produced in this work), ground connected to the chamber shield, a heater with respective shields and several shields to protect the system from the molecular fluxes. **Figure II.12** shows a more detailed scheme of the substrate support system. The substrate spinning speed can be controlled, and, for samples grown for this study, it was fixed at 15 rotations per minute. Spin of the sample during growth is only possible if the substrate temperature is below 700 ^{o}C. For higher temperatures, the durability of the bearings is shortened if rotation occurs. The heater is a graphite resistor, connected to a high power supply in the exterior of the chamber and the heating rate and temperature are controlled by the control unit. A thermocouple is placed in contact with the resistor for temperature control and is used in a feedback

cycle to maintain the temperature stable. The substrate temperature can be controlled from room temperature to up to ≈ 1150 °C. However, the maximum surface substrate temperature achieved for Si wafer is ≈ 900 °C, because of the partial transparency of the Si to the heater emission. The cold down of the heater and substrate occurs by thermal radiation, since the system does not have a forced cooling system.

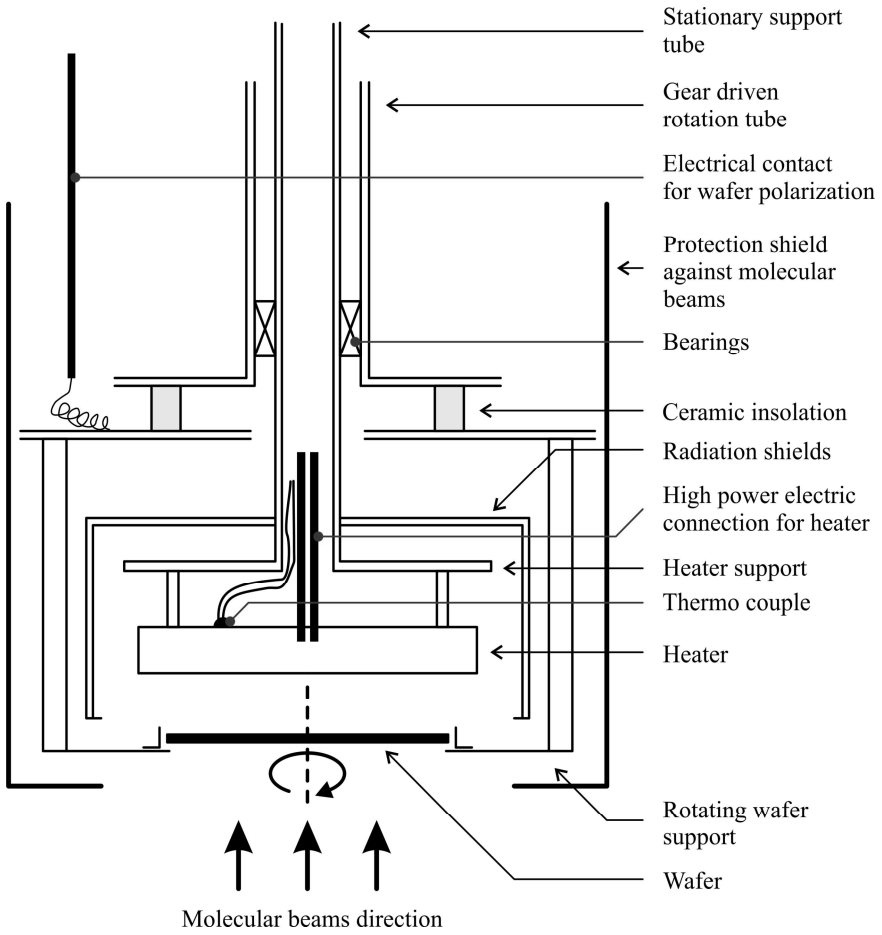

Figure II.12: Scheme showing of the wafer heater incorporated in the MBE-II chamber used in the IHT.

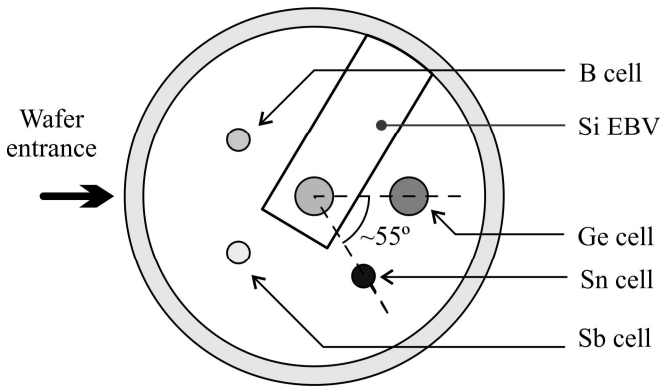

Figure II.13: Scheme showing the position of the e-gun and effusion cells inside the chamber of the MBE-II. The load-lock and central chamber are on the left side, indicated as the wafer entrance.

Si Electron Beam Evaporator

The MBE chamber has an electron beam evaporator (EBV, sometimes called electron gun or e-gun) for the vaporization of Si, aligned with the centre of the substrate position. **Figure II.13** shows the position of the e-gun inside the chamber and the e-gun diagram is presented in **Figure II.14**. As can be seen in that figure, the Si e-gun is surrounded by a massive block of copper that acts as electric ground, material holder and thermal dissipater. The Cu block surrounding the Si e-gun has ≈ 6 cm diameter and ≈ 4 cm height, i.e. an approximately 100 cm^3 volume, with a purity higher than 99,9999 %. The Si (block) melting is not spatially uniform, it melts in the central part (see **Figure II.14**) and at the borders the Si block keeps the solid phase, acting simultaneously, as crucible and material source. This is an important advantage over the effusion cells in which the use of a boron nitride (BN) or carbon crucible is necessary, since the use of these crucibles will originate the contamination of Si with B (a natural doping of Si) for BN and in the case of using C crucibles, originating the formation of SiC.

The electron beam evaporator (EBV) generates a focused beam of ≈ 5 mm on the Si block that can be controlled in power and position (see **Figure II.14**)**.** After the growth of 1 to 2 μm thick layer, the block shape is slightly disturbed (see **Figure II.15**) causing a variation in flux that cause a slow feedback adjust and consequently the deposition rate changes resulting in a undesired or uncontrolled Si layer thickness. To overcome this problem, the surface of the Si block is melted again by moving the beam around the entire Si surface until it is reached a new levelled surface.

Ge Effusion Cell

The Ge is vaporized using an effusion cell with a pyrolytic boron nitride (P-BN) crucible, similar to the one found in **Figure II.16**. The crucible is proximally cylindrical with a ≈ 6 cm diameter and a ≈ 6 cm height. The germanium inside the crucible is typically ≈ 2 cm in height. The cell is controlled by a high power output power supply at constant power. A shutter is used to control the deposition time. The Ge effusion cell is held in place perpendicular to the substrate, due to the physical characteristics of the cell, the same does not happen with the other effusion cells that are included and pointed to the centre of the substrate (see **Figure II.11**).

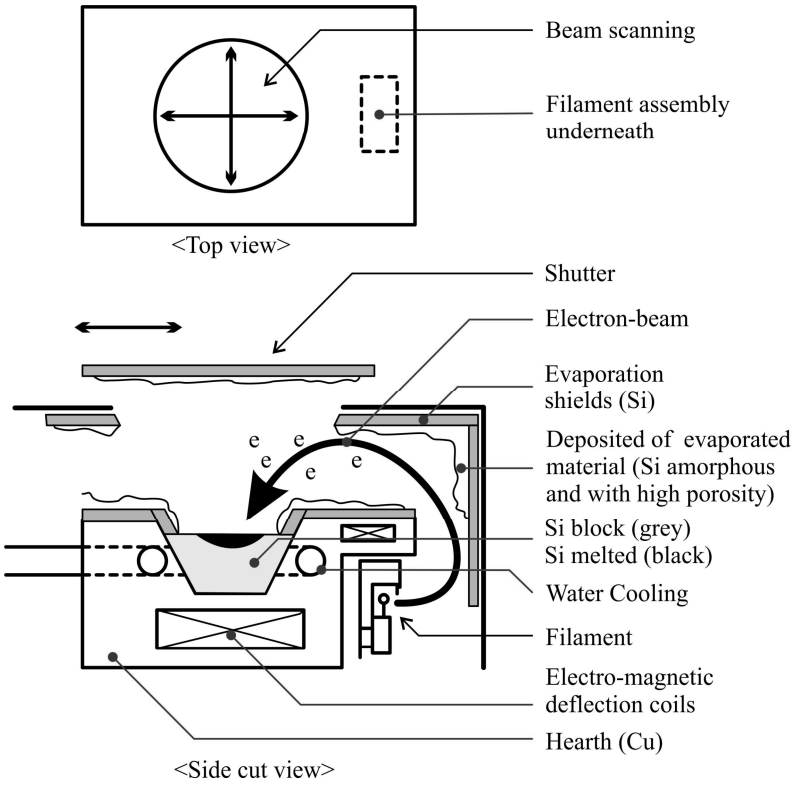

Figure II.14: Schematic diagram showing the major components comprising and electromagnetically focused beam evaporator existing in the MBE chamber. The hearth is made of solid copper with water cooling incorporated to minimize contamination of the charge. In the case specific of Si, only a part of the block is melted, and the temperature is between 1400 and 1800 ºC [II.1]. In the case of Ge, the entire block melts and a crucible is necessary. Thermal contact between the Si block and the copper hearth is poor and it helps keeping the latter functioning. On the other hand, thermal balance of the Si block relies mainly on radiative losses.

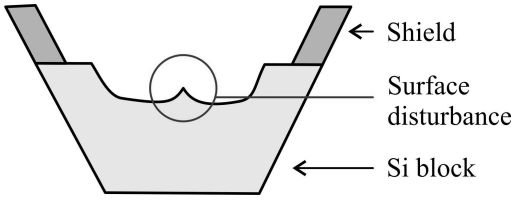

Figure II.15: Qualitative illustration of block shape alteration after 1 ~ 2μm Si growth at the substrate surface. Contrary to a fresh surface, this one surface is not longer flat. The disturbed surface is responsible for high fluctuations in the evaporating flux.

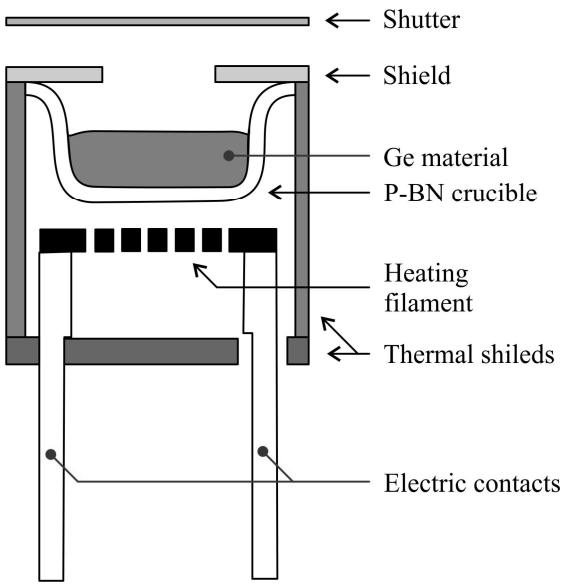

Figure II.16: Schematic diagram of the effusion cell used as Ge source. The shallow crucible with a wide opening is necessary for the high flux output desired (1 Å/s grown at the substrate surface). The high temperature and shape of the crucible causes currents in the liquid germanium that translates in some variation of the flux along the time.

The cell is maintained constantly hot, being only turned-off when an intervention inside the MBE setup is needed, e.g. to break the vacuum inside the MBE chamber. The permanent cell heat is to avoid the crucible crack formation and break, due to the different thermal expansion coefficients of the Ge and P-BN. To avoid damage of the cell, a very slow heat rate variation is used, taking several hours, which is not compatible with daily use. Therefore, the cell is maintained hot enough to avoid Ge solidification, but cold enough to have negligible flux.

Sn Effusion Cell

Sn is vaporized using an effusion cell of Knusden type with a pyrolytic boron nitride (P-BN) crucible. The crucible has a conic shape with an aperture of ≈1.5 cm by ≈10 cm height. The cell operates between 1000 ~ 1300 ^{o}C to grow films of GeSn, although temperatures up to 2000 ºC can be used. The cell is controlled by a high output power supply. The system has a thermocouple for temperature control and a shutter. The cell position inside the chamber makes an angle of ≈55^{o} with the line that passes by the centre of the Ge source and the Si source in the plane of the sources and it has a vertical inclination centred with the substrate face (see **Figure II.11** and **Figure II.13**).

Other Cells

The MBE chamber has two more effusion cells, of Knudsen type, for dopants, namely boron (B) and antimony (Sb). As the other cells, the vaporization is controlled using high output power supplies and the temperature is controlled using thermocouples. Like for the other cells, a shutter is installed to control the deposition time.

Feedback Flux Control

The fluxes of the Si and Ge sources have a certain degree of instability. In the case of the Si source the flux variation is related with the instability generated by the high power electron beam generated by EBV and also due to the large size of the Si block. In the case of the Ge source, the flux instability is related with the shape of the crucible, and the fact that the Ge is entirely in liquid state at high temperature. These factors generate fluctuations on the surface. Using a quadrupole mass spectrometer (QMS) with a high resolution with a narrow solid angle, positioned close to the substrate heater, pointed vertically in the direction of the Si and Ge sources, it is possible to measure the fluxes and, in real time, control them (by a feedback control connected to the Si and Ge power sources). This way, it is possible to stabilize the fluxes and overcome their natural instability.

The flux instability at the other sources does not occur mainly because the flux is generated by Knudsen cells with long crucibles with very stable flux output. The feedback control in these cells is provided uniquely by the thermocouple present at the bottom of each cell.

Pyrometer

The MBE chamber has also a pyrometer to control, in real time, the film surface temperature. The pyrometer is installed in the bottom of the chamber, pointed to the centre of the substrate and works in two wavelengths, 405 nm and 905 nm. It has an optical system and a detector and is used to measure the temperature in a non-contact mode. Also, from the pyrometer readings, is possible to infer qualitative information of the growth morphology. When the film and the substrate have different refractive indices, optical interferences are observed along the growth process. Since MBE is widely used to grow films of materials in metastable phases, as for example GeSn on Si, it is possible to observe changes in the growth of the film. One case is when the epitaxial crystal growth of the film breaks down due to the thickness

and strain. At a certain critical thickness, the film can no longer support the strain and there is a transition from single crystal film to polycrystalline formation (or even amorphous). When this transition occurs, the roughness on the sample surface increases and the interference of the laser is destroyed. This information is given by the pyrometer, in real time, and it is crucial for the control of the crystalline quality of the layers. This case is clearly shown in **Ref. [II.27]** during the growth of GeSn films with up to 25% Sn content.

II.2.1.4. Control Unit and Computers

The control unit is responsible for the control and maintenance of the functioning of the MBE system, including the deposition control, the vacuum control, substrate transfers, etc. The system has two computers, the main one connected to the control unit and a secondary computer linked to devices with no interaction with the control unit (see **Figure II.9**). The main computer receives information from the control unit about the status of the MBE system, like pressures, temperatures, etc. and is used to write the deposition recipes, to upload the recipes, and to give the instructions to the control unit. After the upload of the growth recipe, the control unit is autonomous to execute the proceeding. The secondary computer is used to control the RGA and the pyrometer since no interaction is needed with the control unit.

II.2.2. MBE Calibration

The MBE system is a high precision deposition system. However, the precision is highly dependent of regular calibrations. The samples discussed in **Chapter IV** of this thesis were grown using Si, Ge and Sn sources and heated substrates. This section describes the proceeding for the calibration of the Si, Ge, and Sn fluxes and substrate heater temperature.

The IHT has a policy of use a constant deposition rate (or flux) for epitaxial layers deposition of 1 Å/s, this allows to reduce the number of necessary calibrations. However, for the growth of few monolayers (MLs), the fixed deposition rate (1 Å/s) can no longer be used since the deposition time to grow 1 ML at 1 Å/s is very low (< 0.14s) and impossible to realize. Technically the machine has some limits: 1) the open and close of the sources shutter is between ≈ 0.25 s and ≈1 s; 2) the accumulation of molecular gas inside the sources due to the shutter was closed is not negligible during

the first moments of deposition (when the shutter is opened); and 3) the feedback between the QMS and the sources control temperature for fixing the flux. For these reasons, deposition times shorter that several minutes do not guarantee enough precision in terms of the layer thickness. This is solved by using lower growth fluxes, typically 0.1 Å/s or less.

All the calibrations have to be performed every time after opening the machine (for refill or maintenance) and before the growth of layers with critical thickness or composition. The time duration of the calibrations depends on the maintenance executed and the duration of the time period when the chamber was open (at atmospheric pressure).

II.2.2.1. Si Flux Calibration

The calibrations of the Si flux, is made every time the crucible is refilled and before every series of sample if the layers thickness or composition is of high importance. The Si flux calibration is made by growing epitaxial Si films on a 4" Si (100) wafer using ≈ 1 Å/s, for 2000 s and 600 ^{o}C. The MBE system was design for 6" wafers and a ring adapter is used to support the 4" Si wafer (see **Figure II.10)**. This adapter has an edge of ≈1.5 mm to receive the 4" wafer, which causes a shadowed zone on the wafer during the deposition (see **Figure II.17**). The border on the wafer causes by the shadow, results in a hard edge between the wafer and the grown film. The film thickness (≈ 200 nm) is then easily obtained by profilometry. The calibration is performed by correcting Si e-gun output for a 1 Å/s growing rate.

The film thickness along the wafer is approximately constant due to the wide solid angle of evaporated material generated by the Si EBV (see **Figure II.11**). When modifications to the e-gun are made, for instance, after a new emission filament or a new Si block is installation, the flux can change substantially and a more extensive calibration is needed enough samples for a curve thickness vs input power of the EBV.

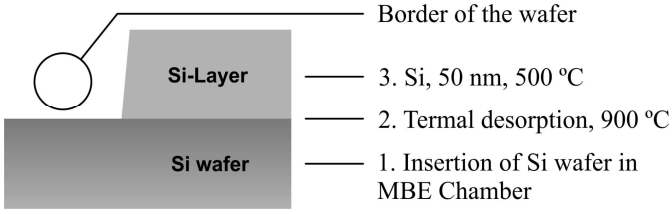

Figure II.17: Illustration of the growing steps used for growing samples in Si evaporator. At the border of the wafer there is a zone without film due to the ring adapter used to introduce 4" wafer in the MBE chamber. The edge is used to measure the film thickness using a profilometer.

II.2.2.2. Ge Flux Calibration

The calibration of the Ge source flux is made following a similar procedure as for Si source flux. The calibrations is made by growing epitaxial Ge films on Si (100) wafers of 4" size for 2000 s at 300 ^{o}C, having in consideration the previous settings (see **Figure II.18**). The thickness, ≈ 200 nm, is measured using spectroscopic ellipsometry (SE). The thickness obtained by SE has higher precision than that obtained by using profilometry. This technique can be used for the Ge flux calibration due to the difference of the optical properties between the Ge layer and the Si wafer. The 200 nm thickness is used to maximise the performance of the ellipsometer. Micro backscattering Raman spectroscopy with a laser excitation of 633 nm is used to determine the Ge layer strain.

The calibration using low flux is always made when very thin films of few MLs are needed and in this case the growing rate is in general ≈0.1 Å/s and grown for 20000 s. Like in the Si EBV, the feedback system does not work effectively for very short periods of time.

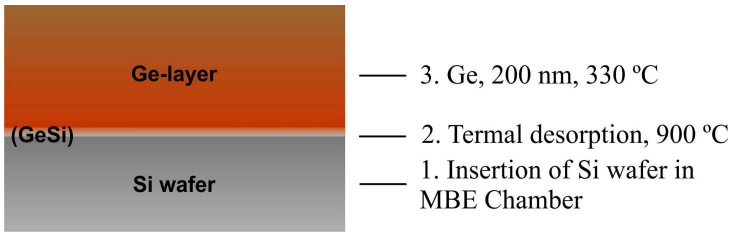

Figure II.18: Illustration of the growing steps used for the growing the samples use in the Ge effusion cell calibration. A small layer of GeSi occurs due to the intermixing of Ge and Si causes by the high temperatures.

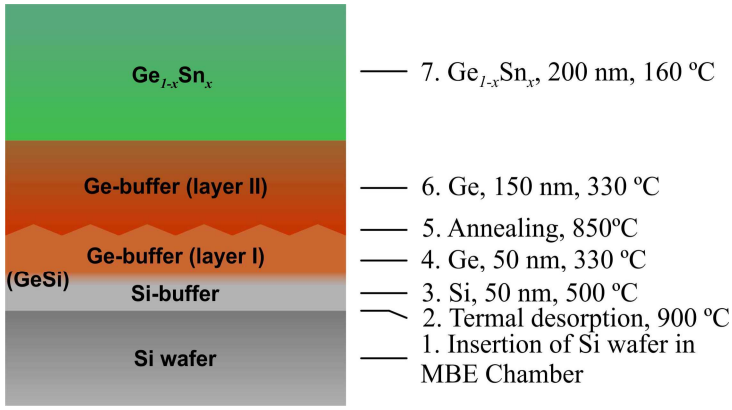

Figure II.19: Illustration of the growth steps used for the Sn Knudsen cell calibration. A small layer of GeSi occurs due to the intermixing of Ge and Si caused by high temperatures.

The film thickness along the substrate is approximately constant when the substrate is continuously rotated, despite the Ge effusion cell not being centered in the chamber (see **Figure II.13**). When modifications or repairments are made to the effusion cell, for instance, after a new heating filament installation (see **Figure II.16**), the flux can change substantially and a more extensive calibration is needed using enough samples to produce a thickness versus input power calibration curve for the effusion cell used.

II.2.2.3. Sn Flux Calibration

The calibration of the Sn flux is made by growing epitaxial thin films of $Ge_{1-x}Sn_x$ on Ge buffer-layers on *c*-Si (100) wafers 4" size (see Ge buffer layer in **Section II.2.3.3**). For 1 Å/s flux calibration, a $Ge_{1-x}Sn_x$ deposition time of 2000s is used (≈ 200 nm) at temperature of 160 ºC (see **Figure II.19**). This very low temperature (for epitaxial regime) is used to reduce the potential Sn precipitation and / or segregation. The absolute concentration of Sn is usually determined by Rutherford backscattering spectrometry (RBS) **[II.28].** Different samples with different concentrations were produced and measured by RBS**.** Since RBS is expensive and time consuming and it is not available in the institute, Raman scattering spectroscopy can be used as an alternative. By using micro backscattering Raman spectroscopy on the $Ge_{1-x}Sn_x$ layers and equivalent Ge layers (*i.e.* grown with the same parameters excepting in Sn content), and together with the samples analyzed by RBS, it is possible to determine the strain and Sn content of new samples.

II.2.2.4. Substrate Heater Calibration

The substrate temperature is controlled by measuring the temperature of the graphite resistor, with a thermocouple and without direct proving of the substrate (see **Figure II.12**). To calibrate the substrate temperature, a special set-up is used, consisting of a Si wafer with a Pt/PtRh thermocouple cemented at the centre of the of the substrate holder surface on the deposition sources side (see **Figure II.20**). The thermocouple it connected to the exterior of the MBE chamber and connected to a precision voltmeter. Since the substrate temperature is influenced by doping of the wafer, a calibration for the most common wafers used is necessary. The temperature

of different substrates can be corrected based on pyrometer measurements (see **Figure II.8** and **Section II.2.1.3**).

The temperature calibration for each substrate type is made roughly once per year, typically when the MBE chamber is at atmospheric pressure for long periods of time or when the substrate heater is changed. All the process can be divided in two parts: installation of the thermocouple and measurements. The first part can be summarised in the following steps: 1) breaking the vacuum of the MBE chamber; 2) opening the chamber; 3) installing the wafer in the substrate support inside the chamber; 4) connecting the thermocouple terminals to the exterior of the chamber; 5) closing the chamber; 6) obtaining vacuum; 7) measuring the sample temperature. The measurements are made during the substrate heating time and also during the cooling time. Typically for this calibration, from room temperature (RT) up to 900 ^{o}C (maximum temperature used on the surface of the wafer). The increase of the temperature is made continuously while the decrease is made by steps to allow the temperature stabilization. The decreasing curve is the one used for the calibration since the usual samples production starts with the highest temperature for substrate degasification followed by the layers growth at lower substrate temperature**.** The increasing temperature curve is compared with the decrease temperature one to confirm the quality of the measurements and calibration. For the calibrations curve, at each temperature, four different parameters are taken: the output value of the calibration thermocouple, the output value of the substrate heater thermocouple, the output power of the heater power supply and the output of the pyrometer (limited to temperatures higher than 350 ^{o}C). For temperatures higher than 200 ^{o}C, the substrate heater thermocouple is used as calibration reference and feedback and the pyrometer as control. For temperatures lower than 200 ^{o}C, the output power of the heater power supply is used as reference since in this range provides better accuracy.

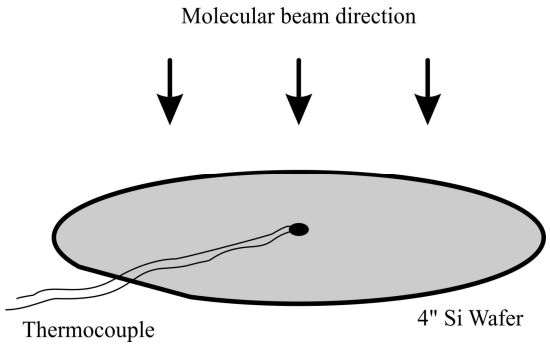

Figure II.20: Illustration of the modified Si wafer used to calibrate the temperature of the substrate heater. A thermocouple is mounted at the centre of the wafer and connected to a voltmeter outside de MBE chamber. The installation of this particular wafer with thermocouple can only be done manually by breaking the vacuum and opening the chamber.

II.2.3. Standard Growth Proceedings

Standard growth proceedings are used to clean substrates and grow buffer layers. The use of standard proceeding reduces the parameters and providing more reproducibility among samples. Bellow are described two surface preparation proceedings, a thermal cleaning procedure made in-situ inside the MBE chamber and a wet cleaning procedure made outside the MBE system. Two other proceedings are described for the growth of the Si and Ge buffer layers.

II.2.3.1. Si Substrate Cleaning and Surface Preparation

The epitaxial growth occurs at relatively low temperatures and is the result of the impinging atoms into adsorption positions (see **Section II.1**). The efficiency of this growth is strongly dependent of the substrate quality, and the substrate surface (crystalline silicon wafer) must be atomically clean. Once clean, the cleanliness of the surface is maintained by the vacuum of the MBE system.

The silicon wafer surface is self-passivated by a thin native oxide layer (SiO_2). The epitaxial growth can only occur if such undesired 'impurities' are removed prior to deposition. In the IHT two proceeding are used: *in-situ* thermal cleaning, and chemical wet bath followed by an *in-situ* low temperature thermal cleaning.

The *in-situ* thermal cleaning (also called thermal oxidation) method involves the vaporization of the silicon oxide layer present on the surface of the silicon substrate. This method uses the substrate heater to increase the silicon substrate temperature.

Heating the substrate to temperatures between 800 and 900 ^{o}C typically result in a clean Si surface, as required prior to epitaxy growth **[II.1]**. In the IHT, the substrate is heated up to 900 ^{o}C for 5 minutes to remove the native silicon oxide layer on its surface by thermal desorption **[II.29]**. The following proceeding step by step is used: 1) the wafer is removed from the wafers factory container and introduced in the load-lock of the deposition system (see **Figure II.8**) and vacuum is made in the load-lock; 2) at a vacuum pressure of 10^{-7} mbar or better the wafer is transferred to the central chamber of the deposition system (see **Figure II.8**); 3) the wafer can then be immediately transferred to the MBE chamber, since degasification of the wafer is not important (the wafer will be heated up); 4) the temperature of the wafer is ramped up to ~900 ^{o}C in a process that takes 20 minutes, providing a good compromise between time and thermal shock; 5) after, the temperature is maintained stable for 5 minutes, this time is enough for a full vaporization of the native oxide layer on the wafer surface; 6) the substrate heater is turned off (for fast cooling) and is only turned on when the substrate temperature reaches the desired value to start the sample growth, typically at 500-600 ^{o}C for growing a silicon buffer layer. The thermal procedure from 4) to 6) takes around 40 minutes and during these steps the substrate is not rotated. **Figure II.21** shows an illustration of the temperature cycle for this thermal cleaning proceedure.

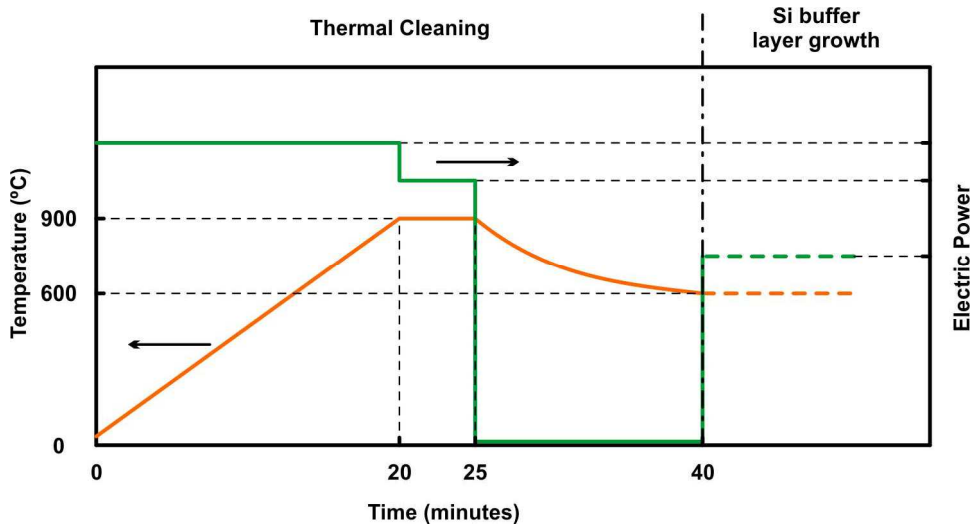

Figure II.21: Illustration of the variation of the temperature (orange curve) of the substrate and electric power (green curve) of the power supply of the substrate heater with time for the thermal cleaning proceedure.

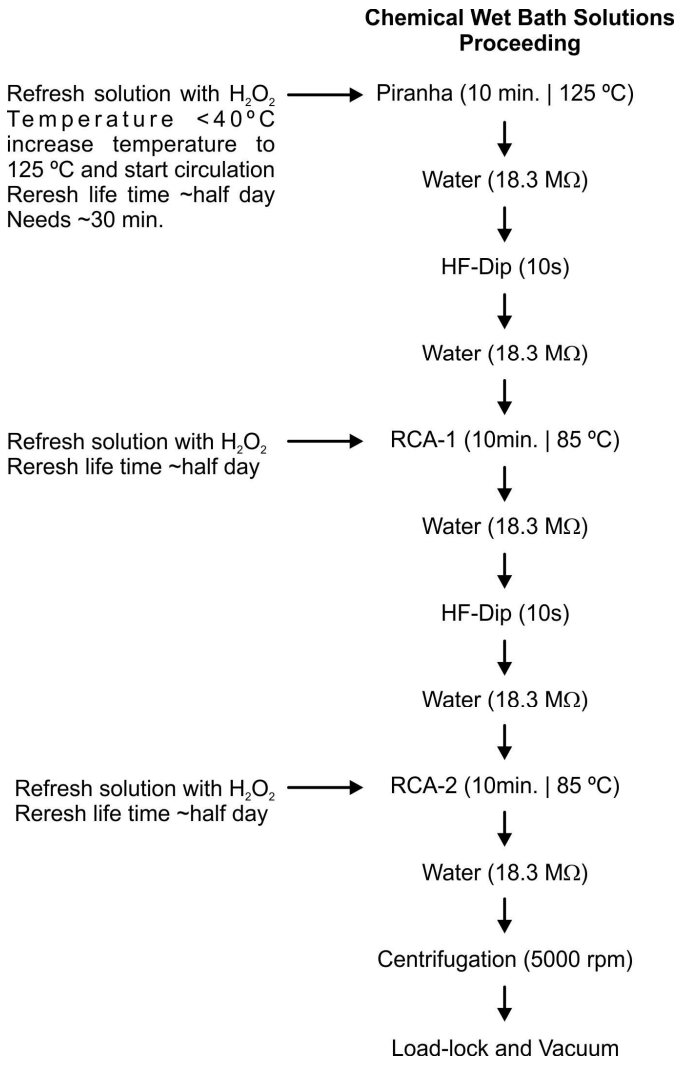

Figure II.22: Illustration of the chemical wet bath cleaning proceeding used in IHT. The process takes around 2 hours to complete.

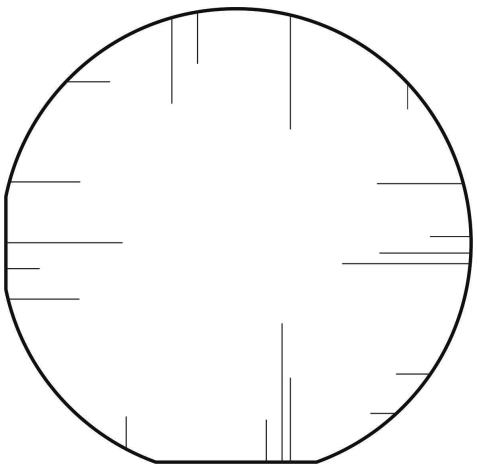

Figure II.23: Illustration of the macroscopic dislocations formed when the wafer is submitted to the thermal cleaning proceeding. This dislocations happen in the (0 0 1) crystal planes.

The wet bath cleaning method (see **Figure II.22**), as referred before, is divided in two parts: the wet baths and the in-situ thermal cleaning. The chemical baths have the following proceeding: 1) refresh Piranha, RCA-1 and RCA-2 chemical bath solutions; 2) heat up Piranha chemical bath solution; 3) dip the substrate in Piranha solution for 10 minutes at 125 ^{o}C temperature; 4) dip the substrate in water until all solution is washed away; 5) dip the substrate in hydrofluoric acid (HF) solution for 10 s; 6) dip the substrate in water until all solution is washed away; 7) dip the substrate in RCA-2 solution for 10 minutes at 85 ^{o}C temperature; 8) dip the substrate in water until all solution is washed away; 9) dip the substrate in HF solution for 10 s; 10) dip the substrate in water until all solution is washed away; 11) dip the substrate in RCA-2 solution for 10 minutes at 85 ^{o}C temperature; 12) dip the substrate in water until all solution is washed away; 13) dry the substrate by centrifugation (see **Figure II.22**). The Piranha solution is used to clean organic contamination from the substrate. The HF solution is used to strip the oxide layer from the substrate. The RCA-1 solution is used to clean organic and particle contamination from the substrate. The RCA-2 solution is used to remove the remaining traces of metallic (ionic) contaminants from the substrate. The full chemical wet baths takes around 2h to be completed. Immediately after, the wafer is transferred to the load-lock of the deposition chamber to avoid contaminations and to reduce the progressive formation of an oxide layer. Finally, the *in-situ* thermal cleaning is similar to the one described above, but here the temperature used is ~700 ^{o}C.

The *in-situ* thermal cleaning procedure has several advantages and disadvantages over the chemical wet bath proceeding. The main advantages are: 1) it is faster, takes around 40 minutes while the wet bath takes 2 hours plus 40 minutes inside the MBE; 2) it is safer, since it does not involve dangerous chemicals; and 3) it is cheaper, since the chemicals used in the wet bath are expensive and some need refrigeration. At the same time, the disadvantages are: 1) macroscopic dislocations appear on the surface of silicon wafer (100) close to the border (see **Figure II.23**) (this happens because of the high temperature the wafer is subjected, J. Matsui discusses their origin in **Ref. [II.30]**); 2) it does not remove as many types of contaminants as chemical wet bath; 3) and higher roughness of the substrate surface.

II.2.3.2. Si Buffer Layer

The surface wafer cleaning mentioned before can still leave contaminants, and furthermore, after the thermal cleaning, the surface roughness is usually naturally higher, due to the previous existent oxidation and the thermal cleaning process. To overcome these problems, a silicon buffer is grown on the top of the wafer surface, covering then the remaining contaminants and smoothen the surface. The buffer layer provides a better surface to grow the desired layers. In the IHT, the silicon buffer layer is used for every sample, using always the same recipe, reducing then potential undesirable variations between samples.

To grow the silicon buffer, the clean substrate is heated to 500-600 ^{o}C and a 50 nm thick homoepitaxial layer is grown at 1 Å/s using the standard substrate rotation of 15 rotations per second. Only then the substrate is in conditions to grow the desired layers of the sample. An illustration of this process can be seen in **Figure II.24**.

The growth of the Si buffer is carried out at (500-600 ^{o}C), mainly because of three reasons: 1) temperatures of this range are high enough to provide a good crystalline quality of the homoepitaxial layer; 2) this temperature range is compatible with industrial production from the economic point of view (the IHT aims at developing devices in similar conditions as in industry); 3) this temperature range is compatible with the use of substrate rotation, needed for getting a uniform silicon layer. Indeed, 600^{o}C is close to the highest temperature supported by the bearings responsible for the rotation of the substrate (see **Section II.2.13**).

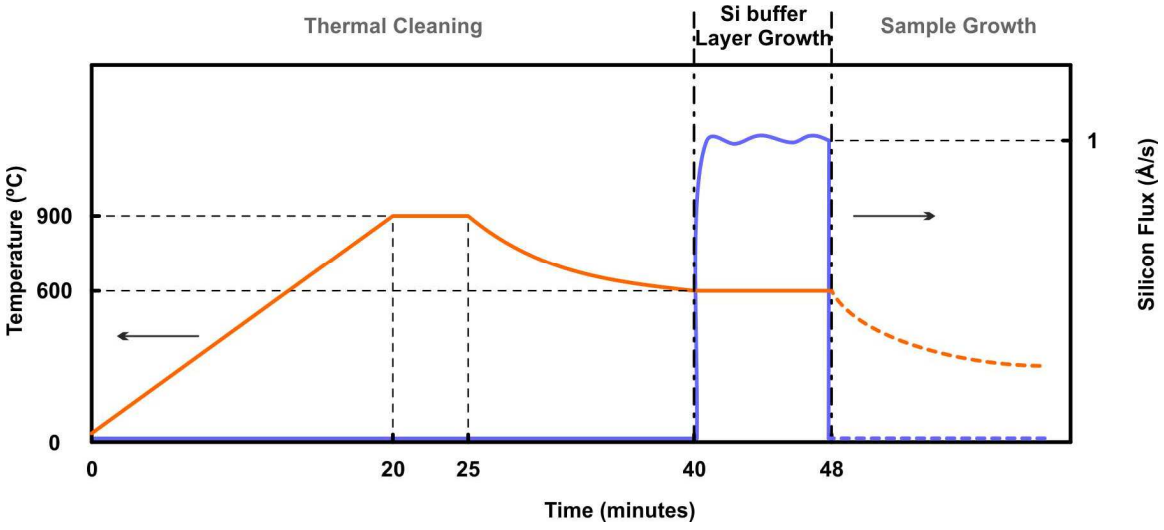

Figure II.24: Illustration of the variation of the temperature (orange curve) of the substrate and the silicon flux (purple curve) generated by the Si evaporator in the MBE chamber with time for the silicon buffer layer growth proceeding.

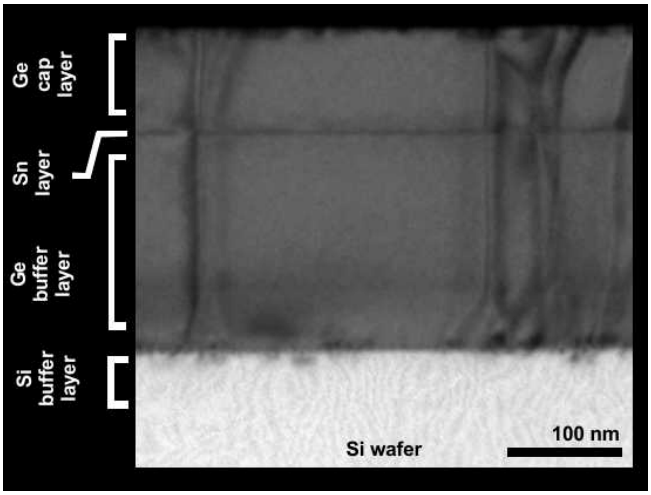

Figure II.25: TEM image of a sample of a 2.25 ML of Sn between two layers of Ge. From the image it is possible to see a very dim interface between the two layers of the Ge buffer layer (see Section II.2.3.3) but the interface between the Si buffer layer and the Si substrate is indistinguishable.

Figure II.25 presents cross-sectional TEM image of a Ge layer grown on the top of a buffer layer, *i.e*. Si wafer/Si buffer layer/ Ge layer. The interface between the silicon-buffer-layer and the substrate is indistinguishable, which is an indication of a high quality epitaxial growth.

II.2.3.3. Ge Buffer Layer and Virtual Substrate

Ge wafers are the most appropriate for the epitaxial growth of Ge layer, however, they are more expensive than silicon wafers, are available in smaller number, smaller sizes and doping variety. Fortunately, the efforts made by the research community to improve the epitaxial growth gave access to hetero-epitaxial layer production with high quality **[II.16]**, allowing then the production of cheaper "virtual" substrates. Thus, it is possible to grow buffer layers with physical proprieties (lattice constant, strain, doping, etc.) similar to the more expensive wafers of the same material. Furthermore, the crystalline quality is appropriate to be used in device fabrication. It is now possible to routinely produce Ge "virtual" substrates.

In the IHT a growth recipe has been optimized for the fabrication of these Ge "virtual" substrates or Ge-buffer layers. The full growth involves three main steps: 1) substrate surface preparation (see **Section II.2.3.1**); 2) growth of a silicon buffer layer (see **Section II.2.3.2**); and 3) growth of the germanium buffer layer. The whole process is performed sequencelly (see **Figure II.26** and **Figure II.27**) to avoid accumulation of 'impurities' at the surface/interface that could reduce the crystalline quality.

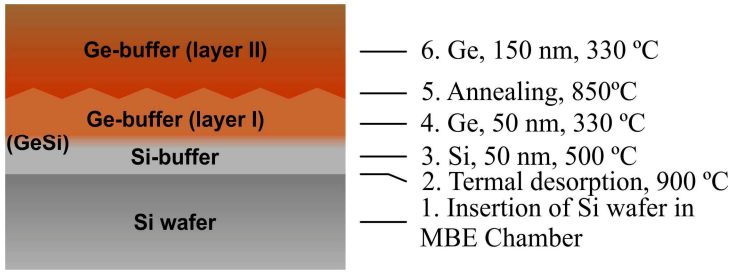

Figure II.26: Illustration of the MBE growth steps used for the buffer layers of Ge on the buffer-layer of Si on Si wafer.

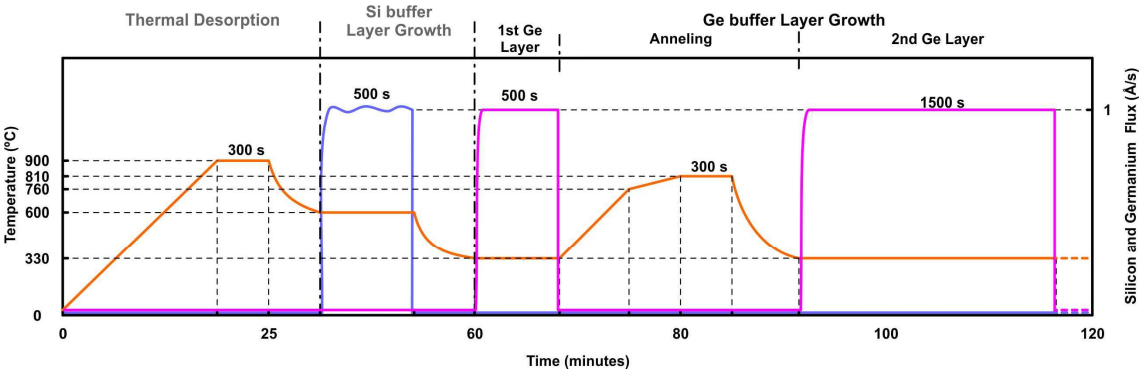

Figure II.27: Illustration of the temperature and silicon and germanium flux with time for all the process to growth of the germanium buffer layer.

The optimized Ge buffer is composed of a sequence of two Ge layers grown at 330 ^{o}C, with an in-situ annealing step made in between, i.e. an annealing of the 1st layer to form the 'virtual' substrate **[II.31, II.32]**. After the silicon buffer layer, the Ge (1st layer) growth proceeds as: 1) the temperature of the substrate is decreased and a stabilised at 330 ^{o}C; 2) the first Ge layer, 50 nm thick, is grown at 1 Å/s; 3) it is followed by an *in-situ* annealing step: increasing the temperature from 330 ^{o}C to 760 ^{o}C in 5 minutes followed by a slower heating rate to 810-820 ^{o}C; 4) this temperature is maintained for 300 seconds; 5) the temperature is finally decreased back to 330 ^{o}C by turning off the substrate heater; 6) the temperature is stabilized again at 330 ^{o}C; 7) and a second Ge layer is growth with 150nm thick.

Like with the silicon buffer layer, the germanium buffer layer is growth at the minimum temperature necessary to obtain high quality layers for device applications.

The 810 – 820 ^{o}C annealing temperature was chosen because is close, but bellow, the germanium melting point temperature, in chamber conditions. At this temperature the mobility to the germanium atoms is high, therefore reducing the threading dislocation density **[II.32]**, and at this temperature it is avoided that the germanium film melts, preventing the polycrystalline layer formation. The annealing step has two undesirable consequences: with the substantial increase of mobility,

intermixing will occur at the interface between the silicon buffer layer and the germanium buffer layer; the other effect is the increase of the Ge surface roughness. Because of the latter, a second layer of epitaxial germanium is grown with a thickness of 150 nm to provide a smoother surface onto high-quality layers can be grown. **Figures II.26** and **II.27** *s*how the layers and steps used in the growth up to the end of the Ge buffer-layer.

The strain of the buffer layer is reduced substantially by the annealing step, but there still is some remaining strain. The density of threading dislocations in the germanium "virtual" substrate can be as low as 10^8 per cm^2. However, a commercial germanium wafer can be close to dislocation free, and a silicon wafer can have the dislocation density less than 10 cm^2. Although the quality of the germanium virtual substrates is not equivalent to wafers, it is enough for device fabrication.

II.3. Sputtering

Sputtering is a film deposition technique that, although developed at the end of the 19^{th} century, only in the last decades has been adapted to large scale production **[II.33, II.34].** Because of the low deposition costs, this technique became interesting for fabrication of multilayers and is the most common technique to grow ZnO films **[II.35, II.36].** The main advantages compared to others are: (1) easy deposition of practically all types of materials (conductors, semiconductors and insulators); (2) the deposited films have good adhesion to the substrates; (3) the films have high purity; (4) the technique enables large areas film growth with high uniformity; (5) it can easily be automated and expanded to large-scale production; (6) and it has low cost. The deposition parameters, such as partial pressure of the gases and substrate temperature play a fundamental role in the final properties of the films.

In this section, it will be described the physical process of vapour formation out of thermal equilibrium created by sputtering, identifying the physical parameters that characterize the plasma. Also, it will be presented the experimental configuration used in the deposition of the ZnO films studied in this work and the role of the different deposition parameters (such as substrate temperature, partial gas pressures, distance to the target and power) in obtaining the good quality ZnO films. A more exhaustive description of the sputtering technique can be consulted in several books and papers **[II.33, II.34].**

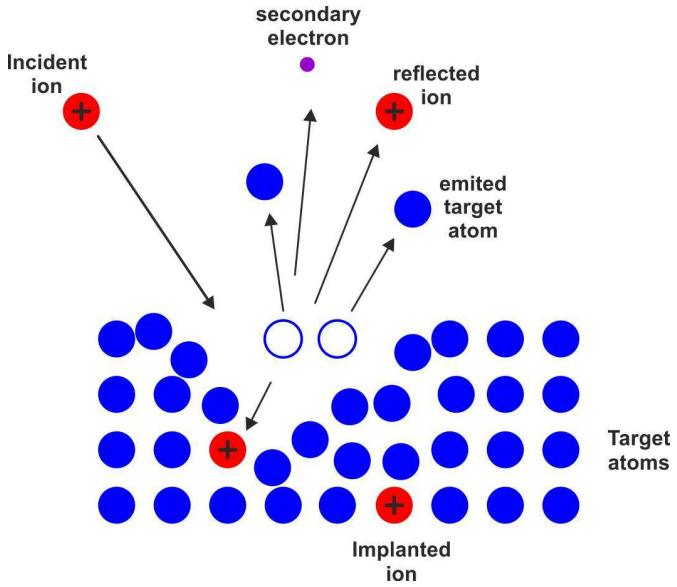

Figure II.28: Illustration of target surface erosion in the sputtering process by the collision of incident ions.

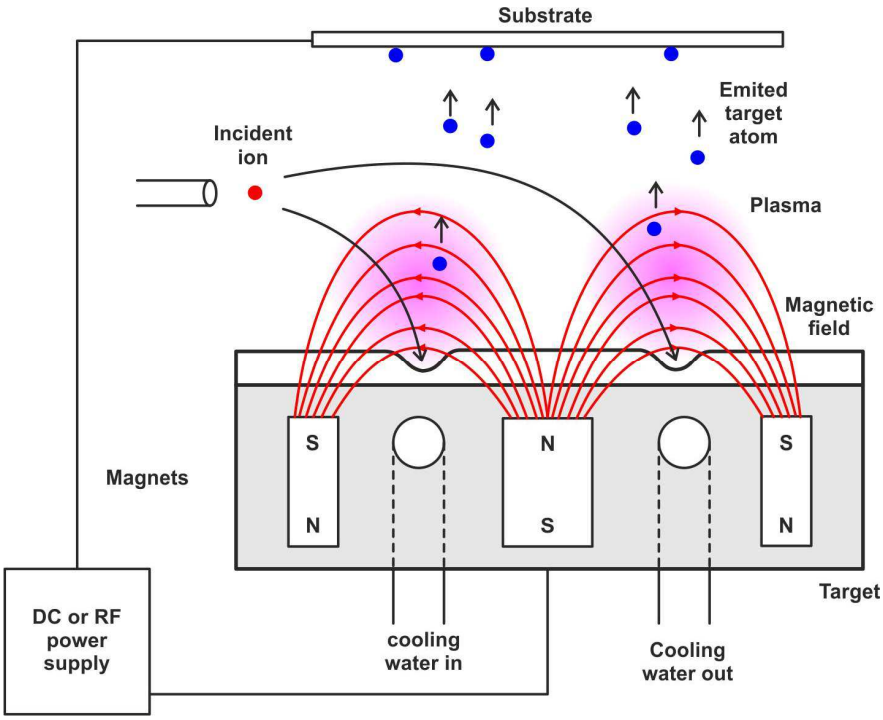

Figure II.29: Schematic illustration of a flat magnetron with a target surface being eroded in the sputtering process.

II.3.1. Sputtering and Reactive Sputtering

Sputtering is a physical vapour deposition (PVD) technique, *i. e.*, the material goes from a condensed phase to a vapour phase and then back to the condensed phase as a thin film. The whole process occurs in a chamber at high vacuum to obtain a high mean free path of contaminant gases (see **Table II.1**). This results in lower levels of contamination in the deposited film and a ballistic travel of the atoms from the target to the substrate. The sputtering technique consists of the erosion of atoms or molecules of a target material through the ion bombardment. These ions are obtained by ionization of a rarefied gas (often an inert gas is used, for example argon, thus avoiding undesirable chemical reactions), through an electric field generated between the target (working as cathode) and the substrate (working as anode). The electric field, not only originates the target ionization, as also accelerates the positive ions towards the target, acquiring then a kinetic energy higher than the target surface binding energy, leading to surface erosion.

Figure II.28 shows some of the processes involved in the collision. As it happens in any electric discharge in rarefied gas, the process is auto sustained by the mechanisms of multiple collisions between ionized particles and secondary electrons. However, many of these electrons are accelerated toward the substrate, and as a consequence their efficiency as ionizing elements is reduced, originating also the degradation of the deposited film. To optimize the ionization yield, a magnetic field is placed under the target. The magnetic field has a configuration that captures the electrons in helical trajectories confined in the plasma near the target, increasing then its density and leading to a higher ionization yield. The device that uses the magnetic field is called a magnetron and is shown in **Figure II.29**. There are different configurations and shapes of magnetrons but they all have to obey two essential requirements: to be conductors to work as cathodes and have good sinks since about 80% of the energy present in the plasma is dissipated as heat.

The use of radio-frequencies (RF) instead of continuous voltage allows the use of this technique to practically all types of targets (conductive and insulating materials) and also allows the operation at low pressures with a high deposition rate, low contamination and high sputtering yield.

The growth rate is one of the parameters that most influences the film growth, having, however, an insignificant role in the properties of deposited films. The films properties are more affected by the energy of the pulverized particles than by their number **[II.33, II.34]**. The growth rate is directly proportional to the radio-frequency power and, consequently, it is possible by this technique to use low RF power leading to a high sputtering efficiency.

Another important parameter is the mean free path of the ionized particles. The following equation establishes the relation between the mean free path and the pressure **[II.37]**, considering the gas described by the Maxwell distribution function:

$$\lambda_L = \frac{m_g v_p^2}{2\sqrt{\pi} S_{pg}^2 P_g} \left(v_p \varphi \sqrt{\frac{m_g}{2 k_B T_g}} \right)^{-1} \qquad \{II.3\}$$

where m_g is mass, v_p velocity, P_g pressure and T_g gas temperature. The parameter S_{pg} corresponds to the number of collisions between the atoms of the gas and a particle with the speed v_p and k_B is the Boltzmann constant. The function φ is derived from the Gauss error function **[II.37]**.

The thickness uniformity of films deposited by RF sputtering depends on different factors such as the working pressure, the target to the substrate distance, the shape of the target and its orientation relative to the substrate. The dependence of the film thickness uniformity along the substrate with the target-distance is expressed by **[II.33]**:

$$\frac{d}{d_0} = \left[1 + \left(\frac{S}{h} \right)^2 \right] \frac{1 + \left(\frac{l}{h} \right)^2 + \left(\frac{l}{h} \right)^2}{\sqrt{\left[1 - \left(\frac{l}{h} \right)^2 + \left(\frac{l}{h} \right)^2 \right]^2 + 4 \left(\frac{l}{h} \right)^2}} \qquad \{II.4\}$$

where d_0 is the thickness at the centre of the film, d is the thickness at a distance l from the centre axis of deposition, h the distance target-substrate and S is the distance to the centre of the erosion ring (see **Figure II.30**). To minimize the lack of uniformity in thickness, due to the geometric effect, during the film growth procedure, the substrate is placed in rotation **[II.34]**.

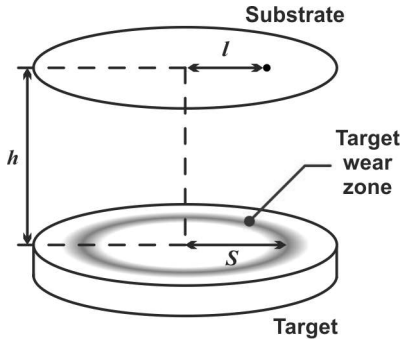

Figure II.30: Schematic representation of the spraying process. The nomenclature and parameters refer to equation {II.4}.

Reactive sputtering is a process where a target composed of a single kind of element, for example Zn, is sputtered in the presence of a gas or a mixture of gases (*e.g.* Ar + O_2) that will react with the target material to form a film of a different chemical composition (*e.g.* ZnO compound). Reactive gas is a type of gas which undergoes chemical reactions with materials in contact. Once a reactive gas, which is a gas that undergoes chemical reactions with materials in contact, is introduced into a process chamber it reacts with the sputtered particles before coating the substrate, as also with the unpassivated surfaces, such as chamber walls and sputtering target. The composition of the film can be controlled by varying the relative pressures of the inert and reactive gases. Film stoichiometry is an important parameter for optimizing films properties (*e.g.* the stress in SiN_x and the index of refraction of SiO_x). However, the presence of reactive gases (*e.g.* oxygen) will affect the deposition rate, since the presence of oxygen may also originate the ejection of atoms or molecules from the growing film **[II.38]**.

As a summary, the physical processes in the films deposited by sputtering can be summarized in the following four steps: (1) positive ions are accelerated towards the target; (2) after the collision of these ions with the target, material is sprayed; (3) the pulverized material is transported from the target to the substrate; (4) the material that reaches the substrate is deposited and some of this material is re-emitted.

The parameters that most influence the deposition kinetics of thin films are the substrate temperature and the mass flow that reaches it. The kinetics of deposition comprises different steps:

- Physical adsorption: that occurs when a molecule or atom undergoes Van der Waals interaction when approaches the substrate and then the molecule or atom can move on the film surface over a certain distance (surface diffusion effect).

- Surface diffusion: this is one of the most important step in the processes that affect the film properties. During this stage the particle can move to an energetically more stable position. Surface diffusion depends on the thermal energy provided by the substrate temperature and the kinetic energy of the adsorbed particle.

- Nucleation: it is one of the intermediate stages of film deposition that most affects the type of growth. Nucleation is strongly affected by the surface tension of the substrate, chemical composition, crystallographic orientation and local morphology.

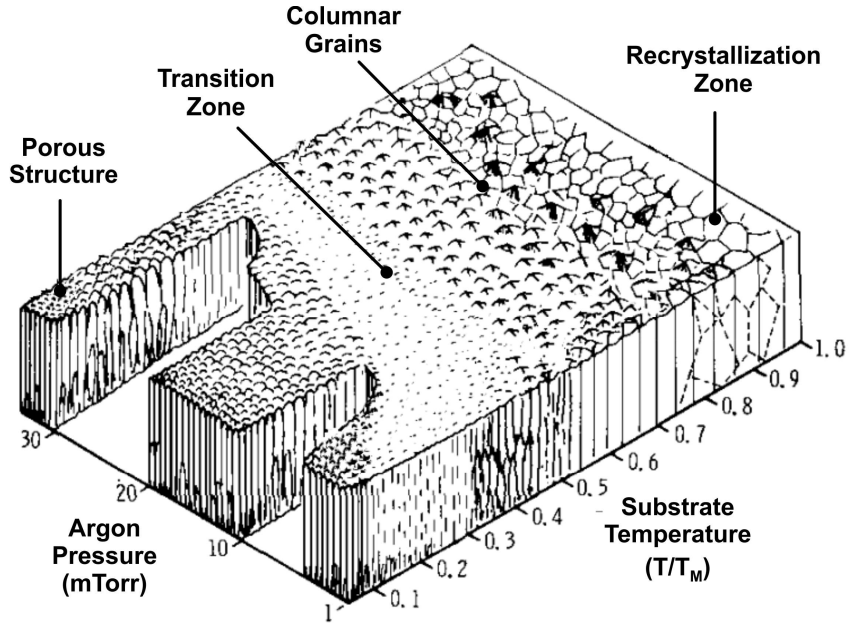

Figure II.31: Diagram showing the different structural zones as a function of argon pressure and temperature (Ts / T_M) ratio. Figure adapted from [II.39].

II.3.2. Microstructure of Sputtered Samples

The sputtering processes (adsorption, diffusion and nucleation) are dependent on the deposition (substrate) temperature (T_S) and the melting temperature of the target material (T_M) to be deposited. For different materials and for different temperature range (T_S/T_M) it is expected to result in differences in the microstructure of the deposited films. Thornton, *et al.* **[II.39]** proposed a model that correlates the final film microstructure and the physical properties with the deposition parameters. **Figure II.31** illustrates the Thornton model, which describes the microstructure as a function of the temperature ratio (T_S/T_M) and the gas pressure inside the chamber. The gas pressure can be seen as the energy of the species that arrive at the substrate. The model shows four different zones, depending on the parameters, but the general conclusion is that although the superficial aspect (more or less dense), the microstructure has always a columnar shape.

II.3.3. Experimental Growth Conditions for ZnO

The ZnO samples reported in this work were grown with an Alcatel SCM 650 sputtering system located at the Centre of Physics of Minho University. The sputtering system is composed of three parts: 1) load-lock, 2) deposition chamber, and 3) control unit. **Figure II.32** shows the chambers (parts 1 and 2). The system supports substrates up to 150mm in diameter. For ZnO samples, a special support was used with capacity of holding nine substrates in a matrix configuration 3 by 3 with approximate 24 x 24 mm in size (see **Figure II.33**).

The chamber has four independent magnetrons each capable to support a target. An electronically controlled handler transfers the substrates holder from the load-lock to the planetary holder inside the deposition chamber. The planetary holder can stay fixed at a position over a magnetron or can be rotated continuously up to 30 rotations per minute. It can also be adjusted in height between 50 to 100 mm of the target. The vacuum in the chamber is supported by a turbomolecular pump in series with a rotary vane pump, while the load-lock uses only a rotary vane pump.

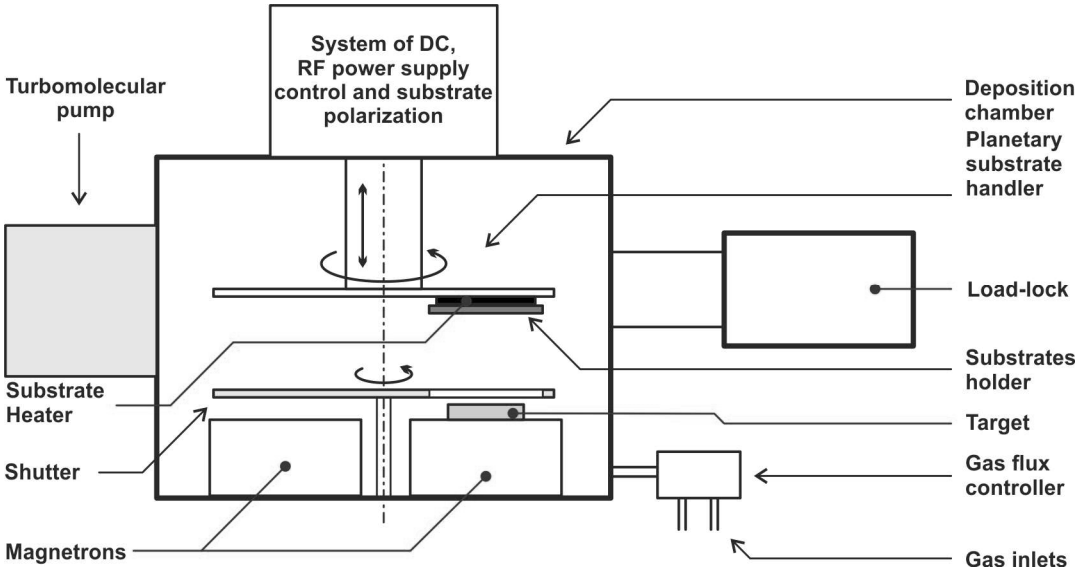

Figure II.32: Simplified schematic illustration of the sputtering system used to grow the ZnO samples.

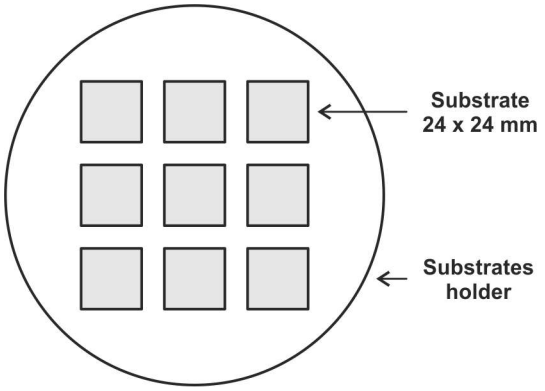

Figure II.33: Schematic illustration of the substrates configuration used to grow the ZnO samples.

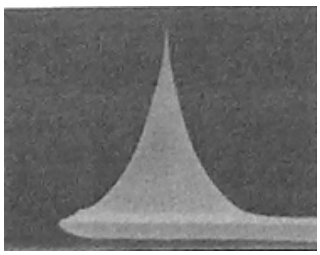

Figure II.34: Scanning electron microscope image of a NT-MDT CSG 10 AFM tip used to measure some of the samples reported in this work. [II.41]

II.4. Morphological and Structural Characterisation Techniques

The morphological and structural characterization of the samples involves the use of multiple techniques. Different techniques provide different and complementary information. In this section a short description of the techniques used with significant results are presented.

II.4.1. Atomic Force Microscopy

Atomic force microscopy (AFM) is a scanning probe microscopy technique used for morphological characterization of the surfaces at a microscopic level, where the information is obtained with a mechanical probe. It is a non-evasive technique with no need of prior preparation of the samples.

The AFM scanning consists measuring the morphology of a samples surface using a cantilever with a sharp tip (probe) at its end (see **Figure II.34**). The technique works by bringing the tip into proximity of a sample surface up to a distant that the AFM system can feed a deflection of the cantilever due to the interaction forces between the tip and the sample (see **Figure II.35** and **Figure II.36**). Depending on the situation, AFM can measure mechanical contact forces, Van der Waals forces, capillary forces, chemical bonding, electrostatic forces, magnetic forces, etc. As shown in **Figure II.36**, the type of interaction that is exerted on the tip and that originates the deflection of the cantilever arm depends of the distance tip and the surface, closer or more distant, and the interaction may be repulsive or attractive, respectively. The scanning modes are then named as contact and not contact mode depending on the type of force that is felt by the tip. A third type of mode, referred to as an intermittent mode, has been developed to overcome some of the disadvantages of the contact mode. For measuring the morphology of the surface sample, the most common modes are the so called contact mode and the tapping mode (or intermittent mode) where the cantilever is vibrated or oscillated at a given frequency.

In the contact mode, a scanning of the surface of the sample is made with the tip at distance smaller then 1~2 Å. This mode has some limitations, namely when the samples have a high roughness, being able to lead to the breaking of the tip.

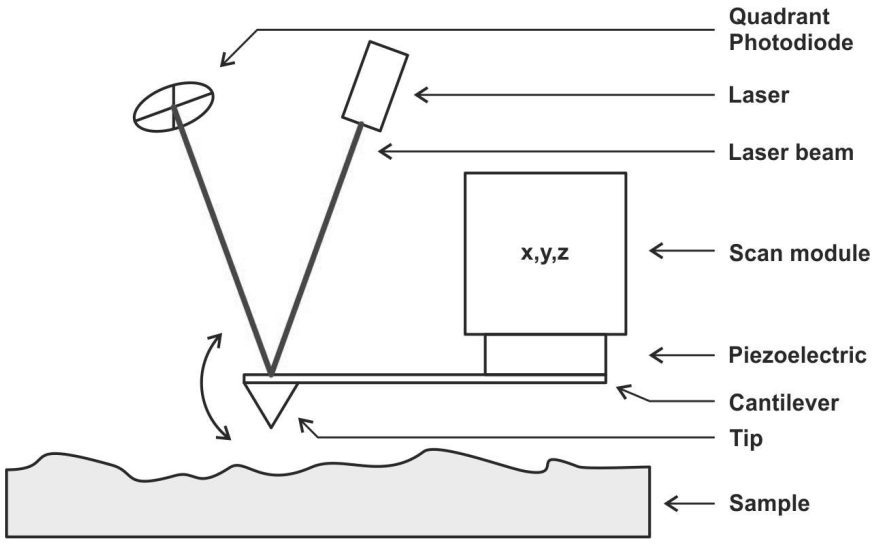

Figure II.35: Schematic diagram of an atomic force microscope. In contact mode, the tip 'touches' the surface sample; the tapping mode, or non-contact mode, the tip oscillates by the action of the piezoelectric and is used to 'feel' the surface of the samples.

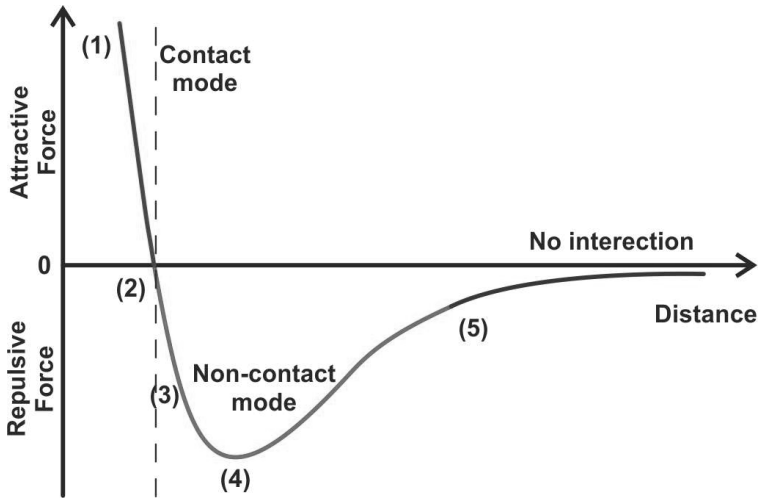

Figure II.36: Typical curve of the Van der Waals interaction divided into three distinct regions corresponding to three scan modes, marked in red, green and blue. (1) net force becomes positive and atoms are in 'contact'; (2) zero net force, the distance between atoms is 1 ~ 2 Å, roughly the length of a chemical bond; (3) as interatomic separation decreases, attractive force weakens; (4) electron clouds electrostatically repel each other; (5) weak atomic attraction.

In the non-contact mode, unlike in the previous case, consists of keeping the distance between the tip and the surface at higher distances, tens to hundreds of angstroms, where attractive Van-der-Waals interactions exist. In this mode the magnitude of the interaction of the surface with the tip is of the order of magnitude of 10^{-12} N **[II.40]**, about six orders of magnitude below the interaction present in the contact mode (10^{-6} N). Consequently, provides a lower resolution.

In tapping mode (see **Figure II.35)**, the tip is oscillated during the scanning with a constant frequency provided by a piezoelectric coupled to the cantilever. The maximum oscillation amplitude occurs when the tip is far away from the surface, so that its effect is negligible. As the tip approaches the surface oscillation amplitude decreases. This mode shows the advantages of the contact mode because in fact the tip 'touches' the surface, however this mode overcome the roughened specimens limitations that occurred in contact mode.

The cantilever is typically made of silicon (applied in all the samples of this work) or silicon nitride. The tip is characterized by its shape (pyramid, cone, etc.), tip radius, angle of the tip and material.

Within the scope of the objectives of the multiple GeSn samples (**Chapter IV**), the morphological analysis of the samples was of primordial importance since it reveals not only the morphology of the surface but also allows to obtain information about the grown of the samples. **Table II.3** shows the characteristics of the cantilevers used in the samples of this work.

Table II.3: Table with the characteristics of the AFM cantilevers tips used for the AFM measurements in this work. [II.41,II.42]

	Tip type #1	**Tip type #2**
Producer	NT-MDT	Bruker
Model	CSG10	TESPA
Material	Si	Si
Tip shape	High aspect ratio conical tip	Pyramid
Tip angle (º)	< 22	Front angle 25±2.5 Back angle 15±2.5 Side angles 22.5 ±2.5
Tip curvature radius (nm)	< 10	8 (max: 12)
Tip height (μm)	10 – 20	10 – 15
Force constant (N/m)	Nominal: 0.1 Minimum: 0.03 Maximum: 0.2	Nominal: 42 Minimum: 20 Maximum: 80
Resonant frequency (kHz)	20 ± 7	320 ± 90

II.4.2. Transmission Electron Microscopy

Transmission electron microscopy (TEM) is a powerful technique for structure characterization. The most important application of TEM is the atomic-resolution real-space imaging of samples. This technique emerged of the need of higher resolution than the one provided by optical microscopes. The resolution of the optical microscopes is limited, and in general, the Rayleigh criterion is used $r = 1.22\lambda/(2n\sin\theta)$, where λ is wavelength used, n is the index of refraction of the media surrounding the radiating points and is the half angle of the pencil of light that enters the objective. Even with ultraviolet light the resolution does not allow to observe structure of thin films samples. TEM takes in consideration the wave – particle duality concept and used electrons instead of photons, being capable to using substantially smaller wavelengths that the ones associated to optical microscopy.

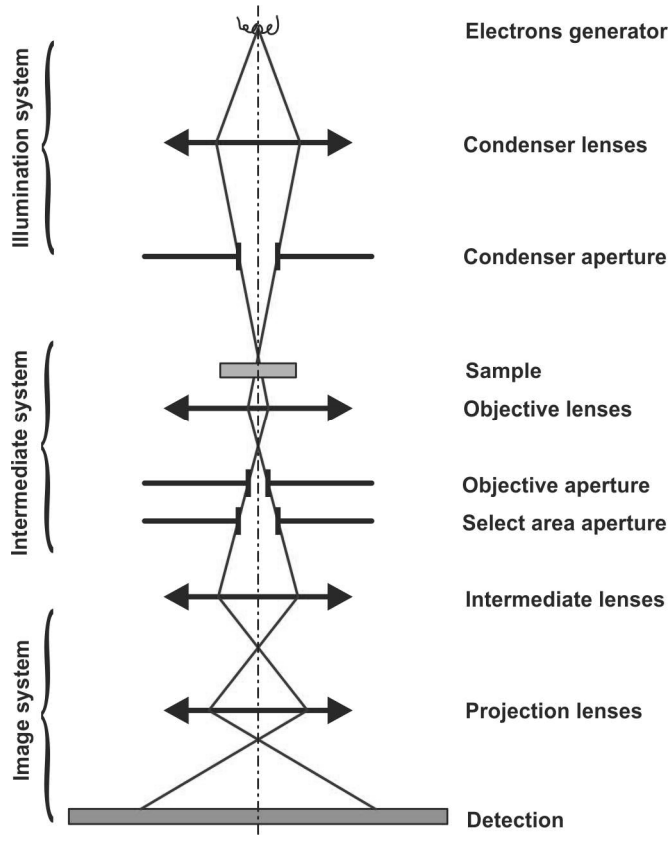

Figure II.37: Schematic diagram of a transmission electron microscope. The TEM works under vacuum conditions and the samples need previous preparation to have the right thickness conditions. The electron generator can be a thermionic or a field electron emission. The lenses form electric and magnetic fields capable to control the electros and the apertures are made of simple metal discs. The detection can be done by photographic film plates or with the use of florescent panels and optoelectronics image deceives like a CCD image sensor.

TEM is a microscopy technique in which a beam of electrons is transmitted through a sample to form an image. The specimen/sample is most often an ultrathin section less than 100 nm thick. An image is formed from the interaction of the electrons with the sample as the beam is transmitted through the sample. The image is then magnified and focused onto an imaging device, such as a fluorescence screen, a layer of photographic film, or a sensor such as a charge-coupled device. This technique not only provides capacity for atomic-resolution lattice image but also allows the obtaining of chemical information at a spatial resolution of 1 nm or better, allowing direct identification the chemistry of a single nanocrystal **[II.43-II.46]**.

A TEM device is composed by (see **Figure II.37**): (1) an illumination system, that takes the electrons from the electron gun and transfers them to the specimen giving either a broad beam or a focused beam; (2) an objective/intermediate lens and sample stage, this combination is the heart of TEM; (3) and the imaging system, includes the intermediate lens and projector lens.

The electrons of the illumination system are generated by a filament, by thermionic process or by a cold field electron emission source. The first one is commonly available and it is simple and cheap. The second one is less common and it has the advantage of high power, high energy and consequently a lower wavelength as the possibility to concentrate the electrons in a smaller spot for higher spatial precision, but it is difficult to operate and is substantially more expensive.

In the central section of the microscope the electron beam interacts with the sample and the resulting electrons are gathered and focussed ready for further magnification steps. The sample is prepared with different thickness depending of the TEM modes used in the analyses. While TEM measurement works with a ~ 100 nm thickness samples, High Resolution TEM (HR-TEM) needs thickness in the order of ~ 10 nm. Samples are commonly thinned in a focused ion beam system.

As the electrons are incident on the sample they may be scattered by several mechanisms. These scattering mechanisms will change the angle of the electrons relative to the optic axis, and the scattering can be elastic (conserving energy) or inelastic (with energy dissipated as heat). It is by measuring the changes to the electrons on passing through the sample, either by measuring the angle that they have been scattered through (such as by studying diffraction patterns or images) or by measuring the amount of energy that they have lost, that information about the sample can gather.

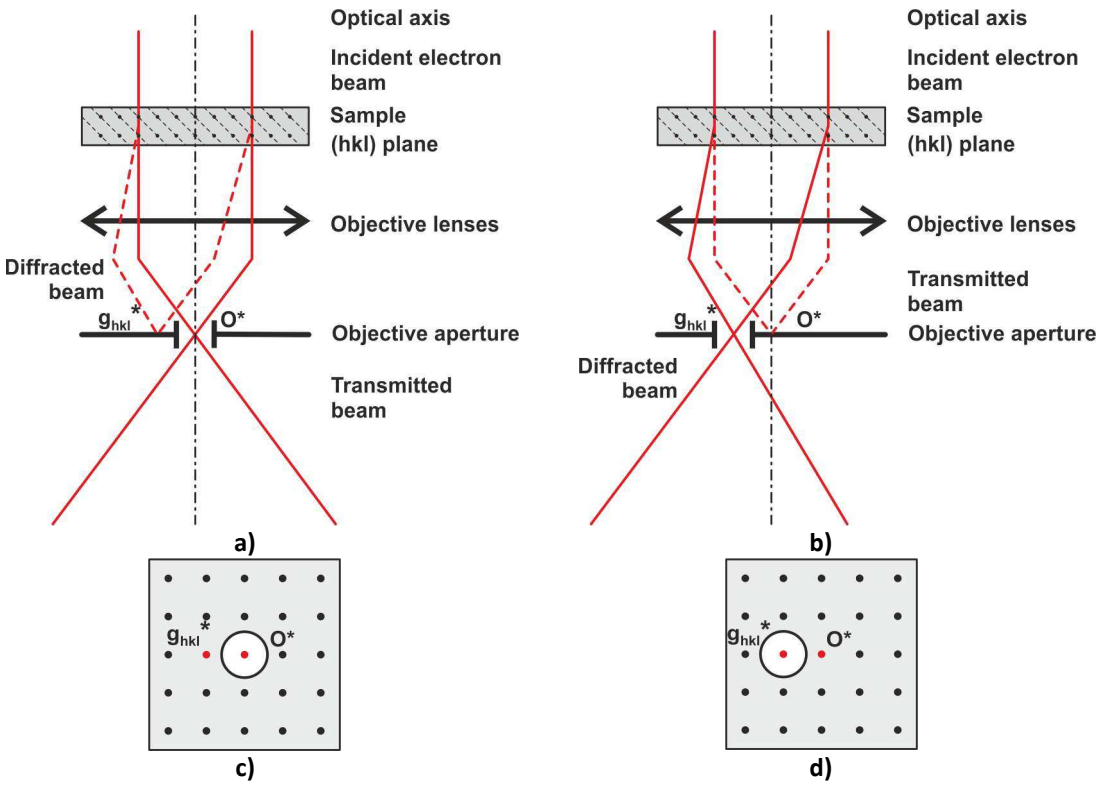

Figure II.38: Schematic diagram showing the mechanism of image formation in a) bright-filed and b) dark-field imaging mode in TEM and respective diffraction patterns, c) and d).

Images in TEM are usually dominated by three types of contrast. The first is diffraction contrast, which is produced due to the perturbation of local strain/defects/dislocation on the intensities of the Bragg reflected beams. This contrast emphasizes the effect of defects on the amplitude of the transmitted wave, and it is also called amplitude contrast. If the image is formed by selecting the central transmitted wave only, the image contrast is most sensitive to defect structures and the image resolution is limited to ~ 2 nm. The second, called phase contrast is produced by the phase modulation of the incident electron wave when it transmits through the crystal potential. This type of contrast is sensitive to the atom distribution in the specimen. The last one is mass thickness or atomic number contrast. Atoms with different atomic numbers exhibit different powers of scattering. If the image is formed by collecting the electrons' scattered to high angles, the image contrast would be sensitive to the average atomic number along the beam direction. This type of imaging is most frequently performed in scanning transmission electron microscopy.

There are two basic modes of TEM operation, namely the bright-field mode, where the (000) transmitted beam contributes to the image (see **Figure II.38a** and **Figure II.38c**), and the dark-field imaging mode, in which the (000) beam is excluded (see **Figure II.38b** and **Figure II.38d**). In the bright field (BF) mode of the TEM, an aperture is placed in the back focal plane of the objective lens which allows only the direct beam to pass. In this case, the image results from a weakening of the direct beam by its interaction with the sample. Therefore, mass-thickness and diffraction contrast contribute to image formation: thick areas, areas in which heavy atoms are enriched, and crystalline areas appear with dark contrast.

The size of the objective aperture in bright-field mode directly determines the information to be emphasized in the final image. When the size is chosen so as to exclude the diffracted beams, one has the configuration normally used for low-resolution defect studies, so-called diffraction contrast. In this case, a crystalline specimen is oriented to excite a particular diffracted beam, or a systematic row of reflections, and the image is sensitive to the differences in the specimen thickness, distortion of crystal lattices due to defects, strain and bending. High resolution imaging is usually performed in bright-field mode by including a few Bragg diffracted beams within the objective aperture. The lattice images are the result of interference among the Bragg reflected beams and the central transmitted beam, forming the phase contrast image.

In dark field (DF) images, the direct beam is blocked by the aperture while one or more diffracted beams are allowed to pass the objective aperture. Since diffracted beams have strongly interacted with the specimen, information about planar defects, stacking faults or particle size can be obtained.

Other mode is the High Resolution TEM (HR-TEM), which allows atomic resolution. As referred before, samples preparation is of high importance for HR-TEM since the required thickness is inferior to ~ 10 nm. Also, this mode needs an electron beam that in the zone of the sample has a long length a diameter small enough to be transmitted and detect single atoms. This is extremely useful in the area of semiconductors, since it allows the visualisation of the growth quality at an atomic level, it is also useful to infer materials intermixing and determine crystalline structure (see **Figure II.39** for an example).

It is also common for TEM systems capable to work in Scanning TEM mode (STEM) to have an Energy Dispersive Spectroscopy (EDS) system associated. In the case of the TEM system used for the analyses of the sample reported in this work, the EDS is capable of work in TEM or HR-TEM mode. The EDS is an analytical technique used for the elemental analysis and/or chemical characterization of the samples. It relies on the analysis of the X-rays emitted by the samples after being ionized by the electron beam of the STEM. Its characterization capabilities are due in large part to the fundamental principle that each element has a unique atomic structure allowing a unique set of peaks on its electromagnetic emission spectrum. This way, EDS can be used to determine which chemical elements are present in a sample, and can be used to estimate their relative abundance. Together, the STEM and the EDS can be used to build an image with an elemental chemical map.

Within the scope of the objectives of the multiple GeSn samples (**Chapter IV**), the structural analysis of the samples was of primordial importance since it reveals the growth quality of the samples with ultra-thin layers and the impact of different layers across the sample structure.

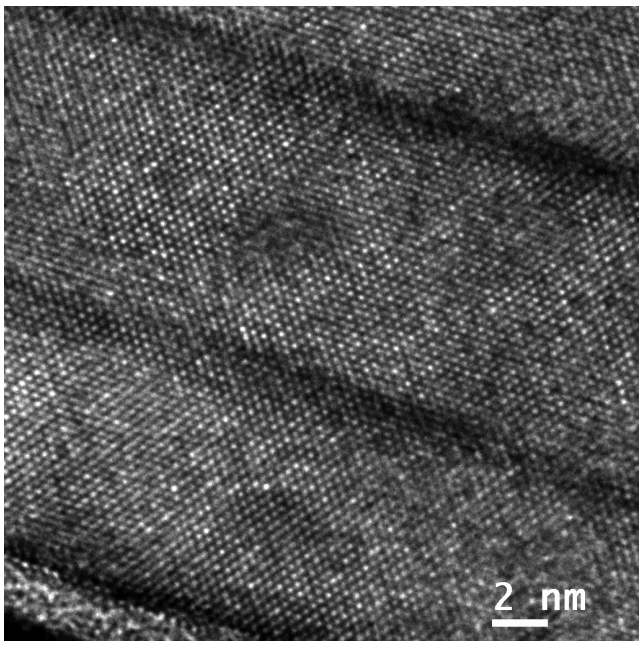

Figure II.39: High resolution transmission electron microscopy image of a sample of multi quantum wells of Ge on Si (see Chapter IV.2.2). The dark zones are mainly made of Ge atoms, while the brighter zones are mainly made of Si atoms.

II.4.3. X-Ray Diffraction

Another technique useful to obtain structural information about condensed materials is X-Ray Diffraction (XRD). The technique uses x-ray radiation with a wavelength comparable to interatomic plane distances of the sample that results in diffraction. The physical phenomenon of diffraction can be described by the law of Bragg **[II.47]**:

$$n\lambda = 2d \sin\theta \qquad \textbf{\{II.5\}}$$

where n is the diffraction order, λ is the wavelength of the X-radiation used, d is the interplanar distance and θ the angle that the incident radiation makes with the tangent to these planes. **Figure II.40** shows an illustration of the interaction of X-rays with a crystalline material. When the Bragg condition **{II.5}** is fulfilled, constructive interference occurs.

By analyzing the diffraction pattern, namely the shape, intensity and position of the diffraction peaks that result from the interaction of X-radiation with matter, several sample information can be obtained: structure, crystallinity (single crystal, polycrystalline, etc.), crystal size, strain, composition, etc. XRD is a non-destructive technique with no need of pre-preparation of the samples.

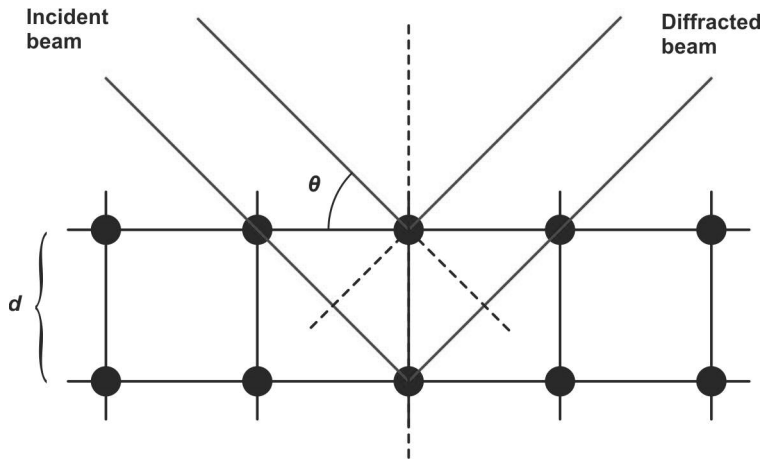

Figure II.40: Ilustrative diagram of the path of different X-rays incident on a sample at an angle θ.

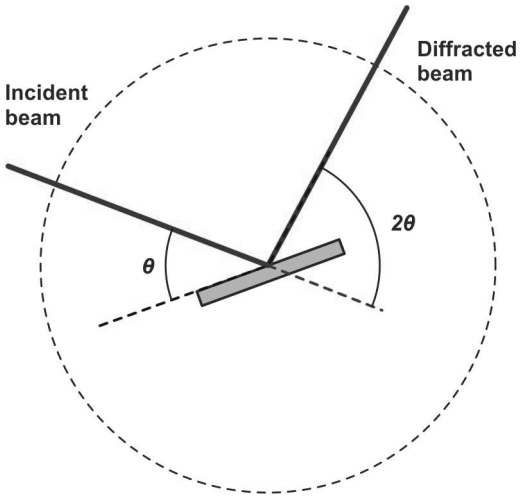

Figure II.41: Illustration of the Bragg-Brentano X-ray diffraction configuration.

II.4.3.1. Bragg-Brentano Geometry

There are different geometries for the X-rays diffraction and reflection studies. The geometry used in the scope of this work was the one of Bragg-Brentano, sometimes also referred to as θ/2θ geometry (see **Figure II.41**). The X-ray diffraction system performs the measurements by scanning in θ, and measuring the intensity of diffracted photons.

The Bragg-Brentano XRD scanning is very useful for structural analysis, being possible to achieve the structure properties and crystalline quality by analyzing the peaks intensity, shape and position of the diffraction peaks. Typically a broadening of the diffraction peaks occurs due to packaging failures, micro strain, grain boundaries, compositional heterogeneity, crystallite size, among others. While, the shift of the peak maximum position is typically associated with the presence of homogeneous stress in the film. The peak shape can be changed if, for instance, the sample has different stress stages, *i.e*. heterogeneous stress.

In order to extract information of the data and be able to quantify the three characteristics that define X-ray diffraction, namely position, shape and width, the different peaks present in the diffractogram are adjusted using different distributions,

such as the Gaussian (Gaussian function), Cauchi (Lorentzian function) and Gauss-Cauchi (pseudo-Voigt function) ones. The X-ray spectra presented in this thesis were fitted using the Lorentzian function. After the peak fit, the maximum peak angle is achieved and this value is used to the lattice parameter estimation and then the interplanar distance. Then the homogeneous deformation (strain) can be obtained as:

$$\varepsilon = \frac{\Delta d}{d_0}, \qquad \textbf{\{II.6\}}$$

where d_0 is the interplanar distance of a relaxed material and $\Delta d = d - d_0$.

The previous **Equation {II.6}** can be generalized to the parallel plane (//) to the surface and the perpendicular axis ($\perp$) to the surface in a cubic lattice and rewritten according to their lattice parameters as:

$$\varepsilon_{\parallel} = \frac{a_{\parallel} - a_0}{a_0} \qquad \textbf{\{II.7\}}$$

$$\varepsilon_{\perp} = \frac{a_{\perp} - a_0}{a_0} \qquad \textbf{\{II.8\}}$$

where a_0 is the lattice parameter of the relaxed sample. Concerning the broadening of the diffraction peaks, typically the Debye-Scherrer model gives information related to the sample mosaicity, namely the coherent “crystal” size, according to:

$$D = \frac{\lambda}{\beta_{2\theta} \cos\theta} \qquad \textbf{\{II.9\}}$$

where $\beta_{2\theta}$ is the integral width of the pseudo-Voigt function and θ is the angle of incidence. The integral width of the pseudo-Voigt function is given by:

$$\beta_{PV} = \eta\beta_L + (1-\eta)\beta_G \qquad \textbf{\{II.10\}}$$

in which β_L and β_G corresponds to the Lorentzian and Gaussian widths, respectively, and η is a fitting parameter.

II.4.4. Rutherford Backscattering Spectrometry

The Rutherford backscattering spectrometry (RBS) technique is based on elastic collisions of ions with matter through their Colombian repulsion by atomic nuclei (see **Figure II.42**). The technique uses an ion beam of well defined energy to analyse samples, in general protons ($^1H^+$) or alpha particles ($^4He^{2+}$). The energy of the beam particles is high enough (0.5 to 5 MeV **[II.48]**) to penetrate the sample (few microns) and interact with the matter but not enough to 'kick' atoms out of the sample (recoil). The energy of the ions decreases along their trajectory due to inelastic collisions with electrons and elastic collisions, of small angles, with the core of atoms **[II.49]**. The inelastic collisions originate other processes of electronic excitation, such as the ionization of the atoms of the sample **[II.49]**. The kinetics of the collisions and the scattering cross section are independent of the chemical bonding, and hence backscattering measurements are insensitive to the electronic configuration or chemical bonding within the target **[II.48]**. After the interaction, the number of the retro-dispersed particles is counted versus their energy and thus provides quantitative information on the interaction of the ion beam with the target. In particular, from the resulting spectrum one can obtain information such as sample composition and stoichiometry, film thickness, morphology and crystalline quality.

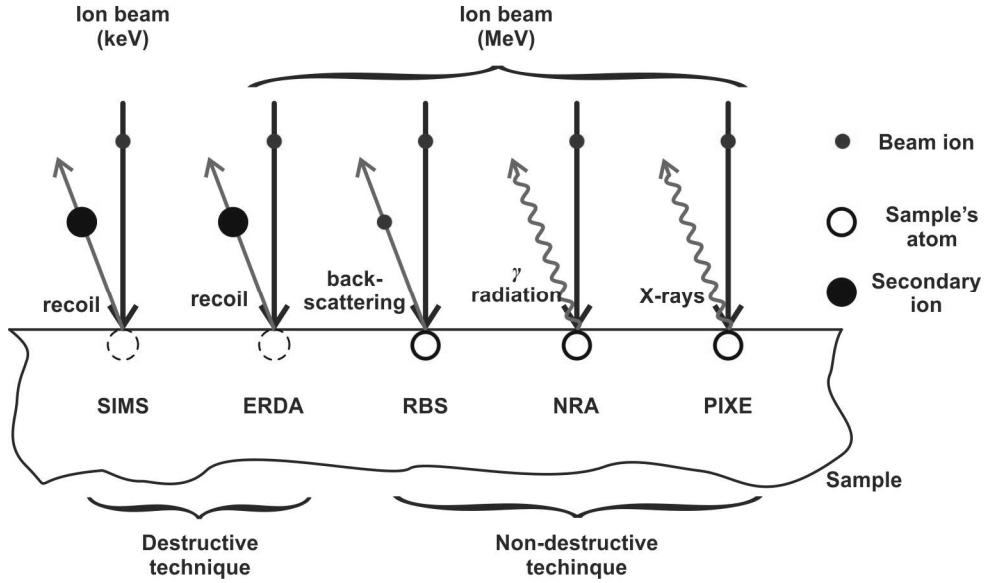

Figure II.42: Schematic illustration of different types of interaction between ion beams and a solid sample. The meaning of the abbreviations: SIMS – Secondary Ion Mass Spectroscopy; ERDA (or ERD) – Elastic Recoil Detection Analysis; RBS – Rutherford Backscattering Spectrometry; NRA – Nuclear Reaction Analysis; PIXE – Particle induced X-ray emission.

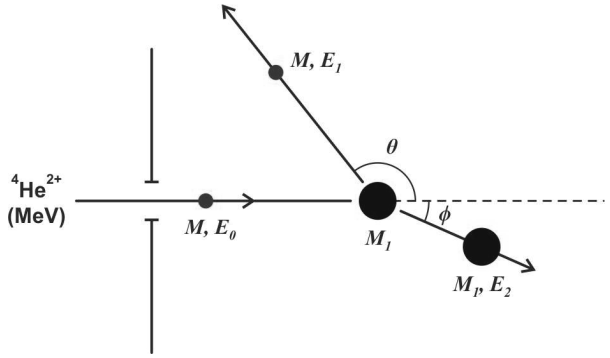

Figure II.43: Schematic illustration of the backscattering process for an alpha particle with energy E_0.

The study of the sample composition by RBS is made by analysing the energy of the dispersed particles according to their scattering angles. **Figure II.43** shows a schematic illustration of the process of backscattering of a beam particle after the collision with a particle of the sample, initially at rest. Applying the principle of conservation of the energy and the linear momentum for an elastic collision between an ion (mass M and energy E_0) and an atom of the sample (mass M_1) it is possible to obtain the ratio between the energies of the incident ion and the backscattered one (energy E_1) as function of the scattering angle, θ:

$$E_1 = \frac{\left(M_1^2 - M^2 \sin^2\theta\right)^{1/2} + M\cos\theta}{M + M_1} E_0 , \qquad \textbf{\{II.11a\}}$$

or, equivalently,

$$E_1 = K_1 E_0 , \qquad \textbf{\{II.11b\}}$$

where K_1 is called the kinetic factor for the element 1. Knowing the energy of the scattered particles in a certain direction, it is possible to determine the core atom mass, M_1, of the deflecting particle and, consequently, proceed to its identification, since the backscattered ions with different energies are deflected by different core atoms.

The incident ions penetrate the sample until they are scattered by the atomic nuclei in the sample. **Figure II.44** shows an illustration of a typical RBS spectrum of a thick sample made of a single chemical element. The two values that characterize a RBS spectrum are the number of counts, H, and the energy of the scattered ion. The number of counts registered by the detector is a function of multiple parameters, such

as the number of incident ions that reach to the sample, the density of atoms in the sample, the depth (δx) at which the scattering occurs (proportional to the interval of energy, δE, in the RBS spectra) and the effective scattering cross-section.

The scattered particle reaches the detector with an energy E_1 (see **Figure II.44)** which is below a certain threshold, KE_0, where the constant K describes the surface scattering. The energy loss,

$$\Delta E = KE_0 - E_1, \qquad \textbf{\{II.12\}}$$

Is due to the interactions with electrons and can be associated with the depth, δx.

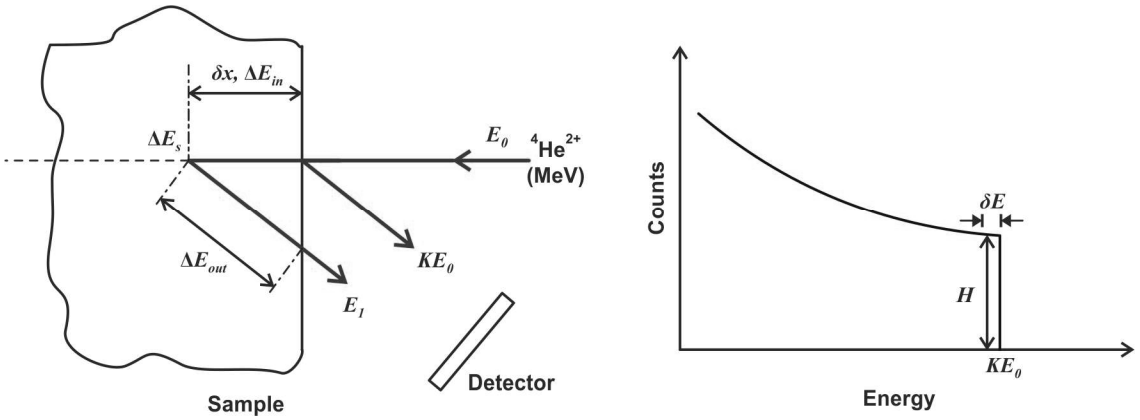

Figure II.44: a) Schematic illustration of the backscattering process with alpha particles (initial energy E_0) in a sample composed of a single element and the respective energy losses; b) the respective Rutherford back scattering spectrometry curve. The ions scattered at the sample's surface have the energy KE_0 (K is a constant) and those scattered inside the sample have a lower energy, E_1.

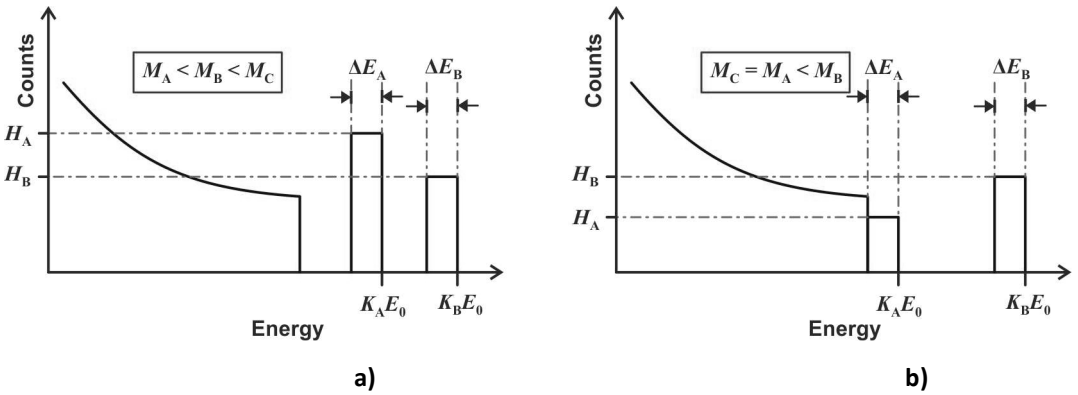

Figure II.46: Illustration of the resulting Rutherford backscattering spectrometry curves of the back scattering process with alpha particles and an initial energy E_0 in a sample made of a thin-film of two elements, A and B, with a substrate composed of a single chemical element S; a) all three elements have different masses; b) the substrate atom and one of the atoms constituting the film have the same mass.

RBS can be used to analyse samples with more than one element and with multiple layers. In **Figures II.45** and **II.46,** it is shown a RBS spectrum of a thin film sample with two elements (A and B) on a substrate. As the incident beam (with particle's energy E_0) penetrates the film, multiple energetic alterations occur. Some incident particles will collide with the atoms at the surface hitting the detector with an energy E_1. The energy of the scattered ion is $E_1^A = K_A E_0$ for the one that collided with an atom of the element A and $E_1^B = K_B E_0$ if it collided with an atom of the element B.

A significant part of the ions penetrates the sample losing gradually energy until scattering occurs. After travelling through the thin film until the scattering moment, the ion will have an energy E_2:

$$E_2 = E_0 - \Delta E_{in}, \qquad \textbf{\{II.13\}}$$

where ΔE_{in} is the energy lost owing to the inelastic interaction with electrons. After the scattering, the energy will be $E_3 = KE_2$ ($E_3 = K_A E_2$ in the case of a collision with an atom A and $E_3 = K_B E_2$ ($E_3 = K_A E_2$ in the case of a collision with an atom B). On its way inside the sample, the ion loses energy to electrons and is reaches the detector with some energy $E_4 = E_3 - \Delta E_{out}$. The qualitative view of the RBS spectra for a thin film sample is shown in **Figure II.46**, from which it can be seen that the analysis must take into account also the chemical composition of the substrate.

The angle of incidence, the beam energy and the sample orientation also are important parameters in this technique. In the case of the RBS system used to measure the samples studied in this work, three detectors are present in the measurement chamber: a standard one at 140^o and two pin-diode detectors located symmetrically, both at 165^o (detector 3 on the same side as the standard detector 2), as shown in **Figure II.47**. The RBS data were analysed with the IBA DataFurnace NDF v9.4g **[II.50]**.

Figure II.48 shows a RBS spectrum of one of the studied ZnO film on sapphire substrate, obtained with a 2 MeV with $^4He^{2+}$ beam, at an angle of incidence of 0º. The results show the existence of barriers that are associated with the presence of different chemical elements that constitute the film (namely, zinc and oxygen), as well the ones that constitute the substrate (aluminium and oxygen). The beam penetrates deeper (few microns) than the film thickness (< 1 μm). The difference in the number of

counts observed is proportional to the product of the concentration of the element and the effective cross-section of deflection which, in turn, is proportional to the square of the atomic number (Z^2). Beyond the features associated with the constituents of the film, one can also see those related to the sapphire, in particular, the oxygen from the substrate.

For thin films, as is the case of the sample shown in **Figure II.48**, it is possible to estimate the width of the different features ("barriers") associated with the chemical elements that constitute the film. This width depends on the thickness and the stopping power of the material (total energy loss) and it is possible to estimate the film thickness from a RBS spectrum.

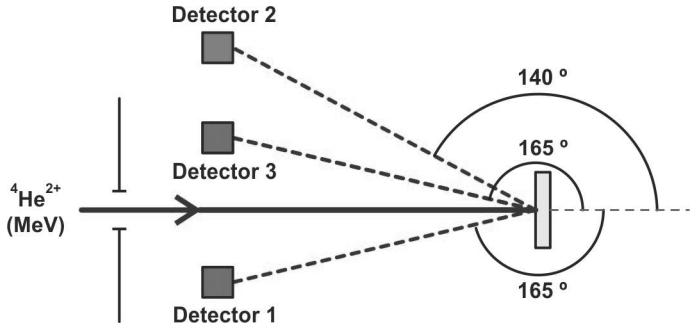

Figure II.47: Schematic illustration of the of the detectors position in the Rutherford backscattering system used to measure the samples reported in the work.

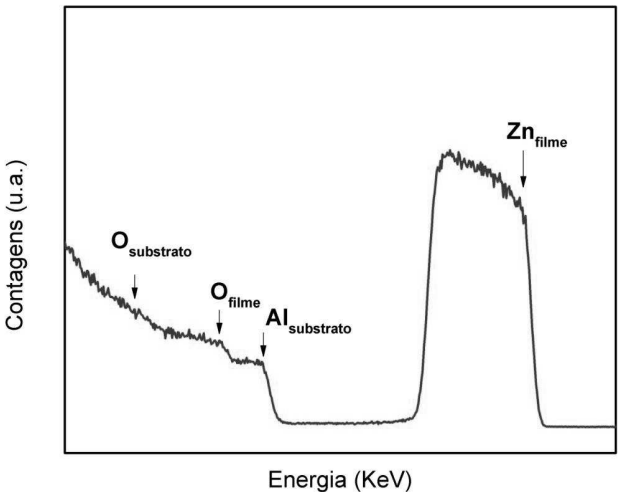

Figure II.48: Rutherford backscattering spectrum of a ZnO thin film grown sputtered on a sapphire substrate using a $^4He^{2+}$ beam with 2 MeV. The extraction of data is made by fitting simulations with the spectrum.

II.5. Faraday Rotation Effect

The interaction of light with matter, in nearly all parts of the electromagnetic radiation spectrum is determined by the electronic structure of the interacting medium. In particular, the interaction is affected by the magnetic state of the medium, and this gives rise to magneto-optic (MO) effects **[II.51]**. These MO effects played an important role in the early history of electromagnetism, providing an experimental support to the electromagnetic theory of light, as well as to both classical and quantum theory of matter including the motions of electron spin and spin-orbit coupling **[II.52]**.

The first magneto-optic (MO) effect was observed in 1845 by Michael Faraday. Faraday found that the azimuth of a linearly polarized light is rotated after travelling parallel to a magnetic field and to the axis of a flint glass rod with polished faces (see **Figure II.42**). The azimuth rotation is proportional to the applied magnetic field and to the length of the glass rod. The phenomenon is known as Faraday rotation or Faraday effect and was the first experimental evidence of that the light and electromagnetism are related. In 1876, John Kerr announced azimuth rotations, however much weaker, upon the reflection of linearly polarized light on a perpendicularly magnetized air-iron interface. The effect is called MO polar Kerr rotation. Later, it was found that the azimuth transformation of the incident wave in the Faraday or MO Polar Kerr effect is only one of the effects resulting from the light propagation in a parallel magnetic field. Often this rotation is accompanied by the transformation of the wave ellipticity, which is a manifestation of circular birefringence and dichroism induced by the magnetization of the medium parallel to the propagation vector and a consequence of the dispersion relations of electromagnetic waves affected by the magnetization. Without entering into much detail, an overview of the Faraday effect is given in this section, since it is important for magnetic transparent semiconductors and was investigated, in particular, for ZnO:Mn, one of the two solid solutions that have been the object of the present study. **[II.52]**

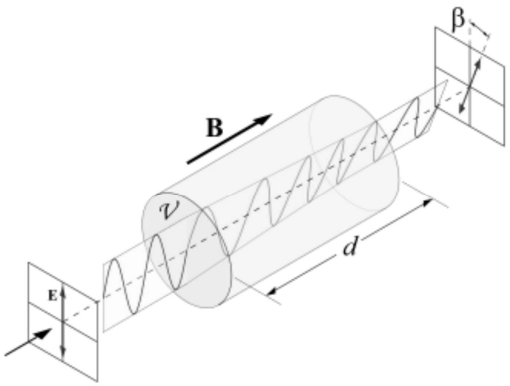

Figure II.49: Faraday effect illustration, where B is the magnetic field and the arrow indicates the direction of propagation and β is the Faraday angle (in many cases denoted by θ_F). Figure adapter from [II.53].

II.5.1. Brief Description of the Faraday Rotation Effect

Faraday rotation effect (FE) or magnetic circular birefringence (MCB) belongs to the category of magneto-optic (MO) effects related with the interaction between light and a magnetic field in a medium and occurs in transmission configuration. The FE is a rotation of the plane of polarization of an incident electromagnetic radiation and this rotation is proportional to the component of the magnetic field in the direction of propagation (see **Figure II.49**).

The Faraday effect is caused by the difference propagating speeds of the left and right circularly polarized waves, induced by the applied magnetic field. The difference of the propagation speeds between two different circular polarisations of light are related with different refractive indices of the medium that described left and right circular polarized waves and the result is a rotation of the plane of polarization. Microscopically, the difference between these refractive indices depends on a weighted average over all electronic transitions in the material, which are split by the applied magnetic field **[II.54].**

The Faraday effect can be phenomenologically understood in terms of the space anisotropy introduced by the axial nature of the magnetic field. Since a linear polarization can be decomposed into the superposition of two equal-amplitude right and left circularly polarized components with different phase, the effect of the magnetic field must be different for each component. The effect of the magnetic field on the right polarized component must be the same as the effect of the opposite magnetic field on the left polarized component. Therefore the refractive index and the

wave propagation velocity are not the same for both directions of polarization and a rotation of the plane of polarization of the linearly polarized radiation will appear. If the medium partially absorbs the radiation, the absorption coefficients will also be different for two directions of polarization and the outgoing beam will be elliptically polarized **[II.55]** – however, this is already a different effect called magnetic circular dichroism.

The refractive indices for the right (clockwise) and left (anticlockwise) polarized radiation are generally represented as η_+ and $\eta-$, respectively. If d is the sample thickness, the difference in optical path for both polarizations, after having crossed the sample, is $(\eta_+ - \eta_-)d$ and the corresponding Faraday rotation angle can be expressed as:

$$\theta_F = -\frac{1}{2}\frac{\omega}{c}(\eta_+ - \eta_-)d \qquad \textbf{\{II.14\}}$$

where ω is the angular frequency of the radiation and c is the speed of light. $(\eta_+ - \eta_-)$ is in general proportional to the applied magnetic field (and magnetization). The sign of the right-hand side of **Equation {II.14}** depends on the choice of expression for a plane wave, either $\exp[i(\omega t - kx)]$ or $\exp[i(kx - \omega t)]$. **Equation {II.14}** assumes the last choice and can be rewritten as:

$$\theta_F = VBd \qquad \textbf{\{II.15\}}$$

where V is called the Verdet constant **[II.55].** It is an optical parameter that describes the strength of the Faraday effect for a particular material. This "constant" is wavelength dependent and for most of materials is extremely small.

Faraday effect measurement is an important characterization technique, (although not so common in research laboratories) and has applications in several fields, namely, in evaluation of the optical rotatory power and remote sensing of magnetic fields (such as fibre optic current sensors). The Faraday effect is used in spintronics to study the polarization of electron spins in semiconductors. Materials having good Faraday rotation signals are the basis of optical isolators and optical circulators, components essentials in optical telecommunications and several laser applications, furthermore these materials can also be used for amplitude modulation of light.

A more detailed description of the Faraday effect in (magnetic) semiconductors is provided in the **Appendix A**.

II.5.2. Magneto-Optic Effects in Semiconductors

The MO effects can be used to perform measurements of spectral response (at a fixed magnetic field) and hysteresis loops of the magnetization vs magnetic field for a fixed wavelength. These two types of measurements have different purposes. Measurements of the spectral response (performed in this work) are more useful to study the electronic structure and the magneto-optical effects the sample, while hysteresis loops allow for the study of the magnetization and the magnetic nature of the samples.

The measurement of the rotation angle can be performed by several different methods. The simplest one is performed directly by sending a polarized beam onto the sample and performing the alignment of the second polarizer in order to obtain the maximum intensity of the beam. However, this method only provides rough estimates of the Faraday rotation. To perform high sensitivity measurements, modulation of the beam is essential to reduce noise. The most common methods to measure Faraday (and Kerr) effect are:

(i) the polarization modulation using a Faraday cell **[II.52, II.56, II.57]**;

(ii) the intensity method **[II.54]** (used here);

(iii) the photoelastic modulator (PEM) technique **[II.58,II.59]**.

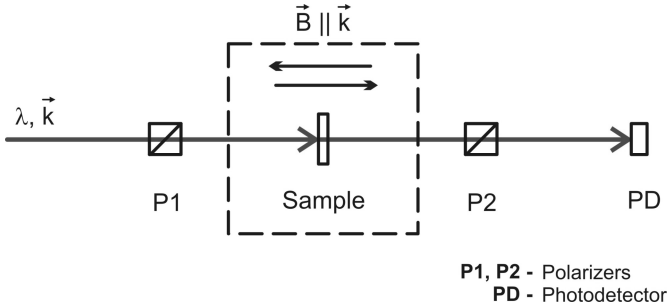

Figure II.50: Faraday angle measurement concept.

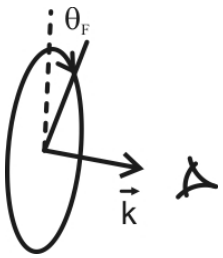

Figure II.51: Convention used for the positive Faraday angle, θ_F.

Table II.4: Dependence of the variation of the light intensity, ΔI, with the applied magnetic field for different angles between the planes of polarization of the two polarizers.

Angle (°)	Mag. Field	ΔI
0	± *B*	< 0
90	± *B*	> 0
+45	+ *B* – *B*	> 0 < 0
–45	– *B* + *B*	> 0 < 0

Table II.5: Faraday angle and Verdet constant signal dependence with the magnetic behaviour of the sample.

Magnetic behaviour	Faraday Angle	Verdet Constant
diamagnetic	+	+
paramagnetic	–	–
ferromagnetic	–	–

II.5.2.1. Fixed Polarizers

Of all three techniques, this is the easiest to implement and it was used in this work. In this technique both polarizers are kept fixed with a pre-defined angle between them (see **Figure II.50**). By measuring the intensity of transmitted light for two directions of the magnetic field, it is possible to obtain the Faraday angle.

Three natural choices of the angle between the planes of polarization of the polarizers are 0^o, 45^o and 90^o. The maximum variation of the intensity is achieved when the polarization angle is 45^o. For this case, a variation of the direction of the magnetic field will result in a positive or negative variation of the light intensity. In the case of 0^o and 90^o the variation with the magnetic field will be always positive or negative, respectively (**Table II.4**). The use of 45^o not only provides a maximization of the variation of intensity, but also has the advantage of provide information about the magnetic nature of the samples.

By convention, the Faraday angle, θ_F, is positive according to **Figure II.51**. The sample will have a positive angle to diamagnetic materials and negative one if the material has para- or ferromagnetic behaviour. The same is valid for the Verdet constant, V (**Equation {II.15}**) – **Table II.5**.

The angle can be determined by:

$$2\theta_F = \frac{I^{\uparrow} - I^{\downarrow}}{I^{\uparrow} + I^{\downarrow}}, \qquad \{II.16a\}$$

$$+B \Rightarrow I^{\uparrow}, \qquad \{II.16b\}$$

$$-B \Rightarrow I^{\downarrow}, \qquad \{II.16c\}$$

where $I^{\uparrow}$ and $I^{\downarrow}$ is the light intensity for two directions of the magnetic field applied to the sample, respectively.

Table II.6: Parameters' ranges allowed in the developed Faraday rotation effect setup.

Spectral Range	340 – 1700 nm
Spectral resolution	0.5 – 6 nm
Magnetic field	[–0.55, +0.55] T
Temperature	10 – 300 K
Faraday angle resolution	< $2x10^{-4}$ rad (<0.01º)

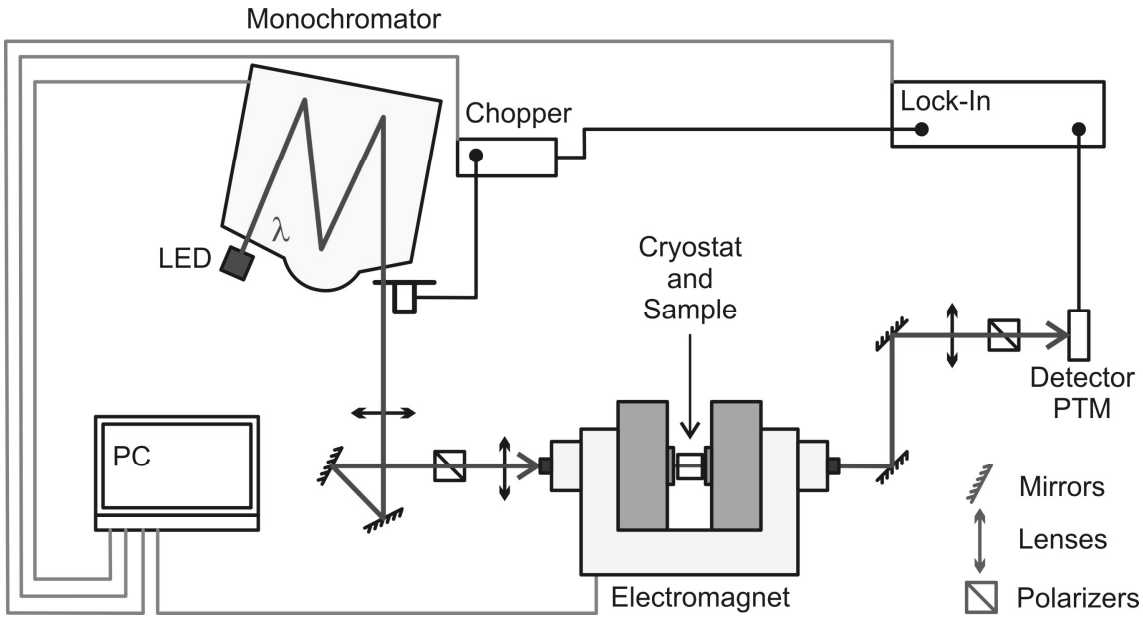

Figure II.52: Illustration of the Faraday rotation setup developed based on the fixed polarizers technique to measure the Faraday angle in spectral response mode.

II.5.3 Faraday Rotation Setup

A setup was developed to perform the Faraday rotation effect spectroscopy. The main objective was to develop a Faraday effect setup capable to measure the spectral response in order to study ZnO:Mn thin films grown on glass substrates near the band gap at low and room temperatures.

The fixed polarizers technique was adopted, mainly because it allows for higher automation only with one lock-in amplifier without the necessity to use complex processing electronics (see **Table II.6** and **Figure II.52**). The developed setup can be adapted to perform measurements in different spectral regions from ultraviolet to near infrared. Measurements in the ultraviolet-blue spectral range (< 425 nm) are made using several LEDs. LEDs are cheaper than Xenon lamps and easier to stabilize the light intensity by using a proper controller with photodiode feedback. The detection is performed by a photomultiplier (PMT) for UV-VIS region. Measurements in the visible and infrared spectral range were performed with a halogen lamp. If visible is the region of interest, a PMT or a Si photodiode is used, while for near infrared range an InGaAs photodiode is used. The used monochromator has three diffraction gratings, each one suitable for each region allowing spectral resolution between 0.5 and 6 nm – higher spectral resolution decreases the light intensity and decreases the Faraday angle resolution. Two Glan-Thompson polarizers are used at 45^{o} to improve the Faraday angle resolution (instead 0º or 90º). A lock-in amplifier is used to read the detector intensity and to control the magnetic field applied by the electromagnet. A computer program was developed in order to control the lock-in reads and the magnetic-field. Low temperature measurements are performed using a close circuit helium cryostat.

II.5.4 Measurement of the Faraday Angle in Thin Films

The Faraday rotation effect in thin films raises some issues that are important for obtaining correct results and need to be taken in account. The first one is that thin film samples are composed of a film and a substrate and it is not possible to separate one from the other to measure only the film. Both of them are measured together and

then the rotation angle due to the film has to be extracted. Other important issue concerns the spectral fringes caused by optical interferences resulting of the reflected and refracted beams at the surfaces and interfaces of the sample (**Figure II.53**). This last issue is especially important in transmission MO effects because typically the samples have low absorption. As explained above, the Faraday rotation effect is related to an unequal refractive index of the medium (in applied magnetic field), with respect to the RCL (right-handed circularly polarized light) and LCL (left-handed circularly polarized light) polarizations of light and is proportional to the optical path. Therefore, the interference effects owing to the multiple reflections in thin films can affect the spectral variation of the Faraday rotation angle.

The most reliable way to determine the influence of these two issues is modelling of the MO spectrum taking into account the effect of multiple reflections of the electromagnetic wave at all interfaces. To test this, an algorithm was developed, based on the transfer matrix formalism presented in **[II.52]**, where the necessary details can be found. **Figure II.54** shows a calculated spectrum based on the Lorentz model for the dielectric function of a slab (mimicking ZnO), showing that the interference effects on the Faraday angle can be neglected, i.e. the interference fringes are much less important in the Faraday effect spectrum than e.g. in the transmittance one. The calculations were performed for a slab with 1 μm of thickness and a material with a resonant energy, E_0, of 4.0 eV and a damping term, Γ, of 0.5 eV. The modulated material is close to the ZnO, as can be see by the transmission of a real ZnO film sample shown in **Figure II.53** and the modulated transmission in the inset of **Figure II.54**.

In the case of samples with high internal absorption, the spectral fringes may not exist, and then it is possible to measure MO spectra in the same way as for a bulk sample, *i.e.* in reflection (so called magneto-optic Kerr effect, MOKE).

Based on the results obtained by the model described above, with the results presented in **Figure II.54**, one can conclude that the Faraday rotation effect in the visible spectral range is not strongly affected by the presence of optical interference effects due to multiple reflections of light at the interfaces for a thin film sample. This

means that the Faraday rotation effect on the film can be separated from the Faraday rotation effect in the substrate. Thus, the first issue presented in the previous section can be easily solved by measuring the substrate alone and then measuring the whole sample (film on the substrate). The Faraday angle for the film is then obtained by subtracting the two spectra (see **Figure II.55**).

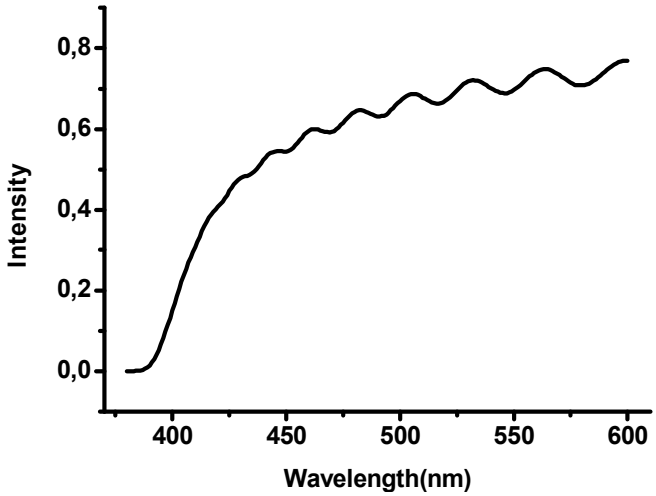

Figure II.53: Measured transmission of a ZnO film on a glass substrate. The spectrum shows the interference pattern with the wavelength, typical of a thin film sample.

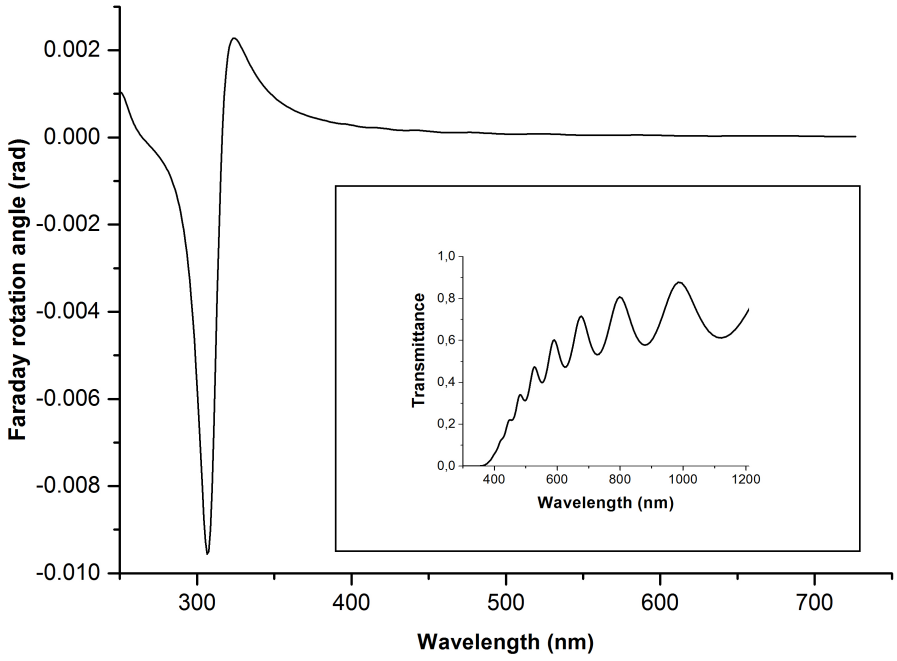

Figure II.54: Calculated transmission and Faraday rotation angle spectra of a slab using the Lorentz model with a thickness of 1 μm, a resonant energy, E_0, of 4.0 eV and a damping term, Γ, of 0.5 eV.

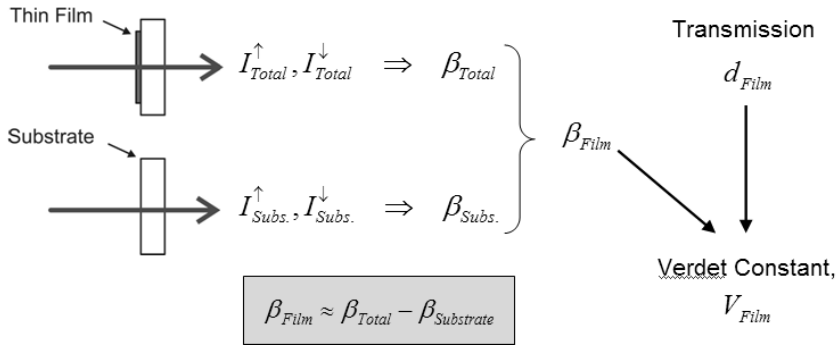

Figure II.55: Illustration of the extraction of the Faraday angle and the Verdet constant for a thin film sample.

Summary

A detailed description of the growth methods used for the samples preparation and the main characterization techniques has been presented. It includes the two growth techniques used for samples preparation, namely, molecular beam epitaxy for GeSn system and RF sputtering for ZnO thin films. The physical foundations of the techniques used for sample characterization have been explained in some detail. Among these techniques, those that provided most relevant information for their characterization were: RBS, XRD, TEM and AFM for the GeSn system and XRD for ZnO thin films. In the last section, the Faraday effect spectroscopy technique, developed by the author of this thesis and used to study ZnO:Mn films was presented. The corresponding results obtained by using these techniques will be presented in the subsequent chapters.

Bibliography

[II.1] Erick Kasper, and John C. Bean. *Silicon-Molecular Beam Epitaxy – Volume I.* CRC Press, Boca Raton, USA, 1-105, (1988).

[II.2] A. Madhukar. *Far from equilibrium vapor-phase growth of lattice matched Group III-Group V compound semiconductor interfaces: some basic concepts and Monte-Carlo computer simulations.* Surf. Sci. **132**, 344, (1983).

[II.3] M. A. Herman. *Semiconductor Superlattices.* Akademie-Verlag, Berlin, Germany, (1986).

[II.4] M. A. Herman, and H. Sitter. *Molecular Beam Epitaxy – Fundamentals and Current Status.* 2nd ed., Springer, Berlin, Germany, 1-32, (1996).

[II.5] B. Lewis, and J.C. Anderson, *Nucleation and Growth of Thin Films.* Academic, New York, USA, (1978).

[II.6] R. A. Stradling, and P. C. Klipstein. *Growth and Characterization of Semiconductors.* Adam Hilger, Bristol, England, (1990).

[II.7] Edited by D. T. J. Hurle. *Handbook of Crystal Growth - Volume la*, North-Holland, Amsterdam, Netherland, (1993).

[II.8] M. A. Herman, W. Richter, and H. Sitter. *Epitaxy, Physical Principles and Technical Implementation.* Springer, Germany, 1-10, (2004).

[II.9] E. Bauer. *Phaenomenologische Theorie der Kristallabscheidung an Oberflaechen. I.* Z. Kristallogr. **110**, 372 (1958).

[II.10] J. A. Venables, G. D. T. Spiller, and M. Hanbiicken. Rep. Prog. Phys. **47**, 399 (1984).

[II.11] H. Liith. *Surfaces and Interfaces of Solids*. 2nd ed., Springer, Germany, (1993).

[II.12] Balykov, and Axel Voigt. *A kinetic model for step flow growth in molecular beam epitaxy.* Surface Science **600**, 3436, (2006).

[II.13] J.M. Howe. *Interfaces in Materials.* Wiley, New York, USA, (1997)

[II.14] Editer by Erick Kasper, and John C. Bean. *Silicon-Molecular Beam Epitaxy – Volume II.* CRC Press, Boca Raton, USA, 9-10, (1988)

[II.15] C.P. Poole Jr., and F.J. Owens. *Introduction to Nanotechnology*. John Wiley & Sons Inc., New Jersey, USA, (2003).

[II.16] R. Bergamaschini, M. Brehm, M. Grydlik, T. Fromherz, G. Bauer and F. Montalenti. Nanotechnology **22**, 285704, (2011).

[II.17] K. Oura, V.G. Lifshits, A. A. Saranin, A. V. Zotov, and M. Katayama. *Surface Science, An Introduction.* Springer-Verlag, Heidelberg, Germany, (2003).

[II.18] Edited by W. K. Liu, and M. B. Santos. *Thin Films - Heteroepitaxial Systems*. World Scientific Publishing Co., Singapore, (2000).

[II.19] G. Brammertz, M. Caymax, M. Meuris, M. Heyns, Y. Mols, S. Degroote, and M. Leys. *GaAs on Ge for CMOS.* Thin Solid Films 517, 148, (3 November 2008).

[II.20] Yury Buzynin, Vladimir Shengurov, Boris Zvonkov, Alexander Buzynin, Sergey Denisov, Nikolay Baidus, Michail Drozdov, Dmitry Pavlov, and Pavel Yunin. *GaAs/Ge/Si epitaxial substrates: Development and characteristics*. AIP Advances **7**, 015304, (2017).

[II.21] Filipe Oliveira, I. A. Fischer, Alessandro Benedetti, P. Zaumseil, Maria F. Cerqueira, M. I. Vasilevskiy, Stefan Stefanov, Stefano Chiussi, and Jörg Schulze. *Fabrication of GeSn-multiple quantum wells by overgrowth of Sn on Ge by using molecular beam epitaxy.* Applied Physics Letters **107**, 262102, (December 2015).

[II.22] O. Gurdal, P. Desjardins, J. R. A. Carlsson, N. Taylor, H. H. Radamson, J.-E. Sundgren, and J. E. Greene. *Low-temperature growyh and critical epitaxial thickneses of fully strained metastable $Ge_{1-x}Sn_x$ (x=0.26) alloys on Ge(001) 2x1*. Journal of Applied Physics **83**, 162, (1998).

[II.23] M. Bauer, J. Taraci, J. Tolle, A. V. G. Chizmeshya, S. Zollner, David J. Smith, J. Menendez, Changwu Hu, and J. Kouvetakis. *Ge-Sn semiconductors for band-gap and lattice engineering*. Applied Physics Letters **81**, 2992, (2002).

[II.24] Armando Rastelli, and Hans von Känel. *Surface evolution of faceted islands.* Surface Science **515**, L493, (2002).

[II.25] A. Rastelli, M. Kummer, and H. von Känel. *Reversible Shape Evolution of Ge Islands on Si(001)*. Physical Review Letters **87**, 25, (17 December 2001).

[II.26] The MBE scheme is an internal figure form the IHT of University of Stuttgart in Germany (2015).

[II.27] M. Oehme, K. Kostecki, M. Schmid, F. Oliveira, E. Kasper, and J. Schulze. *Epitaxial growth of strained and unstrained GeSn alloys up to 25 % Sn*. Thin Solid Films **557**, 169, (April 2014).

[II.28] M. Oehme, E. Kasper, and J. Schulze. *GeSn Photodetection and Electroluminescence Devices on Si.* ECS Trans. **50,** 583, (2013).

[II.29] E. Kasper, M. Bauer, and M. Oehme. *Quantitative secondary ion mass spectrometry analysis of SiO2 desorption during in situ heat cleaning*. Thin Solid Films **321**, 148, (1998).

[II.30] J. Matsui. *Cross-Slip Dislocations and Their Multiplication in (001)-Oriented Silicon Wafers.* J. Electrochem. Soc. **122**, 977, (1975).

[II.31] M. Oehme, J. Werner, M. Jutzi, G. Woühl, E. Kasper, and M. Berroth. *High-speed germanium photodiodes monolithically integrated on silicon with MBE*. Thin Solid Films **508**, 393 (2006).

[II.32] M. Kittler, T. Arguirov, M. Oehme, Y. Yamamoto, B. Tillack, and N. V. Abrosimov. *Photoluminescence study of Ge containing crystal defects*. Phys. Status Solidi **A 208**, 754, (7 February 2011).

[II.33] K. Wasa, and S. Hayakawa. *Handbook of Sputter Deposition Technology: Principles, Technology and Applications.* Noyes Publications, U.S.A, (1992).

[II.34] D. L. Smith. *Thin-Film Deposition: Principles and Practice*. McGraw-Hill, USA, (1995)

[II.35] U. Ozgur, Y. I. Alivov, C. Liu, A. Teke, M. A. Reshchikov, S. Dogan, V. Avrutin, S.J. Cho, and H. Morkoç. *A comprehensive review of ZnO materials and devices.* Journal of Applied Physics **98**, 41301, (August 2005).

[II.36] R. K. Waits. *Planar magnetron sputtering*. Journal of Vacuum Science & Technology **15**, 179, (March 1978).

[II.37] T. Nakano, and S. Baba. *Simulation of particle transport in high pressure sputtering*. Vacuum **51**, 485 (1 December 1998).

[II.38] S.K. Park, and J.H. Je. *Resputtering of the superconducting BiSrCaCuO thin films*. Physica C **254** (1-2), 167 (1995).

[II.39] J.A. Thornton. *Influence of apparatus geometry and deposition conditions on the structure and topography of thick sputtered coatings*. Journal of Vacuum Science & Technology **11**, 666, (1974).

[II.40] G. Binnig, C.F. Quate, and C. Gerber. *Atomic Force Microscope*. Physical Review Letters **56**, 930, (3 March 1986).

[II.41] Datasheet of AFM tip NT-MDT CSG 10.

[II.42] Dtasheet of the AFM tip Bruker TESPA.

[II.43] Edited by Z. L. Wang. *Characterization of Nanophase Materials.* Wiley-CH, New York, USA, (2000).

[II.44] D. B. Williams, and C. B. Carter. *Transmission Electron Microscopy*. Plenum Press, New York, USA, (1996).

[II.45] Z. L. Wang, and Z. C. Kang. *Functional and Smart Materials - Structural Evolution and Structure Analysis.* Plenum Press, New York, USA, 261-339, (1998).

[II.46] R. F. Egerton. *Electron Energy-Loss Spectroscopy in the Electron Microscope*. 2nd ed., Plenum Press, New York, USA, (1996)

[II.47] M. Birkholz. *Thin Film Analysis by X-Ray Scattering*. Wiley-VCH, Germany, (2006)

[II.48] Leonard C. Feldman, and Jamen W. Mayer. *Fundamental of Surface and Thin Film Analysis*. North-Holland, 13-96, (1986).

[II.49] Maria de Fátima Guimarães Cerqueira. *Produção e Caracterização de Filmes Finos de Silício Microcristalino.* Ph.D. thesis, Universidade do Minho, Braga, (1998)

[II.50] N.P. Barradas, and C. Jeynes. *Advanced physics and algorithms in the IBA DataFurnace*. Nucl. Instrum. and Meth. **B 266**, 1875 (2008)

[II.51] Marvin J. Freiser. A survey of magnetooptic effects. IEEE Trasnsactions on Magnetics **4**, 152, (1 June 1968).

[II.52] Štefan Višňovský. *Optics in Magnetic Multilayers and Nanostructures*, CRC Press and Taylor & Francis, Boca Raton, USA, 1-62, (2006).

[II.53] Public domain image. Avaibable at www.wikipedia.com, (2011).

[II.54] Edited by Y. B. Xu, and S. M. Thompson. *Spintronic Materials and Techonogy*. Taylor & Francis, Series in Materials Science and Engineering, Boca Raton, USA, 1-35, (2007).

[II.55] Manuel Cardona. *Faraday Rotation in Semiconductors*. Advances in Solid State Physics **1**, 72, (1962).

[II.56] Frederic J. Kahn, P. S. Pershan, and J. P. Remeika. Physical Review **186**, 891, (1969).

[II.57] P.I. Nikitin, and A. I. Savchuk. *The Faraday effecting semi-magnetic semiconductors*. Soviet Physics Uspekhi **33**, 975, (1990).

[II.58] Mikhail I. Vasilevskiy, and Isabel Calado Ferreira. *Física dos Semicondutores – Fundamentos, Aplicações e Nanoestruturas*. Almedina, Coimbra, Portugal, 181-186, (2005).

[II.59] I. M. Boswarva, R. E. Howard, and A. B. Lidiard. *Faraday effect in semiconductors*. Proceeddings of The Royal Socialty London **A 269**, 125, (1962).

Chapter III

Fundamentals of Raman Scattering in Semiconductors

The inelastic light scattering was first predicted in 1923 by the Austrian theoretical physicist Adolf Smekal **[III.1]**. In 1928[7] **[III.2]**, the Indian physicists Chandrasekhara Raman and Kariamanickam Krishnan observed by the first time the inelastic scattering of the light that later would become know as Raman scattering. Raman observed the inelastic light scattering by using sunlight, a narrow band filter to obtain monochromatic light, and a "crossed filter" to block this monochromatic light. He found that a small amount of light had changed frequency and passed through the "crossed" filter. Raman scattering spectroscopy precision improved substantially with the improvement of spectrometers, development of lasers in the 70s and electronic detectors in the following decades. It has become one of the most used techniques in the study of elementary low frequency excitations of solids.

Nowadays, Raman scattering spectroscopy is used in the study of a broad range of materials. In the area of physics and materials it is suitable to study thin films, crystalline or amorphous, quantum dots, quantum wells, superlattices, polymers, between many others. This technique is used to characterize material from both macro- and microscopic points of view. It allows for determination of atomic vibration frequencies, symmetries of crystals, state of the interface, presence of strain, impurities, defects, etc. This makes Raman spectroscopy a technique of election in the study of semiconductors. Moreover, it is a non-destructive technique[8]. The Raman scattering results are complementary to other techniques, like photoluminescence spectroscopy and X-rays diffraction.

---

[7] In Russia, in 1926, Landsberg and Mandelstam also observed inelastic scattering of the light, but they published there work after Raman and Krishnan. Both works were developed and published without mutual knowledge.

[8] Raman scattering spectroscopy is, in general, a non-destructive technique, although in some configurations like micro Raman scattering, the concentration of the incident light on the sample by the microscope can generate enough heat to alter the medium/sample.

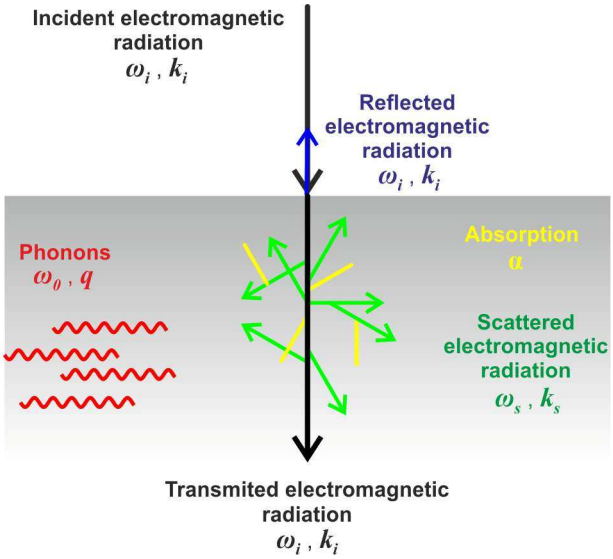

Figure III.1: Illustration of the interaction of the incident light with a solid crystal.

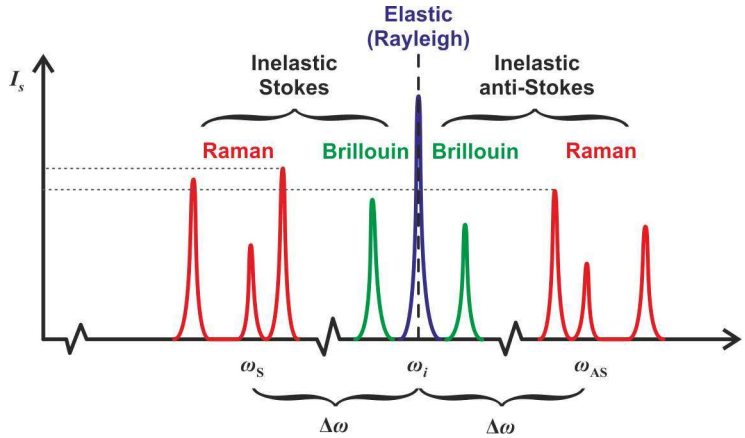

Figure III.2: Illustration of light scattering spectrum in crystalline mediums. The frequencies of the peaks in the spectrum are symmetric in relation to the incident excitation, ω_i. Peaks of Stoke process have higher intensity that the ones of anti-Stokes.

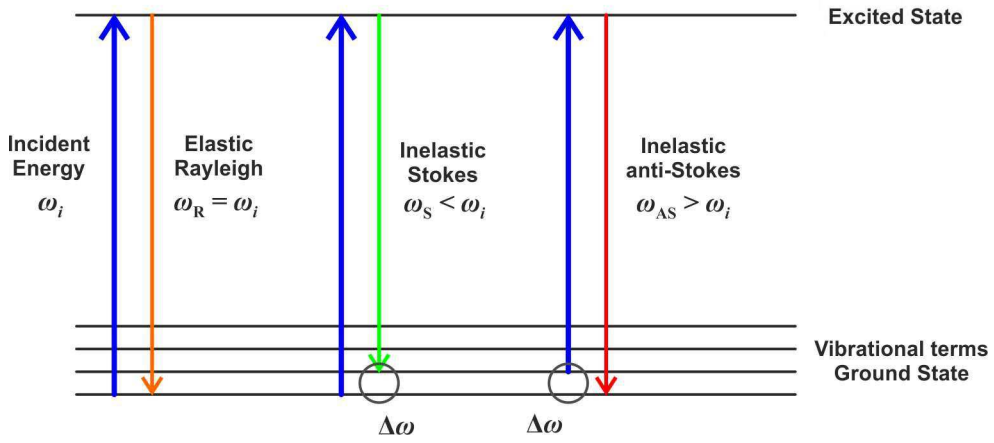

Figure III.3: Illustration of light scattering state transitions. The incident energy can coincide with an energy level (or band) and result in a real excited state (as shown), otherwise it results in a virtual intermediate state.

III.1. Inelastic Light Scattering, Momentum and Energy Conservation

When monochromatic radiation with an angular frequency ω_i impinges on a medium (solid, liquid or gaseous), a part of the radiation is transmitted, another part is scattered (or diffused), and other part of the radiation is absorved (see **Figure III.1**). The scattered radiation has two components: 1) one with unchanged frequency, caused by elastic scattering and 2) other with a different frequency, produced by inelastic scattering. The elastic, or Rayleigh scattering, is the scattering of the radiation with the same frequency as the incident radiation ($\omega_{scatt.} = \omega_i$, where the index '*scatt.*' referees to scattered radiation). The intensity of this scattering is in general in the order of 10^{-3} times of the incident radiation **[III.3]** and is proportional to $1/\lambda^4$. The inelastic scattering is the scattering of the radiation with a different frequency of the incident radiation ($\omega_{scatt.} \neq \omega_i$). When $\omega_{scatt.} < \omega_i$, then is known as Stokes process, or if $\omega_{scatt.} > \omega_i$ then is known as anti-Stokes process (see **Figure III.2**). The inelastic processes are characteristic of the scattering medium, and the frequency shift, $\Delta\omega = |\omega_{scatt.} - \omega_i|$, does not depend of the incident frequency. In the case of crystal samples, $\hbar\Delta\omega$ corresponds to the necessary energy to create or annihilate phonons in the lattice ($\omega_0 = \Delta\omega$, where ω_0 is the phonon frequency). In general, Stokes process has a higher intensity that the anti-Stokes process. This is related with the involved electronic transitions. Anti-Stokes transition occurs from a higher energetic level to a lower one (see **Figure III.3**). The difference in intensity is related with the population of atoms in the fundamental state and the population of atoms in excited states that is described by the Bose-Einstein distribution. Since the difference of intensity between Stokes and anti-Stokes is directly related with the population of the atoms states, it can be used to calculate the temperature of the medium in the analyzed zone.

Among inelastic light scattering processes, it is conventional to distinguish Brillouin and Raman scattering. The former refers to creation or destruction of an acoustic phonon and corresponds to very small frequency shifts (see **Figure III.2**).

Raman scattering is the term used for inelastic processes involving optical phonons (which are the subject of this wok) or other elementary excitations for which $\lim_{\vec{q}\to 0}\omega(\vec{q}) = const \neq 0$. Measurements of the two effects provide complementary information about the sample: Raman spectroscopy can be used to determine the crystal structure, chemical composition and short-range order effects (in solid solutions), while Brillouin scattering can be used to measure the material's properties on a larger scale, such as its elastic behavior. Raman scattering involves excitations of higher energy and, consequently a higher difference in frequency between the incident and scattered radiation when compared to Brillouin scattering.

As mentioned before, each scattered photon is associated with difference in energy $\hbar\omega$ ($=\hbar\Delta\omega$). In the Stokes process is associated with a gain in energy $\hbar\omega$ by the medium:

$$\omega = \omega_i - \omega_S \,, \qquad \textbf{\{III.1\}}$$

and similarly, the medium loses energy $\hbar\omega$ for each scattered photon in the anti-Stokes process:

$$\omega = \omega_{AS} - \omega_i \,, \qquad \textbf{\{III.2\}}$$

where the index 'S' refers to Stokes process and 'AS' refers to anti-Stokes process. The occurrence of scattered photons at a particular frequencies ω_S and ω_{AS} depends upon the ability of the scattering crystal lattice to absorb or emit energy in quanta of magnitude $\hbar\omega$ refereed in **Equations {III.1}** and **{III.2}**, corresponding to a phonon ($\omega_0 = \omega$ is the frequency of the phonon). The intensity peaks in the inelastic scattering spectrum correspond to various excited states of the crystal lattice. The measurement of inelastic electromagnetic radiation scattered spectrum allows the determination of the incident energies shifts from ω_i and the scattered light, $\omega_{scatt.}$. Measurement of the frequency widths of the spectral peaks can also provide information on the excited-state lifetimes. **[III.4]**

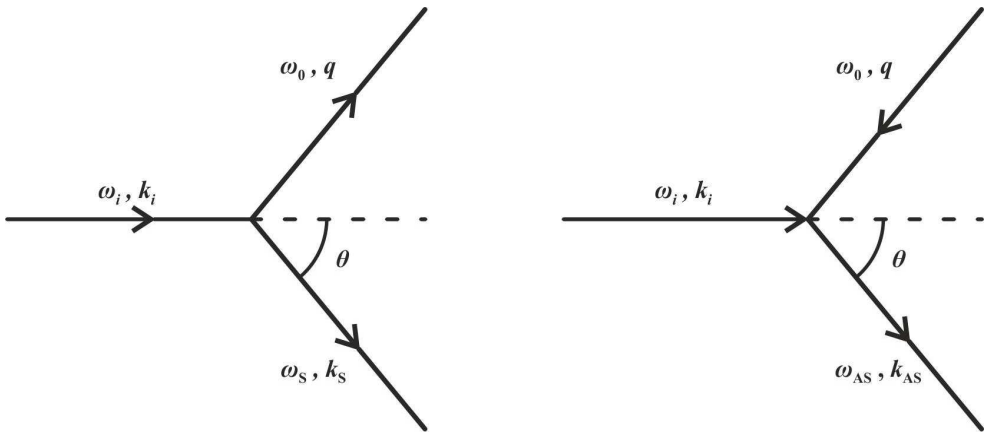

Figure III.4: Vector diagrams for the conservation of the momentum in: a) Stokes scattering, and b) anti-Stokes scattering. [III.4]

The above equations, **{III.1}** and **{III.2}**, express the conservation of the energy in the inelastic light-scattering process. But these processes also must keep a conservation of the momentum. The conservation of the momentum requires that the medium gains a momentum $\hbar|\vec{q}|$ in each Stokes-scattering event:

$$\vec{q} = \vec{k}_i - \vec{k}_S , \qquad \textbf{\{III.3\}}$$

and loses a momentum $\hbar|\vec{q}'|$ in each anti-Stokes scattering event, where

$$\vec{q}' = \vec{k}_{AS} - \vec{k}_i . \qquad \textbf{\{III.4\}}$$

Here $\vec{q}$ and $\vec{q}'$ are the wavevector of the phonon and $\vec{k}_i$, $\vec{k}_S$, and $\vec{k}_{AS}$ are the wavevectors inside the scattering medium of an incident photon, Stokes scattered photon, and anti-Stokes scattering photon, respectively. **[III.4]**

Figure III.4 provides two vector diagrams for the conservation of the momentum in the both kinds of inelastic scattering. Form the **Figure III.4a**, Stokes scattering, one can obtain:

$$q^2 = k_i^2 + k_S^2 - 2k_i k_S \cos\theta . \qquad \textbf{\{III.5\}}$$

The photon wavevectors can be related with their frequencies:

$$k_i c = \eta_i \omega_i , \qquad \textbf{\{III.6\}}$$

$$k_S c = \eta_S \omega_S , \qquad \textbf{\{III.7\}}$$

where η_i and η_S are the refractive indices of the medium for the incident and scattered light. **Equation {III.5}** can be further worked using **Equations {III.2}**, **{III.6}** and **{III.7}**:

$$c^2 q^2 = \eta_i^2 \omega_i^2 + \eta_S^2 (\omega_i - \omega_0)^2 - 2\eta_i \eta_S \omega_i (\omega_i - \omega_0)\cos\theta . \qquad \textbf{\{III.8\}}$$

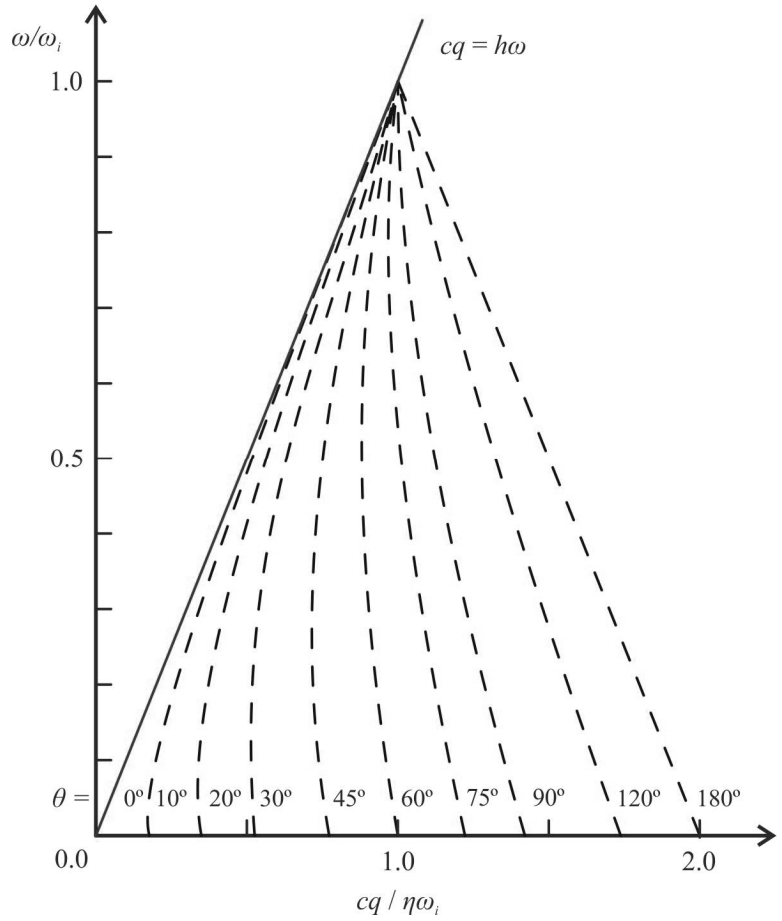

Figure III.5: Accessible region of the frequency ω and wavevector q values of an excitation for Stokes scattering of incident light of frequency ω_i in a medium of refractive index η. The dashed lines show the experimental scans for fixed values of scattering angle θ. Figure adapted from [III.4]

This expression relates the frequency ω_0 and the wavevector $\vec{q}$ of phonons of the crystal lattice that scatter the incident light of frequency ω_i through an angle θ. For the most common case where the refractive indices for the incident and scattered photons are nearly equal ($\eta_i = \eta_S = \eta$):

$$\frac{c^2 q^2}{\eta^2} = \omega_0^2 + 4\omega_i \omega_S \sin^2(\theta/2) \qquad \textbf{\{III.9\}}$$

This relation between ω and q is plotted in **Figure III.5** for various values of θ, where the refractive index is assumed to be constant for all values of the scattered frequency. It is then possible to observe the Stokes scattering by all excitations of the

medium whose frequency and wavevector lie within a triangular region of the ωq - plane, as θ varies continuously from 0º to 180º. **[III.4]**

A similar analysis can be made for the wavevector in the anti-Stokes case illustrated in **Figure III.4b**:

$$\frac{c^2 q^2}{\eta^2} = \omega_0^2 - 4\omega_i \omega_S \sin^2(\theta/2) \qquad \textbf{\{III.10\}}$$

The accessible region of the plane is now a parallel band for constant refractive index, but its baseline is the same as for Stokes scattering and the regions covered in the two cases are not very different for the low-frequency excitations ($\omega/\omega_i << 1$).**[III.4]**

The **Equation {III.9}** [and **{III.10}**] in the limit of small excitation frequencies ($\omega/\omega_i << 1$) is:

$$|\vec{q}| \approx 2\frac{\omega_i \eta}{c}\sin(\theta/2) \qquad \textbf{\{III.11\}}$$

If silicon ($\eta(Si) \sim 3.5$) is taken as a example for light scattering experiments, where visible incident electromagnet radiation is used ($\omega_i/(2\pi) \approx 5\times10^{14}$ Hz), the range of excitation wavevectors accessible to the light scattering experiments is approximately

$$0 < |\vec{q}| < 1.2\times10^{7}\ \text{m}^{-1} \qquad \textbf{\{III.12\}}$$

The wavevector of the phonons in the Brillouin zone is given by:

$$0 < |\vec{q}| \leq \frac{2\pi}{a} < 1.2\times10^{10}\ \text{m}^{-1} \qquad \textbf{\{III.13\}}$$

Thus, the phonon wavevector participating in both light scattering inelastic processes are three orders of magnitude inferior and the phonon wavevector can be considered approximately zero ($\vec{q} \approx 0$).

As shown in the illustration in **Figure III.2**, typically Raman spectra are plotted as intensity of the scattered light versus the Raman shift, $\Delta\omega = |\omega_d - \omega_i|$. In a crystal, each peak corresponds to a phonon mode.

III.2. Phonons in Semiconductors

The concept of the phonon is attributed to the Soviet physicist Igor Tamm, that in 1932 published a paper with his proposal of the concept of surface states. Phonons are quasiparticles that represent collective excitations in periodic and elastic arrangement of atoms (or molecules) in condensed matter. They represent excited states in the modes of vibrations of elastic structures of interacting particles. As mentioned above, Raman scattering involves optical phonons while acoustic phonons participate in Brillouin scattering.

III.2.1. Phonons in Crystalline Semiconductors

Atoms in a crystal are in permanent vibration around their equilibrium positions. Because of this, one would expect a break of the symmetry, however, in practice it only occurs at very high temperatures. For temperatures much lower than the melting temperature of the medium, the atomic vibration amplitudes are small compared to the interatomic distances. These vibrations are nearly harmonic and their quanta are known as phonons[9].

The atomic Hamiltonian can be written in terms of the variations of the instant positions of the atoms with time **[III.5]**:

$$H = \sum_{l,\alpha} \frac{\vec{P}_{l\alpha}^{2}}{2M_{\alpha}} + \frac{1}{2} \sum_{l,l',\alpha,\alpha'} \vec{\vec{A}}_{ll'}^{\alpha\alpha'} \vec{u}_{l'\alpha'} \vec{u}_{l\alpha} \,, \qquad \textbf{\{III.14\}}$$

where $\vec{P}_{l\alpha}^{2}$ are the linear momenta of the atoms, M_{α} are the atomic masses, $\vec{\vec{A}}_{ll'}^{\alpha\alpha'}$ is the dynamical matrix of the crystal, $\vec{u}$ is the atomic displacement, α enumerates the unit cells in the crystal and l enumerates the atoms inside each cell. This matrix has the dimensions $(3sN \times 3sN)$ (where s is the number of atoms per unit cell and N is the number of unitary cells in the crystal) and it is constituted by the second derivatives of the inter-atomic potential with respect to the atomic displacements, in the equilibrium. **[III.5]**

[9] Even for a temperature well bellow the melting temperature, anharmonic effects exist and are important for certain phenomena as thermal expansion. However, these are not the subject of the present study.

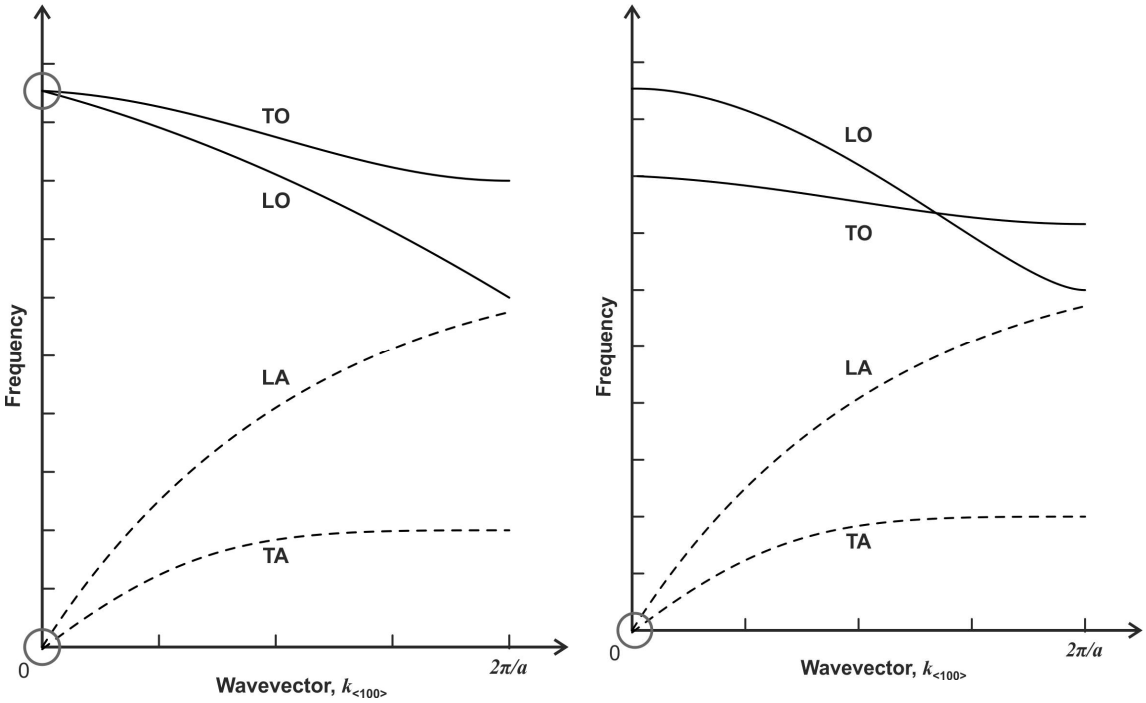

Figure III.6: Qualitative illustration of the dispersion curves for: a) silicon (Si) and, b) gallium arsenide (GaAs), with the indication of the transversal modes (TO, TA) and longitudinal modes (LO, LA). Figures adapted from [III.5]

In general, there are $3s$ branches with *eigen*states $\omega(\vec{q})$, also called dispersion curves. Three of them are dispersion curves of acoustic phonons with $\omega(\vec{q} \to 0) = 0$, while the remaining ones correspond to optical phonons. The optical phonon branches are only present for crystal lattices with more than one atom per unit cell. The diamond structure has two atoms per unit cell (s=2) and, consequently, 3 acoustic branches and 3 optical branches exist. For the limit of high wavelengths ($\vec{q} \to 0$) in the acoustic modes, the two atoms of the unit cell have exactly the same displacement, but in the optical modes, the two atoms of the unit cell have opposite displacements.
In the case of the würtzite structure, there are four atoms per unit cell ($s = 4$), corresponding to 3 acoustic branches and 9 optical branches (see **Chapter III.8**). Phonon dispersion curves for hexagonal ZnO are presented in **Chapter V**.

Both families of branches (acoustic and optical) are polarized. In an infinite crystal there are transversal and longitudinal branches (or phonon polarisations). In cubic crystals, two of the transverse branches are degenerate in the $\vec{q} \to 0$ limit and along some high-symmetry directions, *e.g.* (100) and (111). **Figure III.6** shows a schematic representation of the dispersion curves for Si (cubic diamond structure) and

GaAS (zinc blend structure). These curves are only isotopic in the vicinity of Γ point. The Γ point optical phonon frequencies, ω_{LO} and ω_{TO}, can be measured experimentally by Raman scattering spectroscopy (if Raman active due to selection rules) and reflection or transmision of the radiation in the far infrared (FIR) spectral range.

The vibration energy spectrum of a crystal is quantised. Transitions between two vibrational states (with different occupation numbers) are associated to processes of absorption or emission of phonons, the vibration quanta characterized by a wavevector $\vec{q}$, a branch index (acoustic or optical), and a polarization (longitudinal or transverse).

III.2.2. Electron-Phonon Interaction Mechanisms

The coupling between electrons and phonons can occur via different mechanisms. The most common ones associated with acoustic phonons are the deformation potential mechanism (ADP) and piezo-acoustic interaction mechanism (PA), while for optical phonons these are the Fröhlich mechanism and the optical deformation potential one (ODP).

In the deformation potential mechanism, the displacement of the atoms induces an alteration of the lattice potential that acts over the electrons. The perturbation is given by:

$$H_{ex-L}^{ADP}(\vec{r}_e,\vec{r}_h)=\sum_v \left\{a_c\left[\vec{\nabla}_e\cdot\vec{u}_v(\vec{r}_e)\right]-a_v\left[\vec{\nabla}_h\cdot\vec{u}_v(\vec{r}_h)\right]\right\} \qquad \textbf{\{III.15\}}$$

where $\vec{r}_e,\vec{r}_h$ are the position vectors of the electron and hole, respectively, v is the phonon mode, a_c and a_v are the so called volume deformation potential constants for the conduction and valence band, respectively, $\vec{u}_v$ is the atomic displacement vector. The divergence of the displacement vector is the relative variation of the volume of the crystal under a small deformation. In the case of a deformation induced by a transverse acoustic phonon the variation is zero, and, consequently, this mechanism is associated only with LA phonons.

The piezo-acoustic interaction mechanism occurs in crystals lacking inversion symmetry (for example, III-V and II-IV materials). The deformation in one direction

induces a dipole momentum and, consequently, an electric field that interacts with the electrons. The perturbation is given by[10]:

$$H_{e-L}^{PA}(\vec{r}) = \frac{e}{q^2 \varepsilon_\infty} \sum_v \left[\vec{q} \vec{e}_\sigma^{\,m} \vec{q} \vec{u}_v(\vec{r}) \right], \qquad \textbf{\{III.16\}}$$

where e is the charge of the electron, $\vec{q}$ the wavevector of the phonon, ε_∞ is the high-frequency dielectric constant, $\vec{e}_\sigma^{\,m}$ is a third rank electromechanical tensor for the electronic band σ. This mechanism is important mainly in semiconductors of hexagonal structure like ZnO.

For the Fröhlich mechanism, the electron-phonon interaction Hamiltonian is:

$$H_{ex-L}^{Fr} = e \sum_v \left[\varphi_v(\vec{r}_h) - \varphi_v(\vec{r}_e) \right], \qquad \textbf{\{III.17\}}$$

where φ_v is the electrostatic potential created by the phonon mode v, $\vec{r}_h$ and $\vec{r}_e$ are the position vectors for the hole and electron respectively. The interaction with optical phonons is very strong in polar semiconductors, such as ZnO and (although to a lesser extent) GaAs. The longitudinal optical (LO) phonons generate an electric field known as Fröhlich field, that interacts directly with the electrons and holes. This field can be related with the relative displacement of two ions of the same lattice cell:

$$\vec{w}_l = \vec{u}_{l+} - \vec{u}_{l-} \,. \qquad \textbf{\{III.18\}}$$

When the wavevector of the phonon, $\vec{q}$, approaches a zero value, $\vec{q} \to 0$, the relative displacement is nearly the same for all the lattice cells in the crystal, *i. e.*, it does not depends on l. Consequently, the polarization of the material is homogeneous. The polarization vector is given by:

$$\vec{P} = \frac{e_T}{\upsilon} \vec{w} \,, \qquad \textbf{\{III.19\}}$$

where e_T is an effective charge of the ions (also known as Szigeti charge) and υ is the volume of the unit cell. According to the Gauss law, for a neutral medium the divergence of the electric displacement vanishes:

$$\vec{D} = \varepsilon_\infty \vec{E} + 4\pi \vec{P} = 0 \,. \qquad \textbf{\{III.20\}}$$

Thus, the electric field associated with the longitudinal optical phonon for $\vec{q} \approx 0$ is:

$$\vec{E}_{LO} = -\frac{4\pi}{\varepsilon_\infty} \frac{e_T}{\upsilon} \vec{w}_{LO} \,. \qquad \textbf{\{III.21\}}$$

[10] Here it was used CGS units.

Another mechanism of interaction between the electrons and the optical phonons is the optical deformation potential (ODP) one, with the Hamiltonian given by:

$$H_{e-ph}^{ODP} = \frac{\sqrt{3}d_0}{2a_0}\sum_{v}\left[\vec{D}\cdot\vec{u}_v(\vec{r}_h)\right], \qquad \textbf{\{III.22\}}$$

where d_0 is the optical deformation potential constant, a_0 is the lattice constant, $\vec{D} = \left(D_x, D_y, D_z\right)$ is a vector composed by matrix with columns and rows corresponding to the Bloch states of the sub-bands of the valence band. For example, for a Γ_8 valence band of a cubic semiconductor these matrices are given by **[III.6]**:

$$D_x(D_y) = \frac{1}{\sqrt{3}}\begin{pmatrix} 0 & -1(i) & 0 & 0 \\ -1(-i) & 0 & 0 & 0 \\ 0 & 0 & 0 & 1(-i) \\ 0 & 0 & 1(i) & 0 \end{pmatrix}, \qquad \textbf{\{III.23\}}$$

$$D_z = \frac{1}{\sqrt{3}}\begin{pmatrix} 0 & 0 & i & 0 \\ 0 & 0 & 0 & i \\ -i & 0 & 0 & 0 \\ 0 & -i & 0 & 0 \end{pmatrix}. \qquad \textbf{\{III.24\}}$$

The optical deformation potential mechanism is less strong than the Fröhlich one. However, it is more universal (*i.e.* takes place for non-polar semiconductors such as silicon) and involves both LO and TO phonons.

III.3. Classical Theoretical Approach of Inelastic Light Scattering by Phonons

A phenomenological theory for the light scattering can be developed based on macroscopic properties of the medium described by its electric susceptibility[11], χ, and its derivatives with respect to atomic displacements. In the medium, a plane electromagnetic wave with the electric field, $\vec{F}(\vec{r},t)$, induces a sinusoidal polarization, $\vec{P}(\vec{r},t)$ **[III.7]**:

[11] In general, the electric susceptibility is represented by a second rank tensor. For isotropic media the electric susceptibility becomes a scalar.

$$\vec{F}(\vec{r},t)=\vec{F}_i(\vec{k}_i,\omega_i)\cos(\vec{k}_i\cdot\vec{r}-\omega_i t), \quad \{\text{III.25}\}$$

$$\vec{P}(\vec{r},t)=\vec{P}_i(\vec{k}_i,\omega_i)\cos(\vec{k}_i\cdot\vec{r}-\omega_i t), \quad \{\text{III.26}\}$$

where t is time, $\vec{r}$ is the vector position, $\vec{k}$ is the wavevector and i designates the incident wave. The polarization wave has the same frequency and wavevector as the one of the incident light, and amplitude is given by **[III.7]**:

$$\vec{P}_i(\vec{k}_i,\omega_i)=\vec{\chi}(\vec{k}_i,\omega_i)\vec{F}_i(\vec{k}_i,\omega_i). \quad \{\text{III.27}\}$$

In a crystal, atomic vibrations propagate as waves, which are quantized into phonons. The atomic displacements, $\vec{Q}(\vec{r},t)$, associated with a phonon can be expressed as plane waves **[III.7]**:

$$\vec{Q}(\vec{r},t)=\vec{Q}(\vec{q},\omega_0)\cos(\vec{q}\cdot\vec{r}-\omega_0 t), \quad \{\text{III.28}\}$$

where $\vec{q}$ is the wavevector of the phonon and ω_0 is the frequency of the phonon.

The atomic vibrations modify the electric susceptibility ($\vec{\chi}$). Assuming that the characteristic electronic frequencies which determine the electric susceptibility are much larger than frequency of the phonon (ω_0), then the electric susceptibility can be related with the atomic displacements ($\vec{Q}$). Since at room temperature these vibrations are small compared to the lattice constant, a Taylor series can be used to expand the electric susceptibility in $\vec{Q}(\vec{r},t)$ **[III.7]**:

$$\vec{\chi}(\vec{k}_i,\omega_i,\vec{Q})=\chi_0(\vec{k}_i,\omega_i)+\left(\frac{\partial\vec{\chi}}{\partial\vec{Q}}\right)_0\vec{Q}(r,t)+\ldots, \quad \{\text{III.29}\}$$

where χ_0 is the electric susceptibility of the medium without fluctuations and the second term represents an oscillating susceptibility induced by the atomic displacement wave. The polarization wave can be now related with the atomic displacement wave **[III.7]**:

$$\vec{P}(\vec{r},t,\vec{Q})=\vec{P}_0(\vec{r},t)+\vec{P}_{ind}(\vec{r},t,\vec{Q}), \quad \{\text{III.30}\}$$

$$\vec{P}_0(\vec{r},t)=\chi_0(\vec{k}_i,\omega_i)\vec{F}_i(\vec{k}_i,\omega_i)\cos(\vec{k}_i\cdot\vec{r}-\omega_i t), \quad \{\text{III.31}\}$$

$$\vec{P}_{ind}(\vec{r},t,\vec{Q})=\left(\frac{\partial\vec{\chi}}{\partial\vec{Q}}\right)_0\vec{Q}(\vec{r},t)\vec{F}_i(\vec{k}_i,\omega_i)\cos(\vec{k}_i\cdot\vec{r}-\omega_i t), \quad \{\text{III.32}\}$$

where $\vec{P}_0$ is the polarizations vibrating in phase with the incident radiation and $\vec{P}_{ind}$ is a polarization wave induced by the phonon (or another elementary excitation).

The frequency and wavevector of the polarization wave induced by the phonon ($\vec{P}_{ind}$) can be obtain by changing the dependency of the atomic displacements from $\vec{Q}(\vec{r},t)$ to $\vec{Q}(\vec{q},\omega_0)$ **[III.7]:**

$$\vec{P}_{ind}\left(\vec{r},t,\vec{Q}\right)=\left(\frac{\partial\vec{\chi}}{\partial\vec{Q}}\right)_0\vec{Q}(\vec{q},\omega_0)\cos(\vec{q}\cdot\vec{r}-\omega_i t)\times\vec{F}_i\left(\vec{k}_i,\omega_i\right)\cos\left(\vec{k}_i\cdot\vec{r}-\omega_i t\right) \qquad \textbf{\{III.33\}}$$

$$=\frac{1}{2}\left(\frac{\partial\vec{\chi}}{\partial\vec{Q}}\right)_0\vec{Q}(\vec{q},\omega_0)\vec{F}_i\left(\vec{k}_i,\omega_i t\right)\times\left\{\cos\left[\left(\vec{k}_i+\vec{q}\right)\cdot\vec{r}-\left(\omega_i+\omega_0\right)t\right]+\cos\left[\left(\vec{k}_i-\vec{q}\right)\cdot\vec{r}-\left(\omega_i-\omega_0\right)t\right]\right\}$$

Now $\vec{P}_{ind}$ explicitly consists of two sinusoidal waves, one related with the anti-Stokes scattering (first term in the brackets) and other with the Stokes scattering (second term in the brackets). The respective frequencies and wavevetors are given in **Table III.1**. Thus, in the above scattering processes, both the energy ($\hbar\omega$) and the momentum ($\hbar\vec{k}$) are conserved.

Table III.1: Summary of wavevector and frequency changes in scattering processes

Scattering Process	Frequency	Wavevector
Rayleigh	ω_i	$\vec{k}_i$
Anti-Stokes (Raman or Brillouin)	$\omega_{AS}=\left(\omega_i+\omega_0\right)$	$\vec{k}_{AS}=\left(\vec{k}_i+\vec{q}\right)$
Stokes (Raman or Brillouin)	$\omega_S=\left(\omega_i-\omega_0\right)$	$\vec{k}_S=\left(\vec{k}_i-\vec{q}\right)$

The electric susceptibility **{III.29}** was expanded only up to the first order terms. The first one (zero order term) will result in the Rayleigh diffusion, while the second one (first order term) will result in the one-phonon Raman scattering. The series can be extended to provide the two-phonon Raman scattering or higher order of phonon displacement. In the case of two-phonon Raman scattering, two phonons are involved in the shift with frequencies ω_a and ω_b, where $\omega_a>\omega_b$ are the frequencies of the two involver phonon and respective wavevectors are $\vec{q}_a$ and $\vec{q}_b$. This results in a scattered photon frequency shifted from the excitation frequency by $\pm\omega_a$, $\pm\omega_b$, and a combination will result in $\pm\left(\omega_a+\omega_b\right)$, while a difference of modes will result in $\pm\left(\omega_a-\omega_b\right)$. The conservation of the wavevectors is satisfied when $\vec{q}_a\pm\vec{q}_b\approx 0$. It can happen that the two phonons are identical and in this case the two-phonon Raman

scattering is known as overtone process. Here, the two phonons need to have equal but opposite wavevectors, $\vec{q}_a = -\vec{q}_b$. While one-phonon Raman scattering restricts the phonon wavevector to small values ($q \approx 0$), in the case of the two-phonon Raman scattering the restriction refers to the sum of the phonon wavevectors, as a result, the phonon wavevectors can have any magnitude, as long the sum has small values are approximately zero ($q_a \pm q_b \approx 0$).

III.4. Raman Tensor, Symmetry and Selection Rules

The interaction of a photon with a phonon is ruled by the conservation of the linear momentum and energy:

$$\hbar\vec{k}_s = \hbar\vec{k}_i \pm \hbar\vec{q}\,, \qquad \textbf{\{III.34\}}$$

$$\hbar\omega_s = \hbar\omega_i \pm \hbar\omega_0\,. \qquad \textbf{\{III.35\}}$$

Typically phonon energy ($\hbar\omega_0 \approx 0.05\text{eV}$) is orders of magnitude smaller than the photons energy ($\hbar\omega_i \approx 2.5\text{eV}$),

$$\hbar\omega_s \approx \hbar\omega_i\,, \qquad \textbf{\{III.36\}}$$

$$k_s \approx k_i \approx 10^5\ \text{cm}^{-1}. \qquad \textbf{\{III.37\}}$$

In the case of backscattering geometry:

$$|\vec{q}| \approx 2\left|\vec{k}_i\right| \approx 2\cdot 10^5\ \text{cm}^{-1}, \qquad \textbf{\{III.38\}}$$

and in the case of 90º scattering geometry:

$$|\vec{q}| \approx \left|\vec{k}_i\right| \approx 10^5\ \text{cm}^{-1}. \qquad \textbf{\{III.39\}}$$

In both geometries the wavevector is three orders of magnitude smaller than the first Brillouin zone limit ($\pi/a \approx 10^8\ \text{cm}^{-1}$).

Since in the first Brillouin zone (BZ) the wavevectors of the phonons are between 0 and π/a, then, for any geometry the Raman diffusion can only involve phonon with $q \approx 0$, *i. e.*, the centre of the Brillouin zone. These phonons have long wavelengths, meaning that in these vibration modes all atoms move with nearly the same phase. This selection rule is a consequence of the translational symmetry of an ideal crystal.

The intensity of the scattered radiation, I_s, can be calculated from the time-averaged power radiated by the induced polarizations $\vec{P}_{ind}$ into unit solid angle **[III.7]**. For one-phonon scattering the phonon wavevector is close to zero, $\vec{q} \approx 0$, and the intensity of the scattered radiation can be approximated by **[III.7]**:

$$I_s \propto \left| \vec{e}_i \cdot \left(\frac{\partial \vec{\chi}}{\partial \vec{Q}} \right)_0 \vec{Q}(\omega_0) \cdot \vec{e}_s \right|^2, \qquad \textbf{\{III.40\}}$$

where $\vec{e}_i$ is the polarization on the incident light and $\vec{e}_s$ is the polarization on the scattered light.

A Raman tensor, $\vec{\vec{R}}$, can be defined through the susceptibility derivatives with respect to the displacement vector, $\vec{Q}$:

$$\vec{\vec{R}} = \left(\frac{\partial \vec{\chi}}{\partial \vec{Q}} \right)_0 \cdot \hat{Q}(\omega_0), \qquad \textbf{\{III.41\}}$$

where $\hat{Q}(\omega_0)$ is the unit vector parallel to the phonon displacement. The Raman tensor, like the electric susceptibility is a second-rank tensor. The scattered intensity is propositional to the square of the Raman tensor:

$$I_S \propto \left| \vec{e}_i \cdot \vec{\vec{R}} \cdot \vec{e}_S \right|^2. \qquad \textbf{\{III.42\}}$$

The symmetry of the lattice induces symmetry restrictions in the Raman tensor and the symmetry of the corresponding Raman-active phonon can be obtained by measuring the dependence of the scattered intensity on the incident and scattered polarizations. Experimentally this is obtained by polarizing the incident radiation and measuring the polarization of the scattered light (see Chapter **III.8.**).

Raman scattering measurements can be used to obtain comprehensive information about the medium: 1) frequencies of characteristic phonon modes, 2) symmetry of BZ-centre phonon modes, 3) exciton and/or interband electronic transition energies (Chapter **III.6.5.**), 4) electron-phonon interaction parameters (Chapter **III.6.5.**), and 5) temperature of the sample[12].

[12] The temperature of the sample can be obtained be measuring the relative intensities of the Raman modes (peak areas) for Stokes and anti-Stokes scattering, see **Chapter III.2**.

While the susceptibility tensor ($\vec{\chi}$) is symmetrical, the Raman tensor ($\vec{R}$), strictly speaking, is not because of the difference between the incident and scattered radiation. But in practice this difference can be neglected and the Raman tensor can be treated as a symmetric one. The lattice symmetry and the vibration modes involved in the scattering process are very important. Because of the symmetry, the scattered radiation vanishes for certain choices of the polarizations $\vec{e}_i$ and $\vec{e}_s$ and scattering geometries. It results in the Raman selection rules, which allow for the determination of the symmetry of Raman-active phonons. The symmetry of the Raman tensor in crystals is determined using the group theory that afterwards can be used to obtain the Raman selection rules.

Table III.2 show a list of selection rules for backscattering geometries (most common in the analyses of semiconductors) in zinc blende-type crystals. Selection rules apply only to crystals because *e.g.* in amorphous media the wavevector $\vec{k}$ is not well defined, *i. e.*, it is not a good quantum number.

The scattering efficiency, η, can be defined as the ratio of energy of the electromagnetic waves scattered per unit time divided by the energy of incident electromagnetic modes crossing the scattering area per unit time. By using the expression of the polarization wave induced by the phonon, $\vec{P}_{ind}$, presented above, it is possible to derive the scattering efficiency expression **[III.7]**:

$$\eta = \left(\frac{\omega_s}{c}\right)^4 VL\left|\vec{e}_i \cdot \left(\frac{\partial\vec{\chi}}{\partial\vec{Q}}\right)_0 \vec{Q}(\omega_0)\cdot\vec{e}_S\right|^2, \qquad \textbf{\{III.44\}}$$

$$V = AL, \qquad \textbf{\{III.45\}}$$

$$L = \frac{1}{\alpha_i + \alpha_s}, \qquad \textbf{\{III.46\}}$$

where c is the speed of light in vacuum, L is the scattering length, V is the volume of the medium producing the scattered radiation, A being the area of the incident beam and α_i and α_s are the absorption coefficients of the incident and scattered radiation. In semiconductors when the excitation is not close to a critical point, $\alpha_i \approx \alpha_s$. Detailed calculations of the efficiency can be found in **Ref. [III.8]**, where R. Loudon provided the estimation of the Raman scattering efficiency in crystals.

Table III.2: Raman selection rules for backscattering geometries in zinc-blende-type crystals. D_{TO} and d_{LO} denote the non-zero Raman tensor elements for TO and LO phonons, respectively. y' and z' denote $[011]$ the and $[0\bar{1}1]$ axes, while x'', y'' and z'' denote the set of three mutually perpendicular $[111]$, $[1\bar{1}0]$ and $[11\bar{2}]$ axes. [III.7]

Scattering geometry	Selection rule	
	TO phonon	LO phonon
$x(y,y)\bar{x}$; $x(z,z)\bar{x}$	0	0
$x(y,z)\bar{x}$; $x(z,y)\bar{x}$	0	$\lvert d_{LO}\rvert^2$
$x(y',z')\bar{x}$; $x(z',y')\bar{x}$	0	0
$x(y',y')\bar{x}$; $x(z',z')\bar{x}$	0	$\lvert d_{LO}\rvert^2$
$y'(x,x)\bar{y}'$	0	0
$y'(z',x)\bar{y}'$	$\lvert d_{TO}\rvert^2$	0
$y'(z',z')\bar{y}'$	$\lvert d_{TO}\rvert^2$	0
$x''(z'',z'')\bar{x}''$	$(2/3)\lvert d_{TO}\rvert^2$	$(1/3)\lvert d_{LO}\rvert^2$
$x''(z'',y'')\bar{x}''$	$(2/3)\lvert d_{TO}\rvert^2$	0

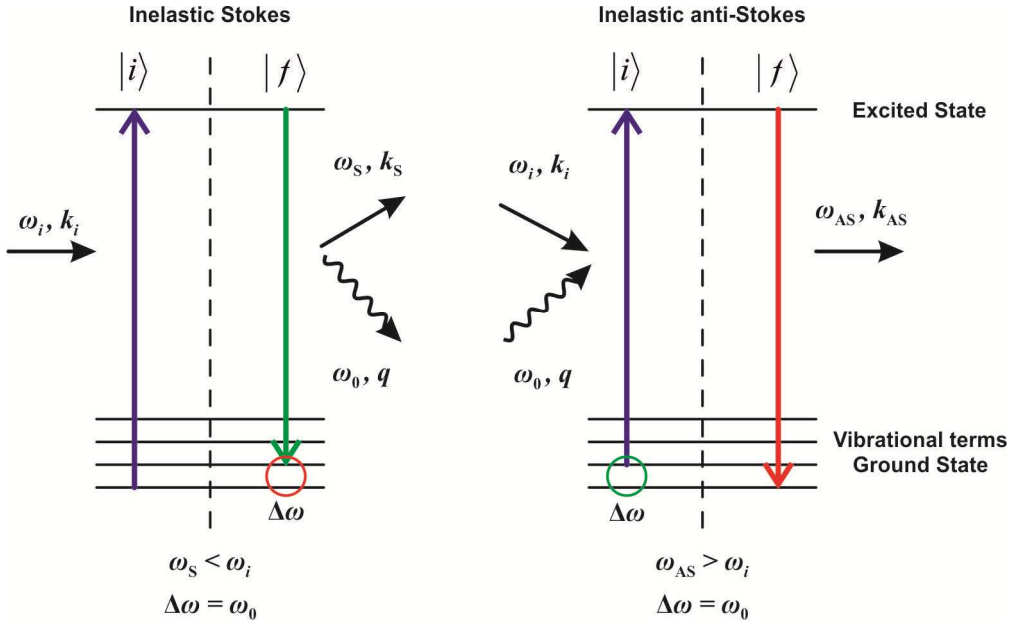

Figure III.7: Illustration of the scattering processes in semiconductors. $|i\rangle$ are the initial states and $|f\rangle$ are the final states. The incident energy can coincide with an energy level (or band) and result in a real excited state (as shown), otherwise it results in a virtual excited state.

III.5. Microscopic (Quantum) Theory of One-Phonon Raman Scattering, Resonant Effects

The quantum description of the inelastic scattering of light by phonons in a semiconductor involves three sub-systems: 1) incident photons with frequency ω_i, and the respective scattered photons with frequency ω_s; 2) electrons in the semiconductor, and 3) the phonons involved (created or destructed) in the scattering.

Figure III.7 shows an illustration of the initial conditions (before scattering occurs) and the final conditions of one scattering interaction in the semiconductor. In the initial state, $|i\rangle$, there is a number of incident photons, $N(\omega_i)$, and a number of scattered photons, $N(\omega_s)$. For simplicity, the semiconductor electron system is in the ground state, with the valence bands filled and the conduction band empty. A number of phonons, N_q, is present in the semiconductor. In the final state, $|f\rangle$, after the Stokes Raman scattering, the number of incident photons has decreased by one, ($N(\omega_i)-1$), the number of scattered photons has increased by one, ($N(\omega_s)+1$), as well as the number of phonons (N_q+1), while the electrons remain unchanged. In the case of anti-Stokes scattering, the interaction occurs between an incident photon and an excited electron, resulting in the destruction of a phonon. Since both Stokes and anti-Stokes processes have identical mathematical treatments, with the replacement $N(\omega_q)+1 \rightarrow N(\omega_q)$, only the first one is discussed.

Raman scattering spectroscopy is frequently performed in semiconductors using lasers in visible or near infrared, since they are the most common ones and provided good monochromaticity. In this case, for the incident photons and the scattered Raman photons are in general couple only to electrons via the electron-radiation interaction. This can be described by the electron-radiation interaction Hamiltonian, $H_{eR} = (-e)r \cdot E$ (e - electron charge, E - electric field). The scattering process can be described in three steps: 1) the incident photon excites the semiconductor to an intermediate state $|a\rangle$ by creation of a electron-hole pair; 2) this electron-pair is scattered to another state, $|b\rangle$, by emitting a phonon via the electron-phonon

interaction; and 3) the electron-hole pair in the previous state $|b\rangle$ recombines with the emission of a scattered photon. The electrons mediate the Raman scattering of phonons although they remain unchanged after the process **[III.7]**. The transitions of the electrons are virtual and, consequently, the conservation of energy is not applied in each sub-process (although it does apply globally), but still there is conservation of the wavevector.

The Raman scattering processes interactions are in general weak, and one can calculate the scattering probability of the phonons by using the third-order perturbation theory together with the help of the Feynman diagrams. One phonon Raman Scattering (Stokes process) can be described by the Feynman diagrams of **Figure III.8**. The six diagrams represent all the possible permutations of the three vertices.

The probability of scattering from the initial state, $|i\rangle$, to other state can be derived using the Fermi Golden Rule. Considering the diagram of the **Figure III.8a**, the scattering probability for the first vertex of the Feynman diagram **[III.7]**:

$$\sum_n \frac{\langle n|H_{eR}(\omega_i)|i\rangle}{\hbar\omega_i - (E_n - E_i)}, \qquad \textbf{\{III.47\}}$$

where $|i\rangle$ is the initial state, E_i is the energy of this state, $|n\rangle$ is an intermediate electronic state, and E_n the respective energy of this state. [13] Adding the second vertex of the Feynman diagram yields **[III.7]**:

$$\sum_{n,n'} \frac{\langle n'|H_{e-ion}(\omega_0)|n\rangle\langle n|H_{eR}(\omega_i)|i\rangle}{[\hbar\omega_i - (E_n - E_i)][\hbar\omega_i - (E_n - E_i) - \hbar\omega_0 - (E_{n'} - E_n)]}, \qquad \textbf{\{III.48\}}$$

where $|n'\rangle$ is another intermediated state and $E_{n'}$ the respective energy. Since $\hbar\omega_0$ represents the emission of phonon, it has a negative sign. The second part of the denominator can be simplified **[III.7]**:

$$\sum_{n,n'} \frac{\langle n'|H_{e-ion}(\omega_0)|n\rangle\langle n|H_{eR}(\omega_i)|i\rangle}{[\hbar\omega_i - (E_n - E_i)][\hbar\omega_i - \hbar\omega_0 - (E_{n'} - E_i)]}, \qquad \textbf{\{III.49\}}$$

The process continues until the last vertex of the Feynman diagram is reached.

[13] The sign of the photon energy is positive for absorption and negative for emission.

The scattering probability (per unit time) is reached by applying the Golden Rule **[III.7]**:

$$P_{ph}(\omega_i,\omega_S)=\frac{2\pi}{\hbar}\left|\sum_{n,n'}\frac{\langle i|H_{eR}(\omega_S)|n'\rangle\langle n'|H_{e-ion}(\omega_0)|n\rangle\langle n|H_{eR}(\omega_i)|i\rangle}{[\hbar\omega_i-(E_n-E_i)][\hbar\omega_i-\hbar\omega_0-(E_{n'}-E_i)]}\right|^2\delta(\hbar\omega_i-\hbar\omega_0-\hbar\omega_S).$$

{III.50}

The total probability of the phonon scattering can be obtained by adding the individual contributions of the other five Feynman diagrams.

The chose of the first diagram to show the calculation was not innocent, since the order of interaction shown in first diagram is the one with higher probability of occurrence. This happens because the energy of the photon is much higher that the energy of the phonon.

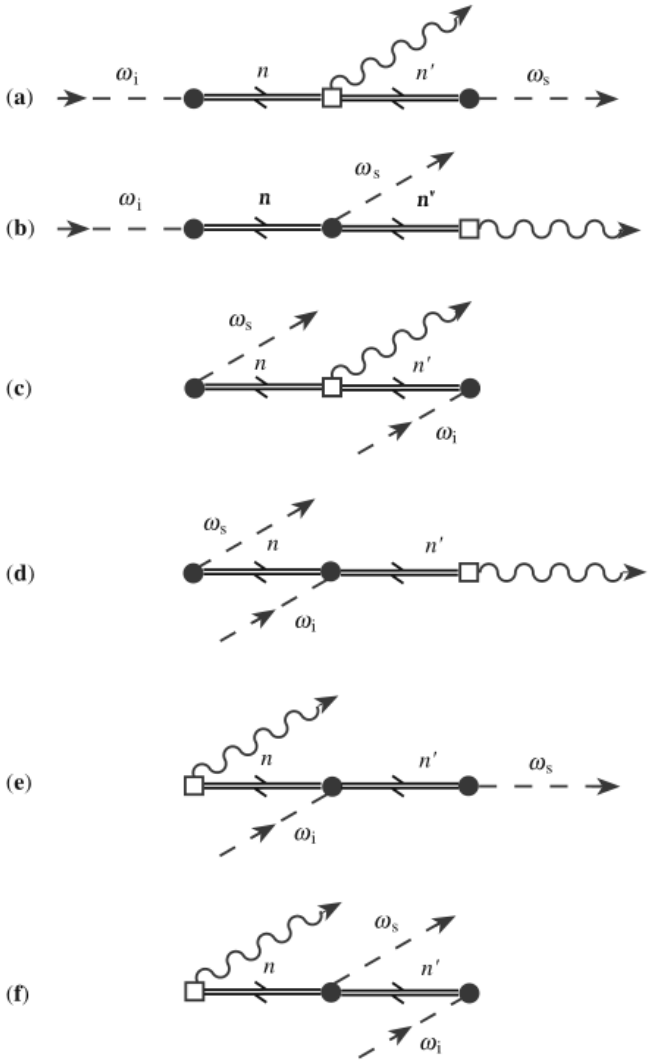

Figure III.8: Feynman diagrams for the six scattering processes that contribute to one-phonon Raman scattering in the Stokes process. [III.7]

The scattering probability is a function of two arguments, the frequencies of the scattered (ω_S) and incident (ω_i) photons. Alternatively, because of the δ-function expressing the global energy conservation, one may see it as a function of ω_i and ω_0, the frequency of the phonon created in the Stokes process. The intensity of the Stokes-scattered beam is $I_s = \hbar\omega_S P_{ph}(\omega_i, \omega_S)$. It is usual to quantify the scattering process in terms of so called differential cross-section, $d^2\sigma/(d\omega_S d\Omega)$ (Ω denotes solid angle). The definition of this quantity is done in **Ref. [III.4]**; since it was not measured its absolute value (only the relative intensity), the lengthy definition of $d^2\sigma/(d\omega_S d\Omega)$ is not reproduce here.

III.6. Resonant Raman Scattering

In the previous **section III.5** it has been shown that Raman scattering is a quantum process involving the summation over many intermediate states. Usually, this summation hinders the extraction of information on the electron–phonon interaction, electron–radiation interaction and the electron band structure that determine the Raman scattering rate because a large number of different intermediate states give comparable contributions. In particular, this is always the case when the incident photon energy, $\hbar\omega_i$, is considerably below the band gap energy, E_g, the situation that will be referred to as "usual" or non-resonant Raman scattering. When many electronic states contribute (as intermediate states) to the scattering process, the details of each of them becomes unimportant and the spectrum is determined only by the phonon mode involved, in particular, by its symmetry. However, the situation changes when one or few intermediate electronic states dominate the scattering process. By using an excitation energy with a strong resonance with a particular interband transition the Raman cross section can be enhanced. This is known as resonant Raman scattering (RRS).

Resonant Raman scattering in semiconductors occurs when the energy of the incident photon is equal or superior to the optical band gap energy ($\hbar\omega_i \geq E_g$). Contrary to the "usual" Raman scattering where the electronic transitions are virtual,

in the resonant Raman scattering the electronic transitions are real and this results in an increased efficiency of the scattering processes. But frequently in Raman scattering the word "resonant" is used in a more restricted sense and is only applied when the incident or scattered photon energy matches a specific resonance in the electronic structure of the material (*e.g.* a critical point, such as a van Hove singularity) or a particular exciton transition. In both cases, the scattering is enhanced and also takes some new features characteristic of the specific transition involved, for instance, the general (crystal symmetry dictated) selection rules may not apply.

Under resonance conditions, the non-resonant terms of the scattering probability can be approximated by a constant **[III.7]**. As mentioned in **Section III.5**, the first Feynman diagram of **Figure III.8** is responsible for the most important contribution, and this is still valid under resonant conditions. Let us assume the initial state to be a ground state, $|0\rangle$, and a resonant intermediate state, $|a\rangle$. In the ground state there are no electron–hole pairs and the ground state energy is zero, $E_0 = 0$. In the intermediate state, the energy is E_a. In the vicinity of the resonant intermediate state, the peak value of the Raman scattering probability for a given phonon mode ω_0, can be approximated by **[III.7]**:

$$P_{ph}(\omega_i) \propto \left| \frac{\langle o|H_{eR}(\omega_s)|a\rangle\langle a|H_{e-ion}|a\rangle\langle a|H_{eR}(\omega_s)|0\rangle}{(E_a - \hbar\omega_i)(E_a - \hbar\omega_s)} + C \right|^2 , \qquad \textbf{\{III.51\}}$$

where *C* is a constant background that includes the contributions of all non-resonant intermediate states and it was omitted the second argument. The difference between $\hbar\omega_i$ and $\hbar\omega_s$ is equal to the phonon energy, $\hbar\omega_0$ (one-phonon Raman scattering) and is usually small compared to the electronic energies. When either the incident ($\hbar\omega_i$) or the scattering photon energy ($\hbar\omega_s$) is resonant with E_a, the right-hand side of the above equation diverges. This can be avoided by introducing a finite lifetime τ_a for the intermediate state $|a\rangle$ due to radiative and non-radiative decay processes. For a resonant discrete state with energy E_a **[III.7]**:

$$P_{ph}(\omega_i) \propto \left| \frac{\langle 0|H_{eR}(\omega_s)|a\rangle\langle a|H_{e-ion}|a\rangle\langle a|H_{eR}(\omega_i)|0\rangle}{(E_a - \hbar\omega_i - i\Gamma_a)(E_a - \hbar\omega_s - i\Gamma_a)} \right|^2 , \qquad \textbf{\{III.52\}}$$

where $\Gamma_a = \hbar/\tau_a$ is the damping parameter. If the phonon involved in the Raman scattering has a non-negligible damping constant Γ_0, it has to be included in the scattering probability and has been done in **Equation {III.52}** by replacing $\hbar\omega_S$ with $\hbar\omega_i - (\hbar\omega_0 - i\Gamma_0)$.

Thus, the resonant Raman scattering behaviour is strongly influenced by the intermediate states, and is dependent on whether these states are continuous or discrete. In the case of resonance with excitons (discrete case), the results will depend on the magnitude of the exciton oscillator strength and respective damping constant.

III.6.1. Free and Bound Excitions

Free[14] and bound[15] excitons have been shown to enhance the Raman cross section by several orders of magnitude because of their small damping constants at low temperatures. This resonance effect helps the observation of phenomena like electric-dipole forbidden transitions, wavevector-dependent electron-LO phonon interaction, and higher order Raman scattering involving multiple phonons. The latter was observed in the present work for ZnO (in **Chapter V**).

The bound excitons have higher oscillator strength and longer non-radiative lifetimes than free excitons. Because of their nature, bound excitons are strongly localized around impurities or defects in the lattice. When these vibrational modes are localized at an impurity, they are called local modes **[III.9]**. When an exciton is bound to an impurity, can result in a specially strong enhancement of the Raman scattering intensity due to a local vibration mode of the impurity atom, allowing the study of localized impurities in the crystal lattice.

It is technically possible (*e.g.* by using a dye laser or a tunable laser) to adjust the excitation wavelength in such a way that $\hbar\omega_i$ is very close to the bound exciton

[14] A free exciton is a linked electron-hole pair capable to move freely as a whole along the lattice of the semiconductor (or an insulator or some liquids).

[15] A bound exciton is an electron-hole pair linked to an impurity or defect in the semiconductor, for example, to an atom vacancy. The link the impurity adds an extra energy contribution to the exciton, thus increasing the oscillator strength and possibly yielding long non-radiative lifetimes.

energy, E_1. Then all other contributions can be neglected and the function $P_{ph}(\omega_i)$ becomes quite simple **[III.7]**:

$$P_{ph}(\omega_i) \propto \left| \sum_{n,n'} \frac{\langle 0|H_{eR}(\omega_i)|1\rangle\langle 1|H_{e-ion}|1\rangle\langle 1|H_{eR}(\omega_s)|0\rangle}{(E_1 - \hbar\omega_i - i\Gamma_1)(E_1 - \hbar\omega_s - i\Gamma_1)} \right|^2 . \qquad \textbf{\{III.53\}}$$

It is proportional to a product of two Lorentzians representing two resonances known as "incoming" and "outgoing" ones. The (squared) matrix elements $\langle 0|H_{eR}(\omega_i)|1\rangle$ and $\langle 1|H_{eR}(\omega_s)|0\rangle$ in **Equation {III.53}** are the same that determine the exciton absorption/emission (*i.e.* the exciton oscillator strength), while $\langle 1|H_{e-ion}|1\rangle$ is the diagonal matrix element for the exciton in its lowest energy state and the considered phonon mode. Thus, one can evaluate the strength of the electron-phonon interaction by combining Raman and photoluminescence data.

III.6.2. Wavevector Dependence of Exciton–LO-Phonon Interaction

The wavevector dependence of the exciton–LO phonon interaction plays an important role in the resonant Raman scattering. Although it is possible to determine the magnitude of this interaction, in general it is rather difficult since it is necessary to know the absolute values of the correspondent Raman cross-section, as referred before in **Section III.5**. But qualitative information or relative magnitudes are easier to obtain.

The Fröhlich interaction Hamiltonian, $H_{F,X}$, for an exciton can be derived assuming parabolic and isotropic electron and hole bands. The expression can be written in terms of creation and annihilation operators for the phonons (C_q^+ and C_q, respectively) and for the excitons, a_K^+ and a_K, respectively, where $\vec{K}$ is the exciton (centre of mass, CM) wavevector. It is **[III.7]**:

$$H_{F,X} = \frac{iC_F}{q}\left[\exp(ip_h\vec{q}\cdot\vec{r}) - \exp(ip_e\vec{q}\cdot\vec{r})\right]\left(a_{K+q}^+ a_K C_{-q}^+ + a_{K+q}^+ a_K C_q\right), \qquad \textbf{\{III.54\}}$$

$$C_F = e\left[\frac{2\pi\hbar\omega_{LO}}{NV}\left(\varepsilon_\infty^{-1} - \varepsilon_0^{-1}\right)\right]^{1/2}, \qquad \textbf{\{III.55\}}$$

$$p_e = \frac{m_e}{m_e + m_h}, \qquad \textbf{\{III.56\}}$$

$$p_h = \frac{m_h}{m_h + m_e}. \qquad \textbf{\{III.57\}}$$

Here $\vec{r}$ is the position of the electron relative to the hole, N is the number of unit cells per unit volume of the crystal, V is the volume of the unit cell, ε_∞ and ε_0 are the high-frequency and static dielectric constants, and m_e and m_h are the effective masses of the electron and hole, respectively. The term $\left(a^+_{K+q}a_K C^+_{-q}\right)$ describes the scattering of the exciton from the state with wavevector $\vec{K}$ to the state $\vec{K}+\vec{q}$ by emission of an LO phonon with wavevector $\vec{q}$. The term $\left(a^+_{K+q}a_K C_q\right)$ describes the absorption of the LO phonon.

The matrix element of **Equation {III.54}** can be calculated explicitly for the hydrogen model of the lowest energy exciton state with an effective Bohr radius a_X and it vanishes for $\vec{q}=0$ and increases as q^2 for $a_X q << 1$ **[III.7]**. It means that the Fröhlich mechanism involves phonons with non-zero wavevectors (because it vanishes exactly in the Brillouin zone centre) and violates the formal symmetry-based Raman scattering selection rules.

III.7. Phonon Modes and Raman Scattering in Solid Solutions

A semiconductor solid solution is a crystalline mixture of, at least, two semiconductor materials, one being the solvent (material in high quantity) and the others the solutes (materials is lower quantity). The final crystal can be considered a solution when the original lattice structure of the solvent is kept and the solution remains in a single homogeneous phase.

The intensions behind the solid solutions are in general to obtain a material with different but similar properties of the original ones. A well know solid solution/ alloy is $Si_{1-x}Ge_x$, were any x content is possible. This mix is used to band structure engineering, allowing one to tune the materials' electric properties to the desired application, but still keeps the original diamond structure. The GeSn solid solutions studied in this work (**Chapter IV**) is a similar example, where a "new" material is engineered so that the diamond structure of the Ge (solvent) is kept, but with the introduction of Sn (solute) changes the band structure to the point of potentially result a group IV semiconductor with direct band gap (see **Section I.2**). The case of ZnO:Mn (**Chapter V**), in principle, can also be considered a solid solution, since even small quantities of Mn result in

significant changes to electric and magnetic properties of the ZnO undoped. Doping should not be considered a solid solution since the intension is to change only the concentration a charge carriers and keeping [ideally] unaltered all the other properties of the material.

With the emerging of solid solutions, an attempt to classify the resulting materials was made having in consideration the phonon dispersion versus the composition. Three types of solid solutions are considered here, although others exist. The two most common ones are the solid solutions of one-mode behaviour (or type I) and two-mode behaviour (or type II), and the difference lies in the variation of the transverse and longitudinal optical phonon modes with composition **[III.10]**.

In the one-mode behaviour (see **Figure III.9**), one LO-type and one TO-type phonon mode exist for the whole range of the solid solution composition. Strictly speaking, in crystalline solid solutions the translational symmetry is lost, since the crystal has an arrangement of different atoms or ions over the lattice sites, which is largely disordered. The phonon *eigenstates* are no longer labelled by a wavevector, so each *eigenstate* may now have a non-zero projection onto zero wavevector when compared to the "average" crystal. Hence, subject to restrictions imposed by the nature of the coupling of the phonons to the photons, a response can be expected over a wide range of frequencies even in a first-order process. The maximum of this spectral response is called LO-type or TO-type phonon mode of the mixed crystal. In the simplest case, as the concentration of components changes, the optical frequencies modes at $\vec{k} \approx 0$ of the solid solution vary continuously with concentration from a frequency characteristic of that of one end-member crystal to that of the other end-member crystal. As this takes place the strength of each mode varies only slightly and often linearly. **[III.10, III.11]**

Two-mode behaviour (see **Figure III.10**) arises from the localised impurity modes in a crystal with a very low concentration of the second compound. If the resulting perturbation due to the substitution of the host atom by an impurity atom is sufficiently strong (mass and/or force constant changes sufficiently large), vibrational states can split off the host crystal phonon bands to produce non-propagating modes, *i. e.* local vibrations. As the concentration of the second material increases, the local vibration mode develops into a band, just like a local electronic level splits into an impurity band in a heavily doped semiconductor. As a result, for each allowed optical

phonon mode, two bands are observed with frequencies in the vicinity of those of the pure compounds. The strength of each of the modes in such solid solutions is roughly proportional to the molar fraction of the components. **[III.10, III.11]**

A third type or the three-mode behaviour exists in group IV mixed crystals. This mode is more specific that the previous two and is characterized by the existence of three well defined dispersion curves of optical phonon modes that change with the concentration of the materials involved. This is the case of SiGe solid solutions (**Figure III.11**) where three distinct interatomic distances between Ge-Ge, Ge-Si and Si-Si atomic pairs occur, generating three corresponding fundamental optical phonon modes. A similar classification, in principle, is valid for GeSn although the Sn-Sn mode usually does not show up in Raman spectroscopy experiments.

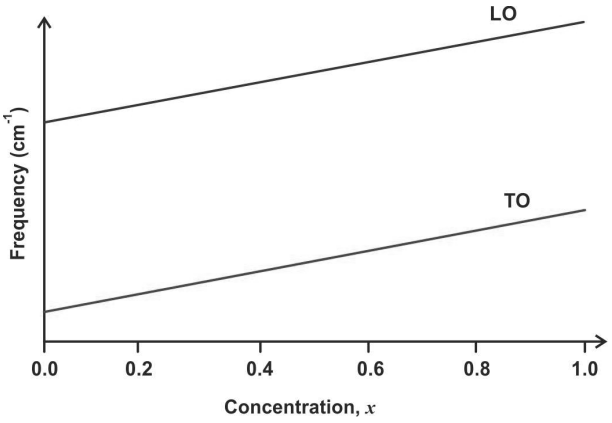

Figure III.9: Illustration of a solid solution of composed of two element (A and B) with phonon frequency one-mode behaviour.

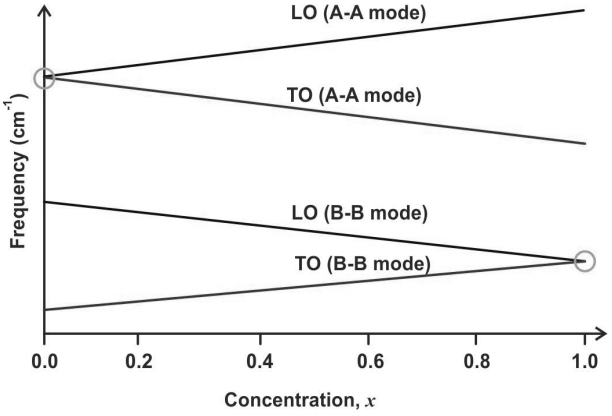

Figure III.10: Illustration of a solid solution of composed of two element (A and B) with phonon frequency one-mode behaviour.

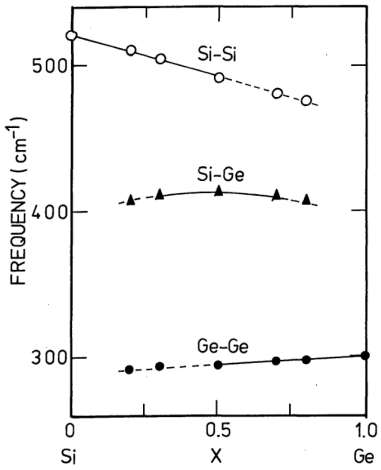

Figure III.11: Concentration dependence of $Si_{1-x}Ge_x$ Raman scattering peaks of Si-Si, Si-Ge and Ge-Ge mode. The three modes, each including a TO and an LO phonon, have very distinct frequencies that differently depend on the composition, typical of a type III solid solution. Figure is reproduced from [III.12].

III.8. Experimental Determination of Raman Spectra

The concept of measuring Raman scattering is simple and has three main parts: 1) a monochromatic incident light is used to excite the medium, 2) the Rayleigh scattering is rejected, and; 3) the Raman scattering is detected. The setups to measure Raman scattering evolved along the history. But mainly two technologies were essential to the development of Raman scattering measurement setups to nowadays need: 1) lasers and 2) optoelectronic detectors.

The most common Raman setup to analyse semiconductor or other condensed materials is the micro-Raman back-scattering spectroscopy (μ-Raman or RS). These setups have a laser for excitation of the medium that is introduced in a microscope and it is focused on the surface of the sample. The scattered (and reflected) radiation is collected by the same microscope. A filtering system is used to remove the undesired reflected and the Rayleigh scattering light coming form the sample. Finally the radiation passes by a spectrometer and detected, in general by an array of optoelectronic detectors. An illustration of this Raman scattering setup configuration is shown in **Figure III.12**. This back-scattering configuration has the advantage over others by being capable of working in transparent and opaque samples to the desired excitation wavelength.

The most common lasers used for Raman scattering measurements of semiconductors are in the visible range or near infrared. **Table III.3** shows a list of common lasers. These lasers are commonly used because they are widely available, provided a high enough output, are cheap and in majority of the cases, no maintenance is required. The choice of a specific excitation wavelength or set of wavelengths can be used to study the medium with different penetration deeps (see **Table III.3**), study the surface and / or obtain resonance effects and increasing the Raman scattering. When the excitation energy is higher than the gap energy of the semiconductor the selection rules are no longer applied for the first order Raman and more Raman modes can be observed.

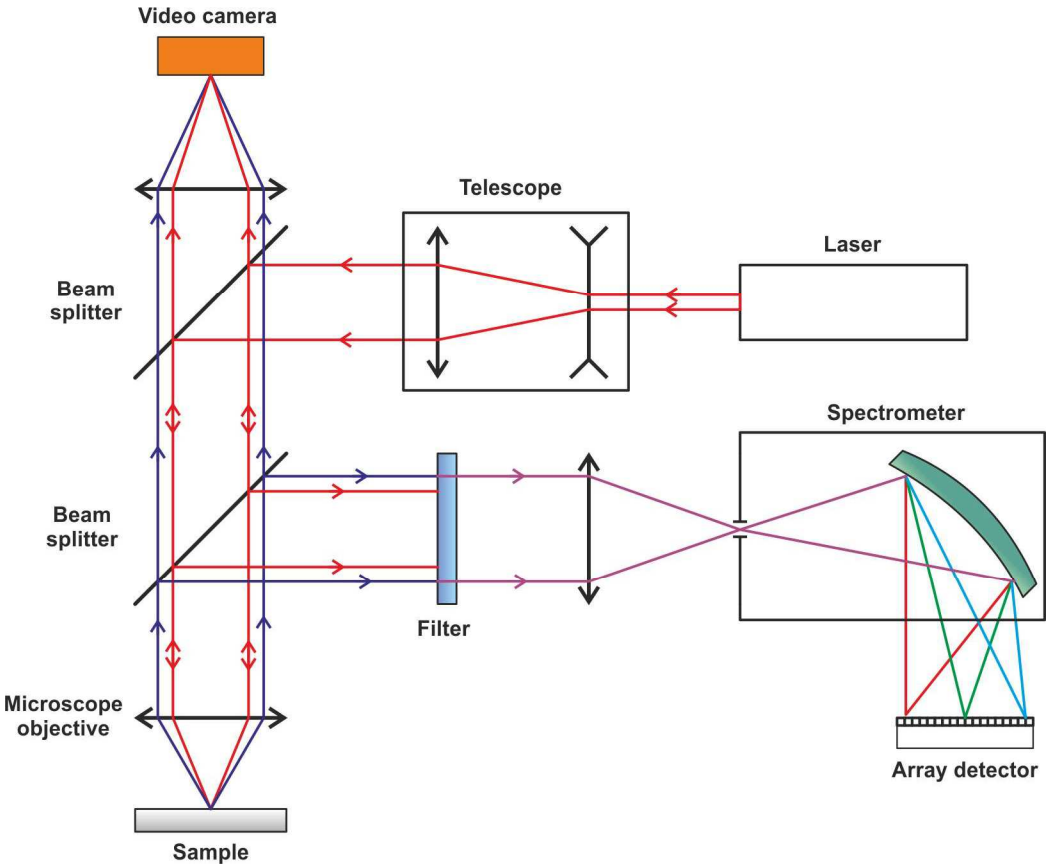

Figure III.12: Illustration of a simplifed micro-Raman back-scattering spectroscopy setup. The laser radiation is inserted in a microscope and it is used to excite the sample. The sample reflects back part of the incident light and produces scattered light (Rayleigh, Brillouin, Raman). The video camera is used to observe the position the sample and assists in the laser focusing. A filter is used to prevent reflected light and Rayleigh scattering to pass to the spectrometer, since they have intensity several orders of magnitude higher. The spectrometer splits the remaining scattered light that is detected by the array detector.

Table III.3: List of common lasers use on Raman scattering measurements of semiconductors and respective penetration deep for Si and Ge. [III.13]

Laser	Wavelength (nm)	Energy (eV)	Penetration deep (μm)	
			Si	Ge
Ar+ (gas)	488	2.54	0.485	0.017
Ar+ (gas)	514	2.41	0.664	0.017
Nd:YAG (solid)	532	2.33	0.817	0.018
He-Ne (gas)	633	1.96	2.571	0.062
GaAlAs (diode)	780	1.59	8.058	0.182

Typically the microscopes used in Raman scattering setups are common microscope. Objectives with magnification of 50x or 100x are extensible used, because of there substantial numerical aperture (around 1) that provides a large solid angle for collection of the scattered light. The large numerical aperture also results in a very small focusing spot, with a size that can roughly be approximated by the Airy disc diameter, ≈ 1 μm.

The filtering system for the reflected and Rayleigh scattering light is typically formed by a high quality filter with high absorption and a very narrow band (notch filter), typically around ±150 cm^{-1} of excitation frequency. The use of a notch filter allows the measurement of Stokes and anti-Stoke scattering. When anti-stokes is not necessary a simpler high quality edgepass filter are commonly used for being significantly cheaper. Less common alternative is the use of a double monochromator in the additive configuration, since this system provides an even narrow band and can be adjusted for the desired wavelength. This last method is frequently used in setups capable to measure Brillouin scattering.

The spectrometer if typical composed of a monochromatic with an array of optoelectronic detector. The use of visible and near infrared laser is also an advantage here, since silicon detectors can be used for these wavelengths. Silicon detectors when compared to other optoelectronic detectors of different semiconductors have a good efficiency and the best signal-to-noise ratio, important characteristics considering the low efficiency of Raman scattering. Array detectors are used instead single detectors by two reasons: 1) increase in resolution **[III.14]**, and 2) fast collection of the spectra.

III.8.1. Description and Characteristics of the Raman Setups Used

The sample analysed in this work were measured using several commercial Raman setups. The reasons for the use of multiple systems are related with the desired excitation wavelength and availability of the system. **Table III.4** provides a list of the setups used, some of their main characteristics, and the respective host institutions. All measurement systems were used exclusively in micro Raman back-scattering spectroscopy configuration. **Figure III.12** shows the typical configurations of the Raman setups 2, 3 and 4.

The Raman System 1 is a Horiba Jobin Yvon Raman T64000 setup, capable of micro- or macro- Raman scattering spectroscopy. The system works with a triple monochromator capable of being used in multiple monochromator configurations to maximaze resolution, power output or low frequency shifts. The system was used exclusively in micro Raman back-scattering spectroscopy configuration with a double-adictive / single monochromator configuration, the first two work as the laser filter and the third for spectral measurements. The excitation was provided by a 2 W argon laser with a multiple laser emissions, being the most impostant three 454.6 nm, 488.0 nm and 514.5 nm. The detection was made with a CCD array detector. A 50x objective was used with a resulting spot size of the excitation on the sample of ≈ 1 μm^2. The incident power was regulated to ≈ 1 mW on the sample.

The Raman System 2 is a WITec Alpha 300 R Raman confocal imaging setup, capable of micro-Raman back-scattering spectroscopy. The system works with a single monochromator together with a CCD array detector for spectral measurements and a filter to block the reflected and excitation radiation. A filter is used for the absorption of the spectrum below + 100 cm^{-1} of the laser line. The system has three laser excitations: two diode lasers with 532 nm and 780 nm emission lines and a gas He-Ne laser with 633 nm emission wavelength. A 50 x objective was used with a resulting spot size of the excitation on the sample of ≈ 1 μm^2. The incident power was regulated between ≈ 4 and ≈ 40 mW on the sample.

The Raman System 3 is a Renishaw inVia Reflex confocal Raman microscope setup, capable of micro-Raman spectroscopy in a back-scattering configuration. The system works with a single monochromator together with a CCD array detector for

spectral measurements and filters to block the reflected and excitation radiation. A Rayleigh filter is used for the absorption of the spectrum between -100 cm^{-1} and + 100 cm^{-1} of the laser line. The system is equipped with a He-Ne laser with a wavelength of 633 nm. An objective of 50x was used with a resulting spot size of the excitation on the sample of ≈ 1 μm^2. The incident power was ≈ 25 mW on the sample.

The Raman System 4 is a Renishaw inVia Qontor confocal Raman microscope setup (same family as the Raman System 3), capable of micro-Raman back-scattering spectroscopy. The system works with a single monochromator together with CCD array detector for spectral measurements and filters to block the reflected and excitation radiation. An edge filter is used for the absorption of the spectrum below + 100 cm^{-1} of the laser line. The system is equipped with a diode laser with a wavelength of 532 nm. A 50 x objective was used with a resulting spot size of the excitation on the sample of ≈ 1 μm^2. The incident power was < 40 mW on the sample.

The Raman System 5 is equivalent to the System1 but has an additional option of excitation with a Ti-saphire laser.

All the Raman setups were calibrated using a silicon wafer as reference.

Table III.4: List of the setups used to measure Raman scattering. All the setups work in the backscattering configuration with a microscope, objectives of 50x or 100x magnification and array detectors. All lasers are polarized.

Setup	Institution	Setup/ Model	Type	Wavelengths
Raman System 1	CFUM	Horiba Jobin Yvon T64000	Triple monochromator	Ar+ laser: 488, 512 nm
Raman System 2	INL	WITec Alpha 300 R	Single monochromator with filter	He-Ne laser: 633 nm Diode laser: 532 nm Diode laser: 780 nm
Raman System 3	IHT	Renishaw inVia	Single monochromator with band filter (+/- 150 cm^{-1})	He-Ne laser: 633 nm
Raman System 4	IPV	Renishaw inVia	Single monochromator with edge filter	Diode laser: 532 nm
Raman System 5	I3N	Horiba Jobin Yvon T64000	Triple monochromator	Ar+ laser: 488, 512 nm Ti-saphire laser: 325 nm

CFUM – Centre of Physics of University of Minho, Braga, Portugal
INL – International Iberian Nanotechnology Laboratory, Braga, Portugal
IHT – Institute of Semiconductor Engineering, Stuttgart, Germany
IPV – Institute of Photovoltaik, Stuttgart, Germany
I3N – Institut for Nanostructures, Nanomodelling and Nanofabrication, Aveiro, Portugal

III.8.2. Analysis of Typical Spectra of Semiconductor Crystals

The group IV materials, Si, Ge and α-Sn, have a diamond structure, with 2 atoms per primitive unit cell (s=2), and consequently 3 acoustic branches and 3 optical branches exist. Group theory provides two sets of normal modes of vibration in the centre of the Brillouin zone (Γ point), one acoustic and one optical with the latter corresponding to the three-dimensional irreducible representation T_2 (or Γ_4 in another notation). Of these, two correspond to transversal optical (TO) phonon modes and one to longitudinal optical phonon mode (LO).

Figure III.13 shows Raman scattering spectra of crystalline Si using several polarization configurations according to the selections rules shown in **Chapter III.4.** Selection rules are important for identification of different phonon modes, since they predict their appearance (or not) in different scattering geometries. The spectra show multiple Raman modes including the one-phonon and two-phonon modes at the Γ point. The frequency shift of one-phonon mode at the Γ point is 520 cm^{-1} **[III.15, III.16]**. Raman spectra for of amorphous Si films are shows in **Figure III.14**. The difference between the crystalline and the amorphous spectra is clear. The peaks present in Raman scattering spectra of crystal with high symmetry are not present in the amorphous samples. The peaks are in different numbers, and have frequency shift positions and widths. In the case of polycrystaly and nanocrystalline mediums, a certain degree of symmetry at low range still exists, and Raman scattering spectra will show modes of the high symmetry points of the lattice. They keep a similar frequency shift position that the peaks found in single crystal mediums, but due to the present disorder, the peaks become broader, as it will be see in **Chapter V**.

Figure III.15 and **III.16** show the Raman scattering spectra of crystalline Ge and Sn, respectively. The spectra show multiple Raman modes including the one-phonon and two-phonon ones at the Γ point. The Raman frequency shift of the Ge-Ge one-phonon mode at the Γ point is 299.7 cm^{-1} **[III.17]** (300.9 cm^{-1} measured with the Raman systems used in this work), while for the Sn-Sn one it is 198 cm^{-1} **[III.19].** As it is observed, the spectrum has a single one-phonon Raman mode, at the Γ point, in concordance with theory show in the first section of the **Chapter III**. All the other

modes in the spectra are two-phonon modes, in concordance with the theory, where $\Delta\vec{k} \approx 0$, but the individual wavelengths of the phonons can assume any value. This can be explained by the existent disorder on the crystal that relaxes the selection rules $\vec{k} \approx 0$, and activates other modes. The spectrum becomes more alike that of the total density of phonon states (see **Figure III.15**).

The spectra of the single crystal Si and Ge have similar band structure (see **Section I.1.1**), resulting also in a similar shape of the Raman scattering spectra (see **Figure III.13** and **III.15**).

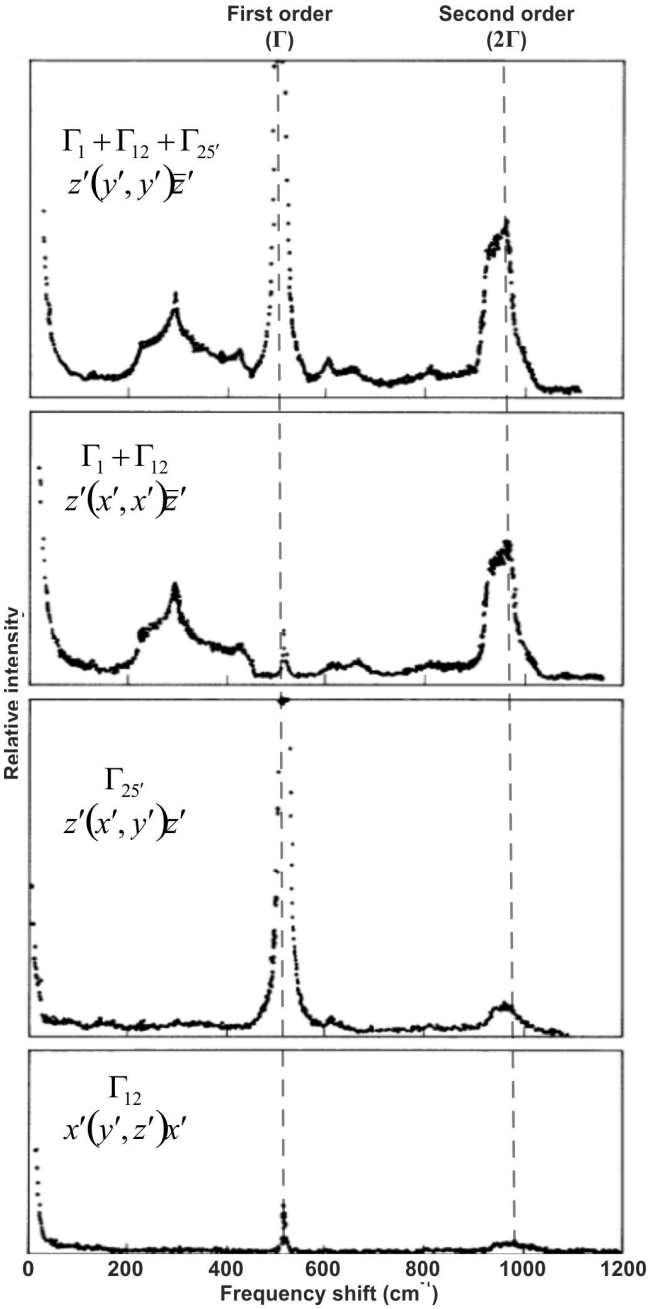

Figure III.13: Raman spectra of crystalline silicon at room temperature with different polarization configurations, using an argon-laser with a wavelength excitation of 488 nm. The polarization reveals different modes according to the selection rules. The peaks of the one-phonon and two-phonon Γ points are indicated by the dashed lines. [III.15]

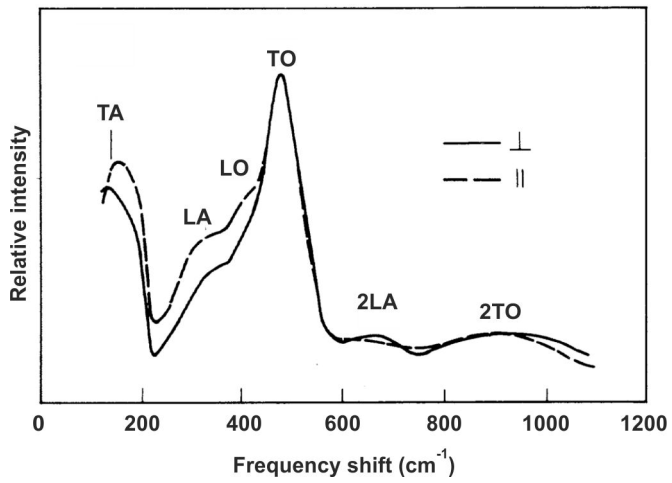

Figure III.14: Raman spectra of amorphous silicon obtained for parallel (‖) and perpendicular (⊥) scattering configurations at room temperature, using a He-Cd laser with a wavelength excitation of 441.6 nm [III.17]

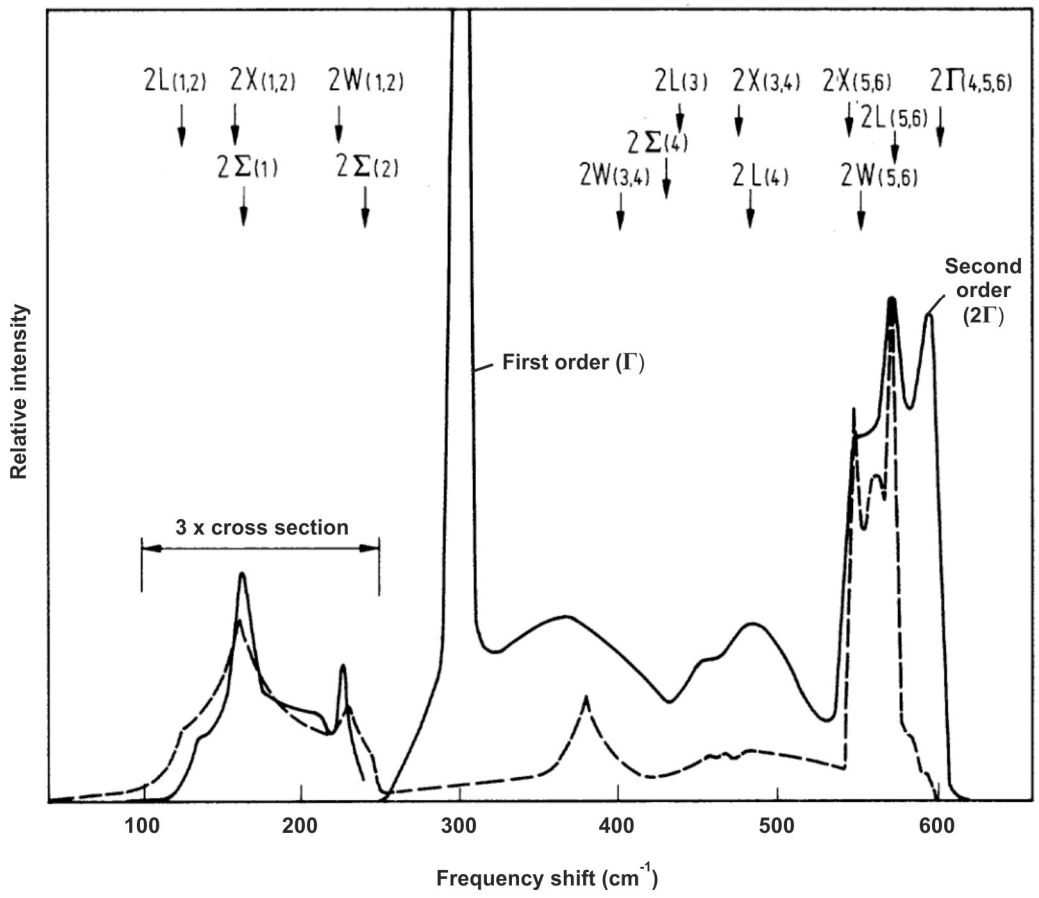

Figure III.15: Raman spectrum (full line) and density of states (dashed line) of crystalline germanium at room temperature, using an argon laser with a wavelength excitation of 514.5 nm. The peaks of the one-phonon and two-phonon Γ points are indicated. The arrows indicate the position of critical points based on neutron data, all of them are correspondent to two-phonon Raman modes. [III.18]

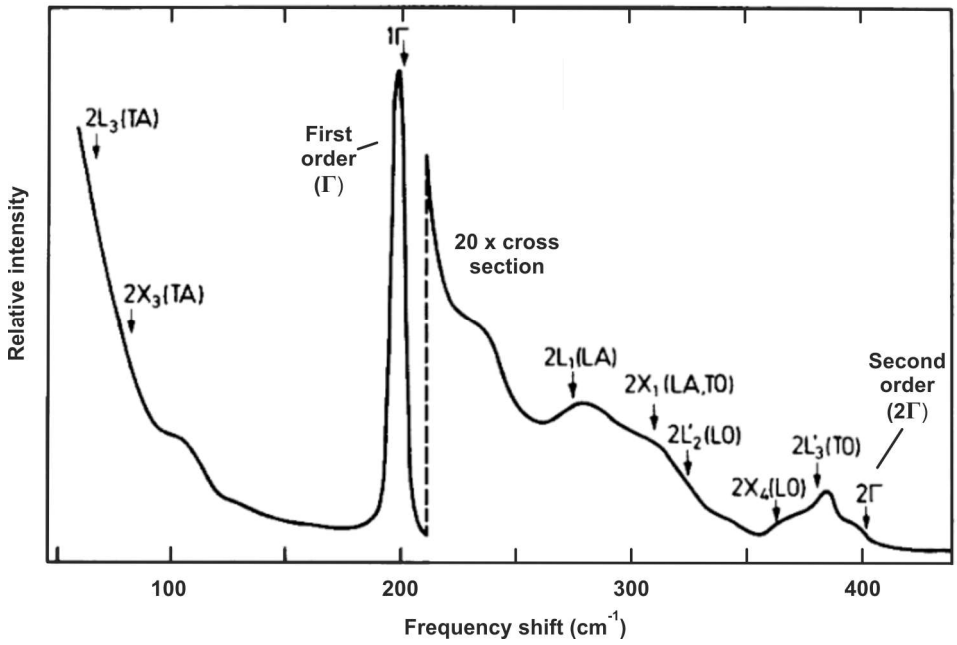

Figure III.16: Second-order Raman scattering spectrum of α-Sn obtain with excitation energy of 1.65 eV. Figure adapted from [III.19]

In the case of ZnO, the electronic band structure and vibrational properties are comprehensively reported in the literature **[III.20 – III.22]**. Given that there are four ions in the primitive unit cell of the ZnO wurtzite structure, a total of twelve vibrational modes are expected. Group theory provides eight sets of normal modes of vibration in the centre of the Brillouin zone (Γ point): $2A_1 + 2E_1 + 2B_1 + 2E_2$. Of these, a set of modes A_1 and E_1 correspond to acoustic modes and the rest are optical phonon modes. In Raman scattering all optical modes are active except for the B_1 ones which are silent. Due to their polar nature, the modes A_1 and E_1 split into longitudinal (A_1-LO, E_1-LO) and transverse (A_1-TO, E_1-TO) optical phonon modes. The modes A_1 and B_1 correspond to atomic displacements along the *c*-axis, while the E_1 and E_2 ones represent atomic displacements perpendicular to it. The A_1 and E_1 modes are polar and therefore IR-active, while E_2 are only seen in Raman scattering spectra. The low frequency E_2 mode is associated with the vibrations of the Zn cations, while the high frequency E_2 mode involves only the anions of O **[III.23]**. The non-polar E_2 mode is only Raman-active and has two distinct frequencies associated with the oxygen and zinc sublattices, designated E_2^{high} and E_2^{low}, respectively. The B_1 mode is not detectable by either Raman or infrared spectroscopy, *i.e.* fully silent.

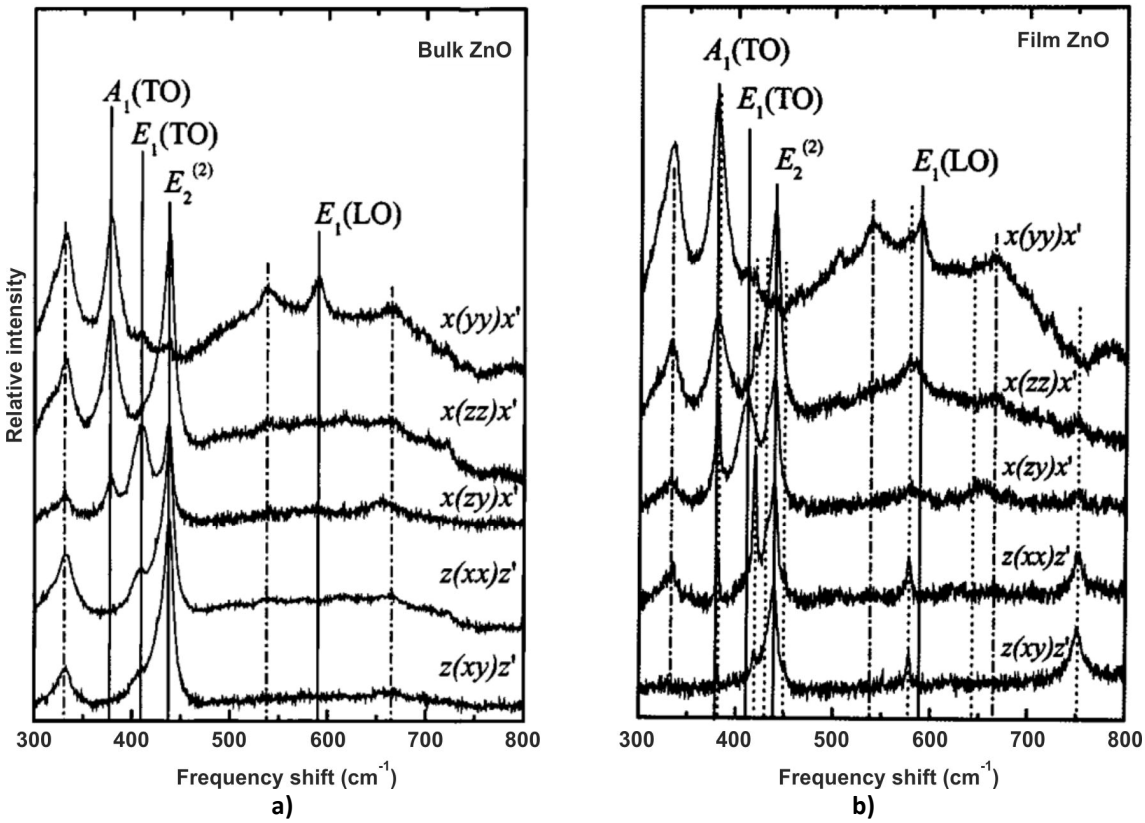

Figure III.17: Raman spectra of a) a bulk ZnO sample, and b) film ZnO on sapphire sample. First-order phonon modes of ZnO are indicated by the vertical solid lines. The vertical dashed–dotted lines mark the features due to multiple-phonon scattering processes. The vertical doted lines indicate the Raman-active sapphire substrate phonon mode frequencies. The measurements were performaned using an argon laser with a wavelength excitation of 514.5 nm and optical power on the samples' surface ≤ 40 mW. [III.24]

Spectra of Raman scattering of bulk and film samples of ZnO are shows in **Figure III.17**. Both groups of spectra (bulk and film samples) are similar. Multiple Raman modes are identified in the figure.

As referred in **Section III.6**, Raman scattering efficiency, and consequently detectable signal, can be increased through Raman resonance. That is archived by using an excitation light source (typically a laser) with a higher energy that the bag gap. Further increase in resonance can be archived by using an excitation with a wavelength close to a van Hover point. These techniques were applied to the group IV samples in **Chapter IV**.

Peaks of the Raman scattering spectra of high structural quality crystalline mediums are in general narrow. Typical peak Full width at half maximum (FWHM) for single crystal are around or bellow a few tens of cm^{-1}, depending on the structure

perfection of the crystal. For example, single crystal samples of Si and Ge have very high structural quality with a very small density of defects resulting in a Raman scattering peak widths at middle height at the Γ point of < 5 cm^{-1} **[III.17, III.18]**. The introduction of disorder in the crystal will result in a broadening of the peaks. In the case of single crystal medium, the increase of disorder is mainly due to structural defects (any kind), impurities and doping elements. Solid solutions are affected not only by the disordering cases mentioned before, but the disorder associated to the random position of each different kind of elements along the lattice. Levels of disorder are naturally high for polycrystalline, nanocrystalline or amorphous state (see comparation between Si spectra of **Figure III.13** and **III.14**). All of these disorders are valid for bulk or thin film samples.

In the growth of epitaxial single crystal film samples in meta-stable condition, like GeSn, the disorder will increase with the thickness of the film. Typically this happens due to a natural increase of the defect that let the crystal relax and consequently growth in more energetically favourable conditions. In some cases, like for GeSn, the growth thickness for a single crystal film can have a limit. This maximum thickness is called critical thickness of the film[16]. After crystal growth breaks done, further growth will no longer result in single crystal. This critical thickness can happen due to the excessive amount of defects at the surface or segregation of one element to the surface, destroying the lattice order at the surface, essential for the epitaxial growth (see **Section II.1**).

The increase of the disorder results in a broadening of the peaks. Since the wavevector, *k*, ceases to have a well-defined value (as it has in a perfect crystal), phonons with somewhat different frequencies become allowed in the scattering process and the broadening can be seen as a superposition of multiple closely spaced spectral peaks representing such slightly different phonon modes.

Such inhomogeneously broadened Raman peaks have rather complex lineshapes but typically close to the Gauss, Lorentz or Voigt functions. Even in high quality samples, like Si wafer, asymmetry is present in the Raman scattering peaks. The disorder not only increases the peak width, it also increases the asymmetry. Sharp peaks, associated to media with low levels of disorder, are typically fitted with the

[16] Critical thickness of the film is different of the critical thickness in the formation of self-assembled dots by the Stranski-Krastanov mode (see **Chapter II.1**).

Lorentz and Voigt functions, while broad peaks, associated to mediums with high levels of disorder, are typically fitted with Gauss functions.

The measurements of the samples with layers with thickness of only a few monolayers are especially difficult to measure due to the very low quantity of material of interest that can be excited. Some techniques can be used to improve the Raman scattering signal: 1) use a resonant excitation, 2) produce samples with multiple stacks, and 3) make two similar samples one with the layer of interest and other without and subtracted the spectra. Raman scattering by different scatterers is not coherent and therefore no interference effects should be expected. This justifies the commonly used procedure of subtracting the spectra (*e. g.* substrate spectrum from that of the whole sample). **Figure III.18** shows an example, where 2 ML of Ge where epitaxially grown in Si (100).

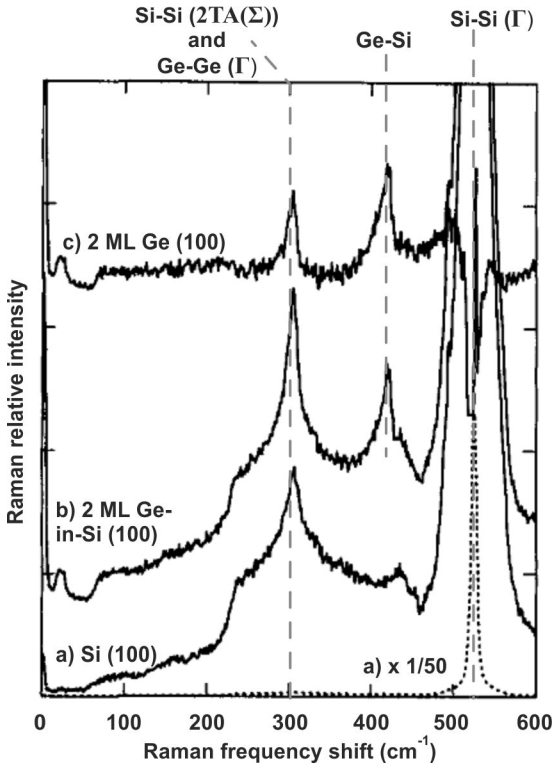

Figure III.18: Raman spectrum of two mono-layers of Ge epitaxially grown on Si (100) and covered by 10 nm of epitaxial Si. Silicon and germanium have peaks close to each other at ≈ 300 cm^{-1}. The low thickness of the Ge layer and consequent low Raman scattering, turns the Ge mode (Γ point) indistinguishable from the Si mode (2TA(Σ)). Subtracting to the whole sample spectrum (b) by the substrate spectrum (a) results in the spectrum of the layers (c). Figure adapter from [III.25]

Summary

In this chapter, theoretical fundamentals of the Raman scattering as well as some practical aspects of the methods of measurement of Raman scattering spectra have been presented along with the respective analysis of experimental data from the literature.

Bibliography

[III.1] A. Smekal. *Zur Quantentheorie der Dispersion*. Die Naturwissenschaften **11**, 873, (1923).

[III.2] C. V. Raman. *A new radiation*. Indian J. Phys. **2**, 387, (1928).

[III.3] D. A. Long. *Raman Spectroscopy*. McGraw-Hill, New York, USA, (1977).

[III.4] William Hayes, and Rodney Loudon. *Scattering of Light by Crystals*. Dover, New York, USA, (2004).

[III.5] Mikhail I. Vasilevskiy, and Isabel Calado Ferreira. *Física dos semicondutores: Fundamentos, Aplicações e Nanoestruturas.* Almedina, Coimbra, Portugal, (Setembro, 2005).

[III.6] M. I. Vasilevskiy. *Exciton-phonon interaction in semiconductor nanocrystals*, In: *Semiconductor Nanocrystal Quantum Dots. Synthesis, Assembly, Spectroscopy and Applications*, ed. A. L. Rogach, Springer, Wien – New York, (2008), pp. 217-256.

[III.7] Peter Y. Yu, and Manuel Cardona. *Fundamentals of Semiconductors: Physics and Materials Properties.* Springer, Germany, 18-47 and 375-426, (1996).

[III.8] R. Loudon. *Raman effect in crystals*. Adv. Phys. **13**, 423, (1964); and, erratum ibid. 14, 621 (1965).

[III.9] A. S. Barker Jr. and A. J. Sievers. *Optical studies of vibrational properties of disordered solids.* Rev. Mod. Phys **47**, S1-178, (1975).

[III.10] Tista Basak, Mala N. Rao, and S.L. Chaplot. *Study of one-mode, two-mode and three-mode phonon behaviour in mixed zinc blende alloys.* Physica **B 407**, 4478, (2012).

[III.11] R. J. Elliott, and I.P. Ipatova. *Optical Properties of mixed crystals*, North-Holland, New York, USA, (1988).

[III.12] T. Ishidate, S Katagiri, K. Inoue, M. Shibuya, K. Tsuji, and S. Minomura. *Lattice Vibrational Properties of Crystalline Si-Ge Alloys.* Journal of the Physical Society of Japan **53**, 2584, (August 1984).

[III.13] D. E. Aspnes, and A. A. Studna. *Dielectric functions and optical parameters of Si, Ge, GaP, GaAs, GaSb, InP, InAs, and InSb from 1. 5 to 6. 0 eV.* Phys. Rev. **B 27**, 985, (15 January 1983).

[III.14] John James. *Spectrograph Design Fundamentals*. Cambridge University Press, USA, (2007).

[III.15] Paul A. Temple, and C. E. Hathaway. *Multiphonon Raman Spectrum of Silicon.* Phys. Rev. **B 7**, 3685, (15 April 1973).

[III.16] J. H. Parker Jr., D. W. Feldman, and M. Ashkin. *Raman Scattering by Silicon and Germanium.* Phys. Rev. **155**, 712, (15 March 1967).

[III.17] Dionisio Bermejo, and Manuel Cardona. *Raman scattering in pure and hydrogenated amorphous germanium and silicon.* Journal of Non-Crystalline Solids **32**, 405, (February–March 1979).

[III.18] B. A. Weinstein, and M. Cardona. *Second-Order Raman Spectrum of Germanium.* Phys. Rev.

B 7, 2545, (1973).

[III.19] M. Iliev, M. Sinyukov, and M. Cardona. *Resonant first-and second-order Raman scattering in gray tin.* Physical Review **B 16**, 5350, (1977).

[III.20] J. M. Calleja, and M. Cardona. *Resonant Raman scattering in ZnO*. Physical Review **B 16**, 3753, (1977).

[III.21] T. C. Damen, S. P. S. Porto, and B. Tell. *Raman Effect in Zinc Oxide*. Physical Review 142, 570, (1966).

[III.22] R. H. Callende, S. S. Sussman, M. Selders, and R. K. Chang. *Dispersion of Raman Cross Section in CdS and ZnO over a Wide Energy Range*. Physical Review B 7, 3788, (1973).

[III.23] H. Morkoç, and U. Ozgur. *Zinc Oxide Fundamentals, Materials and Device Technology*. Wiley-VCH, Germany, (2007)

[III.24] N. Ashkenov, B. N. Mbenkum, C. Bundesmann, V. Riede, M. Lorenz, D. Spemann, E. M. Kaidashev, A. Kasic, M. Schubert, and M. Grundmann. *Infrared dielectric functions and phonon modes of high-quality ZnO films.* Journal of Applied Physics **93**, 126, (1 january 2003)

[III.25] Ed. by Manuel Cardona, and Gernot Güntherodt. *Light Scattering in Solids V*. Topics Appl. Phys. **66**, Springer, Germany, 233-284, (1989).

Chapter IV

Results for Ge-Sn samples

Several sets of samples, based on group IV materials, were grown by molecular beam epitaxy, namely thin film samples and multi-layer structures made of ultra-thin layers of only a few monolayers. Majority of the samples growth involved the deposition of Si, Ge and Sn. The aim was the study of the Sn incorporation on the Ge lattice and the respective consequences on the Ge structure. Seven groups of samples were grown:

a) $Ge_{1-x}Sn_x$ epitaxial thin films (from now on referred to as GeSn);
b) Sn epitaxial ultra-thin films on Ge;
c) Sn epitaxial ultra-thin film in Ge;
d) Sn epitaxial multilayers of ultra-thin films in Ge;
e) GeSn epitaxial ultra-thin films on Si;
f) GeSn epitaxial multilayers in Si (from now on referred to as GeSn/Si);
g) Ge epitaxial multilayers in Si (from now on referred to as Ge/Si).

Although the several kinds of samples grown, only part of them will be explored in this thesis. The groups of samples presented and discussed in this thesis are the ones that present useful Raman data related with the Ge and / or Sn. From the above list, the groups explored here are the samples of a), f) and g).

IV.1. Samples' Description

Two similar MBE systems (designated MBE-I and MBE-II, see **Section II.2.1**) were used to grow the samples mentioned above. The samples of the GeSn thin films group was grown using the MBE-I system, while the other samples were grown with the MBE-II system. A detailed description of the MBE systems can be found in **Section II.2**.

Table IV.1: Short description of three groups of samples studied in this thesis.

Group	Structure	Number of samples	Machine	Machine Sources	Substrate Rotation
GeSn	Solid solution thin film	12x GeSn + 1x Ge (reference)	MBE-I	e-gun: Ge cell: Sn	No
GeSn/Si	Multi-layer	5x GeSn/ Si	MBE-II	e-gun: Si cell: Ge, Sn	Yes
Ge/Si	Multi-layer	4x Ge/Si (references to GeSn/ Si samples)	MBE-II	e-gun: Si cell: Ge, Sn	Yes

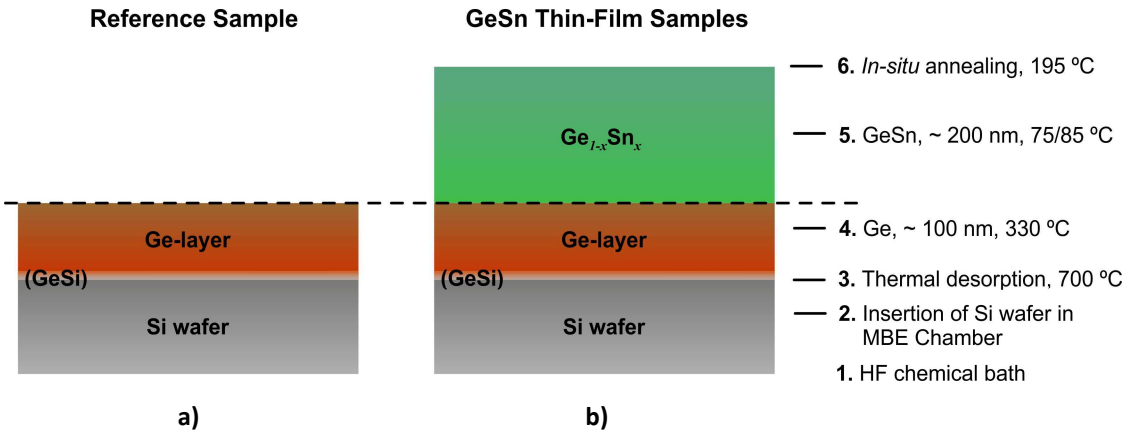

Figure IV.1: Illustration scheme of the GeSn thin film samples growth layers: a) reference sample #0 (layer of pure germanium); b) samples #1 to #12 (layer with different Sn content).

Table IV.2: Samples of GeSn thin films on Ge buffer layer grown on Si wafer (100) and respective differentiator parameters.

Sample	Subs. Temp. GeSn layer (°C)	Sn cell Temp. (°C)	Annealing (in-situ) (°C)
#0	-	-	-
#1	~85	980	-
#2	~85	1000	~195
#3	~85	1020	~195
#4	~85	1040	~195
#5	~85	1060	~195
#6	~85	1080	~195
#7	~75	1100	~195
#8	~75	1120	~195
#9	~75	1140	~195
#10	~75	1160	~195
#11	~75	1180	~195
#12	~75	1200	~195

All the samples (groups) mentioned above were grown on Si (100) wafers with 100 mm diameter. **Table IV.1** shows the main characteristics of the three groups of samples studied in this thesis.

The Si substrates for all the samples/groups were first treated with a wet-chemical etching in a HF bath, to clean the wafer surface and create a hydrogenised layer at the surface. Shortly after, the wafer being introduced into the MBE chamber, was heated, *in situ,* to 700 ^{o}C for a period of 5 minutes to remove the hydrogenised layer on its surface by thermal desorption (see **Section II.2.3.1.**). After this thermal treatment, the Si substrate is ready for the growth of the Ge epitaxial buffer layer. This buffer layer, 100nm thick, was grown at 330 ^{o}C with a growth rate of 0.43 Å/s by e-gun (see **Figure IV.1a**).

Then, the GeSn layer, with a target thickness of 200 nm, was grown over the Ge buffer layer, at a substrate temperature between 75 and 85 ^{o}C. The Ge flux for the GeSn growth was the same as used for the buffer layer and kept constant for all the samples, whereas the Sn flux changed from sample to sample. The Sn flux was controlled by the temperature of the Sn effusion cell, increasing this temperature in steps of 20 ^{o}C, from 980 to 1200 ^{o}C. After the GeSn layer growth, the samples were annealed *in-situ* by ramping-up their temperature to ≈ 195 ^{o}C followed by an immediate ramp-down to room temperature. The very low and not usual substrate temperature (75-85 ^{o}C) used for the GeSn growth was chosen in order to avoid precipitation and / or segregation of Sn, since it is known that Sn has low solubility in Ge (≈ 0.5%, see **Section I.2.**). At IHT, the lowest temperature for growing Ge for device applications is 330 ^{o}C, which corresponds to a compromise between having enough crystal quality for devices and low energy consumption, important aspect for industry production. Further, to improve the crystalline quality, annealing treatment is typically used. To produce the reference sample, #0, (sample without Sn content), the growth ended after the growth of the Ge buffer layer. **Figure IV.1** shows a scheme of the sample structure, thickness and substrate temperature used for the growth. **Table IV.2** provides a list of all samples and the respective distinctive parameters.

The second and third group of samples (GeSn/Si series and Ge/Si series respectively) was grown after the study of the first set, thus already having a preliminary knowledge of the GeSn system and some information concerning the Sn

effect on the Ge lattice. The GeSn/Si group comprises a series of samples with regular stacked multilayers containing multiple layers (n = 1-10) of GeSn self-assembled dots, while the Ge/Si group comprises a series of samples with regular stacked multilayers containing multiple layers (n = 1-10) of Ge. The last group it was taken as reference since no Sn is present in these samples. Both series of samples were grown using similar conditions in order to investigate the Sn influence on the structural properties of the samples. The Si (100) substrates were placed inside the MBE-II system chamber and heated in situ to 900 ^{o}C for 5 minutes to remove the native SiO_2 layer on its surface by thermal desorption (see **Section II.2.3.1.**). This cleaning treatment was followed by the growth of 50 nm of Si (buffer layer), at 500 ^{o}C with a growth rate of 1 Å/s, to cover remaining surface contaminants and to smoothen the surface (see **Section II.2.3.2.**). The different temperature used for the substrate preparation, as also the different buffer layer used, as compared with the GeSn films has been described in detail in **Section II.2.3**, and corresponds to a more refined recipe.

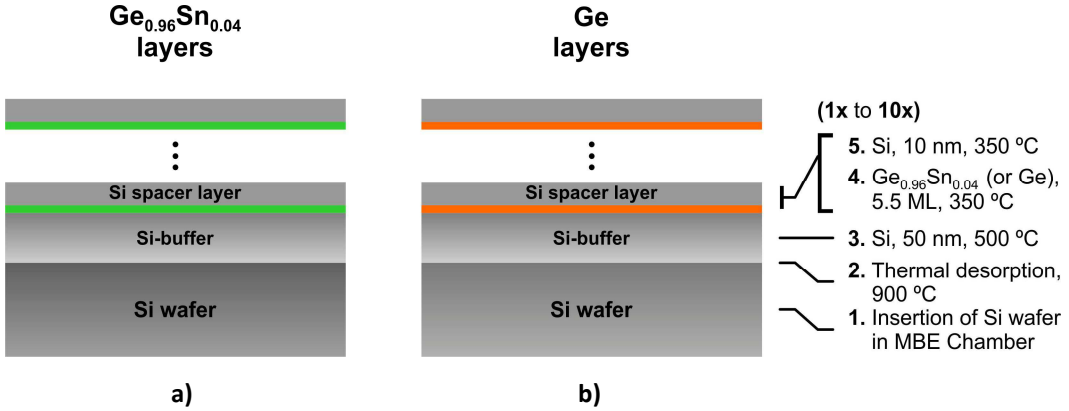

Figure IV.2: Illustration scheme of the a) GeSn/Si and b) Ge/Si samples and respective growing steps.

Table IV.2: Brief description of two groups of the multilayers samples.

Series	Sample	Nº of stacks
GeSn/Si	#1	1
	#2	2
	#3	3
	#4	4
	#5	10
Ge/Si	#1	1
	#2	2
	#3	4
	#4	10

The GeSn/Si series comprises stacks of one, two, three, four and ten layers of 5.5 ML of $Ge_{0.96}Sn_{0.04}$ separated by a 10 nm thick Si spacer layer (5 samples). In order to avoid the Sn precipitation, the substrate temperature was kept at low and constant temperature of 350 ^{o}C, for all the layers and samples of this GeSn/Si series. According to literature **[IV.1]**, the growth of Si layers at such low temperature, when used as cap layers for Ge dots, preserve the dot geometry and reduce the material intermixing. The GeSn layers were grown using a growth rate of 0.097 Å/s, while the Si spacer layers had a growth rate of 1 Å/s. The composition of the 5.5 MLs of $Ge_{0.96}Sn_{0.04}$ was achieved by a precise control of the Ge and Sn fluxes.

The reference samples, *i.e.*, those of the Ge/Si series are composed of stacks of one, two, four and ten layers of 5.5 ML of Ge separated by a 10 nm thick Si spacer layer (4 samples), were grown also at a constant temperature of 350 ^{o}C. The Ge was grown with a growth rate of 0.087 Å/s and the Si growth rate was 1 Å/s, as in the GeSn/Si samples. The ≈ 10 % difference in the growth rate between Ge and GeSn layers is not expected to have an influence on the layers' morphology **[IV.2, IV.3]**.

Figure IV.2 provides a schematic representation of the two groups of samples and the fabrication steps. Details of all MBE growth proceedings and calibrations can be found in **Section II.2**. **Table IV.2** provides the list of samples and the respective distinguishing parameters.

IV.2. Sample Characterization

As usual in the materials science, a large number of characterization techniques are employed since they give complementary informations. Even so, for some of these samples, with very small amount of the material of interest (GeSn), it was a challenge to get enough information to be able to distinguish the effects of, for instance, Sn atoms' inclusion in the lattice. Although several characterization techniques were attempted, only few provided insightful results.

IV.2.1. GeSn Thin Films

The structural characterization of these samples was performed by using the optical profilometry, TEM, AFM, RBS, XRD and μ-Raman scattering spectroscopy (presented in **Section IV.3**)**.** A JEOL 2010F field emission gun TEM was used to analyse the samples crystalline quality. AFM measurements were carried out in air, with a Veeco Dimension Icon, in tapping mode using Si cantilevers, to study the samples surface. RBS analyses were carried to determine the Sn content in the GeSn layers. XRD using a Cu radiation source was used to study the samples microstructure and to determine the strain (if present). μ-Raman scattering experiments were performed at room temperature in a back scattering geometry using the Raman System 2 and 3 described in **Section III.8.1.** Among the techniques used, the RBS, XRD and Raman spectroscopy, which results are presented in the following sections, provided the most useful information.

IV.2.1.1. Morphological Characterization by TEM

The TEM study was performed in the cross-sectional configuration. **Figure IV.3** shows two cross-sectional TEM images of two samples having different Sn content, #7 (Sn content of 1.35%) and #12 (Sn content of 4.2%).

As expected for films grown by MBE, the TEM images demonstrate the epitaxial growth of the layers. Furthermore, no amorphous phase for these two samples was observed. As expected, some threading dislocations are seen, which appear due to the high lattice mismatch between the different layers: Ge/GeSn and Ge/Si interfaces. A detailed analysis of the TEM images indicates that most of the dislocations observed in the GeSn layer come from those pre-existing in the virtual Ge(100) substrate through the GeSn/Ge interface. Furthermore the dislocations observed, for both samples, are located in the Ge buffer layer close to the interface between the Si wafer and the buffer layer, as it is expected from Ge thin films (or with high content of Ge) grown on a Si wafer. It is seen that the first 10 to 15 nm of the Ge buffer layer show a higher density of dislocations as compared to the reminder of the Ge buffer (see **Figure IV.3a**). Beyond this initial zone of defects, there is a region of perpendicular propagation of the dislocations up to the top surface of the sample. The concentration

of dislocations in the GeSn film and in the Ge buffer layer is similar despite the very low temperature used to grow the GeSn layer (in general, the lower the temperature, the lower the kinetic energy of the adatoms and the higher the density of defects). This indicates that the lattice constant of the GeSn layer is similar to that of the Ge buffer layer and their mismatch does not generate more dislocations. Then, it can be concluded that dislocations density in the GeSn layers for the Sn content up to 4.3 % strongly depends on the Ge buffer layer quality for these growth conditions.

The samples have similar roughness at the Ge-Si and GeSn-Ge interfaces as obtained by AFM and TEM. The roughness of the interface GeSn-Ge is similar to the Si wafer. However, at the top surface, while similar for both samples, the roughness is much higher. This roughness increase is, most likely, a direct consequence of the annealing step during the samples growth. The annealing provides energy for the surface reconstruction, reducing then the number of vacancies and other defects. The result is a crystalline quality improvement of the layers at the expense of the higher roughness at the surface. Peak-to-valley values between 20 nm and 40 nm were measured in the top layers by TEM. AFM roughness results are presented in **Table IV.3**. Furthermore, the TEM study did not reveal any evidence of Sn segregation at the surface or precipitation.

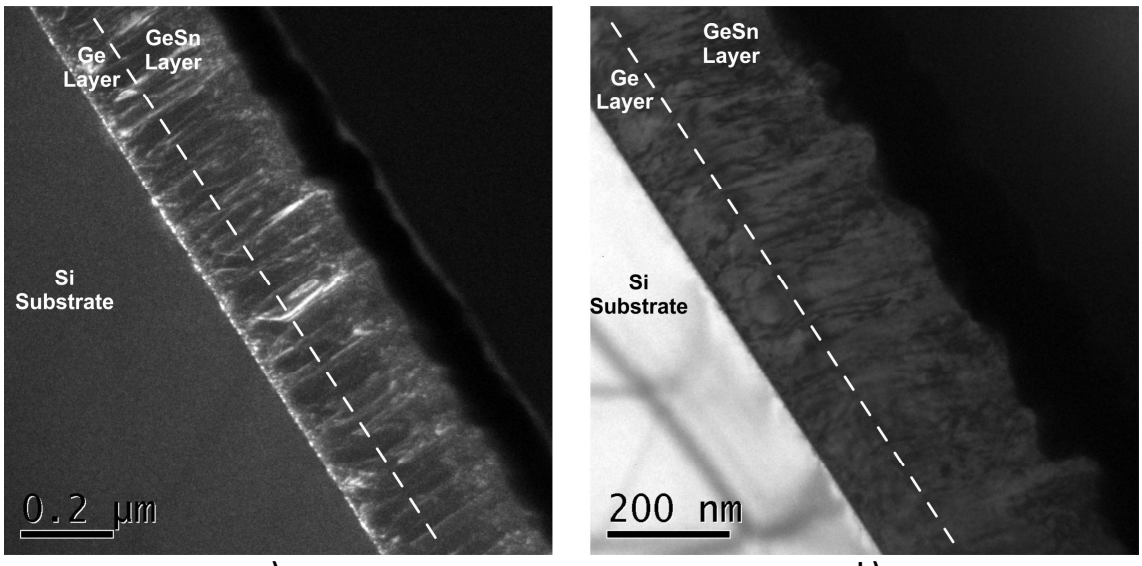

Figure IV.3: Transversal cross-section TEM images of GeSn thin film samples: a) #7 (Sn = 1.36 %) with high contrast; b) #12 (Sn = 4.30 %). The interface between the buffer layer and the GeSn film is indicated with a dashed line.

Table IV.3.: Surface roughness obtained by AFM in a scanning area of (5 x 5) µm^2.

Sample	Average (nm)	Peak-to-Peak (nm)
#0	0.91	9.8
#2	1.47	22.6
#5	1.65	16.6
#8	1.23	11.5
#12	7.60	65.4

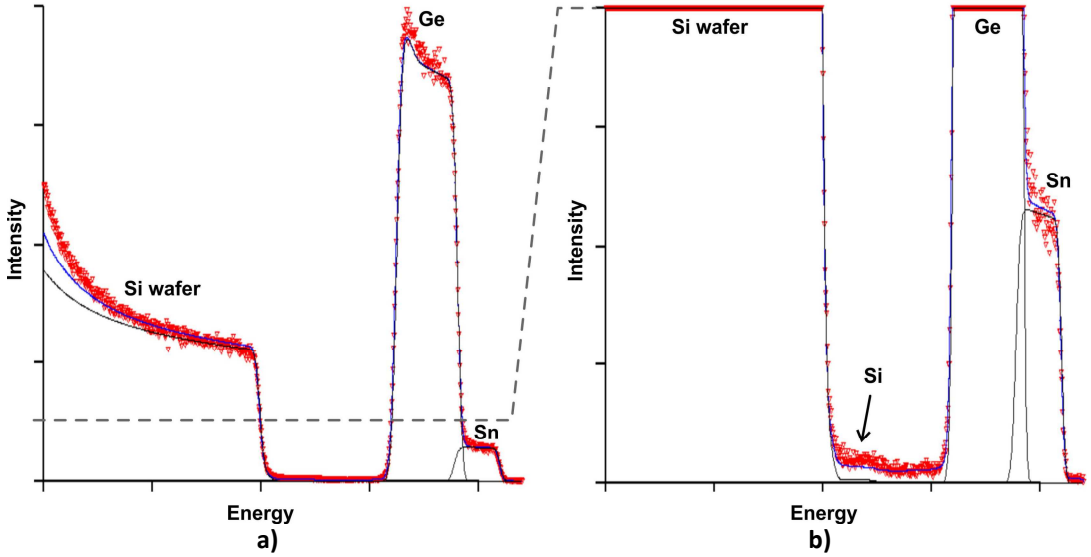

Figure IV.4: a) RBS spectrum of sample #10 (red dots), individual fits (black solid curves) and total fit (blue curve); b) magnification to provide a better visualization of the Sn zone. Grey dashed line indicates the same intensity. The observed Si, Ge and Sn signals are from the deposited film (not Si substrate). Ge is present in both layers of the film (Ge buffer and GeSn layer), as well as Si (due to crucible contamination). Sn is present only in the GeSn layer.

IV.2.1.2. Morphological and Compositional Characterization by RBS

The Sn concentration in the samples (in the GeSn layer), was obtained by Rutherford Backscattering Spectrometry. The RBS measurements were made using an ion beam of $^4He^{++}$ with the energy of 2 MeV, as described in **Section II.4.4**.

Figure IV.4 shows the RBS spectrum of GeSn thin film #10 with the respective fitting curves. The experimental results and the fits were provided by the ITN (Lisbon). **Table IV.4** shows a compilation of the results obtained by fitting the RBS spectra for five samples. **Table IV.5** provides the Sn content values for all samples obtained by means of interpolation, based on the RBS measurements and on the Sn cell temperature. The maximum Sn content obtained was 4.3%, which is below the minimum necessary fraction of tin predicted to obtain direct band gap (see **Section I.2**).

It is necessary to mention that RBS has low sensitivity for detecting Si when its content is low and in the presence of heavier atoms, as is the case of these samples. The results of Si are only indicative and in fact they should be very similar for all the samples, since the Si atoms present in the samples come from the Si crucible used to keep the Ge atoms in the Ge electron gun (see **Section II.2.1.3.**). As Ge melts, a small amount of the crucible is incorporated in the Ge mass. It is so that a value between 1 to 2% of Si can be incorporated in the Ge mass.

Table IV.4: GeSn films composition, obtained by fitting the RBS data. Values inside brackets were fixed in the fitting.

Sample	Layer	Ge (at. %)	Sn (at. %)	Si (at. %)	Layer thickness (nm)
#2	GeSn Ge-buffer Substrate	98.62 99.99 (0.0)	**0.15** (0.0) (0.0)	1.23 0.01 (100.0)	216 123 19820
#5	GeSn Ge-buffer Substrate	99.06 98.97 (0.0)	**0.55** (0.0) (0.0)	0.40 1.03 (100.0)	238 113 33736
#8	GeSn Ge-buffer Substrate	97.71 100.0000 (0.00)	**1.68** (0.0) (0.0)	0.61 - (100.0)	237 118 31196
#10	GeSn Ge-buffer Substrate	96.24 100.00 (0.0)	**3.34** (0.0) (0.0)	0.42 0.00 (100.0)	246 88.4 23314
#12	GeSn Ge-buffer Substrate	94.34 100.00 (0.0)	**4.30** (0.0) (0.0)	1.35 0.0002 (100.0)	281 113 25000

Table IV.5: Sn content (at. %) in the GeSn layers for all the samples. Values marked with * were obtained by interpolation.

Sample	Sn (at. %)
#0	0
#1	0.11*
#2	0.15
#3	0.20*
#4	0.38*
#5	0.55
#6	0.96*
#7	1.36*
#8	1.68
#9	2.39*
#10	3.34
#11	3.73*
#12	4.30

IV.2.1.3 Structural Characterization by XRD

It is possible to characterize the epitaxial layers by the analysis of the diffraction peaks originating from two independent crystal planes of the lattice. This analysis allows to determine the lattice constant of the cubic structure (or the difference between the lattice constants of Ge and GeSn layers) and the strain. These parameters characterize entirely the epitaxial structure. For our system (GeSn), the lattice planes (004) and (224) are commonly used. The XRD geometry usually employed to study epitaxial semiconductors with cubic structure is the geometry known as 'one-dimensional $\omega/2\theta$ rocking curve' of a certain diffraction plane.

Using the angular position of the diffraction peak originated by the (004) planes and applying the Bragg's law it is possible to determine the inter-planar distance, d_{004}, and therefore the perpendicular (or out-of-plane) lattice constant:

$$a_{\perp} = 4d_{004}\,. \qquad \textbf{\{IV.1\}}$$

The parallel (or in-plane) lattice constant, $a_{\parallel}$ (with respect to the substarte surface) can be determined by the analysis of the diffraction peak (224), and the parallel deformation can be calculated afterwards. However, the used XRD setup only allowed the $\theta/2\theta$ configuration, then the analysis of the (224) planes was not possible. To overcome this, the parallel lattice constant, $a_{\parallel}$ was determined indirectly as explain below.

The parallel (or in-plane) and perpendicular (or out-of-plane) deformation (with respect to the substarte surface) can be defined by lattice constant of the deformed layer and the relaxed lattice constant (a) as **[IV.4, IV.5]**:

$$\varepsilon_{\perp} = \frac{a_{\perp} - a}{a}, \qquad \textbf{\{IV.2a\}}$$

$$\varepsilon_{\parallel} = \frac{a_{\parallel} - a}{a}. \qquad \textbf{\{IV.2b\}}$$

For a fully relaxed solid solution, the lattice constant usually follows a linear dependence upon the composition. This dependence (known as Vegard's law) has been verified for Sn_xGe_{1-x}, $a(x) = a_{\mathrm{Ge}}\left(1 + 0.147x\right)$ **[IV.6]**. For the ultimate case of fully strained solid solution (so called pseudomorphic strain caused by the elastic force induced by the substrate with the same crystal structure but with a different lattice

constant) one can expect $a_{\parallel} = a_{\text{substrate}}$ and, if the substrate is not strained germanium, $a_{\text{substrate}} = a_{\text{Ge}} = 0.5658\ \text{nm}$. However, if the substrate (or the buffer layer) is deformed itself, $a_{\parallel}$ is not known *a priori*.

The deformations (*i.e.* the out-of-plane and in-plane components of strain tensor) can be related using the elasticity theory for the case of pseudomorphic strain (see **Appendix C**) as:

$$\varepsilon_{\perp} = -2\frac{C_{12}}{C_{11}}\varepsilon_{\parallel}, \qquad \textbf{\{IV.3\}}$$

where C_{11} and C_{12} are the elastic constants of the material. For the calculations the values of pure germanium were used (since the samples have a very low amount of Sn), which yields $\varepsilon_{\perp} \approx -0.7\varepsilon_{\parallel}$. In this way, by using the second relation, **{IV.2}**, information concerning the parallel (in-plane) lattice constant has been obtained.

A Cu source with emission $K\alpha_1$ (0.154056 nm) and $K\alpha_2$ (0.154439 nm) was used for the XRD measurements. The XRD configuration used for this study was the standard $\theta/2\theta$ scan and the calibration was made with crystalline bulk silicon. Important information is taken by analysing the (004) diffraction peak of Ge, which appears at $2\theta \approx 66^{o}$. Since the used XRD system does not have a monochromator, the XRD spectra have the contributions of the two Cu wavelengths ($K\alpha_1$ and $K\alpha_2$) for each diffraction peak. The XRD analysis was performed in the 2θ region between 24^{o} and 69^{o}. In this 2θ range, the peaks have high intensity, then a variation of the peak position and, consequently, of the inter-planar distance, with the increase of the Sn content, if exist, become evident.

Figure IV.5a shows the XRD spectra for some samples showing peaks in two different 2θ ranges, namely, the diffraction peaks of Ge are seen around 66 ^{o} and the diffraction peaks of GeSn appear between 65 ^{o} and 65.5 ^{o}.

Samples with low Sn content (samples #2 and #5) exhibit only 2 peaks, corresponding to the $K\alpha_1$ and $K\alpha_2$, related diffraction on Ge atomic planes. The low content of Sn is not enough to originate different peaks from the Ge-Ge and the Ge-Sn interatomic distances. Moreover, the absence of Ge-Sn related peaks for these samples indicates that the Ge lattice is little affected by the presence of Sn (for these small Sn contents).

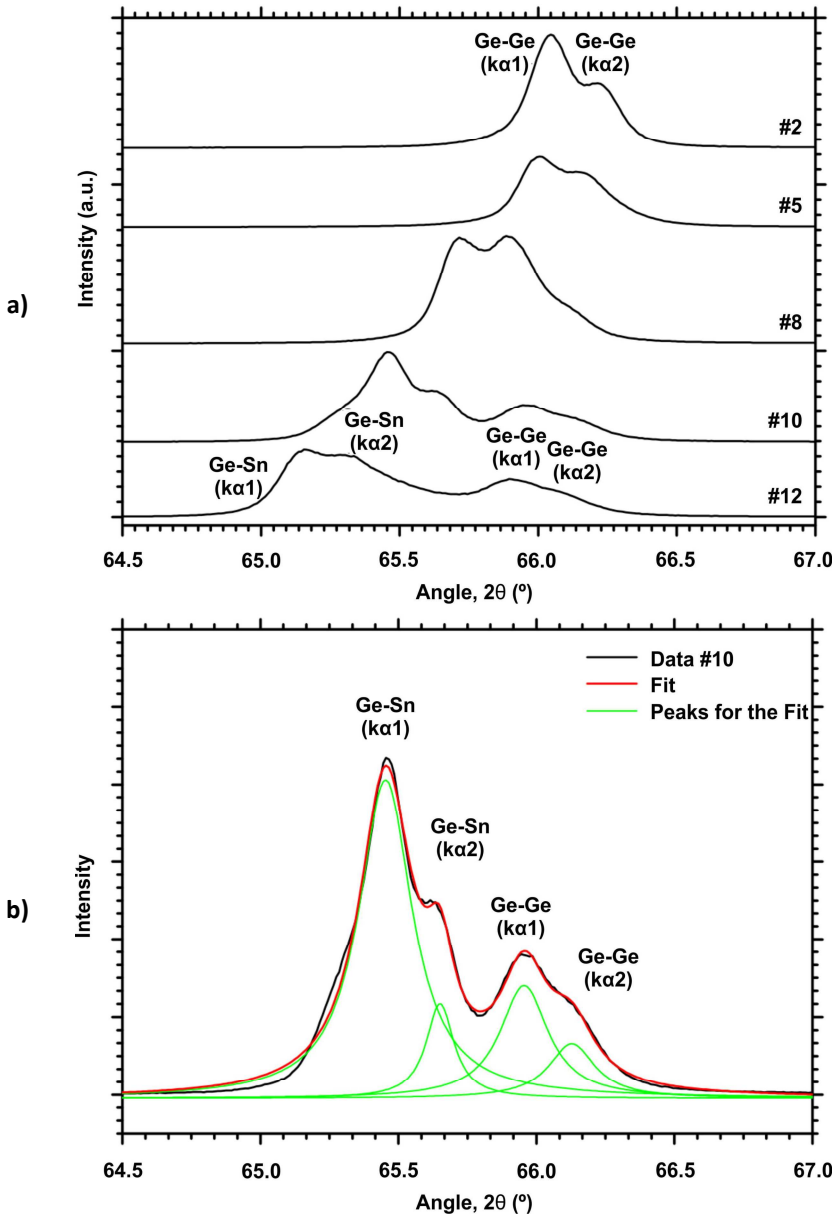

Figure IV.5: a) Measured XRD spectra of five GeSn thin film samples (#2, #5, #8, #10 and #12); b) experimental XRD spectrum of #10 sample (black solid line), the corresponding fit (red solid line) and the individual Lorentzian peak functions used for the fit (green solid lines). The peaks result from the cristalographic planes (004).

The Ge-Sn diffraction peaks are only visible for the samples with high Sn content. As the Sn content increases in the GeSn layer, up to four peaks become visible (samples #8, #10 and #12). Again, some peaks correspond to the $K\alpha_1$ wavelength and others to the $K\alpha_2$. The two peaks at lower angles correspond to the Ge-Sn interatomic distances and the two peaks at higher angles come from Ge-Ge interatomic distances. Sample GeSn #8 only features 3 peaks, since the peaks for Ge-Sn ($K\alpha_1$) and Ge-Ge ($K\alpha_2$) are overlapped.

The XRD spectra were fitted using a Lorentzian function for each peak, as can be seen in **Figure IV.5b**. After the fit and using the 2θ value for the maximum intensity of each peak, the lattice parameters were obtained. **Figure IV.6** shows the peak position for Ge-Ge and Ge-Sn bonds versus the Sn content present in the GeSn samples. The peak position of Ge-Ge is nearly constant only with a small variation to lower angle values, *i.e.*, this behaviour indicates a small increase of the lattice parameter with the increase of Sn. One can observe that at lower Sn content, the Ge-Ge lattice constant is smaller than the one of a bulk Ge crystal, indicating that the layers are not fully relaxed but close to this. For the GeSn peak position, the changes in the lattice parameter are more significant, being directly related to the increase of the Sn content. Since α-Sn lattice constant is bigger than that of Ge, the increase of Sn content in the GeSn layer will increase the lattice parameter of the solid solution.

By the angular position of the diffraction peak originated by the planes (004), obtained after the XRD fit and using the Bragg´s law, it is possible to determine the inter-planar distance, d_{004}, and then the out-of-plane interatomic distances using **Equation {IV.1}**. A weighted average of the Ge-Ge and Ge-Sn interatomic distances provides an estimate of the GeSn lattice constant, $a_{GeSn} \cong a_{Ge-Ge}(1-x)+a_{Ge-Sn}x$. **Figure IV.7** shows the behaviour of the out-of-plane lattice parameter as a function of Sn content (obtained by RBS). For comparison, it is also shown the Vegard´s law prediction using the Sn content obtained by RBS.

The data shown in **Figure IV.7** demonstrate an increase in the out-of-plane lattice parameter for the GeSn layer with the increase of Sn content. It is also seen that the measured out-of-plane lattice constant for each Sn content, is lower than the corresponding Vegard´s one, indicating that the studied GeSn layers are almost fully relaxed.

Using the lattice constant obtained by Bragg's law and the lattice constant of Ge, the strain perpendicular to the GeSn layer has been calculated using **Equations {IV.2}**. Since it was not possible to study the reflection of the planes (224), because of the XRD geometry setup used, the out-of-plane strain was obtained indirectly by using **Equation {IV.3}**. **Table IV.6** summarizes the obtained values for the out-of- and in-plane lattice parameters, the Vegard's law prediction, and the out-of- and in-plane strain components.

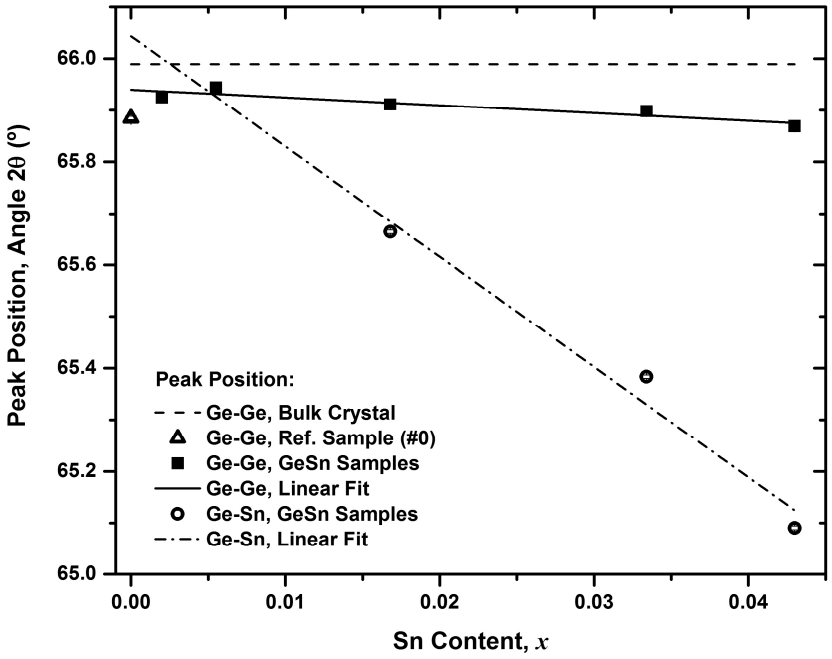

Figure IV.6: Angular position and respective our-of-plane lattice constant of the diffraction peak originated by the (004) planes for Ge-Ge and Ge-Sn interatomic distances with the Cu Kα_1 wavelength as a function of the Sn content for the GeSn samples.

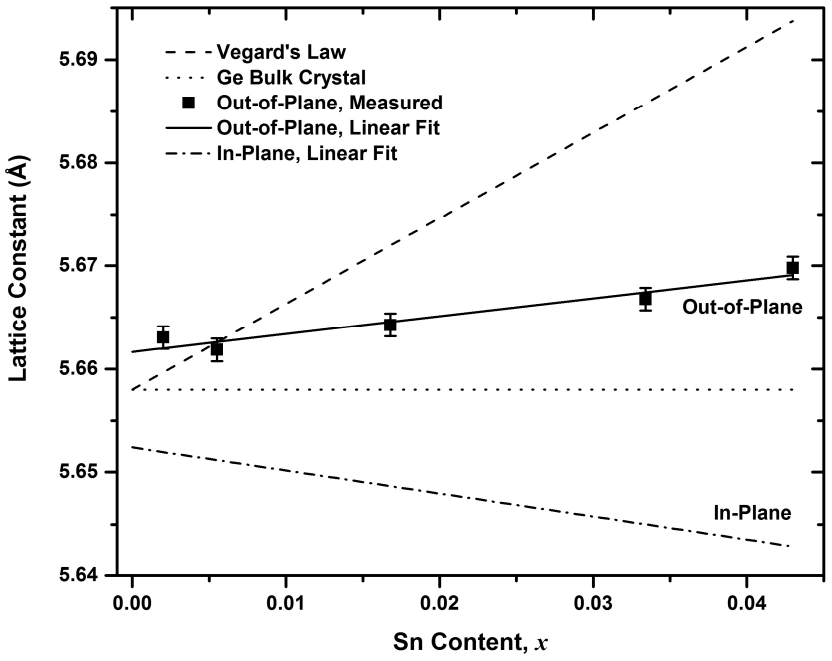

Figure IV.7: Out-of-plane lattice constant (obtained from the XRD data) for the studied GeSn samples with the linear fits for the out-of- and in-plane lattice constant and lattice constant predicted by Vegard's law.

Figure IV.8 shows the strain (perpendicular and parallel) values obtained for samples #3, #5, #8, #10 and #12 as a function of Sn content. The results show that the variation of the in-plane and out-of-plane deformation components have similar behaviour, although with opposite signs, *i.e.*, the in-plane strain decreases as the Sn content increases and an increase is seen for the out-plane strain. This is what one should expect according to Poisson's law for pseudomorphic strain. Overall, the values of strain detected are small, and the samples are close to be relaxed.

Table IV.6: Out-of- and in-plane lattice parameters and strain components for the GeSn layers grown on a virtual Ge substrate on top of a Si substrate. The strain values of the GeSn layer are calculated with respect to bulk germanium. The value of the lattice parameter for a fully relaxed GeSn layer is also given based on Vegard's law.

Sample	$a_{\perp}$(Å)	$a_{\parallel}$ (Å)	a_{Vegard} (Å)	$\varepsilon_{\perp}$ (%)	$\varepsilon_{\parallel}$ (%)
#0	5.6660	5.6465	5.6580	0.142	-0.204
#3	5.6630	5.6508	5.6597	0.089	-0.128
#5	5.6619	5.6525	5.6626	0.068	-0.097
#8	5.6643	5.6476	5.6720	0.129	-0.185
#10	5.6668	5.6473	5.6858	0.132	-0.189
#12	5.6698	5.6414	5.6937	0.205	-0.294

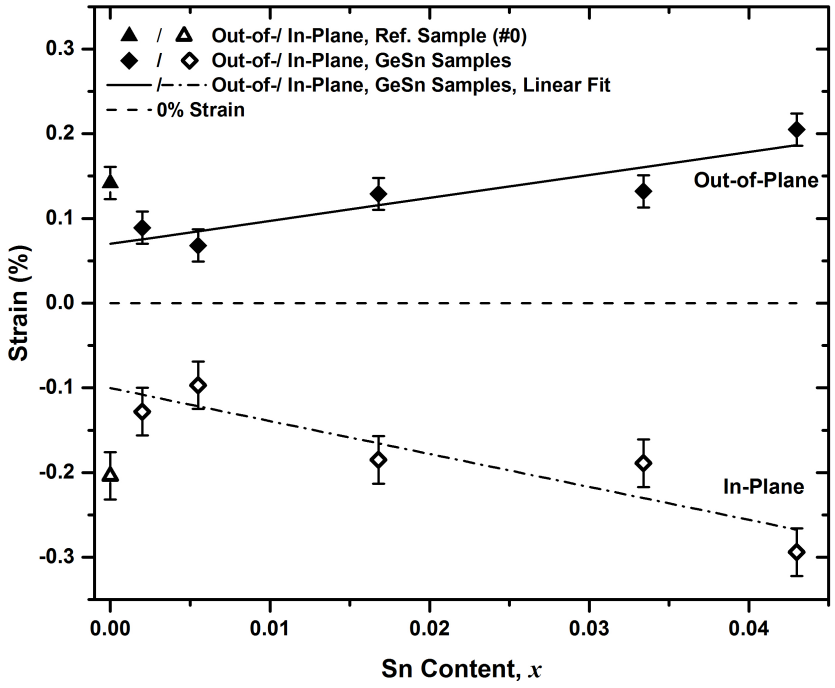

Figure IV.8: Out-of-plane (obtained from the XRD data) and in-plane (calculated) strain components due to lattice mismatch between the GeSn film and the Ge buffer for GeSn samples #3, #5, #8, #10 and #12.

IV.2.2. Multilayer GeSn/Si and Ge/Si samples

The structural characterization of these samples was performed using a JEOL 2010F field emission gun TEM, working in both HR-TEM and STEM modes. This study was complemented by AFM analyses and μ-Raman spectroscopy (presented in **Section IV.3**). AFM measurements were carried out in air, with a Veeco Dimension Icon, in tapping mode using Si cantilevers NT-MDT CSG10 with a cone angle lower than 22^{o}. The typical curvature radius of the tip was less than 10 nm and a constant force of 0.1 N/m was used. The measurements were performed for all samples of the GeSn/Si series to obtain information about the density, shape and size of the dots and also covered area.

IV.2.2.1. Morphological Characterization by TEM

Figure IV.9 (left hand side) shows a TEM cross-sectional image of the sample of the GeSn/Si series with the largest number of quantum dot layers (10 × GeSn)**.** A TEM cross-sectional image of the corresponding reference sample (sample of Ge/Si series with 10 Ge layers (10 × Ge)) is also shown for comparison (right hand side of **Figure IV.9**). Similar images were obtained for the samples with 4 and 2 layers of GeSn and Ge. **Figure IV.9** clearly shows some qualitative differences between the two samples as far as dot formation is concerned. The brighter spacer layers (Si), which separate the GeSn layers (and Ge ones) which appear darker in the figure, can clearly be seen in both samples. Furthermore, it is seen that the GeSn/Si sample shows the presence of dots, whereas no dots are seen in the "equivalent" Ge/Si sample. It is known **[IV.7, IV.5]** that the critical wetting layer (WL) thickness at which the dot nucleation occurs is influenced by the strain and substrate temperature. Since the incorporation of Sn atoms into the Ge lattice, in the case of GeSn films, induces a larger lattice mismatch with respect to the Si substrate, compared to the case of Ge on a Si substrate, it is expected to observe a higher strain in the GeSn/Si system than in the Ge/Si one. This increase of strain in the GeSn system should originate a decrease of the critical WL thickness for the dot formation, at a given growth temperature, when Sn is present in the lattice, as compared to samples without tin. Furthermore, it is also known that the critical WL thickness increases when the growth temperature decreases **[IV.8]**. Then, based on the strain and temperature effect on the WL thickness and on the obtained

results, it can be concluded that the growth parameters (mainly substrate temperature) used were appropriate for the dot formation in the GeSn/Si system but not for the Ge/Si reference sample where the critical WL thickness was not reached (for the growth temperature of 350 °C).

In addition, from **Figure IV.9** (left hand side) it can be seen that the spatial positions of GeSn dots show a vertical correlation between the 2nd and the 4th layer. Indeed, such a vertical correlation of the dot positions was also observed in multilayer Ge dots samples, when the Si spacer layer thickness is below the critical value **[IV.9].** The origin of this correlation is attributed to the inhomogeneous strain field induced by buried dots, which define preferential positions for the subsequent dot nucleation **[IV.10]**. After the 4th layer, it is seen that the layer structure changes, namely the WL is no longer planar and the dot morphology becomes different. These differences are mainly due to the occurrence of local material accumulation. Since *e.g.* optical characteristics are influenced by the homogeneity of the layers, such a morphological change could be detrimental to device operation and need to be understood in order to be avoided.

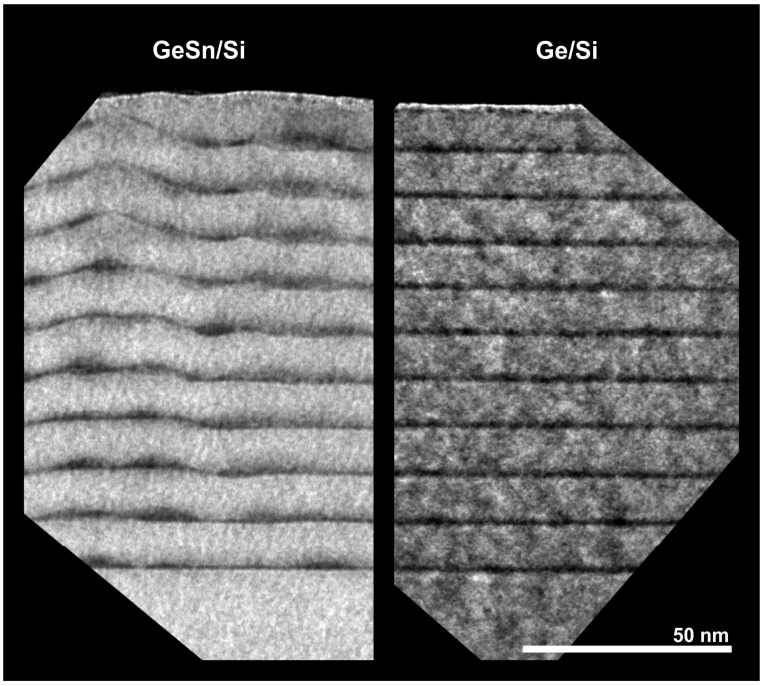

Figure IV.9: Cross-sectional TEM images of the GeSn/Si and reference Ge/Si samples with 10-stacks. For the GeSn sample the formation of several self-assembled dots can be observed, whereas the Ge sample does not show any dots. The Figure is aligned vertically from bottom to top according to the growth direction.

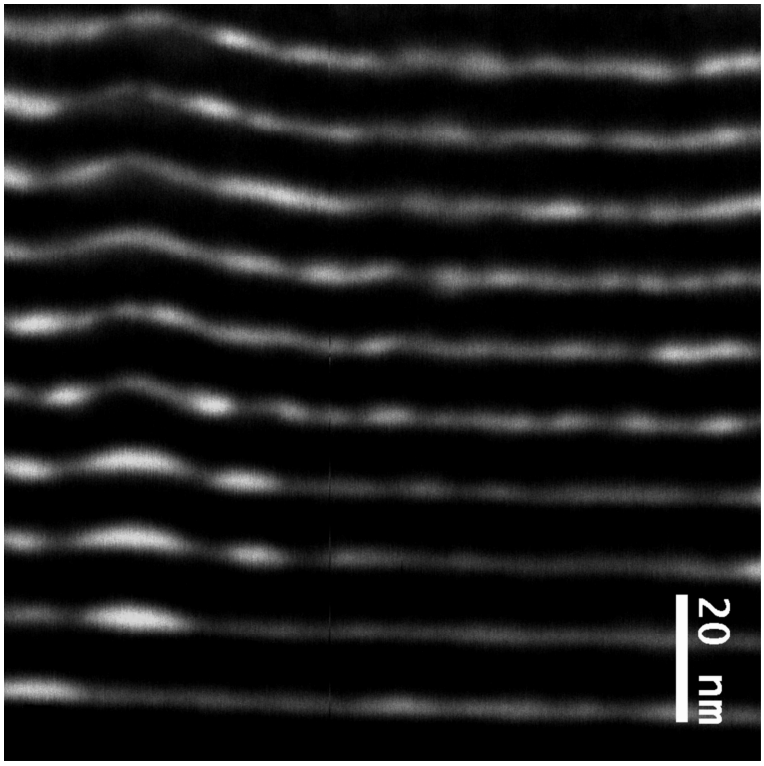

Figure IV.10: Cross-sectional STEM image of the 10-stacks GeSn sample. Contrast in the image mean: darker regions correspond to Si (lighter atoms) and brighter regions correspond to Ge and Sn (heavier atoms). The figure is aligned vertically from bottom to top according to the growth direction.

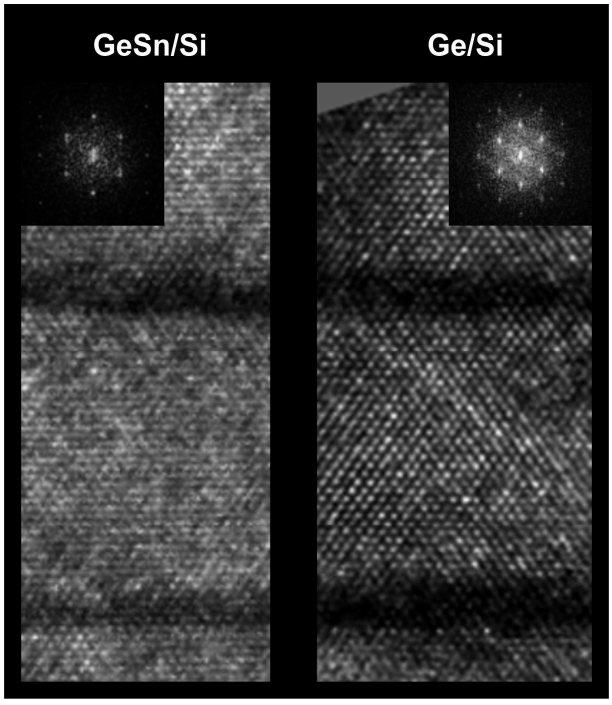

Figure IV.11: Cross-sectional HR-TEM images of 4-stacks samples (GeSn and corresponding Ge reference sample). The inserts are the Fourier transform of the respective images. The figure is aligned vertically from bottom to top according to the growth direction.

Figure IV.10 show the STEM image of the sample whose TEM is presented in **Figure IV.9** (left hand side), in which is also seen the presence of the wetting layer (WL) between dots layers. The same result was obtained for all the samples (n × GeSn/Si). This seems to indicate that the dots are formed according to the Stranski-Krastanov mechanism, as is the case for pure Ge self-assembled dots **[IV.11]**.

Figure IV.11 shows the HR-TEM images obtained for the 4-stacks GeSn/Si sample and corresponding Ge/Si reference sample. By analysing the HR-TEM images it was possible to estimate the WL thickness. For the GeSn/Si sample it was obtained a WL thickness of ≈ 8 ML (measured in the vicinity of a dot, in the lowest layer of the stack). It is interesting that, despite using the same growth conditions for both series, a higher WL thickness of ≈ 10 ML was measured for the Ge/Si reference sample. In both cases, the measured WL is thicker than the target 5.5 ML of material deposited, indicating that material intermixing occurred (Si, Ge and Sn). The difference in the measured WL thickness between the GeSn/Si and the Ge/Si samples can be explained by comparing to the case of self-assembled Ge dots grown on Si, where dot nucleation is accompanied by the transfer of about 1 ML of Ge from the WL to the dots **[IV.1]**. One can expect a similar material transfer to take place during the dot nucleation in the GeSn/Si system, which leads to a reduction in the WL thickness as compared to the Ge/Si reference system, where no such dot nucleation occurs.

The TEM and HR-TEM images do not reveal any segregation or precipitation of Sn. The Fourier Transform for the HR-TEM image contains similar information to an X-ray diffractogram. The inset in **Figure IV.11** shows the Fourier transform of the HR-TEM image for the GeSn/Si and Ge/Si layers (4-stacks) showing a diamond structure for both samples, as well as good crystallinity. However, the addition of Sn can influence surface processes and, therefore, the composition of the dots. Brehm *et al* **[IV.12]** have shown that the composition of Ge dots strongly changes along the growth direction. In particular, even for low growth temperatures, some intermixing between Ge and Si is always present.

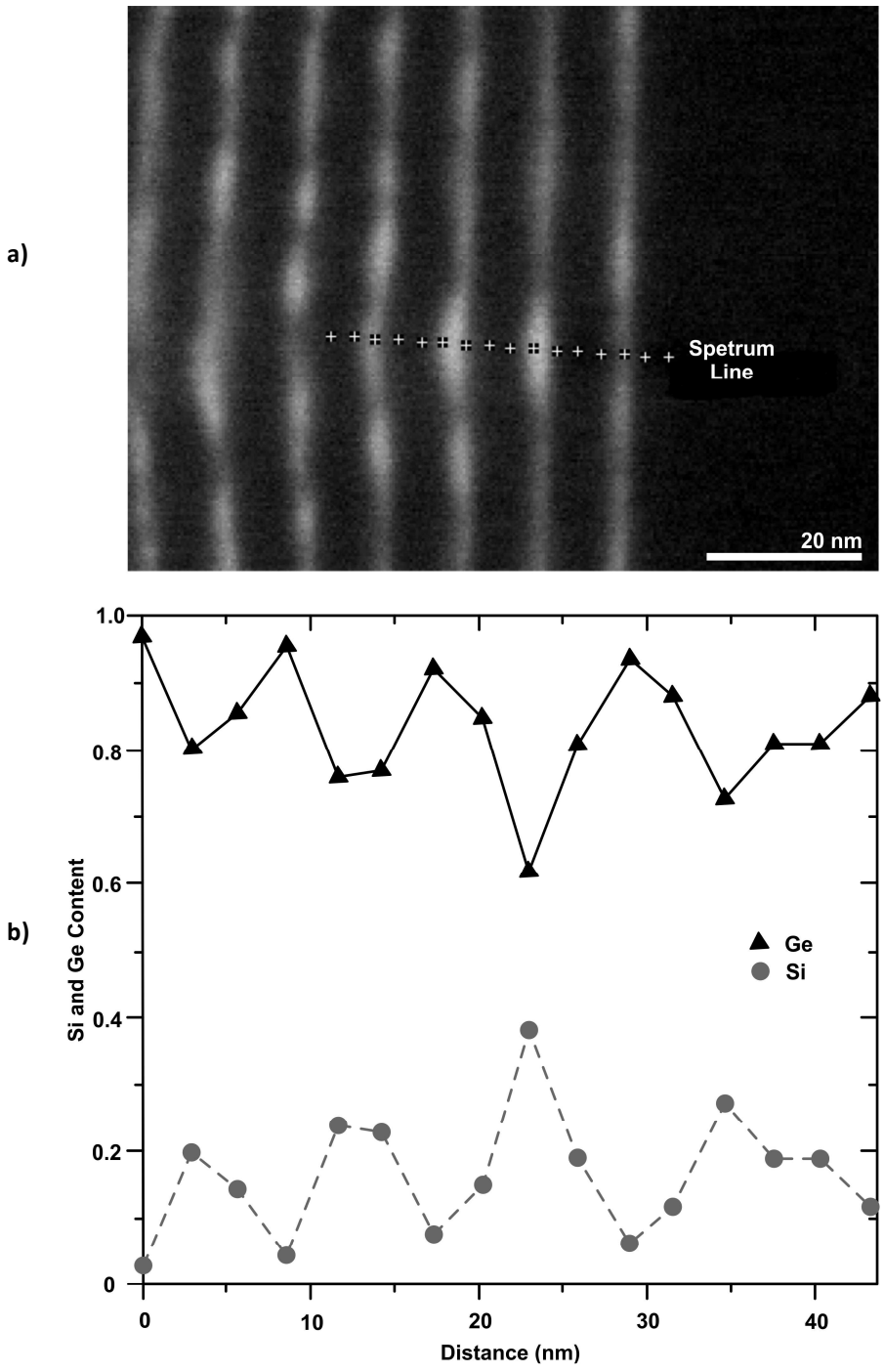

Figure IV.12: a) Cross-sectional EDS image of the 10-stacks GeSn sample; b) EDS spectrum obtained on the line shown in (a) for Si (dots and dashed line) and Ge (triangles and solid line). The Sn concentration is too small to be detected. The image and the plot are aligned horizontally from right to left according to the growth direction.

More information concerning the dots was obtained by STEM analysis of the 10-stacks GeSn/Si sample (shown in **Figure IV.10**). The STEM cross sectional image reveal: (i) a higher concentration of GeSn (bright zones) in the dots than in the WL (darker zones); (ii) inside the dot, the GeSn concentration is higher in the centre than in the borders. From Raman measurements, discussed below, it can be concluded that intermixing with Si also takes place in these samples. Concerning the non-uniform GeSn concentration distribution inside the dot, due to the low Sn concentration it was not possible to make conclusions based on the HR-TEM and STEM study. A composition analysis with sub-nanometre resolution would be useful to investigate such a position-dependent intermixing but the necessary technical means for this were not available.

The TEM-EDS analysis of the same 10-satck GeSn/Si sample, along the line marked with crosses, shown in **Figure IV.12** reveals, as expected, some intermixing between GeSn and Si. The EDS scan shows that a higher concentration of Ge is present in the dots than in the spacer layers, although, because of the horizontal drift (small) of the EDS scan and the low spatial and intensity resolution a precise numerical evaluation is not possible.

IV.2.2.2 Morphological Characterization by AFM

The AFM images (250 x 250 nm^2) of all the GeSn/Si samples reveal that the topmost layer of each sample contains dots, as seen in **Figure IV.13**. However, both the density and the shape of the dots change with the number of sample stacks. For the 1-stack sample all the dots have a nearly spherical shape, changing to a truncated quadrangular pyramid with the base aligned along the (110) direction as the number of stacks increases (see **Figure IV.13** and **IV.14**). Indeed, it is seen that the dots shape becomes less spherical (compared to the 1-stack sample) for the 2-stack sample and for the 3-stack sample, in which dots with round and quadrangular pyramid shapes can be clearly seen to coexist with spherical ones (in their uppermost layer). However, for the 4-stack sample, only quadrangular pyramid shaped dots are seen in the uppermost layer, and the 10-stack sample contains, in addition, some big 'dots'. A more detailed analysis of the dots with truncated quadrangular pyramid shape observed in the uppermost layer of the 4-stacks GeSn/Si sample shows than the dots have a sidewalls

with angles in the range 17 – 19°, corresponding to (130) crystal planes (see **Figure IV.14**). It is noted that this differs from the 11° slope of the {105} side facets that are usually observed in pyramidal "hut cluster" Ge islands on Si **[IV.13 – IV.15]**. However, in the GeSn/Si system, studied in this work, the dots shape (on the top layer) is not only a consequence of the top most layer, as in the "hut cluster" Ge islands, but also depends on the material accumulation in the layers below, as evidenced by the change in dots shape (in the topmost layer) as a function of the total number of dot layers below. Furthermore, comparing the results obtained in our GeSn/Si with the literature results for Ge/Si system with quantum dots, one can conclude that the material accumulation and dot shape must be related with the presence of Sn, since in a Ge/Si system the dot shape does not change considerably with the number of stacks.

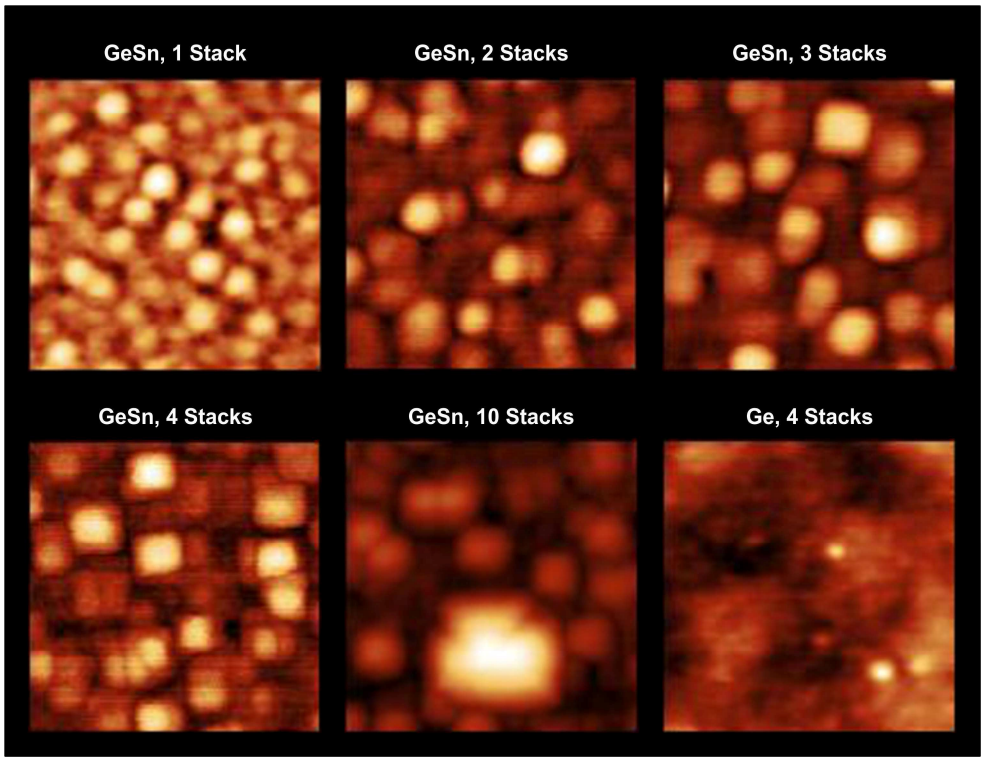

Figure IV.13: AFM images with 250 x 250 nm^2 of the surface of the GeSn samples (1- to 10-stacks) and the Ge reference sample with 4-stacks. A transition from round dots to square pyramid like dots with the top truncated is seen with the increase of the number of stacks in the GeSn samples. Domes are visible only in the 10-stacks GeSn sample. The Ge reference sample shows a much lower density and smaller size of dots than the ones present in the GeSn samples. The height (provided by the colour) is not normalized between images. The pyramid like dots are aligned with the lattice structure of the substrate.

As already mentioned, the AFM image of the 10-stack GeSn/Si sample (see **Figure IV.13**) shows the presence of few large dots with a height of ≈ 15 nm. As can be inferred from the STEM image of the same 10-stack sample (**Figure IV.10**), the larger dots seen by AFM in the uppermost layer are not formed in the same way as GeSn-rich dots within one layer. Rather they are the result of local material accumulation in the layers below. Excluding these large ones, the dots in the layers can be classified according to their height (irrespective of their shape) in two categories: (i) "pre-dots", with a height between one and three lattice constants (in this case, 4 to 12 ML for diamond lattice) and (ii) "dots", which are higher than three lattice constants. The "pre-dots" observed in these samples do not necessarily have a square base, differing therefore from the reported "pre-pyramids" observed as the first stage of morphological evolution of Ge dots identified in **Refs. [IV.15, IV.16]**. This difference can either be attributed to the very low growth temperature used (350 °C compared to a minimum growth temperature of 550 °C used in **[IV.15]**) or to the presence of Sn.

The dot density and size was estimated from the AFM measurements. **Figure IV.15** shows, for all GeSn samples, the average size (diameter for round dots and side length for pyramid-like ones), height and the density of pre-dots and dots per μm^2, with the respective standard deviations, as a function of the stacks number in the sample. It can be seen from **Figure IV.15** that the number of pre-dots (black squares) decreases as the number of stacks increases, reaching a minimum density for the 3-stack sample. For a higher number of stacks their density slightly increases and seems to stabilize (the 4- and 10-stack samples have similar dot densities). Concerning the pre-dots size it first increases with the number of stacks, reaching a maximum for 2- and 3- stacks, then decreases slightly and stabilizes for larger numbers of stacks (see **Figure IV.15**). Concerning the dots (red circles), it is seen that their density increases as the number of stacks increases ($n \geq 2$). The same behaviour, with the number of stacks, is observed for the dots height, while the height of the pre-dots remains almost constant (consequence of definition of pre-dot). This behaviour of the dot height is consistent with the presented TEM study (see **Figure IV.9**), as also with the vertical dot position alignment between the 2^{nd} and the 4^{th} layers, which can cause a progressive dot height increase, as observed by the AFM analysis. Concerning the dot size, a similar behaviour to the pre-dot is observed: a first increase with increasing number of stacks and then a size stabilization for 2 or more layers.

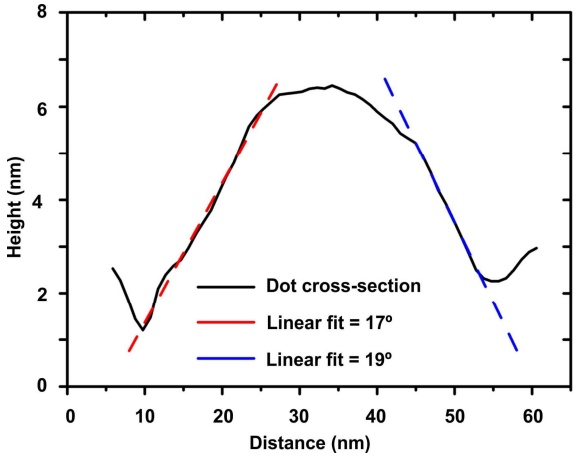

Figure IV.14: Cross-section of a dot of 4-stacks GeSn sample with a shape of trunked pyramid like (black solid line). Linear fit of both opposite "walls" of the pyramid (dashed lines). The linear fits have an angle coincident to (130) Miller planes.

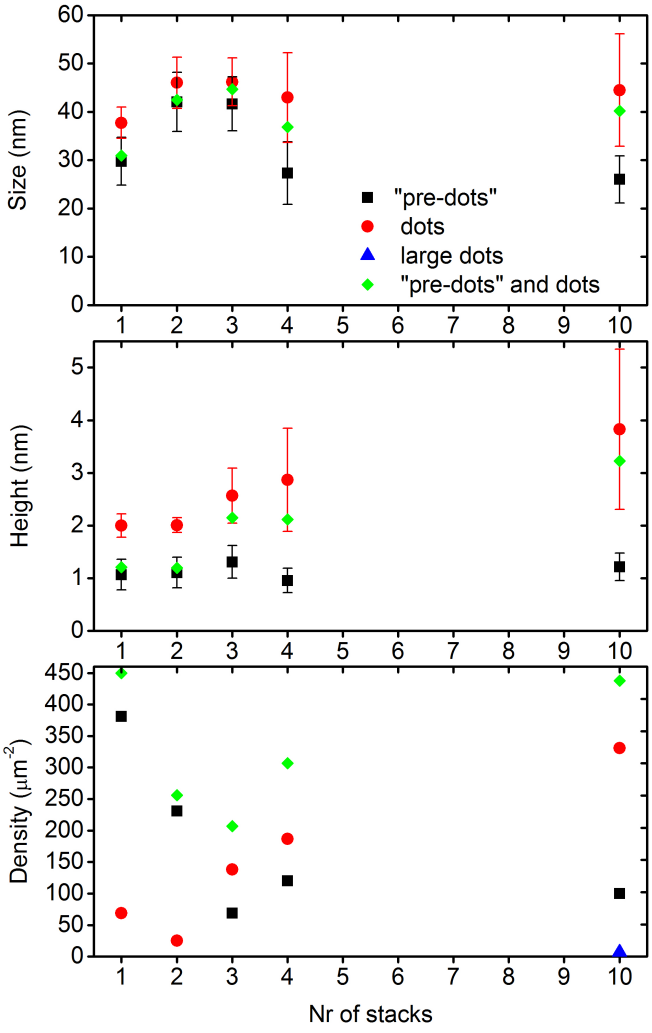

Figure IV.15: Influence of the number of stacks on the average size (a), height (b) and density (c) of dots, "pre-dots" and large dots.

Since it is reported in the literature that Ge dots in multilayers of Ge in Si can acquire a lateral ordering of Ge islands **[IV.17],** it was performed the following study. The nearest-neighbour angular distribution function was calculated, by computing the angles obtained from the lines connecting the centre of each island to its nearest neighbours with respect to (110) direction, for several hundred islands in each sample of the GeSn/Si series and the result was a homogeneous distribution of angles, which means that lateral ordering does not take place in any of these samples.

IV.3. Raman Spectroscopy Results

In **Section III.8.1** a short description of the micro-Raman scattering setups used for the samples measurements is provided. From these setups, the systems named as Raman system 2, 3 and 4 (see **Table III.4** in **Section II.8.1**) were used to study the samples of Group IV elements reported in this chapter. All the measurements were performed at room temperature in a backscattering geometry and calibrated using a Si wafer.

As discussed in **Chapter III**, the Raman frequency shift in semiconductor solid solutions (and alloys) is affected by compositional variation and strain **[IV.18, IV.19]**. Raman scattering experiments performed on strain-relaxed Ge-Sn solid solutions revealed that the peak frequency of the Ge-Ge phonon mode decreased linearly with the increase of the Sn content **[IV.20, IV.21].** However, different values for this linear frequency-shift coefficient are found in the literature, namely, Li *et al.* reported a value of - 68.0 cm^{-1} **[IV.20]** while later D'Costa *et al.* obtained -75.4 cm^{-1} **[IV.21]**.

Raman studies performed on pseudomorphic-strained Ge-Sn solid solutions also revealed a linear relationship between the Ge phonon peak position and the Sn concentration **[IV.6].** Here one should expect the Ge-Ge Raman phonon mode peak to appear at higher wavenumbers compared to that of strain-free (relaxed) alloys. This blue shift is believed to be caused by a compressive biaxial strain. Yet, the experiment yielded a composition shift coefficient of -76.8 cm^{-1} **[IV.6]**, which is close to the abovementioned results obtained for *relaxed* alloys by Li **[IV.20]** and D'Costa **[IV.21]**.

Despite this apparently controversial behaviour, the two effects on the Ge-Ge phonon peak position, namely (i) local environment changes with composition and (ii) pseudomorphic strain, indeed must be present, as known for other (better studied)

systems, such as Si-Ge. In principle, they can be separated by combining the results of Raman scattering and XRD measurements. The net effect can be written formally as:

$$\Delta\omega_{Ge-Ge} = \Delta\omega_{composition} + \Delta\omega_{strain} \ . \qquad \textbf{\{IV.4\}}$$

It is expected that the first term, $\Delta\omega_{composition}$ should be always negative because its nature is similar to the phonon confinement effect in nanocrystals. Indeed, a cluster of Ge atoms surrounded by much heavier tin atoms that do not support the Ge-Ge vibration mode looks like a small size nanocrystal and the allowed wavevector values for it should be finite. As known for nanocrystals **[IV.22],** such a finite size effect leads to a downward shift of the confined phonon frequencies because of the negative curvature of the bulk phonon dispersion curves. It is hard to estimate this effect analytically but numerical lattice dynamic calculations do allow for evaluation of the composition dependence of this effect (see **Section IV.5**).

In contrast, the second term in **Equation {IV.4}** may have any sign. Within the validity of the Vegard's law, the magnitude of $\Delta\omega_{strain}$ should depend linearly on the in-plane strain $\varepsilon_{\parallel}$ according to (see **Appendix C** for details):

$$\Delta\omega_{strain} = -\frac{2}{3}\omega_0\varepsilon_{\parallel}\left[(3\gamma+\beta)-\frac{C_{12}}{C_{11}}(3\gamma-2\beta)\right] \qquad \textbf{\{IV.5\}}$$

where ω_0 is the phonon frequency for the relaxed bulk alloy, C_{11} and C_{12} are the elastic constants, γ is the Grüneisen parameter (the logarithmic derivative of the phonon frequency with respect to the volume change under hydrostatic pressure) and β is a similar parameter corresponding to shear strain, introduced in **[IV.23]**:

$$\gamma = -\frac{(p+2q)}{6\omega_0^2}; \qquad \beta = \frac{(p-q)}{2\omega_0^2}, \qquad \textbf{\{IV.6\}}$$

where p and q are the anharmonic deformation parameters introduced and measured in **Ref. [IV.23]**. In **Equation {IV.5}** it has been assumed that the strain components $\varepsilon_{\perp}$ and $\varepsilon_{\parallel}$ are related by **Equation {IV.3}** (pseudomorphic strain).

Thus, systematic Raman studies of a set of GeSn samples with different composition, extended to other fundamental vibration modes can provide information about the composition, the presence of different kinds of bonds (Ge-Sn, Ge-Ge, Ge-Si, *etc*.) and the strain.

IV.3.1. GeSn Thin Films

Raman spectra of GeSn thin films measured in this work are shown in **Figures IV.16** and **IV.17.** In particular, **Figure IV.17** shows a fragment of the Raman spectra of (the highest Sn content) sample #12 obtained with 532 and 633 nm excitations, normalized to the Ge-Ge phonon mode intensity. According to the structure of this sample, it is expected to observe several features, namely:

1) Ge-Ge phonon mode (near 300 cm^{-1}), either from the GeSn layers or from the Ge buffer layer or both;
2) TO-LO phonon mode of the Si substrate (521 cm^{-1});
3) a vibration mode due to the Ge-Sn bonds (around 260 cm^{-1});
4) a weak band around 185 cm^{-1}, tentatively attributed to Sn-Sn vibration mode.

It can be seen in **Figure IV.17a** that the Ge-Sn vibration mode is considerably enhanced for the excitation wavelength $\lambda_{exc} = 633$ nm, compared to 532 nm. The sample in this case was a relatively thick GeSn film ($d \approx 200$ nm). With the literature data for the absorption coefficient of germanium ($\alpha_{\mathrm{Ge}}(633\ \mathrm{nm}) \approx 1.4\times10^{5}\ \mathrm{cm}^{-1}$, $\alpha_{\mathrm{Ge}}(532\ \mathrm{nm}) \approx 5.6\times10^{5}\ \mathrm{cm}^{-1}$ **[IV.24]**), one can find that $\alpha_{\mathrm{Ge}} d << 1$ for any of these wavelengths and it is only a thin near-surface layer that contributes to the scattering, while the buffer layer (pure germanium) can not influence it in a λ-dependent way.

It was noticed that there is a critical point called E_1 resonance in the band structure of pure germanium, located at 2.11 eV **[IV.25]**, which corresponds to the wavelength $\lambda =$ 588 nm. With Sn doping, the band gap energies shrink due to the crystal lattice expansion and this critical point should shift to larger wavelengths, thus approaching the excitation wavelength $\lambda_{exc} =$ 633 nm and moving away from the other excitation lines used in this work. It explains the enhancement of the Raman signal related to the Ge-Sn vibration mode observed with the 633 nm excitation, which therefore was used for all samples.

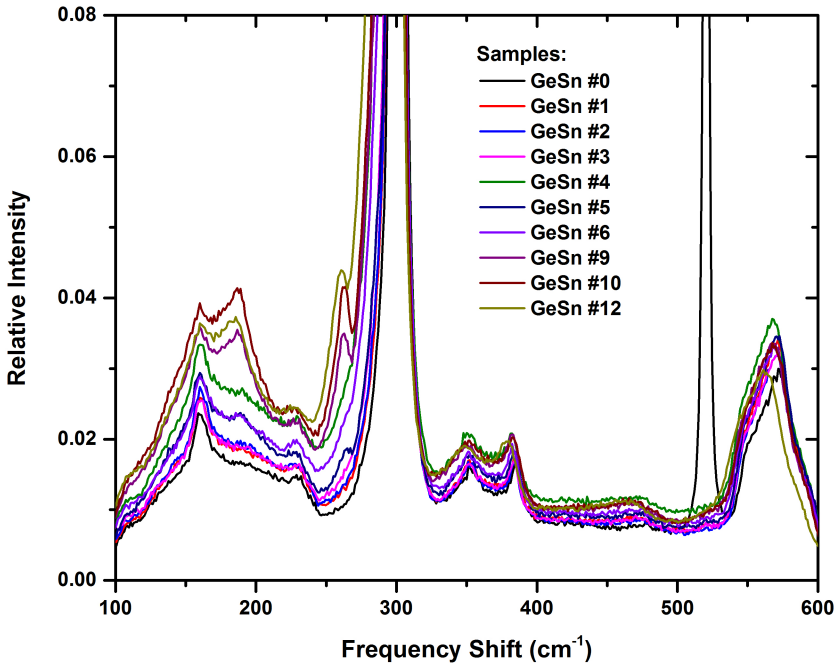

Figure IV.16: Raman spectra of all GeSn thin film samples. The measurements were performed with Raman system 3 (see Chapter III.8.1) using the polarized laser excitation 633 nm, with ≈ 25 mW optical power on the samples' surface and a total acquisition time of 2400 s.

Figure IV.17b shows three Raman spectra obtained with the Raman System 3 setup (see **Section III.8.1.**) with the same acquisition conditions, for three different samples: bulk c-Ge (Ge wafer), reference film sample of germanium without Sn (#0) and the GeSn sample #12. The reference sample exhibits the Ge-Ge phonon mode (the only one seen for the c-Ge) and also the bulk Si-Si phonon mode from the substrate (≈ 520 cm^{-1}). This happens because this sample is thinner since it does not have the GeSn layer (only the Ge buffer layer is present, see **Figure IV.1a**). Also seen is the Raman phonon mode at about 385 cm^{-1} assigned to the Ge-rich SiGe alloy. The presence of this Ge-Si phonon mode indicates that probably related with the silicon used to contain the germanium in the e-gun (see **Section II.1**).

Concerning the Raman spectrum of the GeSn sample #12, besides the Ge-Ge and the Ge-Si phonon modes it also exhibits two peaks that are absent in the other samples' spectra, namely, peaks at ≈ 260 and ≈ 185 cm^{-1}. The peak at ≈ 260 cm^{-1} is attributed to Ge-Sn vibrations and the other one is, probably, related to the tin optical phonon (Sn-Sn phonon mode). The Sn-Sn Γ point phonon peak position for α-Sn is ≈ 195 cm^{-1}. In Ge-Sn alloys with low tin content, the Sn-Sn mode can originate from compact clusters of tin atoms that are not big in size. It originates mechanical

confinement effects that result in a shift of the mode to lower frequencies. As mentioned above, it is similar to phonons confined in nanocrystals **[IV.22]**. However, D'Costa *et al.* **[IV.21]** expressed a different opinion, based on their polarized Raman spectroscopy studies: this feature may be just a disorder activated longitudinal acoustic (DALA) mode.

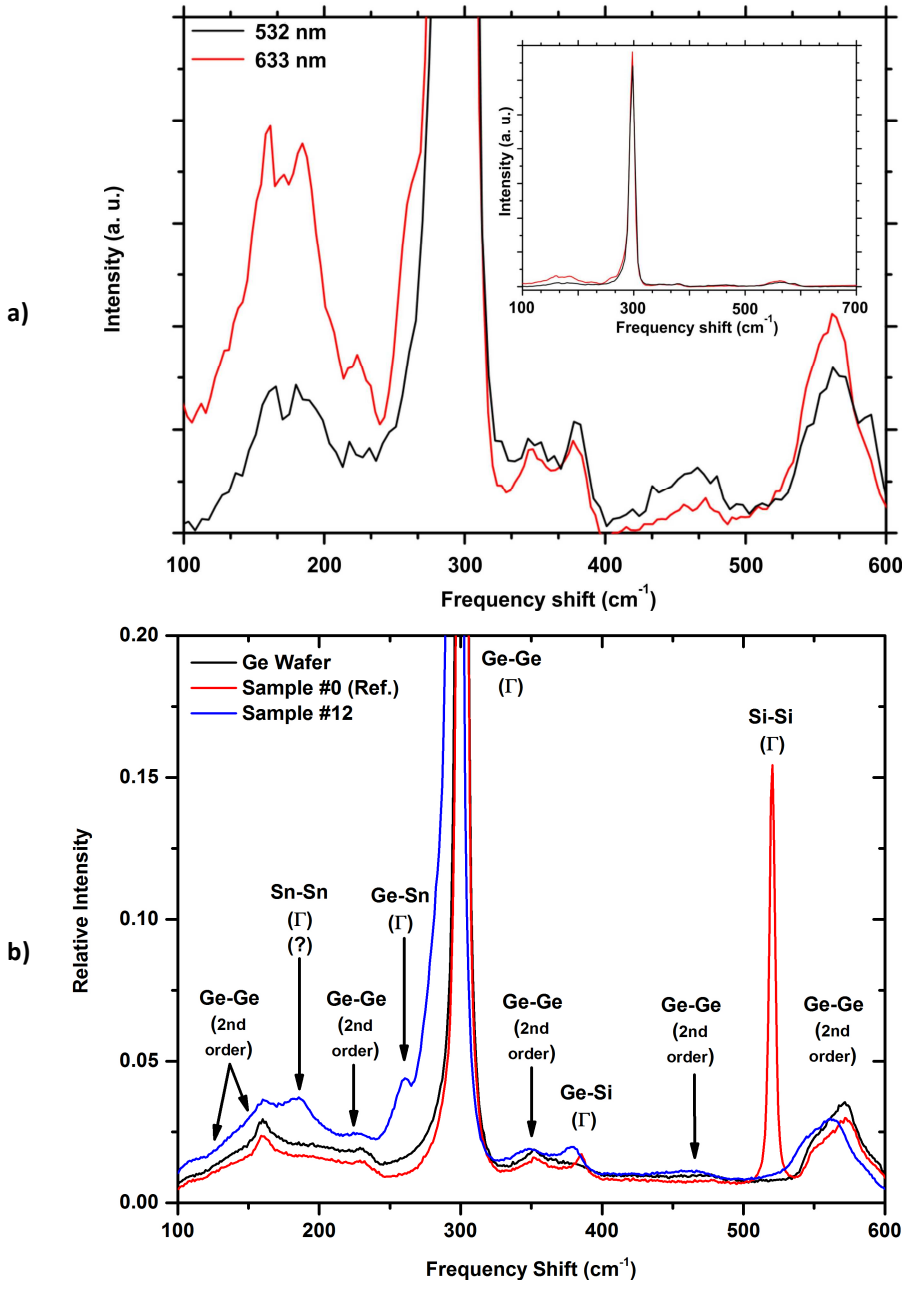

Figure IV.17: a) Raman spectra of sample #12 recorded with 532 and 633 nm excitation using Raman System 2 (see Chapter III.8.1) with ≈ 4 mW optical power on the samples' surface; b) Raman spectra of the reference sample #0 (Ge), #12 (GeSn) and Ge wafer recorded with 633nm excitation using Raman System 3 (see Chapter III.8.1) with ≈ 25 mW optical power on the samples' surface. The Ge-Sn peak is more intense with 633 nm excitation.

It has been reported in the literature that the intensity of the Ge-Sn Raman mode increases with the Sn content **[IV.6**, **IV.21]**. Furthermore, several changes are seen in what concerns the Ge-Ge Raman phonon mode: the peak position shifts to lower wavenumbers, the phonon mode becomes broader and its shape modifies. The Ge-Ge phonon mode becomes increasingly asymmetric with a tail towards the low wavenumbers. These changes in the Ge-Ge phonon mode, namely the downshift and the broadening can be explained with the 'spatial-correlation' model **[IV.26]** in which the broadening is attributed to compositional fluctuations and local disorder. The same can be observed in Ge-Si samples **[IV.27]**.

IV.3.1.1. Ge-Ge Phonon Mode Details

Figure IV.16 clearly shows the effect of the increase of the Sn content on the tail of the Ge-Ge phonon mode. One can also notice the increase of the Ge-Sn phonon mode intensity with the increase of the Sn content. **Figure IV.18a** shows in detail the Ge-Ge range, in which the shift in the Ge-Ge peak position is clearly seen for the samples with different Sn content. The Raman spectra have been fitted using Voigt functions for each peak, and the obtained peak position for the Ge-Ge phonon mode is plotted as a function of the Sn content in **Figure IV.18b**, showing a shift to lower wavenumbers as the Sn content increases.

However, the Raman analysis is not linear, since in this kind of material, as mentioned before, two contributions are present, the compositional (*i.e.* mass and bond strength) effect and the macroscopic strain one. These two contributions have the opposite influence on the Ge-Ge peak position. It is known that with the increase of the Sn content the peak position of the Ge-Ge peak should move to lower wavenumbers (red shift), while under compressive strain the peak should appear at higher wavenumbers (blue shift). The measured Raman peak position of the Ge-Ge phonon mode is the result of these two competing effects and its position with respect to the case of pure Ge can be expressed as a sum of two terms: (i) a local contribution, mostly due to the very different masses of the host and impurity atoms, and (ii) a contribution due to the bond distortions as the system tries to accommodate the lattice constant mismatch between the Ge-Sn layer and the underlying Ge substrate (pseudomorphic strain effect), as given by **Equation {IV.5}**.

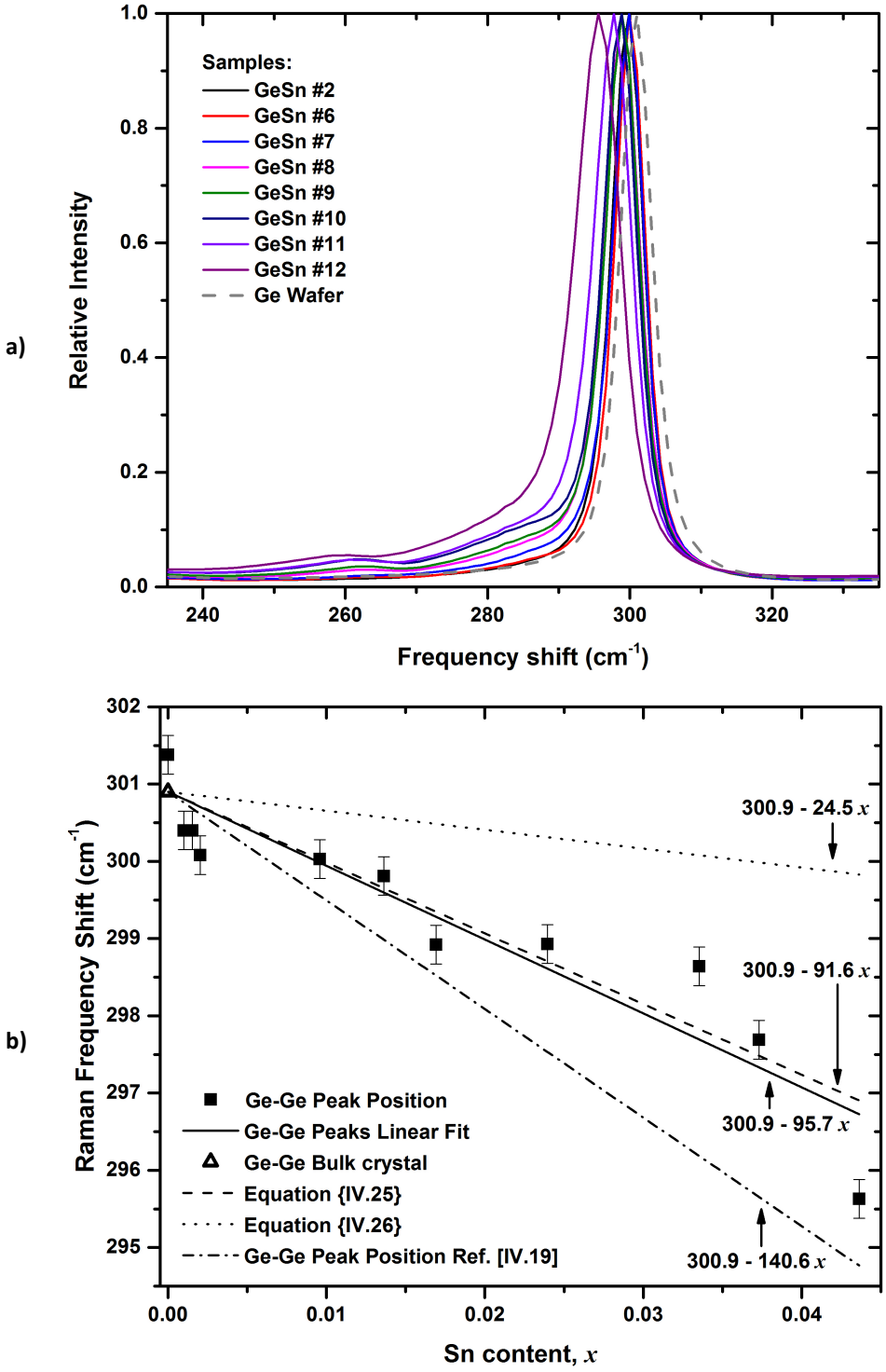

Figure IV.18: a) Detail of the Raman spectra of the GeSn samples (with Raman system 3 with 633 nm excitation; see Figure IV.16) in the range of the Ge-Ge Raman phonon mode; b) peak position of the Ge-Ge phonon mode as a function of Sn content; squares are the values obtained by peak fitting, the solid line is a linear fit to the experimental data represented by the squares, the dashed line (dotted line) represents calculated peak positions for fully relaxed (subjected to pseudomorphic strain) Ge-Sn solid solutions (see Section IV.5). The dashed-doted line is the linear dependence proposed by Rojas-Lopez *et al.* [IV.6] for a fully relaxed Ge-Sn layer. The open triangle indicates the peak position for a bulk germanium crystal.

If the strain magnitude is known, for instance, from the XRD study, then it is possible, according to **Equation {IV.5},** to estimate the expected shift in the Ge-Ge phonon mode owing to the strain. For low Sn contents all these parameters can be taken as for pure germanium, *i.e.*, $\gamma \approx 1$, $\beta = 0.23 \pm 0.02$ **[IV.23]**, $C_{11} = 1.29 \times 10^{12}\,\mathrm{dyn/cm^2}$ and $C_{12} = 0.48 \times 10^{12}\,\mathrm{dyn/cm^2}$ **[IV.28]**, then **Equation {IV.5}** yields:

$$\Delta\omega_{strain} = 67.1x \quad [\mathrm{cm^{-1}}] \qquad \textbf{\{IV.7\}}$$

since $\varepsilon_{\parallel} = -0.147x$ for in-plane isomorphic strain in low x GeSn solid solutions deposited on unstrained Ge substrate. After calculating $\Delta\omega_{strain}$, the local composition contribution to the Raman band shift can be evaluated from the experimentally measured shift using **Equation {IV.4}.** The results of such separation of the two effects are presented in **Table IV.7** for all studied samples.

Table IV.7: Experimentally measured shift of the Ge-Ge Raman band, with respect to the Ge bulk phonon mode (column 3), and shift due to strain calculated by Equation {IV.5} (column 4).

Sample	Sn at.%	$\Delta\omega_{experimental}$ cm^{-1}	$\Delta\omega_{strain}$ cm^{-1}
#0	0	0.48	---
#1	0.100	-0.50	---
#2	0.153	-0.50	0.10
#3	0.204	-0.82	0.14
#4	0.380	-0.85	---
#5	0.551	-0.89	0.37
#6	0.959	-0.87	---
#7	1.362	-1.09	---
#8	1.693	-1.98	1.14
#9	2.395	-1.97	---
#10	3.353	-2.26	2.25
#11	3.731	-3.21	---
#12	4.363	-5.27	2.93

IV.3.1.2. Ge-Sn Phonon Mode

Figure IV.19a shows in detail the Ge-Sn peak for the samples with high Sn content. As before, the Raman spectra were fitted with Voigt functions and the obtained peak position is shown in **Figure IV.19b.** It is seen that the position of Ge-Sn phonon mode shifts to lower wavenumber with the increase of Sn, and this behaviour has a good linear fit with a slope higher than in the Ge-Ge phonon mode (see **Figure IV.19b**).

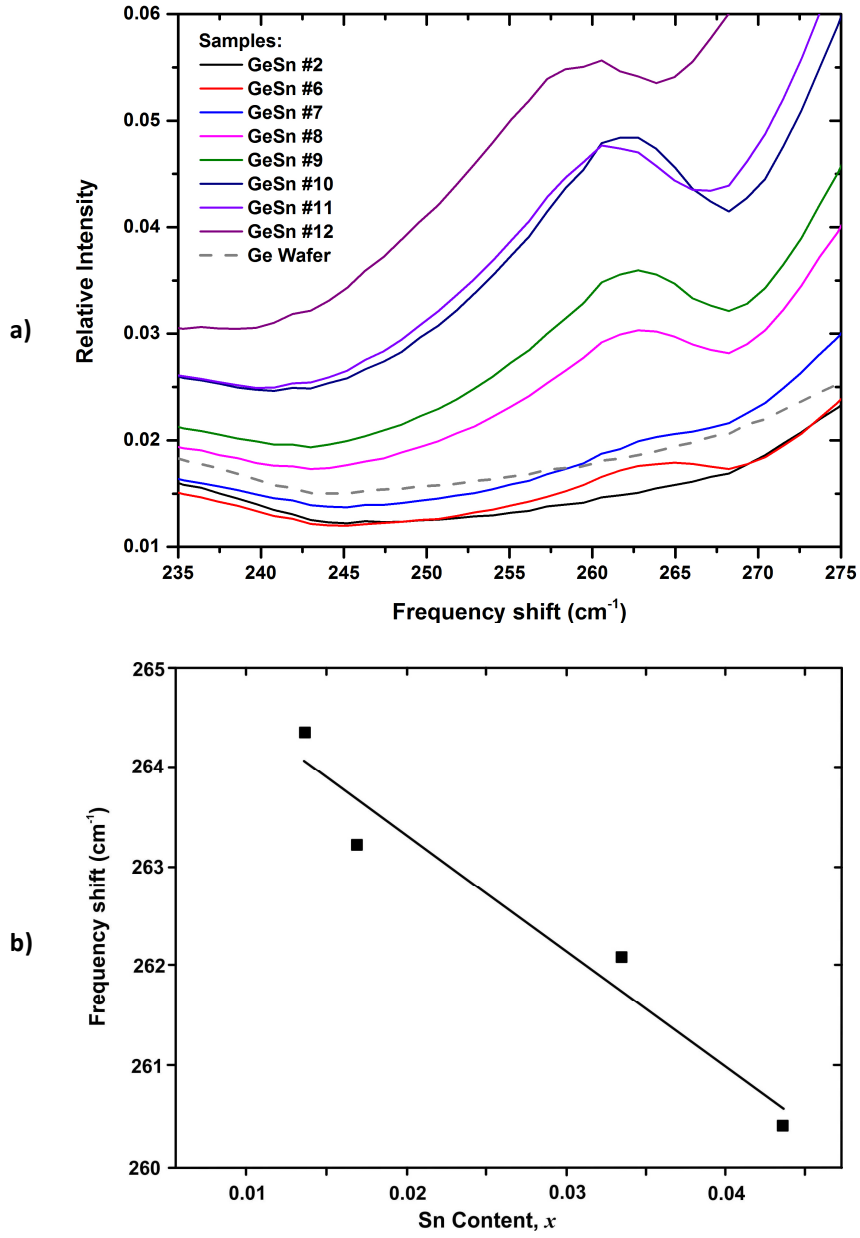

Figure IV.19: a) Detail of the Raman spectra in the range of the Ge-Sn phonon mode. b) Ge-Sn phonon mode peak position as a function of the Sn content.

IV.3.2. Multilayers GeSn/Si and Ge/Si Samples

Figure IV.20 shows the Raman spectra of all GeSn/Si multilayer samples and also of a *c*-Si sample, taken as a reference spectrum for comparison. All the samples exhibit the prominent Si optical phonon mode at 520.8 cm^{-1} as well Si related two-phonon modes, namely, 2TA (Σ) at 433 cm^{-1} and 2TA (X) at 302.5 cm^{-1}. In addition to the Si related phonon modes, the Raman spectra of the GeSn/Si samples show the characteristic Ge-Ge band at 300.7 cm^{-1} and also a phonon mode at ≈ 418 cm^{-1} which is the signature of mixed Ge-Si bonds **[IV.28 – IV.30]**. The presence of Sn is not seen directly in these samples, since no Sn-related phonon modes were detected (*i.e.* Ge-Sn, Si-Sn or Sn-Sn phonon modes **[IV.31 – IV.33]**). The absence of Sn related phonon modes can be attributed to the low amount of Sn (less than 0.3 at. % in volume) corresponding to a low overall number of Ge-Sn, Sn-Sn and Si-Sn bonds in our samples. However, even without the presence of Sn-related phonon modes, the effect of tin doping is evidenced by the changes of the peak position and shape of the Ge-Ge phonon mode, as observed and concluded in the studies of GeSn films presented in the previous section.

In Raman spectroscopy, the peak position and full width at half maximum (FWHM) values are parameters related with the sample microstructure. The former is related to the type of atom and its vibration mode and the latter reflects the crystalline quality of the sample (beyond the homogeneous broadening related to the finite phonon lifetime due to anharmonic processes, which is of the order of few cm^{-1}). Furthermore, the peak position (Raman shift) and the integrated intensity of the Raman band are the parameters that allow to compare different samples. Indeed, changes in the peak position are related to strain and/or alloy composition, while the peak area is related to the composition and short-range order of the alloy **[IV.29, IV.30]**. The observed peak position of the Si-Si (Ge-Ge) phonon mode in the studied samples is shifted relatively to the position of the corresponding phonon mode in the Si (Ge) bulk sample. As already mentioned, for this kind of materials, a shift in the peak position is usually related with composition and strain as follows: tensile strain or the influence of heavier atoms in the lattice shifts the peak position to lower frequencies

(red shift); while lighter atoms or compressive strain shifts the peak to higher frequencies (blue shift).

Concerning the Si-Si phonon mode of the alloy in the Raman spectra of these samples, it is not possible to distinguish the contributions from the LO-TO Γ-point phonon of the Si substrate, the buffer layer and the spacers (see **Figure IV.20**).

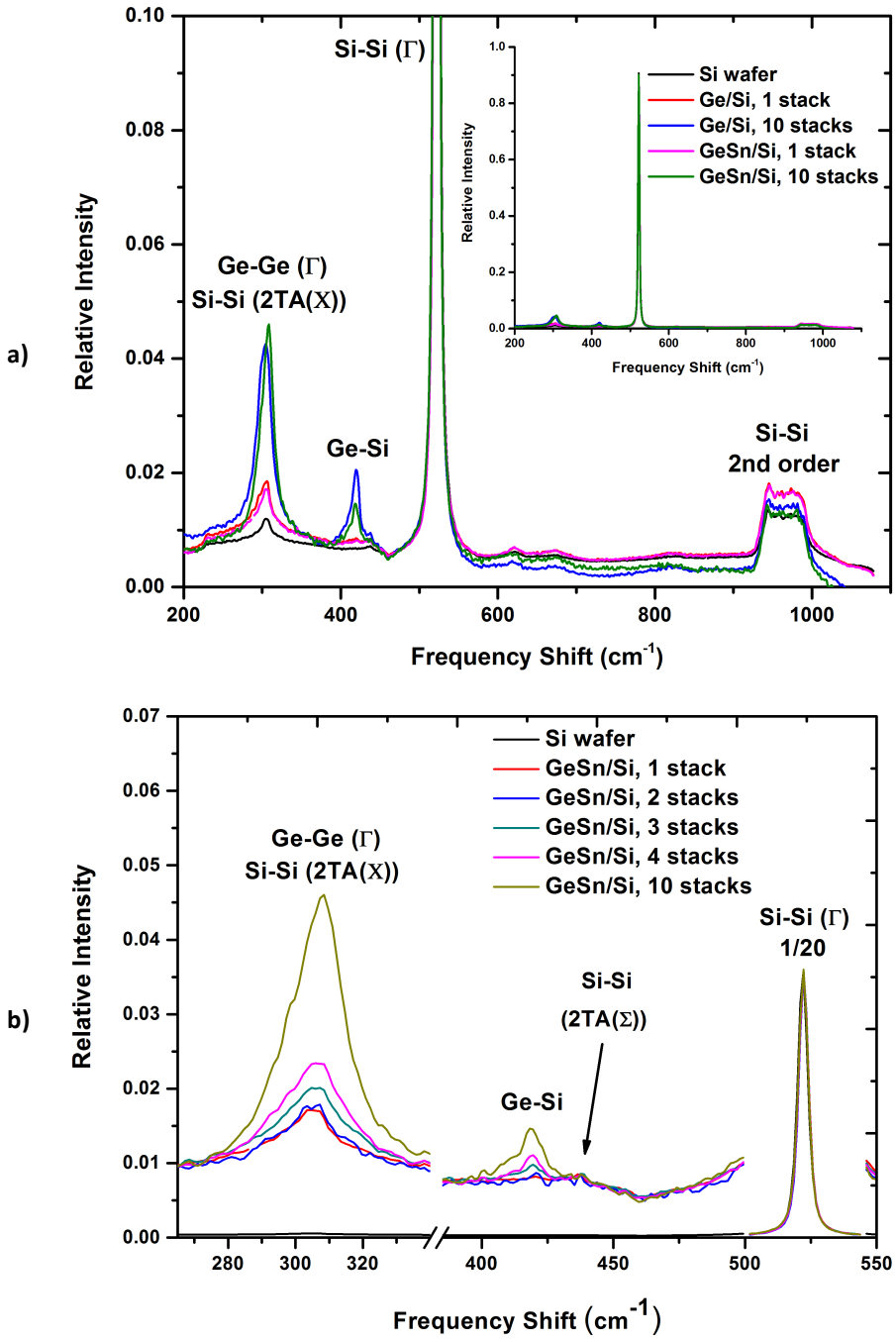

Figure IV.20: a) Raman spectra of GeSn/Si multilayers samples, and Ge/Si multilayers samples and c-Si (100) substrate wafer for comparison. b) Details of the Raman spectra of the GeSn/Si samples and c-Si (100) for comparison. The measurements were performed with a Raman system 4 (see Chapter III.8.1) with the laser excitation 532nm.

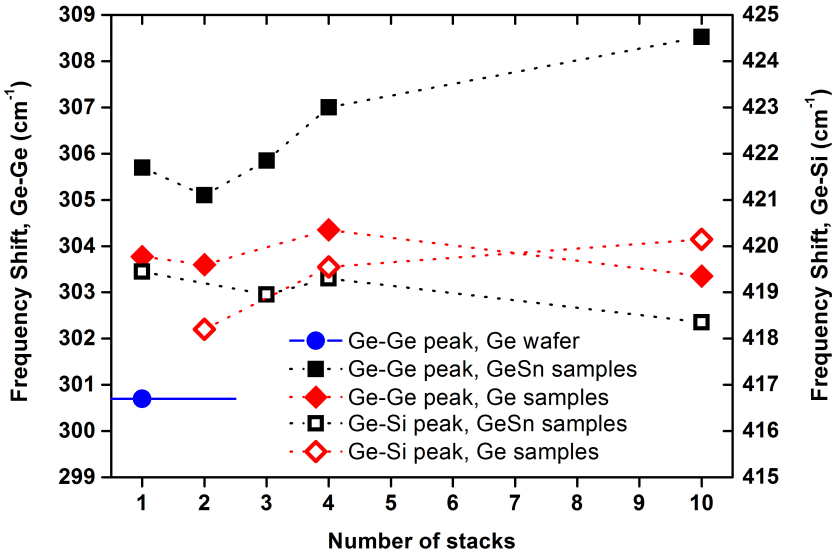

Figure IV.21: Peak position as a function of the number of stacks for the Ge-Ge and Ge-Si Raman bands for the GeSn/Si self-assembled dot samples and corresponding spectra of Ge/Si reference samples (after c-Si Raman spectrum subtraction).

The Ge-Ge and the Si-Si 2TA phonon modes are both present in the samples at spectral positions that nearly coincide. In order to extract information concerning the Ge-Ge phonon mode it was followed the procedure of **Ref. [IV.29]** (see also **Chapter III.8.2.**) and subtract the Si spectrum, I_{Si}, from the sample spectrum, I_S, in the following way: $I_S - F\, I_{Si}$ where F is a scaling factor equal to the ratio of the Si-Si phonon mode peaks at 520 cm^{-1} in both spectra. Thus, the contribution of the Si-Si (2TA(X)) phonon mode is removed. By fitting the resulting spectra with a set of Voigt functions it is possible to obtain the peak positions of the Si-Si, Ge-Ge and Ge-Si phonon modes. **Figures IV.21** and **IV.22** show the dependence of the peak positions and the integrated intensities of these phonon modes upon the number of GeSn/Si and Ge/Si stacks.

The peaks of the Ge-Si phonon mode for the studied samples (GeSn/Si and Ge/Si series) lie between 416 and 419 cm^{-1}, higher than the 410 cm^{-1} value reported in the literature for unstrained Ge-Si alloys, for any Ge content **[IV.30]**. This position is real because the Si-Si phonon mode is 520.8 cm^{-1}, as in *c*-Si. As the composition effect (of the Ge-Si alloy) does not justify this phonon mode to be above 410 cm^{-1}, it must be due to the presence of the Sn-caused strain. Furthermore, such a high blue shift of the Si-Ge phonon mode has already been observed in Ge/Si quantum dot samples **[IV.29, IV.34]** and attributed to the strain effect **[IV.29]**. It is interesting to note that the effect

of the number of stacks and the presence of Sn on the position of this Ge-Si phonon mode is small ($\Delta\omega_{(1\text{-}10stacks)} \approx 1$ cm^{-1} for GeSn samples and ≈ 2 cm^{-1} for the Ge reference samples).

From **Figure IV.21** it can be seen that the Ge-Ge peak position, for all samples, is also shifted to higher frequencies as compared to that in bulk Ge. Furthermore, it shifts with the number of stacks, which is not the case for the Ge-Si phonon mode. Indeed, the Ge-Ge phonon mode position is affected by the presence of heavier atoms in the lattice (namely, Sn, which causes a red shift) and lighter atoms (Si, which causes a blue shift) and yet by tensile strain along the axis normal to the surface (causing a blue shift as well). However, the shift observed for this phonon mode in the GeSn/Si samples is quite large in comparison with the bulk material (≈ 5 cm^{-1} for 1-stack sample and ≈ 8 cm^{-1} for the 10-stack sample) and with the Ge/Si reference samples (≈ 3 cm^{-1} for 1 stack sample and ≈ 2.5 cm^{-1} for the 10-stack sample). A possible explanation for the different behaviour of the Ge-Si and Ge-Ge phonon modes is that Sn atoms preferably intermix with Ge rather than with Si and then the strain is introduced mostly in the Ge-rich regions. It happens because the covalent radius of Sn atoms is close to that of Ge than to Si.

Finally, looking at the peak area results shown in **Figure IV.22**, it can be seen that the peak area increases proportionally to the number of stacks for both Ge-Ge and Ge-Si phonon modes, which indicates that all the layers contribute to the scattering by these phonons involving vibrations of Ge atoms. Then the Raman spectra of the GeSn/Si samples with two, three, for and ten stacks of GeSn dots include contributions from all quantum dot layers. Furthermore, as already mentioned, it is found that the number of stacks has a marked influence on the peak position of the Ge-Ge phonon mode in the GeSn/Si samples. It seems reasonable to assume that there is not only a morphological evolution of the dot shape with the increase of the number of layers, as evidenced by our AFM and TEM measurements, but also a variation of composition and strain between the different dot layers, which could explain this shift in Ge-Ge peak.

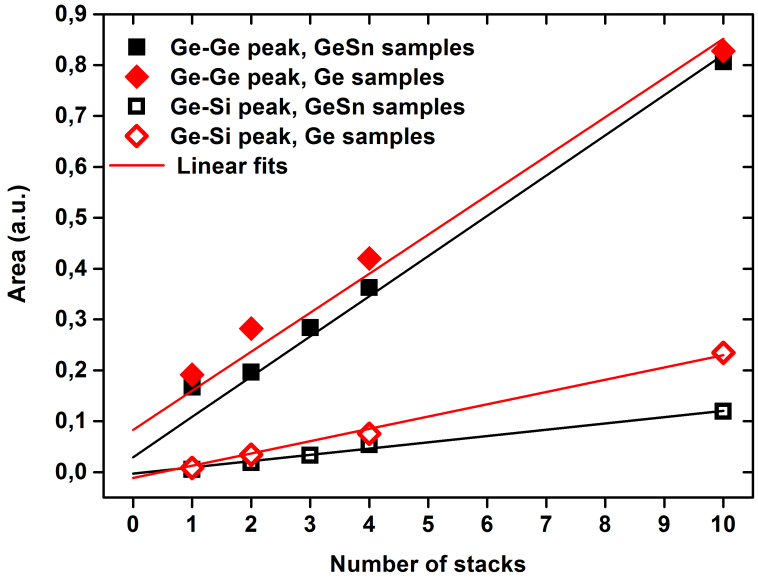

Figure IV.22: Peak area variation and its linear fit with the number of stacks for the Ge-Ge and Ge-Si Raman modes of the GeSn/Si self-assembled dots and Ge/Si samples (after c-Si Raman spectrum subtraction). The results were obtained with 532 nm excitation and normalized by the Si-Si phonon mode peak intensity.

IV.4. Modelling Using Semi-Empirical Potentials: Distribution of Bond Lengths and Angles

Rojas-Lopez *et al.* **[IV.6]** made a Raman spectroscopy study of Ge-Ge mode of GeSn layers with different Sn content of fully strain samples. They obtained a linear variation of the deviation of the peak position from that in bulk Ge with the Sn content, quantified as $(-76.8x)$ cm^{-1} for their strained samples. These authors made an estimate of $(-140.6x)$ cm^{-1} for a (hypothetical) fully relaxed sample. On the other hand, Li *et al.* reported a substantially lower value of $(-68.0x)$cm^{-1} for their "nearly relaxed" samples **[IV.30]**. Having in consideration the existing uncertainty in these values **[IV6, IV.20,IV.21]**, a numerical modelling of the lattice dynamics of Ge-Sn solid solutions was undertaken in this work in order to better understand the effects of Sn content and strain on the characteristic Raman modes.

It has been pointed out earlier that Ge-Sn and Ge-Si systems have similar behaviours. Having this in mind, in this section we present a summary of the work done on the Ge-Si system and then try to extrapolation it to the Ge-Sn and Si-Ge-Sn ones. The electronic and vibrational properties of these systems (with alloy disorder)

are influenced by several factors, simultaneously involved in confined systems, such as non-local elastic strain **[IV.34]**, interplay between phonon confinement and (competing with it) localization owing to alloy disorder **[IV.35]**, formation of percolating clusters **[IV.30]**, or non-random distribution of two types of atoms in the alloy **[IV.36]**.

Several works have been performed, devoted to the calculation of phonon properties and Raman spectra of $Si_{1-x}Ge_x$ alloys **[IV.30, IV.36 – IV.44]** and GeSn **[IV.45],** some of which considered nanostructures **[IV.30, IV.36, IV.39 – IV.43]**. Among them, only those which used the empirical potentials due to Tersoff **[IV.46]** and due to Stillinger and Weber **[IV.47]** will be discussed. Owing to the similarity of the GeSi and GeSn systems, these potentials will be applied to the latter.

Both potentials take into account three-particle interactions, which means that they depend on the inter-bond angles, which variation is known to contribute to the strain relaxation in the alloy where the end members have different lattice constants **[IV.48]**. These potentials are often used for calculations of lattice properties of Si-Ge alloy crystals. The advantage of using the Stillinger-Weber (SW) and Tersoff potentials, in comparison with the widely used valence force field (VFF) model (employed *e.g.* in **Refs. [IV.39, IV.40, IV.44]**), is that these potentials can be used for building a crystal by relaxing it to thermodynamic equilibrium (for a given composition), before considering the lattice vibrations, while the VFF model approach is limited to the harmonic approximation (eventually with anharmonic corrections **[IV.44]**). Therefore, it is possible to take into account the realistic three-modal distribution of bond lengths in these alloys using the Tersoff and SW potentials, which are briefly described in the following sections.

IV.4.1. Stillinger-Weber Potential

The Stillinger-Weber (SW) semi-empirical potential **[IV.49]** was built having in mind a tetrahedral crystal and it has been successful in providing fairly realistic description of crystals with diamond structure. However, this potential does not work so well for other crystal structures and it is difficult to use the potential under conditions different from those it was designed for.

The SW potential is composed by a two-body term and a three-body term:

$$E_{tot} = \sum_{i<j} v_2(\vec{r}_i, \vec{r}_j) + \sum_{i<j<k} v_3(\vec{r}_i, \vec{r}_j, \vec{r}_k) \qquad \textbf{\{IV.8\}}$$

The two terms are, respectively:

$$v_2(r_{ij}) = \varepsilon f_2\left(\frac{r_{ij}}{\sigma}\right), \qquad \textbf{\{IV.9a\}}$$

$$v_3(r_i, r_j, r_k) = \varepsilon f_3\left(\frac{r_i}{\sigma}, \frac{r_j}{\sigma}, \frac{r_k}{\sigma}\right), \qquad \textbf{\{IV.9b\}}$$

where ε, and σ are energy and length unit, and

$$f_2(r) = \begin{cases} A\left(Br^{-p} - r^{-q}\right)\exp\left(\frac{1}{r-a}\right), & r < a \\ 0, & r \geq a \end{cases} \qquad \textbf{\{IV.10a\}}$$

$$f_3(r_i, r_j, r_k) = h(r_{ij}, r_{ik}, \theta_{jik}) + h(r_{ji}, r_{jk}, \theta_{ijk}) + h(r_{ki}, r_{kj}, \theta_{ikj}) \qquad \textbf{\{IV.10b\}}$$

and

$$h(r_{ij}, r_{ik}, \theta_{jik}) = \lambda \exp\left(\frac{\gamma}{r_{ij}-a} + \frac{\gamma}{r_{ik}-a}\right) \cdot \left(\cos\theta_{jik} + \frac{1}{3}\right)^2. \qquad \textbf{\{IV.11\}}$$

Here θ_{jik} is the angle formed by the ij bond and the ik bond, and hI is related to a decaying function with a cut-off between the first- and the second-neighbour shell. The functions presented above depend on a number of fitting parameters ($\lambda, \gamma, a, A, B, p, q$) which are obtained by adjusting the experimentally known values of some physical properties. To get diamond structure bond angles, the term ($\propto \cos\theta_{jik}$) must be ≈ - 1/3, making the structure more stable than the compact structure, as it should be.

Historically the SW potential was probably the first three-particle semi-empirical potential that has been successfully applied to a number of tetrahedrically bonded materials in bulk and nanocrystal forms **[IV.28], [IV.50].** Later J. Tersoff **[IV.46]** proposed a more sophisticated semi-empirical potential based on similar ideas and containing more fitting parameters than the SW potential that has proved more universal.

IV.4.2. Tersoff Potential

The Tersoff potential is the common name given to a set of potentials developed by Tersoff **[IV.46]**, based on the concept of bond order, *i.e.*, taking into account the fact that the strength of a bond between two atoms is dependent on the local environment. The total crystal energy is given by:

$$E_{tot} = \frac{1}{2}\sum_{i \neq j} V_{ij} \,, \qquad \textbf{\{IV.12\}}$$

where V_{ij} has two contribution, one repulsive (subscript R) and the other attractive (subscript A):

$$V_{ij} = f_C(r_{ij})\left[f_R(r_{ij}) + b_{ij} f_A(r_{ij})\right] \qquad \textbf{\{IV.13\}}$$

where r_{ij} is the distance from atom I to atom j, and f_C is merely a smooth cutoff function.

In the previous equation the "force fields" are given by:

$$f_C\left(r_{ij}\right) = \begin{cases} 1, & r_{ij} < R_{ij} \\ \frac{1}{2} + \frac{1}{2}\cos\left(\pi \frac{r_{ij} - R_{ij}}{S_{ij} - R_{ij}}\right), & R_{ij} < r_{ij} < S_{ij} \\ 0, & r_{ij} > S_{ij} \end{cases} , \qquad \textbf{\{IV.15\}}$$

$$f_A\left(r_{ij}\right) = A_{ij} \exp\left(-\lambda_{ij} r_{ij}\right), \qquad \textbf{\{IV.16\}}$$

$$f_R\left(r_{ij}\right) = -B_{ij} \exp\left(-\mu_{ij} r_{ij}\right). \qquad \textbf{\{IV.17\}}$$

The term b_{ij} in **Equation {IV.13}** is the bond order for the bond joining atoms I and j, and it is a decreasing function of a "coordination'' assigned to the bond:

$$b_{ij} = \chi_{ij}\left(1 + \beta_i^{\,n} \zeta_{ij}^{\,n}\right)^{-\frac{1}{2n_i}} , \qquad \textbf{\{IV.18\}}$$

$$\zeta_{ij} = \sum_{k \neq i,j} f_C\left(r_{ik}\right) g\left(\theta_{ijk}\right), \qquad \textbf{\{IV.19\}}$$

$$g(\theta_{ijk}) = 1 + \frac{c_i^{\,2}}{d_i^{\,2}} - \frac{c_i^{\,2}}{d_i^{\,2} + (h_i - \cos\theta_{ijk})^2} \,. \qquad \textbf{\{IV.20\}}$$

where θ_{ijk} is the bond angle between bonds *ij* and *ik*.

The parameters β, n, c, d, h depend upon one (site) index only and they are listed in **Table IV.8** for the different types of atoms. The parameters with two indices, *i.e.* $A, B, \lambda, \mu, R, S,$ for like atoms occupying sites i and j are also given in the table and for unlike atoms they were taken as arithmetic mean values of those corresponding to pure materials.

Table IV.8: Tersoff potential parameters used in the present work.

	Si	Ge	Sn
***A* (eV)**	1830.8	1769	2848
***B* (eV)**	471.18	419.23	658.62
λ **(Å^{-1})**	2.4799	2.4451	2.25
μ **(Å^{-1})**	1.7322	1.7047	1.62
β	1.1×10^{-6}	0.90166×10^{-6}	6.01×10^{-7}
n	7.8734×10^{-1}	7.5627×10^{-1}	0.74
c	100390	106430	1.4×10^{5}
d	16.217	15.6652	14.5
h	-5.9825×10^{-1}	-4.3884×10^{-1}	-0.502
***R* (Å)**	2.7	2.8	2.8
***S* (Å)**	3.0	3.1	3.2

The idea of the Tersoff potentials is that the bond ij is weakened by the presence of other bonds ik involving the atom i. The amount of weakening is determined by where these other bonds are placed. Angular terms appear necessary to construct a realistic model. This system works in a broader spectrum of situations than the Stillinger-Weber potential, however, the fitting is more difficult with six functions to fit and the angular terms.

It was found in **[IV.50]** that both Stillinger-Weber and Tersoff potentials are suitable for modelling both static bond length distributions and lattice dynamics in Si-Ge alloys, although the latter is more convenient, less time-consuming and yield results that are in a better agreement with available experimental data on the variation of bond length and phonon-related Raman peaks with alloy composition. There is at least one publication **[IV.46]** where the Tersoff potential was used for the Sn-Ge system (and none, to the best of our knowledge, used SW potential for it), so the choice in this work is also the Tersoff potential. The parameters for Si and Ge were taken from the literature **[IV.46]**, while those for tin were obtain by fitting experimental values of the cohesion energy of α-Sn **[IV.45]**.

IV.4.3. Building Relaxed Ge-Sn Structure

For lattice dynamics modelling, the Sn_xGe_{1-x} crystallites were built by randomly distributing xN tin and $(1\text{-}x)N$ germanium atoms over the sites of a diamond lattice, starting from a central atom and filling its 1st, 2nd,… coordination shells. The starting lattice constant was chosen according to Vegard's law:

$$a = a_{Ge}(1-x) + a_{Sn}x\,, \qquad \textbf{\{IV.21\}}$$

where a_{Ge} = 5.64613 Å and a_{Sn} = 6.48920 Å are the lattice constants of the crystalline Ge and Sn, respectively. The system retained the T_d symmetry with perfect tetrahedric bonding. Typical size of the crystallite was ≈1000 atoms.

The Tersoff potential was used to describe the interactions between the atoms. The parameters are listed in **Table IV.8**. Periodic boundary conditions were applied. The lattice was allowed to relax to the minimum of its total energy by letting the atoms to move in response to the forces produced by their neighbours. For this relaxation, a molecular dynamics method employing the Verlet algorithm[17] **[IV.51]** was used. The equations of motion were integrated at each temporal step (not exceeding 10^{-15} s) until the equilibrium of the lattice was achieved. The crystallite no longer possessed the T_d symmetry (unless for x = 0 or 1) after the relaxation.

IV.4.4. Bond Length Distribution

The average bond length, in the first approximation, is described by the phenomenological Vegard's law **{IV.21}**. However, both experiment and calculations **[IV.52 – IV.56]** show deviations from it, which are more substantial than for Si-Ge alloys. A better approximation for Sn_xGe_{1-x} solid solutions is provided by the following expression:

$$a_{GeSn}(x) = a_{Ge}(1-x) + a_{Sn}x + \theta(1-x)x\,, \qquad \textbf{\{IV.22\}}$$

where θ is called the slope parameter. Notice that experimental data exist only for $x < 0.2$, while some calculations go beyond this value of Sn content.

[17] Verlet algorithm or Verlet integration is a numerical method used to integrate equations of motion.

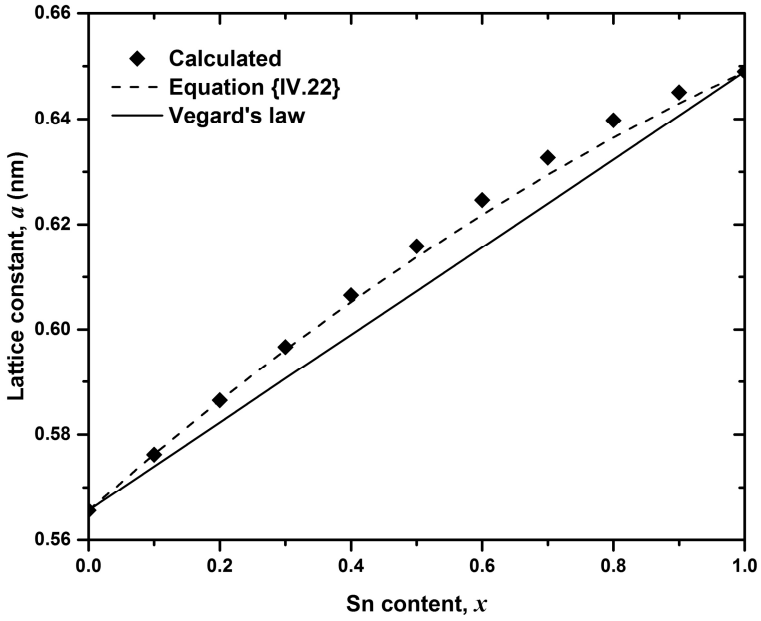

Figure IV.24: Average lattice constant as a function of Sn content. Solid straight line represents Vegard's law {IV.21}, rhombs are our calculated data and dashed line is Equation {IV.22}.

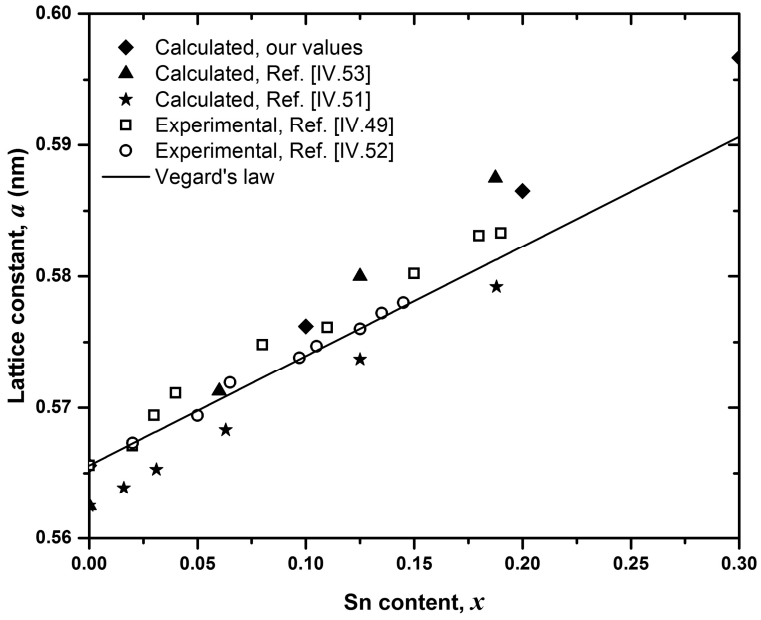

Figure IV.25: Comparison of the average lattice constant in the region of low Sn contents. Solid straight line represents Vegard's law {IV.21}, full rhombs are our calculated data, open squares are experimental data of Ref. [IV.56], open circles are experimental data of Ref. [IV.55] and full triangles and full stars are Density Functional Theory (DFT) results for random [IV.54] and partially ordered [IV.52] Sn-Ge solid solutions, respectively.

Calculated results obtained in this work, at 0 K temperature and with composition step Δx = 0.1 are shown in **Figure IV.24**. The maximum deviation is reached for x = 0.6. The best fit to available experimental data is obtained for the slope parameter θ = 0.026 nm. **Figure IV.25** shows comparison of the obtained results with literature data in the practically important range of alloy compositions x < 0.2. In general, the results compare well with the literature data in this range where deviations from Vegard's law are rather small.

It is interesting to analyse the lengths of different bonds, *i.e.*, Sn-Sn, Sn-Ge and Ge-Ge separately. These are presented in **Figure IV.26** which demonstrates a three-modal distribution of bond lengths. It means that the relaxed Sn-Ge lattice is not a diamond crystal structure any more. Similar conclusions were derived for Si-Ge alloys **[IV.50]** but for the tin-germanium system the effect is more pronounced because of the larger difference of the lattice parameter of α-Sn from that of Ge than in the case of silicon. It is also possible to conclude that the strongest variation with composition is characteristic of the mixed Sn-Ge bonds, while Sn-Sn bond length is less dependent of x. The latter was also concluded in **Ref. [IV.45]** although these authors found a stronger compositional variation for Ge-Ge bond length.

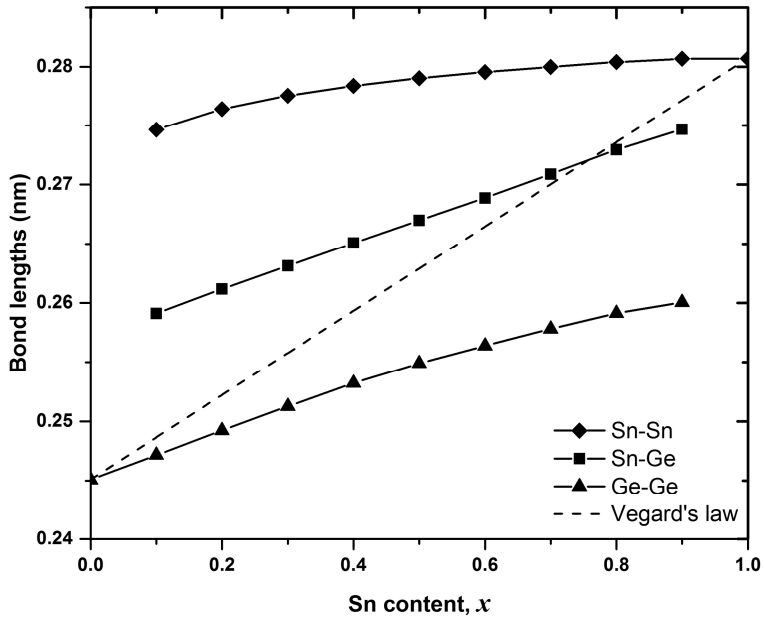

Figure IV.26: Calculated bond length dependence upon Sn content for three types of bonds (Sn-Sn – rhombs, Sn-Ge – squares, Ge-Ge – triangles). Dashed line represents the Vegard's law.

Another way to see the alloy disorder introduced by the substitution of germanium with tin atoms is provided by the pair correlation function, which gives the probability to find a second atom within a spherical shell of radius r and thickness dr, with the first atom in its centre. The pair correlation function is a measure of alloy short-range order. The calculations followed the procedure proposed in **Ref. [IV.51]** and the results are shown in **Figure IV.27**. Each peak corresponds to a certain coordination sphere of the reference atom (either Ge or Sn). At it is seen from this plot, short-range order is different for tin and germanium atoms only for the first coordination sphere (the first peak is shifted), that reflects the difference in the Ge-Ge and Sn-Sn bond lengths. For further coordination spheres, no such shift between Sn and Ge atoms is seen and the same behaviour is verified also for other compositions. It can be understood by compensation of the bond length difference by the variation of the inter-bond angles, another composition-dependent effect verified in the calculations made in the present work. Notice that the broadening of the peaks is related to static alloy disorder only and not to thermal displacements of the atoms.

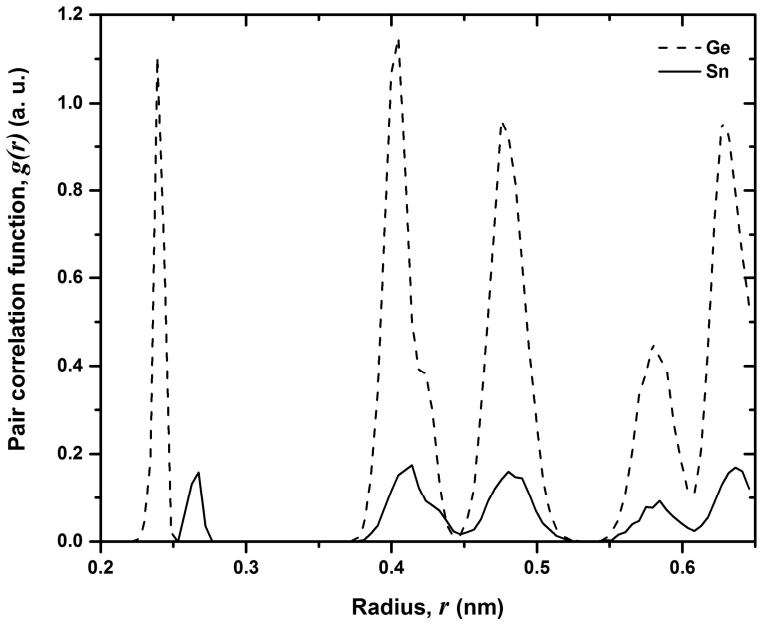

Figure IV.27: Pair correlation function (gI) for Ge-Sn solid solution with x = 0.25 calculated separately for Ge-Ge and Sn-Sn pairs.

IV.5. Calculated Raman Spectra and Comparison with Experiment

In the previous section it was explained how relaxed alloy crystallites were built and their static structure was analysed. Given the atomic coordinates and the (Tersoff) potentials acting on each of them, the dynamical matrix of the crystallite (constituted by the second derivatives of the atomic potential energy with respect to the spatial coordinates at equilibrium) was obtained. The vibration modes (*i.e. eigen*mode frequencies and the corresponding *eigen*vectors, which are normalised atomic displacements, u_l^j, for the l-th atom and j-th vibration mode) were calculated by diagonalizing the dynamical matrix.

With these data at hand, non-resonant Raman spectra were calculated using the bond polarizability model **[IV.57]**, where three second-rank tensors are defined for each (j-th) phonon mode as follows:

$$\vec{\vec{\alpha}}_1 = \sum_{l=1}^{N}\sum_{i=1}^{4}\left(\hat{r}_{li}\otimes\hat{r}_{li} - \frac{\vec{\vec{I}}}{3}\right)u_l^j\cdot\hat{r}_{li}, \qquad \textbf{\{IV.23a\}}$$

$$\vec{\vec{\alpha}}_2 = \sum_{l=1}^{N}\sum_{i=1}^{4}\left[\frac{1}{2}\left(\hat{r}_{li}\otimes u_l^j + u_l^j\otimes\hat{r}_{li} - \frac{\vec{\vec{I}}}{3}\right)\right]u_l^j\cdot\hat{r}_{li}, \qquad \textbf{\{IV.23b\}}$$

$$\vec{\vec{\alpha}}_3 = \vec{\vec{I}}\sum_{l=1}^{N}\sum_{i=1}^{4}u_l^j\cdot\hat{r}_{li}, \qquad \textbf{\{IV.23c\}}$$

where $\hat{r}_{li}$ is a unit vector directed from atom l to its neighbour I, u is the displacement of the phonon amplitude, and $\vec{\vec{I}}$ is the unit dyadic. The l summation is over all atoms, while the I summation is over all bonds of an atom. The tensor $\vec{\vec{\alpha}}_1$ represents the polarizability modulation due to bond stretching and is responsible, *e.g.*, for the Raman peak of pure crystalline Ge at ≈ 300.9 cm^{-1}. The $\vec{\vec{\alpha}}_2$ and $\vec{\vec{\alpha}}_3$ contributions represent angular distortions and vanish in the case of perfect tetrahedric bonding. The (polarization-averaged) Raman scattering intensity was calculated as:

$$I(\omega)\propto\frac{[n_{BE}(\omega)+1]}{N\omega}\sum_j\frac{\left(\alpha_{1xy}^2+\alpha_{1xz}^2+\alpha_{1yz}^2\right)}{3}\delta(\omega-\omega_j), \qquad \textbf{\{IV.24\}}$$

where $n_{BE}(\omega)$ is the Bose-Einstein function. For computational purposes, the δ-function in **Equation {IV.24}** was replaced by a Lorentzian. Such a procedure has been used before to model Raman spectra of bulk pure Si and Ge, Si-Ge alloy and corresponding nanocrystals **[IV.37, IV.50, IV.56, IV.58]**.

Figure IV.28 presents calculated spectra of Sn_xGe_{1-x} solid solutions (alloys) with different composition including x = 0 (pure germanium). They are considerably different from those obtained in **[IV.50]** for Si_xGe_{1-x} using essentially the same model. As it was seen in **Chapter III**, Raman spectra of the Si-Ge system are characterised by three principal phonon modes corresponding to the Ge-Ge, Si-Ge and Si-Si vibration (neglecting the fine structure). Here (**Figure IV.28**) peaks corresponding to the vibrations involving Sn-Sn and Sn-Ge bonds are hardly seen for small and medium values of x. Experimentally, Raman spectra of this system indeed are dominated by the Ge-Ge peak, while a weak Ge-Sn feature could also be observed (**Section IV.3.1**). In the calculated results, the latter appears as a shoulder of the main (Ge-Ge) band and cannot be identified as a clear peak. This is because of the smoothening of the calculated spectra obtained for small size crystallites and averaging over different realizations of alloy disorder. Nevertheless, it is seen that the role of the Sn-Ge feature increases with the increase of tin content. As for the Sn-Sn vibrations attributed by some authors to a rather broad, low intensity band observed around 190 cm^{-1} **[IV.33, IV.59 – IV.61]**, the calculations performed to this work do not provide any evidence of this.

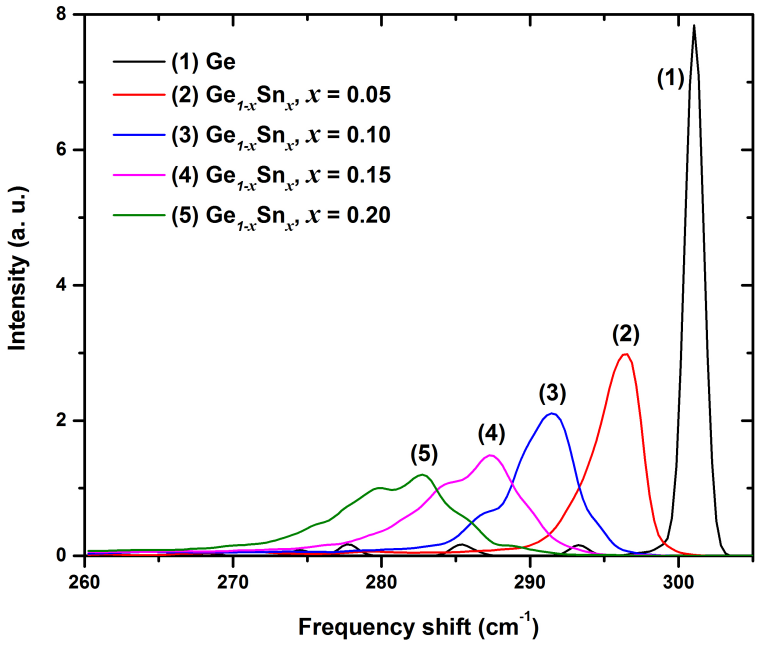

Figure IV.28: Raman scattering intensity calculated for relaxed $Ge_{1-x}Sn_x$ solid solutions of different composition: (1) x = 0 (pure germanium), (2) x = 0.05, (3) x =0.10, (4) x = 0.15, (5) x = 0.20.

The peak position of the Ge-Ge band in the calculated spectra of fully relaxed crystallites can be approximated by the following linear relation:

$$\omega_{\mathrm{Ge-Ge}}^{relaxed} = 300.9 - 91.6x \quad [\mathrm{cm}^{-1}]. \qquad \textbf{\{IV.25\}}$$

It should be identified with the first term, $\Delta\omega_{composition}$, in **Equation {IV.4}.** The coefficient in the linear term is close to that obtained in previous works **[IV.21, IV.62]** for samples where stress was fully relaxed by either formation of misfit dislocations or because of the presence of Si atoms in ternary alloy Ge-Sn-Si; the reported coefficient value was $94 - 95\ \mathrm{cm}^{-1}$.

On the other hand, combining it with the effect of stress induced by the substrate, **Equation {IV.7}**, one obtains for Ge-Sn solid solution subjected to pseudomorphic strain:

$$\omega_{\mathrm{Ge-Ge}}^{strained} = 300.9 - 24.5x \quad [\mathrm{cm}^{-1}]. \qquad \textbf{\{IV.26\}}$$

A similar weak dependence of the Ge-Ge peak position upon x was reported in **[IV.62]**, with the reported linear coefficient value $\approx 30\ \mathrm{cm}^{-1}$.

The computational model here reported also allows for investigating the effect of macroscopic strain on the vibration modes of Sn_xGe_{1-x} solid solutions under elastic stress (*e.g.* caused by hydrostatic pressure or stress induced by substrate), without using the macroscopic model leading to **Equation {IV.5}**. In the numerical experiments, the strain was imposed by changing the crystallite size in one, two or three directions (coinciding with the principal axes of the underlying diamond lattice). The deformation (for simplicity assumed independent of composition) was counted with respect to the crystallite size corresponding to the average lattice constant value for the given composition x as presented in **Figure IV.24**.

As it can be seen from **Figure IV.29**, the position of the peak and even the shape of the Raman band are strongly influenced by the macroscopic strain. The sign of the shift (with respect to the unstrained case, curve 1 in the plot) correlates with the sign of the trace of the strain tensor. Compressive strain (curves 2, 4 and 5) produces a blue shift that compensates the red shift caused by the local effect associated with the tin doping [remind that two terms in **Equation {IV.4}** have opposite signs]. The most realistic case is the one represented by curve 5. Indeed, for a Sn-Ge layer grown on a germanium substrate, the in-plane components ε_{xx} and ε_{yy} should be negative (compression) while ε_{zz} (denoted $\varepsilon_{\perp}$ in **{IV.2}**) should be positive. In fact, the lattice

constant in the growth direction, $a_{\perp}$, measured in **Ref. [IV.62]** was larger than the equilibrium lattice parameter corresponding to the given Sn content. Comparing curves 4 and 5 in **Figure IV.29**, it can be noticed that the Poisson effect (artificially excluded for the curve 4, $\varepsilon_{zz} = 0$) partially compensates the blue shift associated with strain. This is in agreement with the analytical formula, **Equation {IV.5}**, where the second term in the brackets represents the effect of ε_{zz}.

The shift of the Raman band in the case of uniaxial traction applied to Sn-Ge bulk crystals that was investigated in **Ref. [IV.60]** is corroborated by the calculated results. The sign and the value of the Raman peak shift calculated here agree rather well with the experimental data of that work, $\varepsilon_{xx} \approx 0.0123$ and $\Delta\omega_{\text{strain}} \approx -2.5\,\text{cm}^{-1}$ (compare curves 6 and 1 in **Figure IV.29**). Notice that a double peak structure appears in this case (in the spectrum 6). The uniaxial strain splits the three-fold degenerate Brillouin zone phonon peak into a singlet and a doublet (**Ref. [IV.23]**, see also **Appendix C**) and, for certain scattering configurations both modes can be Raman active **[IV.23]**. Interestingly, a similar effect has been observed for uniaxially strained ehaviou **[IV.63]**.

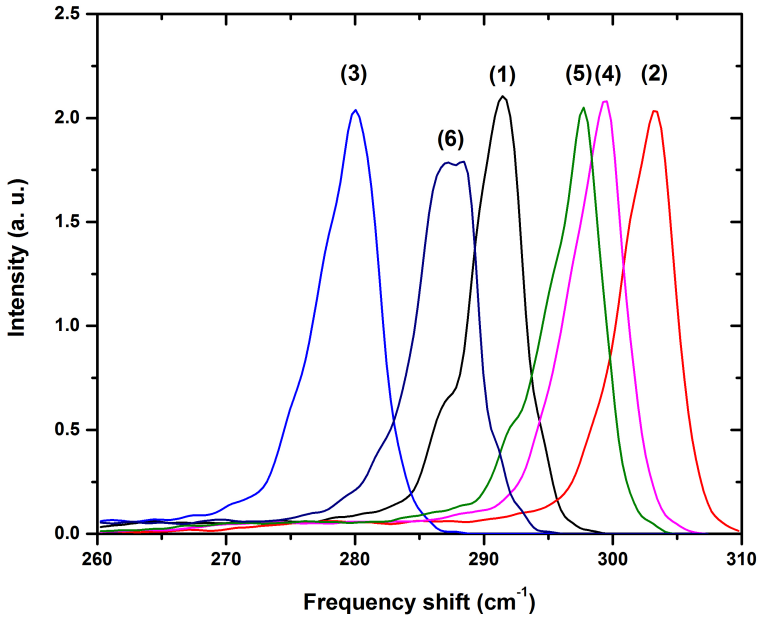

Figure IV.29: Influence of different types of strain on the Raman band of $Sn_{0.1}Ge_{0.9}$: (1) $\varepsilon = 0$ (no strain), (2) $\varepsilon_{xx} = \varepsilon_{yy} = \varepsilon_{zz} = -0.01$ (hydrostatic compression), (3) $\varepsilon_{xx} = \varepsilon_{yy} = \varepsilon_{zz} = 0.01$ (isotropic expansion), (4) $\varepsilon_{xx} = \varepsilon_{yy} = -0.01$, $\varepsilon_{zz} = 0$ (compression in the plane of the layer), (5) $\varepsilon_{xx} = \varepsilon_{yy} = -0.01$, $\varepsilon_{zz} = 0.005$ (compression in the plane of the layer and expansion in the perpendicular direction), (6) $\varepsilon_{xx} = 0.01$, $\varepsilon_{yy} = \varepsilon_{zz} = 0$ (uniaxial traction).

Comparing the experimental results presented in **Section IV.3.1.1** (see **Figure IV.18**) with the modelling results obtained for this system without applying stress (see **Figure IV.28**), a good agreement on the Ge-Ge peak position variation with the increase of the Sn content can be certified. Both the experimental and modelling results show a shift of the Ge-Ge mode to lower wavenumbers, accompanied by an increase of the width of the Raman band. The experimental peak positions of the Ge-Ge mode measured for the $Ge_{1-x}Sn_x$ thin films lie in the range 300 – 297 cm^{-1} for x = 0 – 0.037, respectively. The variation with Sn content is in agreement with **Equation {IV.25}**, which is expected since the experimentally studied Ge-Sn layers are nearly relaxed, in correspondence with the assumption behind this equation. Indeed, the measured (through X-ray diffraction) out-of-plane lattice constant yields strain components that are much lower than predicted by the $\varepsilon_{\parallel} = -0.147x$ relation expected for pseudomorphically strained GeSn layers on unstrained Ge substrate (see **Figure IV.8**). For sample #12 (x = 0.043) the red shift is bigger than expected even assuming that it is fully relaxed but the most plausible reason is an error in the evaluation (namely, underestimation) of the Sn content in it.

Equation {IV.26}, which is derived from the macroscopic model based on the bulk deformation potentials describes quite well the shift of the Raman peak (2.9 cm^{-1}) obtained by numerical calculations in the case where the assumed strain components mimic the pseudomorphic strain for x = 0.1 (curve 5 in **Figure IV.29**). It was not possible to confirm these theoretical predictions experimentally because of the lack of "fully strained" GeSn layers in this study.

Conclusions

Samples of GeSn thin films on a Ge buffer layer deposited on a Si substrate were grown by MBE with a tin content up to 4.3 % as determined by RBS, XRD and TEM studies showed high crystalline quality of the solid solution layers and no evidence of Sn segregation on the surface or precipitation inside the layer. From the presence of the Ge-Sn vibration mode in the Raman spectra it can be concluded that the Sn atoms are mainly in substitutional positions. The Ge buffer layer is almost fully relaxed (as are the Ge-Sn films deposited later on top of it), according to the value of the out-of-plane lattice constant extracted from X-ray diffractograms corresponding to (004) crystal planes and confirmed by the very small shift of the Raman peak (Ge-Ge mode) in the reference sample with respect to bulk germanium crystal.

The characterization of the GeSn thin films was essential to the growth of samples with higher complexity: multilayer structures with 1 to 10 stacks of layers were grown, each consisting of 5.5 MLs of $Ge_{0.96}Sn_{0.04}$ followed by 10 nm of Si. It was shown that it is possible not only to produce self-assembled GeSn dots in this way but, even more importantly from the technological point of view, to overgrow the GeSn dots using Si substrates making their incorporation into Si-based devices possible. The structural characterization revealed that in some aspects, such as the dot shape, GeSn/Si samples seem to differ from their Ge counterparts.

Experimental Raman spectroscopy results of GeSn system reveal the Ge-Ge and Ge-Sn expected vibrational modes, in agreement with previous studies. The Sn-Sn mode is intrinsically weak (because of the large mass of tin atoms) and very hard to observe. Experimental spectra obtained in this work showed a weak mode in the vicinity of 185 cm^{-1} (not far from the intrinsic optical phonon mode of α-Sn), however, an alternative explanation of this spectral feature as disorder-activated longitudinal acoustic mode (DALA) is also possible.

The strain state of the Ge-Sn thin films and its impact on the Ge-Ge Raman peak position was investigated in detail. According to the XRD data, the solid solution layers are almost fully relaxed with the in-plane and out-of-plane strain components not exceeding 0.30%, well below the values corresponding to the pseudomorphic strain for

the Sn contents of the studied samples. The effect of strain on the Ge-Ge vibration mode was evaluated by means of a macroscopic model from the literature and also from numerical modelling using the semi-empirical Tersoff potentials.

Experimental Raman spectroscopy results for this system corroborate the above conclusion and are in agreement with the numerical modelling results. It has been possible to identify multiple phonon modes peaks in the experimental Raman spectra, related to the Ge-Ge, Ge-Sn, Ge-Si and Si-Si (from the spacers or the substrate) modes. The Sn-Sn mode does not appear in the calculated spectra, which makes the interpretation of the abovementioned 185 cm^{-1} Raman feature as DALA mode more plausible.

Numerical calculations that were performed allowed for understanding not only the composition and strain effects on the Ge-Ge vibration mode but also the bond length distribution in the Ge-Sn solid solutions. Calculated bond length dependence upon Sn content has a three-mode behaviour which represents the three types of bonds (Sn-Sn, Sn-Ge and Ge-Ge). Each of this bond lengths changes gradually with the composition but none follows the Vegard's law because the latter represent a "virtual" bond length, average over the three types of real bonds.

Bibliography

[IV.1] M. Brehm, M. Grydlik, H. Groiss, F. Hackl, F. Schäffler, T. Fromherz and G. Bauer. *The influence of a Si cap on* self-*organized SiGe islands and the underlying wetting layer.* J. Appl. Phys. **109**, 123505, (2011).

[IV.2] A. I. Yakimov, A. I. Nikiforov, A. V. Dvurechenskii, V. V. Ulyanov, V. A. Volodin, and R Groetzschel*. Effect of the growth rate on the morphology and structural properties of hut-shaped Ge islands in Si(001)*. Nanotechnology **17**, 4743, (2006).

[IV.3] B. Cho, T. Schwarz-Selinger, K. Ohmori, D. Cahill, and J. E. Greene. *Effect of growth rate on the spatial distributions of dome-shaped Ge islands on Si (001).* Phys. Rev. **B 66**, 195407, (2002).

[IV.4] B. K. Tanner, and D. K. Bowen. *Advanced X-ray scattering techniques for the characterization of semiconducting materials.* Journal of Crystal Growth 126, 1, (1993).

[IV.5] D. K. Bowen. *Interpretation of rocking curves from epilayers.* Bede Scientific Instruments Application Note 8, (1993).

[IV.6] M. Rojas-Lopez, H. Navarro-Contreras, P. Desjardins, O. Gurdal, N. Taylor, J.R.A. Carlsson, J.E. Greene. *Raman scattering from fully strained $Ge_{1-x}Sn_x$ ($x \leq 0.22$) alloys grown on Ge (001) 2× 1 by low-temperature molecular beam epitaxy.* J. Appl. Phys. 84, 2219, (1998).

[IV.7] Yu. N. Drozdov, D. N. Lobanov, A. I. Nikiforov, A. V. Novikov, V. V. Ul'yanov, and D. V. Yurasov. Influence of Elastic Strains in Sublayers on the Critical Thickness of the Stranski–Krastanow Transition for the GeSi/Si(001) System. Journal of Surface Investigation, X-Ray, Synchrotron and Neutron Techniques **3**, 548, (2009).

[IV.8] R. Bergamaschini, M. Brehm, M. Grydlik, T. Fromherz,G. Bauer, and F. Montalenti. *Temperature-dependent evolution of the wetting layer thickness during Ge deposition on Si(001).* Nanotechnology **22**, 285704, (2011).

[IV.9] O. G. Schmidt, O. Kienzle, Y. Hao, K. Eberl, and F. Ernst. *Modified Stranski–Krastanov growth in stacked layers of self-assembled islands.* Appl. Phys. Lett. **74**, 1272, (1999).

[IV.10] Edited by M. Henini. Handbook of Self Assembled Semiconductor Nanostructures for Novel Devices in Photonics and Electronics. Elsevier, Amsterdam, The Netherlands, 1-51, (2008).

[IV.11] S. N. Santalla, C. Kanyinda-Malu, and R. M. de la Cruz. *Stranski–Krastanov growth mode in Ge/Si(001) self-assembled quantum dots.* Journal of Crystal Growth **253**, 190, (2003).

[IV.12] M. Brehm, M. Grydlik, F. Hackl, E. Lausecker, T. Fromherz, and G. Bauer. *Excitation intensity driven PL shifts of SiGe islands on patterned and planar Si (001) substrates: evidence for Ge-rich dots in islands.* Nanoscale Research Letters **5**, 1868, (2010).

[IV.13] D. E. Jesson, K. M. Chen, and S. J. Pennycook. *Kinetic Pathways to Strain Relaxation in the Si-Ge System.* MRS Bulletin **21**, 31, (1996).

[IV.14] B. Voigtländer. *Fundamental processes in Si/Si and Ge/Si epitaxy studied by scanning ehaviour microscopy during growth.* Surface Science Reports **43**, 127 (2001)

[IV.15] A. Rastelli, M. Stoffel, U. Denker, T. Merdzhanova, and O. G. Schmidt. *Strained SiGe islands on Si (001): Evolution, motion, dissolution, and plastic relaxation.* Phys. Status Solidi **A 203**, 3506, (2006).

[IV.16] A. Vailionis, B. Cho, G. Glass, P. Desjardins, David G. Cahill, and J. E. Greene. *Pathway for the strain-driven two-dimensional to three-dimensional transition during growth of Ge on Si (001).* Phys. Rev. Lett. **85**, 3672, (2000).

[IV.17] G. Capellini, M. De Seta, F. Evangelisti, V. A. Zinovyev, G. Vastola, F. Montalenti, and Leo Miglio. *Self-ordering of a Ge island single layer induced by Si overgrowth.* Phys. Rev. Lett. **96**, 106102, (2006).

[IV.18] J.C. Tsang, P.M. Mooney, F. Dacol, and J.O. Chu. *Measurements of alloy composition and strain in thin Ge_xSi_{1-x}layers.* J.Appl.Phys.**75**, 8098, (1994).

[IV.19] M.Z. Hossain and H.T. Johnson. *Effects of composition, strain, and atomic disorder on optical phonon frequencies in $Si_{1-x}Ge_x$*. J. Appl. Phys. **107**, 073515, (2010).

[IV.20] S.F. Li, M.R. Bauer, J. Menendez, and J. Kouvetakis. *Scaling law for the compositional dependence of Raman frequencies in SnGe and GeSi alloys.* Appl. Phys. Lett. **84**, 867, (2004).

[IV.21] V.R. D'Costa, J. Tolle, R. Roucka, C.D. Poweleit, J. Kouvetakis, and J. Menendez. *Raman scattering in $Ge_{1-y}Sn_y$ alloys*. Solid State Commun. 144, 240, (2007).

[IV.22] A. G. Rolo and M. I. Vasilevskiy. *Raman spectroscopy of optical phonons confined in semiconductor quantum dots and nanocrystals.* J. Raman Spectroscopy **38**, 618, (2007).

[IV.23] F. Cerdeira, C.J. Buchenauer, F.H. Pollak, and M. Cardona. *Stress-induced shifts of first-order Raman frequencies of diamond-and zinc-blende-type semiconductors.* Phys. Rev. **B 5**, 580, (1972).

[IV.24] G.E. Jellison Jr. *Optical functions of GaAs, GaP, and Ge determined by two-channel polarization modulation ellipsometry*. Opt. Mat. **1**, 151, (1992).

[IV.25] L. Viña, S. Logothetidis, and M. Cardona. Temperature dependence of the dielectric function of germanium. Phys. Rev. **B 30**, 1979, (1984).

[IV.26] P. Parayanthal and F. H. Pollak. *Raman Scattering in Alloy Semiconductors: "Spatial Correlation" Model*. Phys. Rev. Letters 52, 1822, (1984).

[IV.27] A. S. Vasin, O. V. Vikhrova, and M. I. Vasilevskiy. *Effects of alloy disorder and confinement on phonon modes and Raman scattering in Si_xGe_{1-x} nanocrystals: A microscopic ehaviour* J. Appl. Phys. **115**, 143505, (2014).

[IV.28] J. J. Wortman,R. A. Evans. *Young's Modulus, Shear Modulus, and Poisson's Ratio in Silicon and Germanium*. J. Appl. Phys. 36, 153, (1965).

[IV.29 P. H. Tan, K. Brunner, D. Bougeard, and G. Abstreiter. *Raman characterization of strain and composition in small-sized self-assembled Si/Ge dots.* Phys. Rev. **B 68**, 125302, (2003).

[IV.30] O. Pagès, J. Souhabi, V. J. B. Torres, A. V. Postnikov, and K. Rustagi. *Re-examination of the SiGe Raman spectra: Percolation/one-dimensional-cluster scheme and ab initio calculations.* Physical Review **B 86**, 045201, (2012).

[IV.31] V. R. D'Costa, J. Tolle, C. D. Poweleit, J. Kouvetakis, and J. Menéndez. *Compositional dependence of raman frequencies in ternary $Ge_{1-x-y}Si_xSn_y$ alloys.* Phys. Rev. **B 76**, 035211, (2007).

[IV.32] M. Iliev, M. Sinyukov, and M. Cardona. *Resonant first-and second-order Raman scattering in gray tin.* Physical Review **B 16**, 5350, (1977).

[IV.33] J.-H. Fournier-Lupien, S. Mukherjee, S. Wirths, E. Pippel, N. Hayazawa, G. Mussler, J. M. Hartmann, P. Desjardins, D. Buca, and O. Moutanabbir. *Strain and composition effects on Raman vibrational modes of silicon-germanium-tin ternary alloys* Appl. Phys. Lett. **103**, 263103, (2013).

[IV.34] A. I. Yakimov, A. V. Dvurechenskii, A. I. Nikiforov, A. A. Bloshkin, A. V. Nenashev, and V. A. Volodin. *Electronic states in Ge⁄Si quantum dots with type-II band alignment initiated by space-charge spectroscopy.* Phys. Rev. B 73, 115333, (2006).

[IV.35] E. S. Freitas Neto, S. W. da Silva, P. C. Morais, M. I. Vasilevskiy, M. A. Pereira-da-Silva, and, N. O. Dantas. *Resonant Raman scattering in CdSxSe1−x nanocrystals: effects of phonon confinement, composition, and elastic strain.* J. Raman Spectrosc. **42**, 1660 (2011).

[IV.36] L. Z. Liu, X. L. Wu, Y. M. Yang, T. H. Li, and Paul K. Chu. *Si–Si optical phonon ehaviour in localized Si clusters of SixGe1−x alloy nanocrystals.* Appl. Phys. **A 103**, 361, (2011).

[IV.37] M. I. Alonso, and K. Winer. *Raman spectra of c-$Si_{1-x}Ge_x$ alloys.* Phys. Rev. **B 39**, 10056, (1989).

[IV.38] V. A. Volodin, M. D. Efremov, A. S. Deryabin, and L. V. Sokolov. *Determination of the composition and stresses in $Ge_xSi_{(1-x)}$ heterostructures from Raman spectroscopy data: Refinement of model parameters.* Semiconductors **40**, 1314 (2006).

[IV.39] S.-F. Ren, W. Cheng, and P. Y. Yu. *Microscopic investigation of phonon modes in SiGe alloy nanocrystals.* Phys. Rev. **B 69**, 235327, (2004).

[IV.40] W. Cheng, D. Marx, and S.-F. Ren. *Microscopic phonon theory of Si/Ge nanocrystals.* Front. Phys. China 3, 165, (2008).

[IV.41] A. D. Zdetsis, C. S. Garoufalis, and E. N. Koukaras. *Mixed silicon-germanium nanocrystals: a detailed study of Si_xGe_{47-x}:H.* J. Math. Chem. **46**, 942, (2009).

[IV.42] M. A. Abdulsattar. *SiGe superlattice nanocrystal infrared and Raman spectra: A density functional theory study*. J. Appl. Phys. **111**, 044306, (2012).

[IV.43] S. De Gironcoli. *Phonons in Si-Ge systems: An ab initio interatomic-force-constant approach.* Phys. Rev. **B 46**, 2412, (1992).

[IV.44] M. Franz, K. F. Dombrowski, H. Rucker, B. Dietrich, K. Pressel, A. Barz, U. Kerat, P. Dold, and K. W. Benz. *Phonons in $Ge_{1-x}Si_x$ bulk crystals.* Phys. Rev. **B 59**, 10614, (1999).

[IV.45] V.G. Deibuk, and Y.G. Korolyuk. *Molecular-dynamics simulation of the structure properties of $Ge_{1-x}Sn_x$ solid solutions.* Fizika Tverdogo Tela **35**, 283, (2001)

[IV.46] J. Tersoff. *New empirical approach for the structure and energy of covalent systems.* Physical Review **B 37**, 6991, (1988).

[IV.47] F. H. Stillinger, and T. A. Weber. *Computer simulation of local order in condensed phases of silicon.* Phys. Rev. **B 31**, 5262, (1985).

[IV.48] P. Venezuela, G. M. Dalpian, and J. R. da Silva. *Ab initio determination of the atomistic structure of Si_xGe_{1-x} alloy.* Phys. Rev. **B 64**, 193202, (2001).

[IV.49] Frank H. Stillinger and Thomas A. Weber. *Computer simulation of local order in condensed phases of silicon.* Phys. Rev. **B 31**, 5262, (1985).

[IV.50] A. S. Vasin, O. V. Vikhrova, and M. I. Vasilevskiy. *Phonon modes and Raman scattering in Si_xGe_{1-x} nanocrystals: microscopic modelling.* Phys. Status Solidi **C 10**, 701, (2013).

[IV.51] L. Verlet. *Computer "Experiments" on Classical Fluids. I. Thermodynamical Properties of Lennard-Jones Molecules.* Phys. Rev. **159**, 98, (1967).

[IV.52] M. Bauer, J. Taraci, J. Tolle, A.V.G. Chizmeshya, S. Zollner, David J. Smith, J. Menendez, Changwu Hu, and J. Kouvetakis. *GeSn semiconductors for band-gap and lattice engineering*. Appl. Phys. Lett. **81**, 2992, (2002).

[IV.53] J. Kouvetakis, J. Menéndez, and A.V.G. *Chizmeshya. Tin-based group IV semiconductors: new platforms for opto- and microelectronics on silicon*. Ann. Rev. Mater. Res. **36**, 497, (2006).

[IV.54] Y. Chibane and M. Ferhat. *Electronic structure of Sn_xGe_{1-x} alloys for small Sn compositions: unusual structural and electronic properties*. J. Appl. Phys. **107**, 053512, (2010).

[IV.55] N. Bhargava, M. Coppinger, J. Prakash Gupta, L. Wielunski, and J. Kolodzey. *Lattice constant and substitutional composition of GeSn alloys grown by molecular beam epitaxy*. Appl. Phys. Lett. **103**, 041908, (2013).

[IV.56] A.V.G. Chizmeshya, M.R. Bauer, and J. Kouvetakis. *Experimental and theoretical study of deviations from Vegard's law in the Sn_xGe_{1-x} system.* Chem. Mater. **15**, 2511, (2003).

[IV.57] R. Alben, D. Weaire, J. E. Smith, and M. H. Brodsky. *Vibrational properties of amorphous Si and Ge.* Phys. Rev. **B 11**, 2271, (1975).

[IV.58] M. Cardona (Ed.). Light Scattering in Solids, Springer, Berlin, Germany, (1975).

[IV.59] E. Kasper, M. Kittler, M. Oehme, and T. Arguirov. *Germanium tin: silicon photonics toward the mid-infrared.* Photon. Res. **1**, 69, (2013),

[IV.59] R. Cheng, W. Wang, X. Gong, L.F. Sun, P.F. Guo, H.L. Hu, Z.X. Shen, G.Q. Han, and Y.C. Yeo. *Relaxed and strained patterned germanium-tin structures: A Raman scattering study.* ECS J. Solid State Science and Technology **2**, 138, (2013).

[IV.60] C. Chang, H. Li, T.P. Chen, W.K. Tseng, H. Chen, C.T. Ko, C.Y. Hsie, M.J. Che, and G. Sun. *The strain dependence of $Ge_{1-x}Sn_x$ (x = 0.083) Raman shift*. Thin Solid Films **593**, 40, (2015).

[IV.61] S.J. Su, W. Wang, B.W. Cheng, W.X. Hu, G.Z. Zhang, C.L. Hue, Y.H. Zuo, Q.M. Wang. *The contributions of compositional strain to the phonon shift in $Ge_{1-x}Sn_x$ alloys.* Solid State Communications **151**, 647, (2011).

[IV.62] J. Zheng, S. Wang, T. Zhou, B. Cheng, and Q. Wang. *Single crystalline $Ge_{1-x-y}Si_xSn_y$ alloys on Si (100) grown by magnetron sputtering.* Optical Materials Express **5**, 287, (2015).

[IV.63] T. M. G. Mohiuddin, A. Lombardo, R. R. Nair, A. Bonetti, G. Savini, R. Jalil, N. Boninni, D. M. Basco, C. Galiotis, N. Marzari, K. S. Novoselov, A. K. Geim, A. C. Ferrari. *Uniaxial strain in grapheme by Raman spectroscopy: G peak splitting, Gruneisen parameters and sample orientation.* Phys. Rev. **B 79**, 205433, (2009).

Chapter V

Results on ZnO:Mn Thin Films

In this chapter we report the study on the structure, optical and electrical properties of undoped and doped-ZnO thin films that had been produced by RF-magnetron sputtering. The influence of the different replacing atoms on the structure and properties of the films will be explored.

V.1 Samples Description

ZnO thin films were grown by reactive sputtering on glass substrates. The target consisted of a 99.99% metal zinc wafer placed, inside the vacuum chamber, parallel to the substrate and 60 mm apart (see **Figure V.1**). A mixture of O_2 and Ar gases were used, with a relative oxygen fraction of 0.23. The growth was performed at a constant pressure of the order of 10^{-3} mbar and at substrate temperature of 50^{o}C. Some specific growths were performed at 400^{o}C, and these samples will be identified in the text. Radio frequency (13.56MHz) reactive sputter deposition was carried out after the chamber had reached a base pressure near 10^{-6} mbar. The deposition rate was between 1.2 to 3.4 nm min^{-1} and the grown layers had in general a sub-micrometer thickness.

Five groups of samples were prepared (see **Table V.1**). The first group comprises sputtered undoped ZnO thin films (for reference). The second group consisted on ZnO samples doped by implantation with different contents of Al or Mn ions. A high flux ion implanter (Danfysic model S1090) was used with an implantation energy of 150 keV and fluencies ranging from 1 x 10^{15} to 10 x 10^{15} atoms cm^{-2}. The third group includes ZnO doped thin films prepared by co-sputtering placing small pieces of Al or/and Mn (both 99.99% pure) above the Zn target but outside the erosion area, as illustrated in **Figure V.1b**. A forth group of samples consists of co-sputtered ZnO:Al thin films

followed by implantation with Mn ions. The fifth group of samples is composed of ZnO:Mn thin films grown by co-sputtering with two different Mn contents. This last group was designed for magnetic measurements. All samples were grown at 50°C and then annealed at 500 °C for 60min in air at atmosphere pressure.

The list of the samples used is indicated in **Table V.1**. For an easy identification of the samples, the terms '(sp)' or '(imp)' are added to indicate the method of preparation/ doping used.

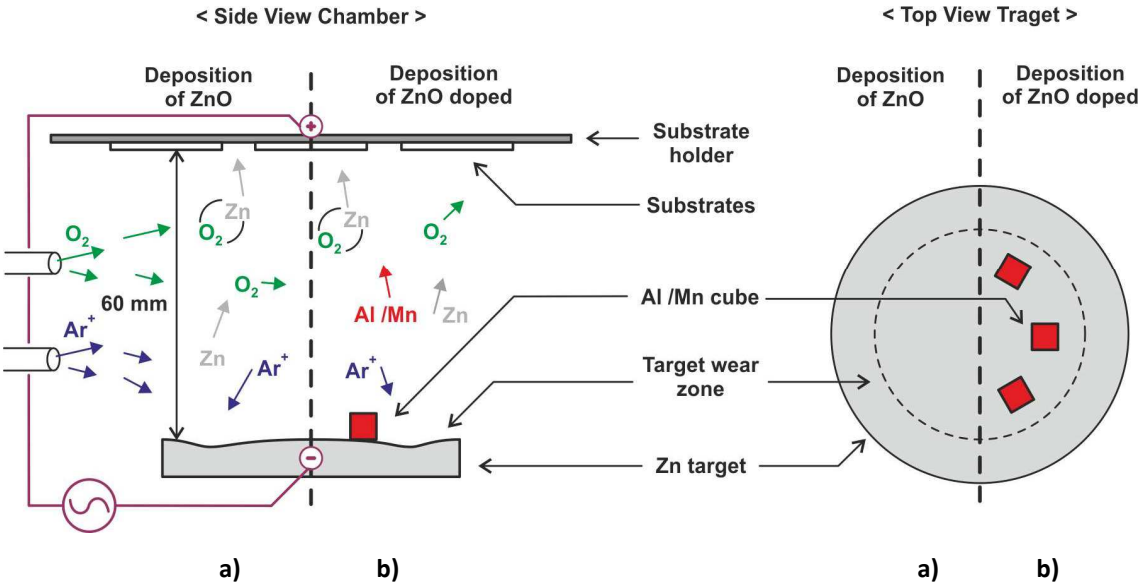

Figure V.1: Geometry and configuration of the essential elements necessary for the samples deposition. a) Configuration used to grow undoped ZnO thin films by RF-sputtering; b) Configuration used to growth doped ZnO with Al and / or Mn by RF- sputtering.

Table V.1: Description of the ZnO samples produced and used in this thesis.

Sample	Group	Preparation method	Dose
#1	1	ZnO(sp)	-
#2	2	ZnO(sp):Al(imp)	D1
#3		ZnO(sp):Mn(imp)	D1
#4			D2
#5			D3
#6	3	ZnO(sp):Al(sp)	
#7		ZnO(sp):Mn(sp)	D1
#8			D2
#9		ZnO(sp):Al(sp):Mn(sp)	
#10	4	ZnO(sp):Al(sp):Mn(imp)	D1
#11			D2
#12	5	ZnO(sp):Mn(sp)	D1
#13			D2

The ion doping implantation profile used for all samples was centred at ≈ 50 nm bellow the surface. For all the samples, the centre of the profile implantation is much lower than the film thickness. The samples annealing at 500 ^{o}C was performed to recover the sample crystallinity (destroyed by ion implantation and also to promote the ion diffusion and activation. In order to verify if the post-annealing treatment carried out was efficient to spread the Mn ions into the ZnO thin film, a gradual etching of the sample surface was performed with diluted hydrochloric acid (3% HCl in de-ionized water at room temperature) and the sample analysed by Raman scattering. After removing at least 350 nm, the presence of the Mn ions is still observed by Raman spectroscopy, meaning that Mn ions diffuse over a larger distance than that corresponding to the effective implantation depth.

The thickness and optical parameters of the ZnO films were determined by optical transmittance measurements in the UV-vis-NIR range (300–2500 nm), using a Shimadzu UV-3101-PC spectrophotometer. The electric resistivity of the samples was measured, at room temperature, in a dc system using the Van der Pauw technique. The composition of the films was determined by TOF-ERDA (time-of-flight elastic recoil detection analysis), RBS (Rutherfore Back Scattering) or/and PIXE (Proton Induced X-Ray Emission). TOF-ERDA measurements were done using 25.5 MeV iodine ions. The beam current during the measurement was ≈ 3 nA. Detector was placed at 37.5^{o} and the angle between beam and sample surface during the measurements was 20 ^{o}. For the 5th group of samples, the Mn content in the films was obtained by means of a combination of RBS together with PIXE experiments, using an energy of 2 MeV and two detectors, namely, Si(Li) and Passivated Implanted Planar Silicon (PIPS). The micro-structure of the films was analyzed by means of X-ray diffraction and micro-Raman scattering. X-ray experiments were performed at room temperature in a Philips PW1710 diffractometer using Cu Kα radiation, in a Bragg–Brentano geometry, in the range 10 ^{o} < 2 θ < 80 ^{o}. Room temperature micro-Raman scattering spectra were measured in a backscattering geometry on a Jobin–Yvon T64000 spectrometer equipped with a liquid nitrogen cooled CCD detector, in a frequency range of 200–780 cm^{-1}, using the 514.5 nm excitation line of an Ar^{+} laser, with an incident power of 4 mW in a ≈ 1 μm spot. Resonant Raman scattering spectra were measured at room temperature using a Jobin-Yvon LabRaman HR spectrometer equipped with a multio-

channel air cooled (-70 ^{o}C) CCD detector, in a backscattering geometry, using the 325 nm excitation line of a He-Cd laser. The photon energy (3.815 eV) is well above the E_g of all the films studied.

V.2. Optical, Electrical, Chemical and Structural Characterization Results

V.2.1. Optical Characterization

All the ZnO thin films produced, undoped and doped, are highly transparent in the visible-near IR range, with the Mn doped samples having a light yellow tinted colouring. The transmission spectra were fitted using the Minkov method **[V.1]** and a classical Lorentz function for the dispersion of the ZnO dielectric function. From this, the thickness and the optical parameters of the films were obtained. **Figure V.2a** and **V.2b** shows two typical transmission spectra and corresponding fit for undoped ZnO and Mn-doped ZnO, respectively.

Table V.2 provides the relevant characterization parameters of the analysed samples and the film thickness obtained by the transmission fit is shown. The band gap of ZnO is known to increase with Mn doping **[V.2]** and our fit also confirmed it.

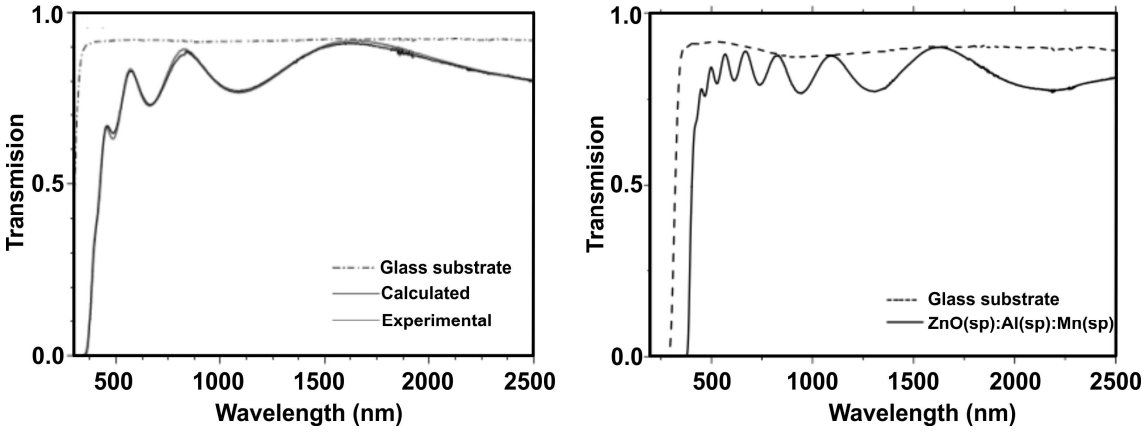

Figure V.2: Transmittance spectrum and corresponding fit of (a) undoped ZnO sample (#1) and (b) ZnO(sp):Al(sp):Mn(sp) sample (#9). The spectrum of glass substrate used in each case is also shown for comparison.

Table V.2: Relevant characterization parameters of the samples presented here. sp – sputtering; imp – ion implantation.

Sample	Preparation method	Thickness (nm)	Al (at. %)	Mn (at. %)	Crystallites size (nm)	Resistivity (Ω cm)
#1	ZnO(sp)	625	-	-	25.5	>2 x 10^8
#2	ZnO(sp):Al(imp)	350	≈ 0.5	-	21.3	≈ 0.1
#3	ZnO(sp):Mn(imp)	515	-	1.1	18.4	>2 x 10^8
#4	ZnO(sp):Mn(imp)	515	-	3.3	20.5	>2 x 10^8
#5	ZnO(sp):Mn(imp)	515	-	5.3	20.5	>2 x 10^8
#6	ZnO(sp):Al(sp)	780	0.5	-	20.0	≈ 0.05
#7	ZnO(sp):Mn(sp)	900	-	0.4	18.4	>2 x 10^8
#8	ZnO(sp):Mn(sp)	830	-	1.1	11.8	>2 x 10^8
#9	ZnO(sp):Al(sp):Mn(sp)	412	1.1	1.6	11.8	>2 x 10^8
#10	ZnO(sp):Al(sp):Mn(imp)	780	0.5	1.5	19.0	≈ 0.05
#11	ZnO(sp):Al(sp):Mn(imp)	780	0.5	2.2	20.5	≈ 0.05
#12	ZnO(sp):Mn(sp)	907	-	1.8	-	-
#13	ZnO(sp):Mn(sp)	854	-	2.9	-	-

V.2.2. Compositional and Structural Characterization

Figure V.3 shows a typical X-ray diffraction spectra obtained using the Bragg-Brentano geometry of one ZnO thin film, in the as-grown form and after the annealing treatment.

The X-ray diffraction results, indicates that ZnO thin films have a Wurtzite structure, polycrystalline and strongly preferential orientated with the *c*-axis, *i.e.*, perpendicular to the substrate surface, independent of the doping method and concentration. From the XRD results it is also seen, as expected, that the annealing treatment results in the crystalline quality increase of the samples (crystal size and crystalline fraction). **Figure V.4** shows typical X-ray diffractograms, in the region of the (002) peak, for two Mn implanted doses (ZnO:Mn), in which is seen a light shift of the peak position, for higher 2θ values, with the increase of Mn in the ZnO lattice, keeping however the peak shape and the FWHM. In **Figure V.5** the impact of the Mn doping on the ZnO lattice is shown by the dependence of the ZnO *c*-parameter on Mn content. It is assumed that hydrostatic strain in the films is relaxed because they are polycrystalline. The observed decrease of the c-parameter as the Mn concentration increases is in agreement with the behaviour observed for low Mn content **[V.3, V.4]** where it was verified that only above a certain threshold the *c*-parameter starts to increase with the increase of the Mn content. The average domain size (D) was

calculated analysing the (002) diffraction peak, according the Scherrer procedure described in **Ref. [V.5]** and the results are presented in **Table V.2**. The contents of Al or/and Mn, obtained by TOF-ERDA are also given in **Table V.2**.

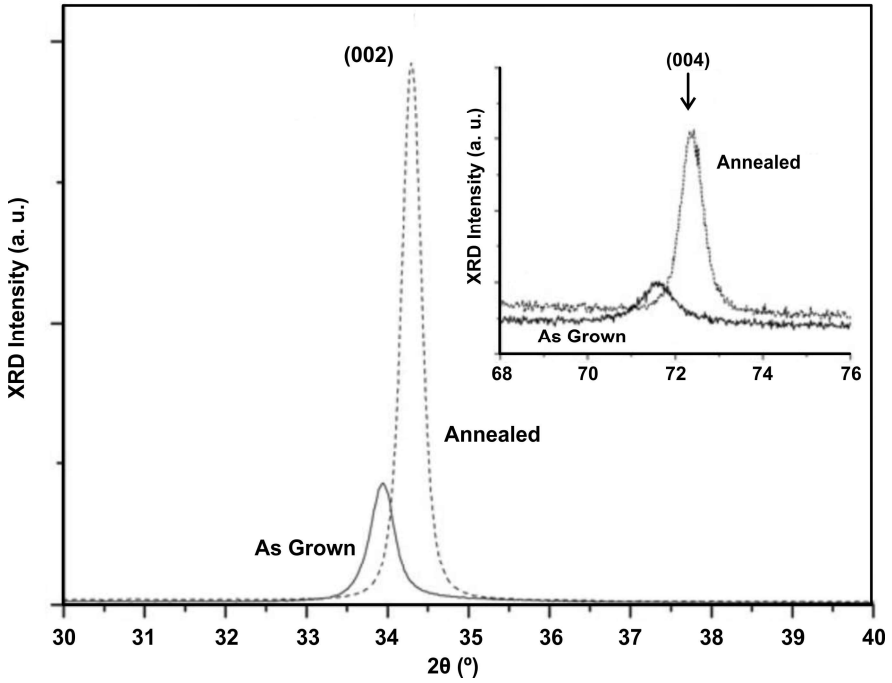

Figure V.3: XRD patterns, in the 30-40° range, of one undoped ZnO sample (#1), before and after the annealing treatment. Inset shows the XRD in the range 68-76° for the same sample.

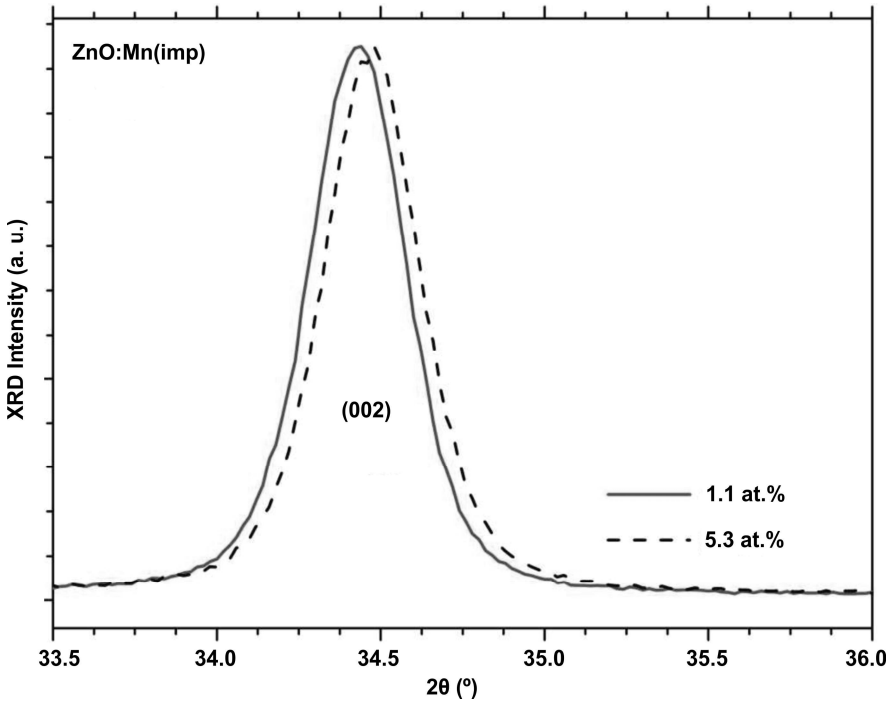

Figure V.4: XRD patterns, in the (002) Bragg reflection peak region, of two Mn implanted ZnO samples.

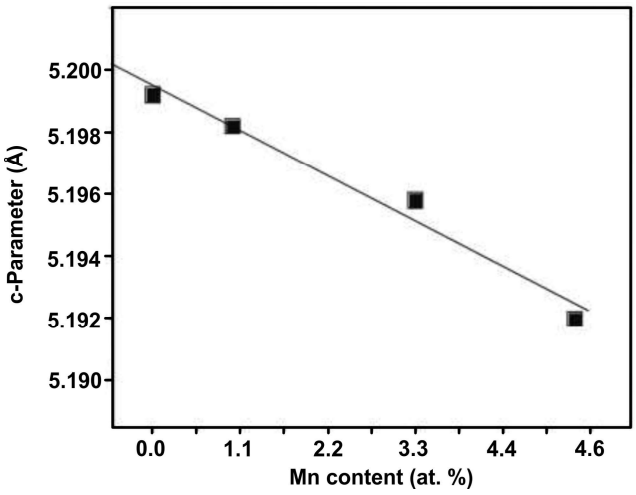

Figure V.5: ZnO c-parameter as a function of the Mn content.

V.2.3. Electrical Characterization (Van der Pauw)

The electrical resistivity (ρ) of the films was measured using the Van der Pauw method and the results are presented in **Table V.2**. According to the literature, ZnO as-grown typically presents a *n*-type behaviour, associated with the O vacancies or Zn interstitials **[V.6]**. Our nominally pure ZnO thin films are highly resistive (>2x10^8 Ωcm), in contrast Al doped films are conductive (≤ 0.1 Ωcm), either the ones prepared by co-sputtering (sample ZnO(sp):Al(sp) #6) or the ones implanted (sample ZnO(sp):Al(imp) #2). Moreover, the incorporation in the ZnO lattice even of very small amount of Mn, either by co-sputtering (samples ZnO(sp):Mn(sp) #7 and #8) or by implantation (samples ZnO(sp):Mn(imp) #3, #4, and #5) result in a strongly increase of the resistivity. However samples doped with both ions (Al and Mn) exhibit different electrical behaviours, depending on the doping method. If Mn is implanted into a conductive ZnO(sp):Al(sp) film, it remains conductive (samples ZnO(sp):Al(sp):Mn(imp) #10 and #11); nevertheless, if Mn and Al are simultaneously co-sputtered, samples are highly insulating (sample ZnO(sp):Al(sp):Mn(sp) #9). This effect was also observed in other Al–Mn co-sputtered samples (not shown in here).

These results seem to indicate that, if Al ions are previously incorporated in the ZnO crystal lattice, mainly occupying Zn sites and acting as shallow donors **[V.7]**, the subsequent implantation of Mn ions does not strongly modify the lattice and so the films remain conductive. In contrast, the co-sputtered samples are highly resistive (more than five orders of magnitude higher) which seems to indicate that, when both

ions are simultaneously incorporated, Al ions are not able to replace properly Zn atoms in the lattice. This huge difference in the conductivity of these two sets of ZnO:Al:Mn samples, is too large to be attributed just to a decrease in the electron mobility due to additional lattice defects.

V.3. Spectroscopy of Faraday Rotation

The spectroscopy of Faraday rotation was performed only for ZnO(sp):Mn(sp) samples. Since it was been predicted that ZnO **[V.8]**, among other non-magnetic oxide semiconductors and insulators **[V.9]**, could become ferromagnetic at room temperature after doping with Mn, just a few percent (below the solubility limit), an intense research activity on ZnO started. As already mentioned in **Chapter I**, ZnO is a potentially interesting material for spintronics, simultaneously magnetic, semiconducting and optically transparent. Numerous studies of ZnO:Mn produced by a variety of techniques, undertaken so far, have not been able to convincingly confirm this prediction, even thought there are several reports in the literature appointing to the ferromagnetism of ZnO:Mn thin films at room temperature **[V.10, V.11]** or below it **[V.12]**. It was suggested **[V.13]** that the ferromagnetism of ZnO films doped with magnetic ions is unrelated to the ions and is rather due to native defects like oxygen vacancy, similar to other diamagnetic oxides like TiO_2, HfO_2 and In_2O_3 **[V.14]**. Such defects, of course, exist already in undoped materials, although the doping can enhance their formation **[V.12]**. However, surfaces and grain boundaries are more important than the doping, in the opinion of the authors of Refs. **[V.13, V.14]**, so the ferromagnetism can be observed only in very thin films or nanostructures. An extensive study **[V.15]** was published, based on an analysis of the data from the literature and new experiments, suggesting that grain boundaries and related vacancies are the intrinsic origin for room temperature ferromagnetism in ZnO. Based on this conclusion, nanograined pure and Mn-doped ZnO films were prepared, which have revealed reproducible ferromagnetism at room temperature, even for pure ZnO films **[V.15]**. Inspired by these findings, a new attempt to achieve the ferromagnetism in nanocrystalline ZnO thin films grown by RF co-sputtering with a different Mn fraction was undertaken.

V.3.1. Experimental Details

The samples of the fifth group (see **Table V.1**), ZnO(sp):Mn(sp), were produced for the study of the Faraday effect, as described previously. In addition to the measurements performed to all samples, *i.e*. XRD, optical transmittance and Raman spectroscopies, RBS and PIXE, two additional analyses were performed: magnetic resonance and Faraday rotation.

The electron paramagnetic resonance measurements were performed in the X band (~9.5 GHz) at room temperature using a Bruker ESP 300E spectrometer. Angular dependence of the magnetic resonance signal was measured in the in-plane and out-of-plane geometry.

The Faraday rotation measurements were performed using a setup including a GMW 5403FG electromagnet (magnetic field up to 1 T), a Xe and/or halogen lamp, two polarizers, a Triax 320 monochromator and a UV–VIS PTM detector, as explained in S**ection II.5.3**. The polarizers were set to form an angle of 45° between their axes in order to achieve the highest resolution **[V.16]**. The Faraday rotation angle was determined by the relation,

$$2\theta_F = \frac{I^{\uparrow} - I^{\downarrow}}{I^{\uparrow} + I^{\downarrow}} \qquad \textbf{\{V.1\}}$$

where $I^{\uparrow}$ and $I^{\downarrow}$ are the intensities of the transmitted light for two directions of the magnetic field.

V.3.2. Results

The ZnO(sp):Mn(sp) samples used had a film thickness of the order of 1 μm. This means that the material possesses a large overall area of grain boundaries and therefore one might expect ferromagnetism in it according to the results reported by others authors **Ref. [V.15]**. The films are transparent and nanocrystalline, with wurtzite-structure grains with a typical size of 20 nm and with a preferential orientation of *c*-axis perpendicular to the surface. According to the Raman spectroscopy data (presented and discussed in next section), Mn mostly substitutes Zn in the lattice sites.

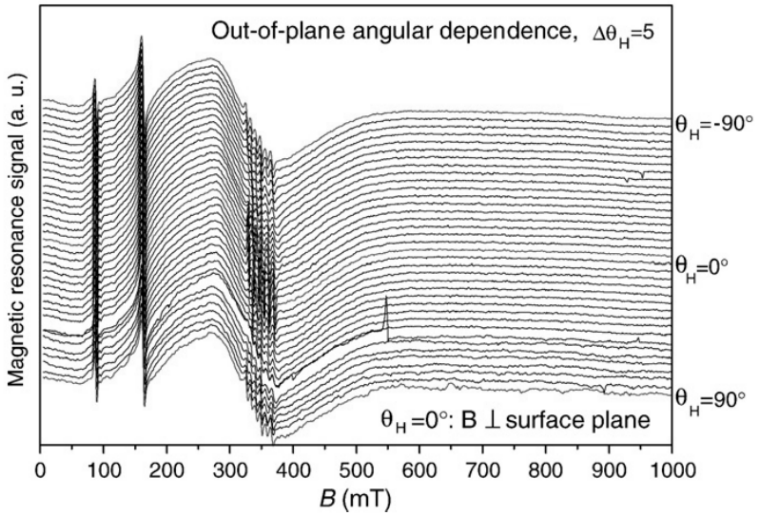

Figure V.5: Out-of-plane angular dependence of MR measured at room temperature for sample ZnO(sp):Mn(sp) #12.

V.3.2.1. Magnetic Resonance

Figure V.5 shows a set of magnetic resonance curves of one of the ZnO(sp): Mn(sp) films, measured for different angles between the magnetic field (B) and the *z*-axis (perpendicular to the film surface). From **Figure V.5** it can be seen that no angular dependent signal was found. The magnetic resonance shows two narrow lines at B ≈ 100 mT and B ≈ 170 mT, a broad band centred at ≈ 350 mT and narrow lines superimposed to the broad band. It was checked that the narrow paramagnetic line at B ≈ 100 mT has its origin in a contamination of the resonance cavity, and the second narrow line at B ≈ 170 mT appears also in the spectrum of the substrate (measured alone). Only the broad band centred at approximately 350 mT is related to the film and can be attribute to paramagnetic Mn^{2+} ions. The narrow lines superimposed to the broad band can be interpreted as being due to the hyperfine structure of isolated Mn^{2+} ions incorporated in the ZnO host on Zn sites. In specific regions with higher concentration of magnetic ions, the line width should increase due to the dipole–dipole interaction of the paramagnetic ions, so that a broad band appears, with the hyperfine structure of the spectra being obscured by the dipole–dipole broadening and breaks down due to the exchange interaction. Furthermore, the broad band is isotropic, with no out-of-plane angular dependence that should appear due to the demagnetization factors of a film, if the signal were of ferromagnetic origin **[V.17]**. Since no temperature-dependent magnetic resonance measurements were

performed, it is not completely excluded that an anti-ferromagnetic interaction between the Mn ions can exist. Such an interaction, tentatively attributed to anti-ferromagnetic parasitic phases, was detected in **Ref. [V.18]**, however, for a higher Mn content (5 % at.). The absence of any considerable nearest-neighbour interaction between the Mn ions in these samples is suggested by the proportionality of the magnetic resonance signal to the Mn content.

V.3.2.2. Faraday Effect

The spectral dependence of the Faraday rotation angle, θ_F, was measured independently for (i) the ZnO:Mn films on glass substrates and (ii) the corresponding substrates. As a first approximation, the contribution of the film to ϑ_F was evaluated by subtracting the two spectra. Such a simplified procedure is justified by the fact that the interference fringes, manifest of the multiple reflections of light at the film/substrate interface, are not significant either in the measured Faraday effect spectra (see **Figure V.6**) or in the transmittance spectrum (inset to **Figure V.6**).

The validity of this approximation was checked by the calculation of the corresponding spectra using the transfer matrix formalism **[V.19]**. The dependence of ϑ_F on magnetic field was found linear in the range of 0 – 1.0 T in all cases. The spectra of the Verdet constant, $V = \vartheta_F / (Bd)$ for the two films of **Figure V.6** and also for ZnO(sp):Mn(sp) #13 film are shown in **Figure V.7**.

From **Figures V.6** and **V.7** one can see that the Faraday effect in the ZnO(sp):Mn(sp) film is negative ($\vartheta_F < 0$), which is associated with paramagnetism, while the Verdet constant is positive ($V > 0$) for pure ZnO, in the spectral range well below the gap, which is characteristic of diamagnetic materials, as expected since pure crystalline ZnO is diamagnetic **[V.20]**. In the latter case, as the photon energy approaches E_g from below, the Verdet constant changes its sign. This is typical of non-magnetic semiconductors where the (paramagnetic) Faraday effect, in the vicinity of the energy gap, is associated with excitonic transitions **[V.21]**. However, the negative Faraday effect observed for the ZnO(sp):Mn(sp) film in the whole spectral range indicates its paramagnetism, presumably due to the presence of the Mn ions. The complex spectral behaviour of the Faraday rotation spectra in Mn-doped II–VI semiconductors is attributed to several mechanisms acting simultaneously **[V.21]**, such

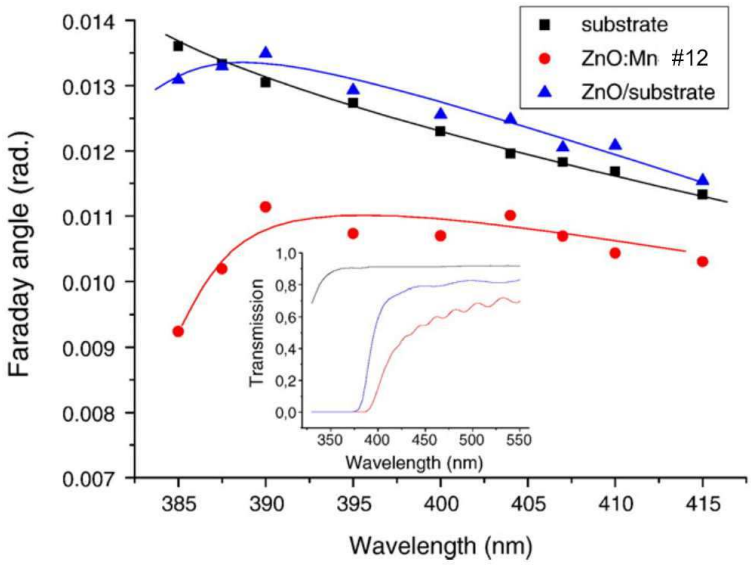

Figure V.6: Spectral dependence of the Faraday rotation angle for glass substrate, ZnO(sp):Mn(sp) sample (#12), and undoped ZnO film on glass substrate (#1). The lines are guides to the eye. Inset: transmittance spectra of the three samples.

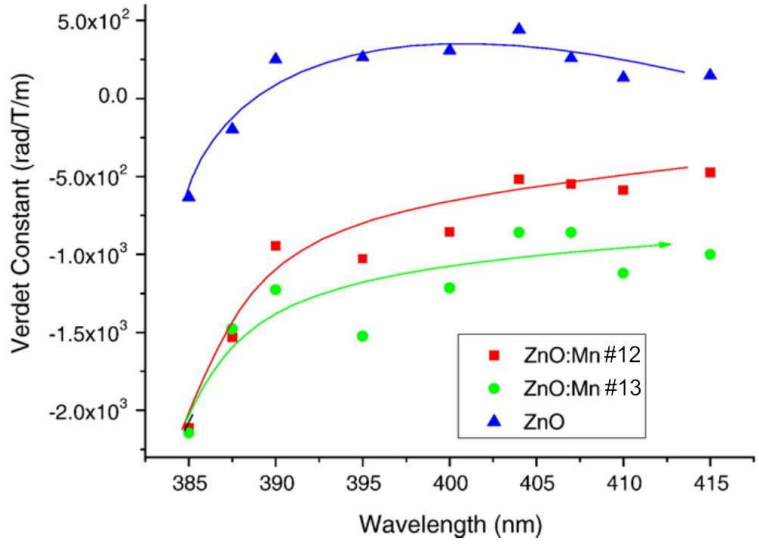

Figure V.7: Spectral dependence of the Verdet constant obtained from the spectra of Figure V.6 and a similar spectrum of sample ZnO(sp):Mn(sp) (#13). The lines are guides to the eye.

as the excitonic one and that involving transitions within the $3d^5$ multiplet of the Mn^{2+} ion. By comparing the spectra of samples ZnO(sp):Mn(sp) #12 and #13 with different Mn contents (1.8 and 2.9 at.%, respectively) in **Figure V.7**, one can conclude that the Mn^{2+} ion-related Faraday effect mechanism dominates below the gap since the shape of the spectrum is similar for both doped samples and the measured value of the Verdet constant increases proportionally with the Mn content. When the photon

energy approaches E_g (≈ 3.2 eV for doped films), the samples ZnO(sp):Mn(sp) #12 and #13 show nearly the same Faraday effect implying that a mechanism not directly related to the presence of Mn^{2+} ions, takes over. The maximum absolute value of the Verdet constant obtained is approximately 3 times smaller than that found for $Zn_{0.9}Mn_{0.1}O$ single crystal in Ref. **[V.20]**, which might be simply due to a smaller E_g (higher Mn content) in the sample studied here. If it is taken into account that the band gap energy in the undoped sample is larger than in ZnO(sp):Mn(sp) #12 and #13 (see inset in **Figure V.6**), one can guess that this mechanism also becomes stronger as $\hbar\omega \to E_g$ in this sample (although the setup did not allow for reliable measurements beyond 385 nm). Then, most likely, the Faraday rotation mechanism involves just the interband optical transitions (not bound excitons), which are less affected by the Mn-doping.

V.4. Non-resonant Raman Spectroscopy Results

V.4.1. Undoped ZnO: Symmetry Analysis

The wurtzite-type lattice structure has a basis of four atoms (n = 4) in the unit cell (see **Figure I.21** in **Section I.4**). In the case of a ZnO wurtzite crystal, two molecular units of Zn-O are present. The number of phonon modes amounts to $3n$ = 12, with three acoustic (one longitudinal, LA, and two transverse, TA) and nine optical phonon branches (three longitudinal, LO, and six transverse, TO), as shown in **Table V.3**. In the Γ-point of the Brillouin zone, the optical phonons have the following irreducible representations **[V.22]** (see **Section III.8.2.**):

$$\Gamma_{opt} = A_1 + 2B_1 + E_1 + 2E_2$$

Table V.3: Phonon modes for ZnO

Type	Quantity		Short Designation	Quantity	Modes
Acoustic	3	Longitudinal	LA	1	A_1
		Transverse	TA	2	E_1
Optical	9	Longitudinal	LO	3	A_1, E_1
		Transverse	TO	6	A_1, E_1, E_2

where A and B modes are non-degenerate, while the *E* modes are two-fold degenerate. One A_1 mode and one E_1 mode are the acoustic phonons. The nine optical phonons are divided into one A_1 branch (both Raman and IR active), one doubly degenerate E_1 branch (both Raman- and IR active), two doubly degenerate E_2 branches (Raman-active only, non-polar modes) and two inactive B_1 branches. Therefore there are four Raman-active phonons at the centre of the Brillouin zone. The Raman and IR active phonons A_1 and E_1 are polar modes and, therefore, each of them splits into LO and TO modes, with different frequencies, due to the macroscopic electric field of the LO phonons. Note that it does not mean an increase of the total number of modes because, exactly in the Γ-point, the LO and TO modes remain degenerate since the electric field vanishes at infinity and for any small but finite wave vector only three $A_1 + E_1$ modes exist. For instance, for $\vec{q}$ parallel to the *c*-axis, only the A_1 (LO) and (double degenerate) E_1 (TO) modes exist, while for $\vec{q}$ perpendicular to the c-axis, the two TO modes correspond to different representations, $A_1 + E_1$. The TO–LO splitting is considerably larger than the anisotropy-related $A_1 - E_1$ separation **[V.23]**. The (near) zone-centre optical phonon frequencies lie between approximately 100 and 600 cm^{-1}.

The Raman scattering cross-section of the LO phonon modes is determined by both optical deformation potential (ODP) and Fröhlich electron–phonon interaction. The Fröhlich mechanism is forbidden by the formal selection rules, which correspond to phonons with exactly zero momentum ($\vec{q}$ = 0) **[V.24]**. However, when the excitation approaches the band gap energy, a strong LO resonance is observed which is mainly driven by the Fröhlich interaction of free excitons and phonons close to (but not exactly at) the Γ-point, while the less pronounced TO resonance is due to interaction with continuum electron-hole states via the ODP **[V.25]**.

For polycrystalline samples, the Raman mode frequencies may depend on growth conditions affecting the sample crystalline quality, orientation, and size of the crystallites. The Raman modes are typically located around the following values: A_1(TO) $\cong$ 380 cm^{-1}, A_1(LO) $\cong$ 574 cm^{-1}, E_1(TO) $\cong$ 407 cm^{-1}, E_1(LO) $\cong$ 583 cm^{-1}, $E_2^{low} \cong$ 100 cm^{-1}, and $E_2^{high} \cong$ 438 cm^{-1}. Moreover, possible relaxation of the Raman selection rules can occur, for instance caused by disorder, and the result is that some "forbidden" (by selection rules) modes can appear in the Raman spectra. The frequency of the B_1 (low and high) silent modes has been calculated as 260 and 540 cm^{-1} **[V.26]** or 260 and 552 cm^{-1} **[V.27]**, respectively. **Table V.4** lists all these Raman modes.

Table V.4: Optical Raman modes frequencies of ZnO wurtzite-type lattice structure

	Mode	Type	Mode short name	Frequency (cm^{-1})
"Allowed" modes	A_1	Polar, Transverse	A_1(TO)	≅ 380
		Polar, Longitudinal	A_1(LO)	≅ 574
	E_1	Polar, Transverse	E_1(TO)	≅ 407
		Polar, Longitudinal	E_1(LO)	≅ 583
	E_2	Non-polar	E_2^{low}	≅ 100
		Non-polar	E_2^{high}	≅ 438
"Forbidden" modes	B_1	Non-polar	B_1^{low}	≅ 260
		Non-polar	B_1^{high}	≅ 540

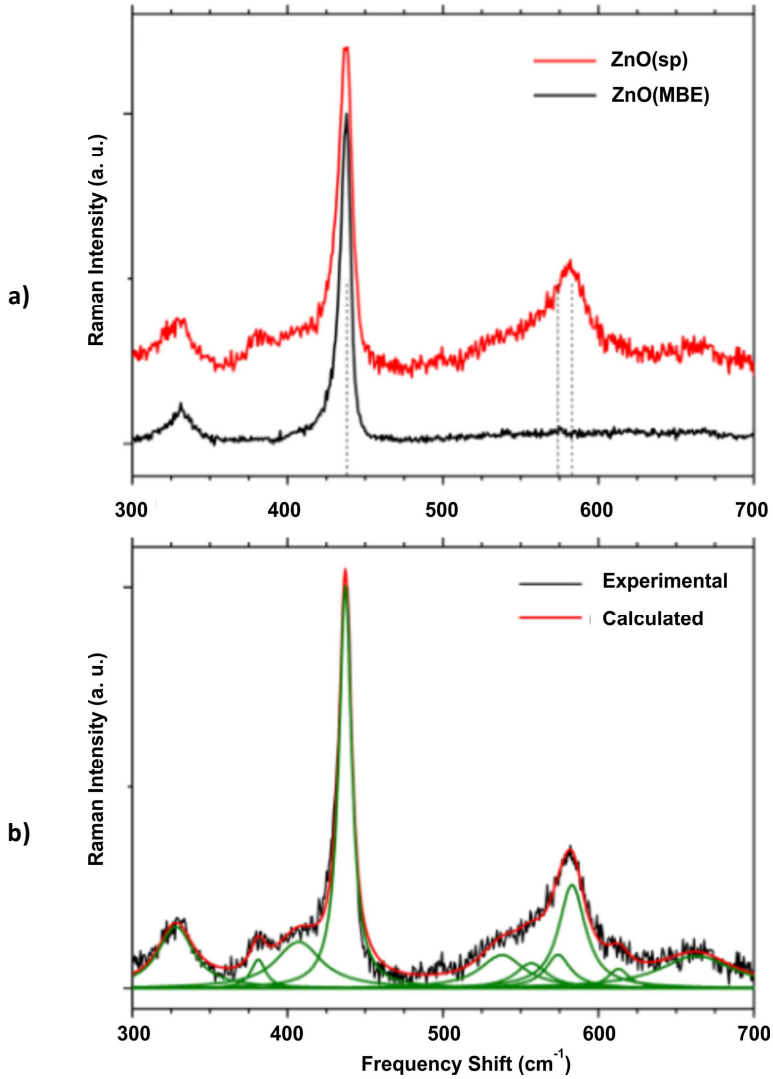

Figure V.8: (a) Raman spectra of two ZnO samples, one grown by MBE and the other by RF-sputtering. Dashed vertical lines in this and subsequent figures are at 438, 574, and 583 cm^{-1} corresponding to the E_2^{high}, A_1(LO) and E_1(LO) modes, respectively. (b) Experimental Raman spectra of the ZnO(sp) film (black curve) and corresponding fit (red curve). Also shown the ten Lorentzians used for the fit (green curves), centred at 328 (E_2^{high}-E_2^{low}), 381 (A_1(TO)), 407 (E_1(TO)), 437 (E_2^{high}), 538 (B_1^{high}), 574 (A_1(LO)), 583 (E_1(LO)), 557 (B_1^{high}), 613 (TA + A_1(TO)), and 663 (TA + A_1(TO)) cm^{-1}. The measurements were performed with Raman system 1 (see Section III.8.1) with the laser excitation 512 nm, and an optical power on the samples' surface of ≈1 mW (low power was used to avoid anneling of the fim).

Figure V.8a shows the Raman spectra of two undoped ZnO samples, one grown by MBE and the other grown by RF-sputtering. The positions of the main Raman-active modes of ZnO, indicated by the vertical dashed lines, are 438, 574, and 583 cm^{-1}, that correspond to E_2^{high}, A_1(LO) and E_1(LO) modes, respectively. The main difference between these two Raman spectra is observed in the range of the A_1(LO) and E_1(LO) phonon modes (570–590 cm^{-1}), where a broad band appears only in the spectrum of the sputtered sample. For Raman backscattering from a (001) crystal plane, only E_2 and A_1(LO) modes are allowed by the symmetry selection rules **[V.28]**. This is valid for the MBE-grown sample, except that (i) there is a mode at 330 cm^{-1} and (ii) the A_1(LO) mode is unexpectedly too weak. The peak at $\cong$ 330 cm^{-1} is probably the second-order scattering associated to (E_2^{high} - E_2^{low}) **[V.25, V.28]** and has been observed for both single crystal and polycrystalline samples in various configurations **[V.24-V.29]**. The low intensity of the allowed A_1(LO) has been attributed to the "destructive interference" between the Fröhlich and ODP mechanisms **[V.23, V.30]**.

Figure V.8b shows the measured Raman spectrum of the sputtered ZnO(sp) thin film fitted with ten Lorentzian curves. Besides the already mentioned difference in the region of the A_1(LO) and E_1(LO) phonon modes (broad band in the 570–590 cm^{-1} range), some smaller features are also revealed by the fitting. Among these, the TO-type phonon modes (A_1(TO) at 381 cm^{-1} and E_1(TO) at 407 cm^{-1} **[V.23]**) are identified. Their presence in the spectra can be understood by random orientation of the crystallites in the film, since these modes can be allowed only for certain scattering configurations. However, the major cause of the clear relaxation of the $\vec{q}$ = 0 selection rule, verified in the spectrum of the RF-sputtering grown films, is probably related to crystal lattice disorder due to intrinsic defects. Indeed, this is also the likely reason for the large enhancement of the LO-phonon-related scattering (the 570–590 cm^{-1} band). It may be due to the "forbidden" Fröhlich interaction, which becomes overwhelming under resonance conditions as have been shown before for similar samples **[V.31]**. Here, far from interband resonance, it can be enhanced by the presence of defects **[V.30, V.32]**. In the impurity-induced process, the momentum conservation is relaxed and phonons with $\vec{q}$ vectors away from the Γ-point can participate in the Raman scattering. Indeed the larger vectors greatly enhance the Fröhlich contribution, which

is known as Gogolin–Rashba mechanism **[V.32]**. The enhancement of the Fröhlich mechanism of Raman scattering can also be associated with phonon confinement in nanocrystalline grains as reported for quantum dots (QDs) **[V.33]**; however, this effect is unlikely to be important in these samples, since most of the grains are considerably larger than typical QDs.

As shown in **Figure V.8b**, the TO and LO-type bands activated by crystal lattice disorder in the ZnO(sp) sample are located around 380–407 cm^{-1} and 573–582 cm^{-1}, respectively. These frequencies may slightly change with the orientation of the crystallite *c*-axis in respect to the $\vec{q}$ vector transferred by the scattered photon. Three further contributions (557, 613, and 663 cm^{-1}) are necessary to fit the spectrum. These contributions have been observed before (see **Table V.5**) but their assignment is not unanimous.

Table V.5: Characteristic phonon modes observed in the spectra of undoped ZnO(sp) samples.

Raman shift in this work (cm^{-1})	Literature data (cm^{-1})	Process	Brillouin zone points
328	330 **[V.23]**	E_2^{high} - E_2^{low}	Γ
381	380 **[V.25]**	A_1(TO)	Γ
407	407 **[V.25]**	E_1(TO)	Γ
437	437 **[V.25]**	E_2^{high}	Γ
538	526 **[V.34]**	$E_2^{high} + E_2^{low}$	Γ
557	552 **[V.29]**	B_1^{high}	Γ
574	574 **[V.25]**	A_1(LO)	Γ
583	583 **[V.25]**	E_1(LO)	Γ
613	648 **[V.23]**	TA + A_1(TO)	H, M
663	666 **[V.23]**	TA + A_1(LO)	M

V.4.2. Mn- (and Al)- Doped ZnO

The main objective here is to study the effect of the Mn doping in the ZnO lattice on the vibrational modes. Let us recall that our goal has been to obtain ZnO-based thin films conductive, transparent and magnetic. As already pointed out in **Section V.2.3**, the desired electrical properties are only achieved if the lattice is doped with Al. In this way, samples containing both doping elements were chosen for the vibration spectroscopy study.

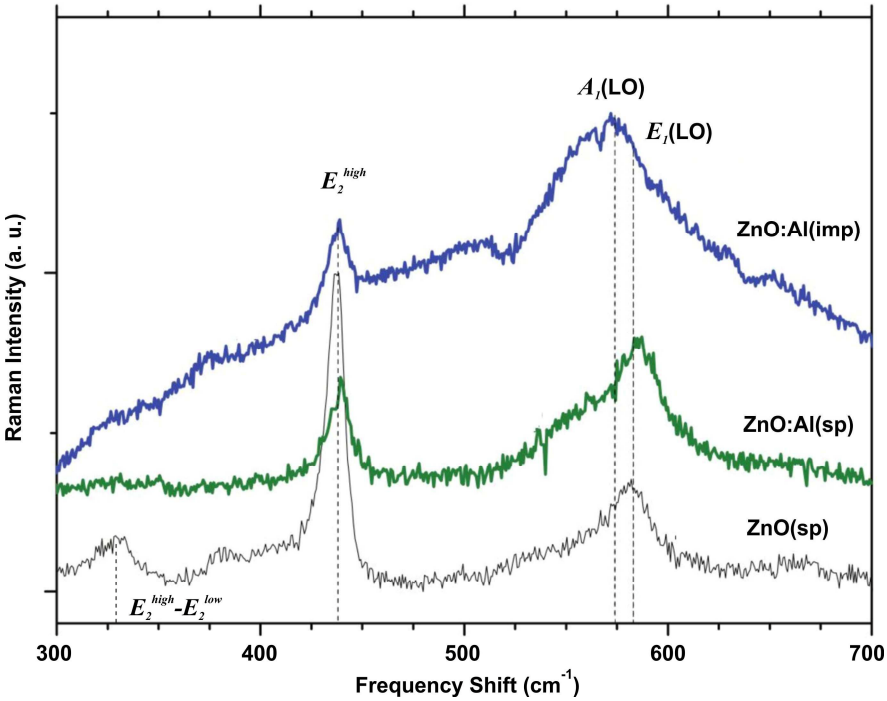

Figure V.9: Raman spectra of ZnO thin film (black curve) and ZnO thin films doped with Al (≈ 0.5 at. %) by co-sputtering (sp: (#6)) (green curve) and by ion implantation (imp: (#2)) (blue curve). The measurements were performed with Raman system 1 (see Section III.8.1) with the laser excitation 512 nm, and an optical power on the samples' surface of ≈1 mW (low power was used to avoid anneling of the fim).

V.4.2.1. ZnO:Al Samples

Raman spectra of two ZnO:Al (aluminium concentration ≈ 0.5 at. %) samples, one doped by co-sputtering, ZnO(sp):Al(sp), and the other by implantation, ZnO(sp):Al(imp), are shown in **Figure V.9**). The spectrum of the ZnO(sp) (as-grown one, i.e. undoped) sample is also shown for comparison. As expected, the inclusion of a dopant, independently of the doping method used, deteriorates the ZnO crystalline quality as seen in **Figure V.9** by the strong intensity reduction of the E_2^{high} mode. Observing the spectra of these samples, it is seen that only Raman features related to ZnO lattice are present, *i.e.* no spectral features associated with Al atoms are seen, in agreement with a previous report on Raman scattering spectroscopy in this material **[V.35]**.

The relevant ZnO Raman modes remain for both methods of doping. The peak position of the 438 cm^{-1} non-polar mode (E_2^{high}) keeps constant indicating the absence of considerable strain in the ZnO lattice for this amount of Al. However, the intensity ratio between this mode, E_2^{high}, and the polar longitudinal modes in the region

560–590 cm^{-1} (A_1(LO) and E_1(LO)) decrease in both samples, being this reduction higher for the implanted sample than for the co-sputtered one. The 330 cm^{-1} two-phonon mode (E_2^{high} - E_2^{low}), present in the non-doped ZnO sample, is not observed in the Al doped samples, in agreement with the observed decrease of the E_2^{high} mode intensity probably caused by the decrease of the crystalline quality with the doping.

In the LO phonon range, it is seen that the already characterized bands become broader and the peak positions are slightly changed. The fitting results (using Lorentzian functions) show a red shift for the Al-implanted sample and a small blue shift for the sputtered one, as compared to the undoped ZnO sample. It was also verified that the blue shift (sputtered samples) does not change when the Al content increases to 1 at. % (spectrum not shown). Therefore, this shift cannot be attributed to LO phonon coupling to plasmons in heavily n-type doped samples as observed for some other materials **[V.28]**, probably because the plasmons are overdamped. Moreover, it is not possible to attribute these small shifts to strain since such effect is not present for the E_2^{high} mode. Most likely, the influence of the Al doping on the polar phonon modes occurs through the electronic system, despite its independence of the Al concentration. Their might be a saturation effect in the free carrier concentration introduced by Al doping due to the fact that not all aluminium atoms occupy (electrically active) lattice sites. Finally, the Al effect in the Raman spectra of ZnO, is also seen by a decrease in the intensity ratio of the modes, E_2^{high} /LO, associated with an increase in the full width at half-maximum (FWHM) of the 438 cm^{-1} mode. These two effects are associated with the decrease in crystalline quality of the ZnO lattice, as expected due to the doping.

V.4.2.2. ZnO:Mn Samples

Figure V.10 shows the Raman spectra of ZnO thin films doped with Mn. In **Figure V.10a**, the effect of the doping method: ion implantation and co-sputtering is illustrated for Mn content ≈ 1.1 at. %. In **Figure V.10b** and **Figure V.10c**, the Mn dose effect is demonstrated for both doping methods. The Raman spectra study shows that independently of the doping method used, the characteristic ZnO E_2^{high} mode is present but, in the 500–600 cm^{-1} range, a considerable difference between pure ZnO and ZnO:Mn is seen. In this region, the LO band ($A_1 + E_1$) remains but a new strong contribution, around 520–530 cm^{-1} appears when Mn is present.

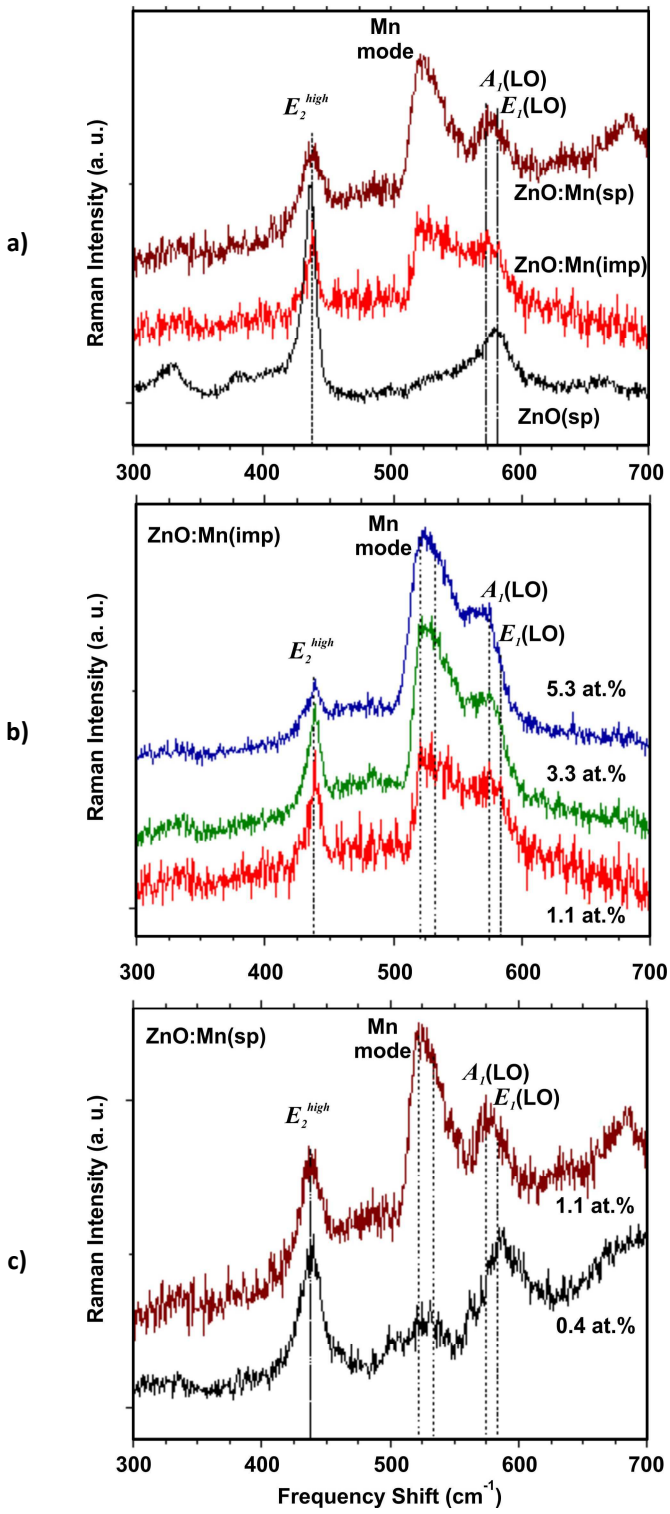

Figure V.10: Raman spectra of ZnO thin films doped with Mn (≈ 1.1 at. %) by co-sputtering (sp:#8) (dark red curve) and by ion implantation (imp:#3) (light red curve). The Raman spectrum of the pure ZnO film is also shown (#1: black curve). (b) Raman spectra of ZnO:Mn thin films doped by ion implantation for different Mn contents (#3, #4, #5). (c) Raman spectra of ZnO:Mn thin films doped by co-sputtering for two different Mn contents (#7 and #8). The measurements were performed with Raman system 1 (see Section III.8.1) with the laser excitation 512 nm, and an optical power on the samples' surface of ≈1 mW (low power was used to avoid anneling of the fim).

The Mn doping effect on ZnO Raman spectra has been widely discussed in the literature **[V.34, V.36 – V.42]** but the assignment of the new Mn-related feature observed is neither unique nor consensual. However, some conclusions can be drawn from these studies. First, the broad band at 520–530 cm^{-1} is specific of Mn doping and has not been observed for other studied impurities incorporated into ZnO, such as Ti **[V.37]**, Co **[V.38, V.39]**, Fe, and Ni **[V.40]**. Secondly, there is a direct correlation between the Mn content and the intensity of this band **[V.34, V.38, V.41, V.42]**, also observed in the samples presented here (see **Figures V.10b** and **V.10c**), even though it is not quite linear. Thirdly, this Mn-doping effect is universal with respect to the material preparation methods used. Indeed, it is observed in our ZnO films grown by sputtering and doped by either implantation or co-sputtering, and has also been reported for ZnO:Mn bulk crystals **[V.37]** as also for thin films produced using other growth methods, such as MOCVD **[V.33]** or ion implantation **[V.38]**.

Since Mn atoms are lighter than Zn atoms and certainly substitute the latter in the cationic sublattice of the ZnO crystal, at least partially **[V.7]**, the most natural explanation for the 520–530 cm^{-1} peak would be to associate with a local vibrational mode (LVM) of these substitutional atoms. Indeed, this 520–530 cm^{-1} peak/ Mn-LVM association was suggested in **Ref. [V.36]** reporting the first (as far as we know) observation of this band and discussed as plausible by other authors **[V.34, V.37, V.39, V.41]**.

However, the lack of supporting computational results and some peculiarities in the experimental data related to this band, namely, the non-linear dependence of its intensity upon the Mn concentration and its "fine structure" consisting of two modes resolved in some of the studies **[V.37 – V.39]** (particularly clear in the spectra of bulk ZnO:Mn crystals **[V.37]**) caused some doubts among the researchers and speculations about possible alternative explanations.

Structural disorder introduced by the incorporation of manganese can activate the silent modes of ZnO. Using *ab initio* calculations, Serrano *et al.* **[V.27]** predicted that the B_1^{low} and the B_1^{high} silent modes of wurtzite ZnO occur at 261 and 552 cm^{-1}, respectively, so the contribution in the region of 520–530 cm^{-1} eventually could be attributed to a disorder activated $2\,B_1^{low}$ mode, as suggested by the authors of **Ref. [V.38]** for one of the additional spectral features introduced by the Mn doping while the other one, at 520 cm^{-1} still could be related to a local vibration mode of Mn.

The possibility that manganese oxides can be responsible for some Raman peaks has also been considered in the literature **[V.42]**. Raman peaks of Mn_2O_3 have been found to occur at approximately 525 and 645 cm^{-1} but the intensity of the 645 cm^{-1} mode is much stronger than the 525 cm^{-1} one **[V.43]**, removing this possibility concerning the samples reported here. Since no extra peaks were detected on the XRD spectra, it also seems to refute the presence of Mn_2O_3 in these samples. In **Section V.5** we will discuss further the 520–530 cm^{-1} band interpretation.

In the Raman spectra shown in **Figure V.10b** and **V.10c**, it is possible to observe a decrease in the intensity of the E_2^{high} mode, with respect to the modes in the 500–600 cm^{-1} range, as the Mn dose increases, in either sputtered or implanted samples. This effect, already noticed for Al doping, is possibly due to an increase in the ZnO lattice damage. However, alloy disorder itself (without radiation damage) can also introduce broadening and shift of Raman modes **[V.38]** as has been observed for sol–gel derived ZnO:Mn nanoparticles **[V.46]**. As also observed for the ZnO:Al doped samples in the LO phonon range (540–590 cm^{-1}), the multi-Lorentzian fit of the Raman spectra reveals a red shift in the implanted samples as compared to the sputtered ones, which can be related to relaxed crystal vibration modes due to the large number of point defects present.

V.4.2.3. ZnO:Al:Mn Samples

As already discussed, ZnO samples doped simultaneously with Al and Mn by co-sputtering, are transparent but non-conductive (**Table V.2**, sample #9). On the other hand, when Mn doping is achieved by ion implantation on previously conductive ZnO(sp):Al(sp) co-sputtered samples (**Table V.2**, samples #10 and #11), the films remain conductive. Possibly it is just a compensation effect, which is only partial in the latter case.

In **Figure V.11**, it can be seen the effect of Mn ion implantation on the Raman spectra of the ZnO(sp):Al(sp) (#10 and #11). As the Mn concentration increases, the 438 cm^{-1} ZnO characteristic Raman peak becomes less intense indicating that the crystalline quality of the ZnO lattice is deteriorated. This effect is accompanied by a considerable increase of the intensity of the modes located in the 520–580 cm^{-1} region.

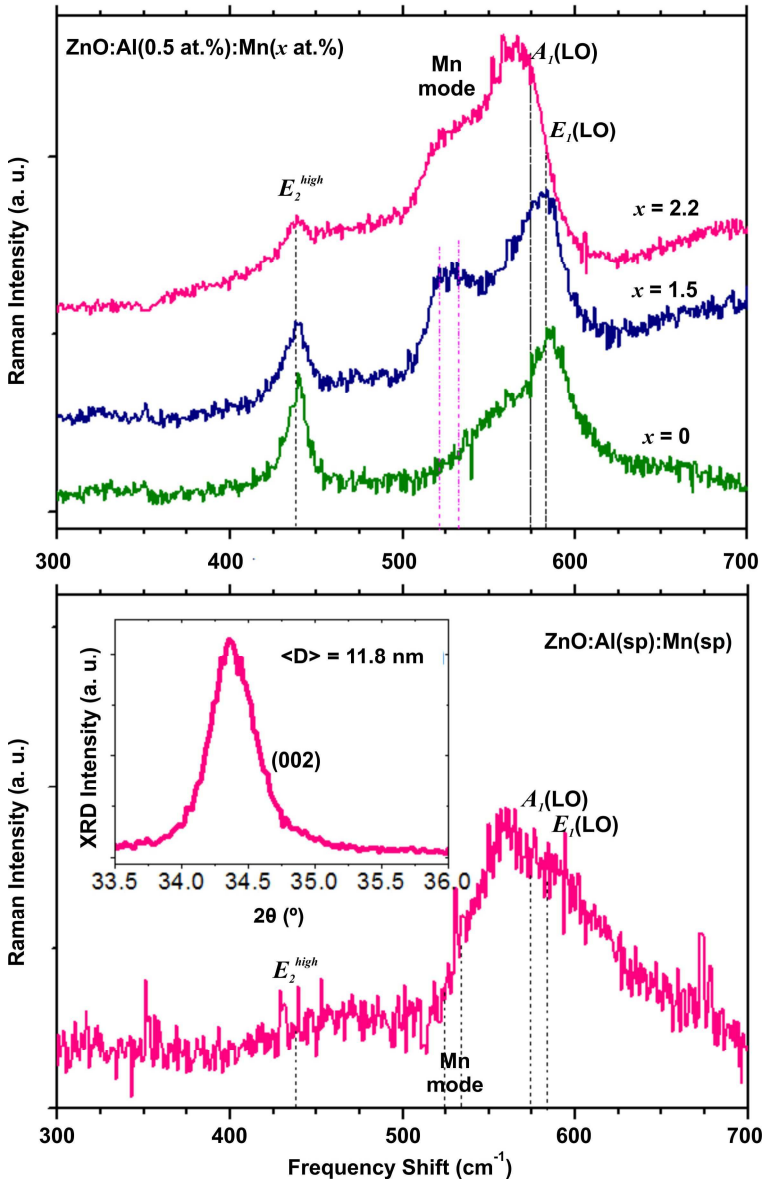

Figure V.11: (a) Raman spectra of ZnO(sp):Al(sp):Mn(imp) thin films for two different Mn contents (#10 and #11). (b) Raman spectra of a ZnO(sp):Al(sp):Mn(sp) sample (#9). The inset shows the XRD pattern of the same sample.

As expected, the 520–530 cm^{-1} mode is only observed in samples with Mn and increases with the increase of Mn content. In the 550–580 cm^{-1} range, the already observed and discussed effect associated with the doping by ion implantation can be seen, *i.e.*, the contributions in this region, whose importance increases with the increase in dopant concentration, shift to lower wavenumbers. Nonetheless, even with high levels of doping, the main Raman features of the ZnO lattice persist, which manifests that the films remain polycrystalline and, concomitantly, conductive. In contrast, whenever the magnetic dopant (Mn = 1.6 at.%. as the lower Mn implanted

dose) is co-sputtered simultaneously with the Zn and Al ions, the damage in the ZnO lattice is dramatic, as can be seen in **Figure V.11b**, and the films become non-conducting. However, as shown in the XRD spectrum in the inset of **Figure V.11b**, ZnO crystallites still are present.

V.5. Theoretical Estimation of the Mn Local Vibration Mode

The analysis of the Raman spectra presented in **Section V.4.2.2** indicates that the Raman signal in the frequency range of 520 – 530 cm^{-1} is intrinsically related to the Mn impurity in ZnO lattice. As known, interstitial atoms are weakly linked to the crystal lattice **[V.45]** and, therefore, cannot vibrate at such a high frequency. The formation of a new phase, such as Mn_2O_3 , has been excluded based on the XRD data. Therefore, it can be assumed that Mn atoms substitute Zn in the cationic sublattice of the ZnO crystal, which is not surprising because in many aspects Mn behaves as a usual Group II doping element **[V.7]**.

Using available calculated results for pure crystalline ZnO **[V.27, V.46]** and the lattice dynamics theory for imperfect crystals **[V.47, V.48]**, it is possible to make some estimations concerning the Mn effect in the ZnO lattice. Let us assume that a substituting Mn atom can be modelled as an isotope defect of strength:

$$\varepsilon = 1 - \frac{M_{Mn}}{M_{Zn}} \qquad \{V.2\}$$

where M_{Mn} and M_{Zn} are atomic masses. The local harmonic vibration frequency, ω^*, can be obtained from the following equation **[V.49]**:

$$\varepsilon\omega^{*2}\sum_{\sigma}\left|\chi_{\sigma}^{(1)}\right|^2\int\frac{g_{\sigma}\left(\omega'^2\right)}{\omega^{*2}-\omega'^2}d\omega'^2 - 1 = 0 \qquad \{V.3\}$$

where σ enumerates branches of the phonon spectrum of the unperturbed crystal, $g_{\sigma}\left(\omega'^2\right)$ is the density of states (DOS) of the corresponding branch (per unit cell), and $\chi_{\sigma}^{(1)}$ is the vibration *eigenvalue* amplitude on the sublattice where the impurity atom is cationic, as in this case. For any optical phonon branch it can be estimated as:

$$\left|\chi_{\sigma}^{(1)}\right|^2 = \frac{1}{1+\frac{M_{Zn}}{M_O}} \qquad \{V.4\}$$

where M_O is the atomic mass of oxygen, since the *eigenvectors* of optical phonons are inversely proportional to the square root of the atomic mass. This estimation is consistent with the data presented in **Ref. [V.27]**. Then, introducing an effective defect strength of the cation isotope defect:

$$\varepsilon' = \varepsilon\left|\chi_{\sigma}^{(1)}\right|^2 \qquad \textbf{\{V.5\}}$$

which yields a value of ≈ 0.04 for these samples. **Equation {V.3}** is a simple generalization of the equation that was derived in **Ref. [V.47]** for a Bravais lattice. In fact, it can be extended to non-isotope defects as far as they introduce only a local change of the interatomic force constants (for electronic systems it would mean that the perturbation potential is very short-ranged and its Fourier-transform is nearly independent of the k-vector). Having this in consideration, ε' can be treated as a fitting parameter.

Equation {V.3} can be solved by making a simple approximation for the unperturbed densities of states (normalized to unity), *e.g.*, using the following Lorentzian function

$$g_{\sigma}\left(\omega^2\right) = \frac{\nu}{\pi}\frac{\Gamma_{\sigma}\omega_{\sigma}}{\left(\omega^2 - \omega_{\sigma}^2\right)^2 + \left(\Gamma_{\sigma}\omega_{\sigma}\right)^2} \qquad \textbf{\{V.6\}}$$

where ω_{σ} is the DOS peak frequency, Γ_{σ} is a parameter describing the width of the phonon band, and ν is a degeneracy factor ($\nu = 1$ for longitudinal and $\nu = 2$ for transverse modes). With this approximation**,** the integral in **Equation {V.3}** is calculated analytically and the equation for ω^{*2} is easily solved.

By inspecting the calculated DOS data presented in Figure 1 of **Ref. [V.27]** (reproduced here as **Figure V.12**), it is possible to distinguish a TO-type phonon band (400 – 520 cm^{-1}) and a narrower LO-type band (520 – 570 cm^{-1}). All other bands can be neglected since they are too far from the interesting frequency range. DOS peaks normally correspond to the Brillouin zone edges where the group velocity vanishes.

Taking the values of the phonon frequencies at some high symmetry points **[V.27, V.46]**, the DOS was approximated by three Lorentzians, namely ω_1 ≈ 450 cm^{-1}, Γ_1 ≈ 30 cm^{-1}, ω_2 ≈ 490 cm^{-1}, Γ_2 ≈ 40 cm^{-1}, and ω_3 ≈ 550 cm^{-1}, Γ_3 ≈ 20 cm^{-1}. The result is shown in **Figure V.13a**, and the corresponding spectral dependence of the left hand side of **Equation {V.3}** is presented in **Figure V.13b**. Depending on the value of ε',

some of the roots can be complex (and come conjugate pairs) and only those with negative imaginary part of the frequency should be considered as meaningful; they correspond to strongly damped modes. For a certain value of ε', a bifurcation is observed and this is where the local mode appears (*e.g.*, at $\varepsilon' \approx 0.05$ in **Figure V.13c**).

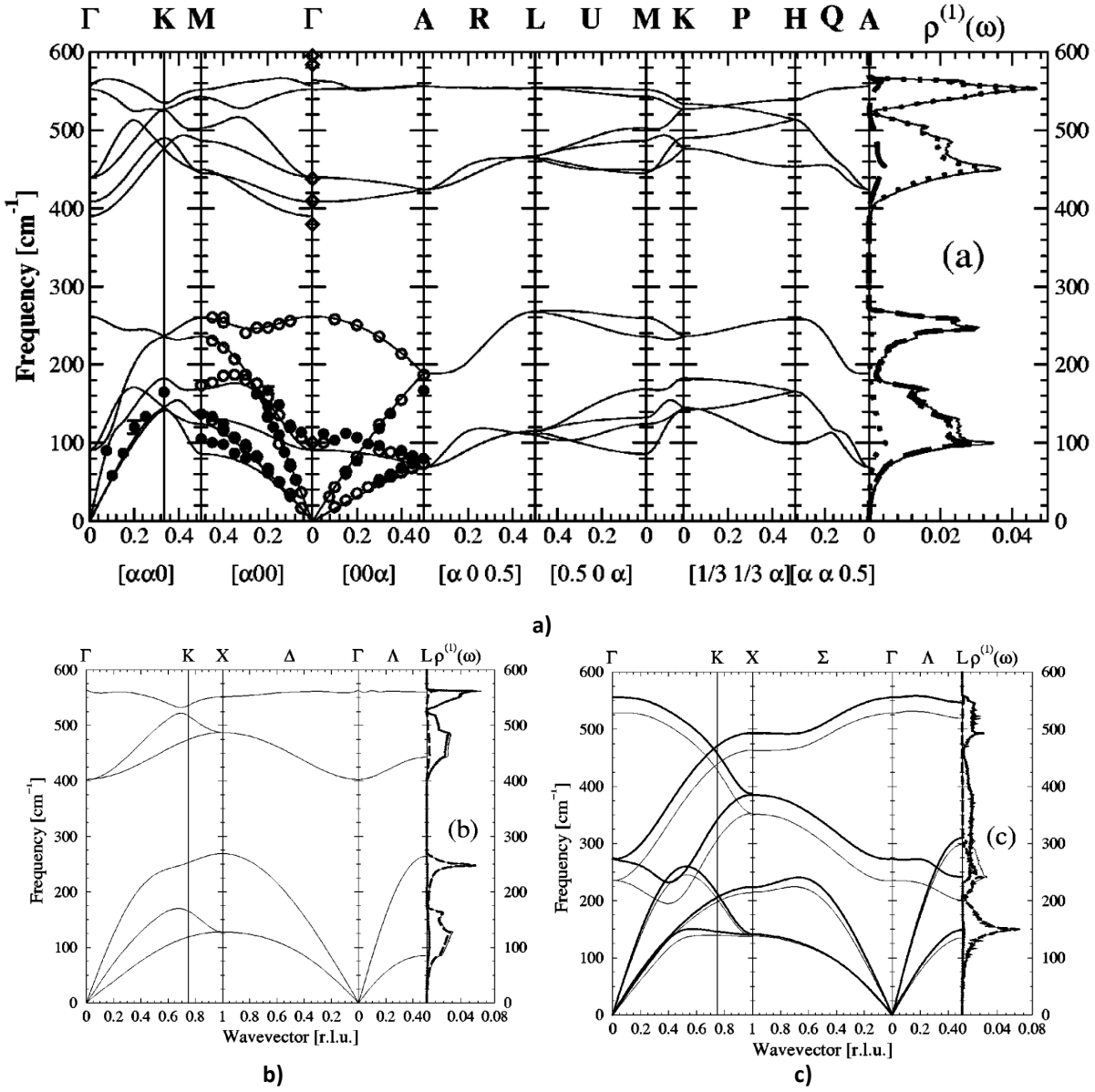

Figure V.12: Phonon-dispersion relations and one-phonon DOS [$\rho_1(\omega)$] of (a) wurtzite, (b) zinc blend, and (c) rocksalt phases, calculated at the equilibrium volume (zero pressure and temperature, thin lines). The thick lines in (c) display the dispersion relations of the rocksalt phase at 8 GPa, i.e., close to the phase transition. On the right-hand side of each plot, the solid curves represent the one-phonon DOS, whereas dashed and dotted curves display the projected DOS corresponding to zinc and oxygen displacements, respectively. The diamonds stand for Raman data reported in Ref. [V.50] whereas the solid and open circles display inelastic nuclear scattering (INS) data from Refs. [V.51, V.53].

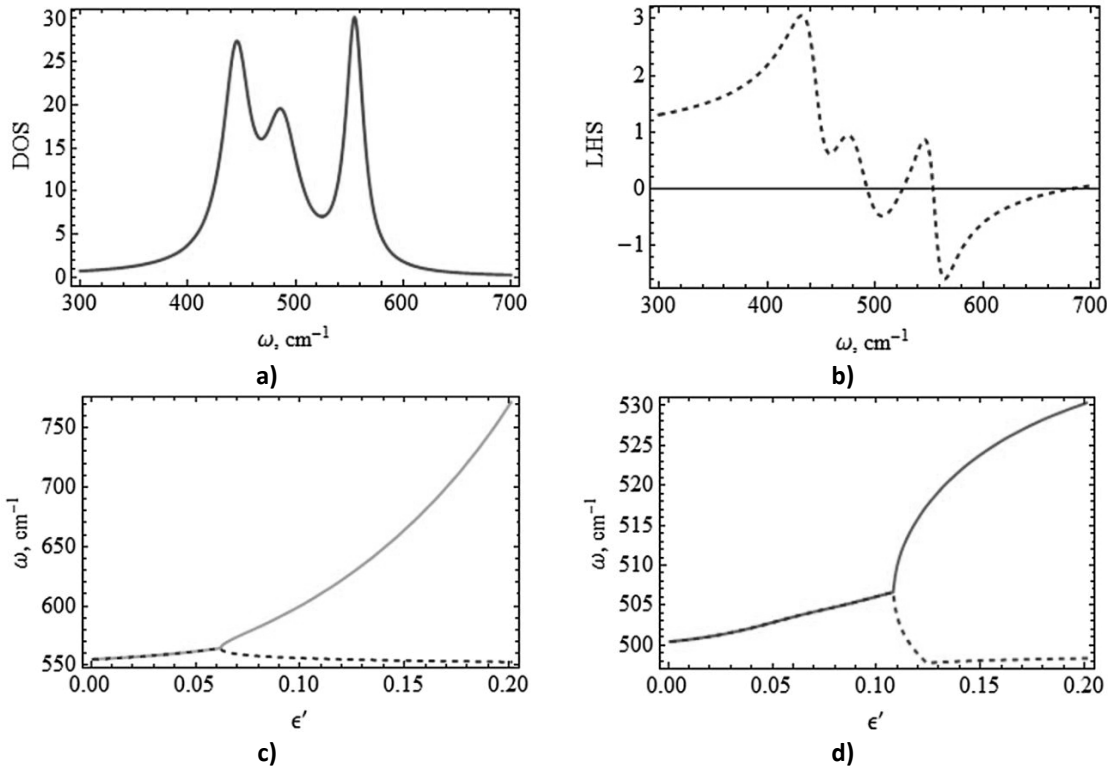

Figure V.13: Density of states in the optical phonon region simulated with three Lorentzians with parameters given in the text (a) and the corresponding spectral dependence of the left-hand side (LHS) of Equation {V.3} (b); two pairs of solutions of Equation {V.3} versus effective defect strength (c and d). Below the bifurcation point, two modes originating from the same [LO, plot (c), or TO, plot (d)] phonon band of ZnO have complex conjugated frequencies.

The frequency (ω_1^{LO}) of the lower of the two modes related to the LO band, occurring for $\varepsilon' > \varepsilon'_C$ is found very close to ω_3; the difference does not exceed just few cm^{-1} for any values of the other parameters. Therefore, it lies most likely within the continuum of phonon states, it is called resonant and its vibration amplitude behaves as a spherical wave ($\propto \sin(q_0 r)/r$) with a certain wavevector determined by its frequency separation from the band edge. Since this q_0 should not be small, the contribution of the resonant mode to the Raman scattering must be insignificant. In contrast, if ω^* falls outside the LO band, which is the case of the upper mode in **Figure V.13c** (ω_h^{LO}), its vibration amplitude decreases exponentially with the distance from the site occupied by the impurity atom. Such a mode is not characterized by any specific $\vec{q}$, while the nearby continuum modes correspond to large phonon wavevectors, close to the edges of the Brillouin zone where phonon's group velocity is close to zero. These large $\vec{q}$ modes are Raman inactive, while the local vibration can contribute to the Raman scattering.

A similar scenario takes place for solutions originating from the TO band (**Figure V.13d**), although here ε'_C is higher. Importantly, there is a gap between the LO and TO parts of the phonon DOS **[V.27]** at approximately 525 cm^{-1} (it is not reproduced by this Lorentzian model where only a minimum appears (**Figure V.13a**)). If the upper of the two modes as shown in **Figure V.13d**, ω_h^{TO}, eventually falls into this gap, it will have similar characteristics to the local mode just discussed above.

If we associate ω_h^{TO} with the Mn-related Raman peak, we have to admit ≈ 0.15 for the value of the defect strength parameter, ε', which is very large compared to the expected value considering Mn as an isotope defect in the cationic sublattice of ZnO. However, we notice the real existence of a gap in the phonon DOS, not only because the phonon dispersion curves were studied using inelastic neutron scattering but also because the DOS were recalculated in the more recent work by Serrano *et al.* **[V.46]** and their result confirm the existence of the gap, even though its exact position may be slightly different from that presented in the earlier work **[V.27]** (unfortunately, the DOS is not presented in **Ref. [V.46]**). Our simple model shows the possibility that one of the modes produced by Mn atoms substituting Zn in the cationic sublattice of the ZnO crystal can fall into the gap that does exist slightly below 530 cm^{-1}. Interestingly, if ε' ≈ 0.16 is taken, then it is obtain ω_h^{TO} ≈ 525 cm^{-1} and ω_h^{LO} ≈ 682 cm^{-1}. This is close to the frequency of a spectral feature seen in the spectra of sputtered ZnO:Mn samples (see **Figure V.10**) and, therefore, can be considered as an additional argument in support of the presented model.

The intensity of the experimentally observed feature grows strongly with the increase of Mn content. According to the theory developed in **Ref. [V.48],** at finite concentration of impurity, the local mode broadens and develops into a band because of the fluctuating distances between neighbouring impurity atoms. Because of the concentration-dependent broadening, the magnitude of the impurity vibration band is not simply proportional to the Mn concentration. Moreover, if the interaction between Mn atoms in the lattice is short-range, so that it decreases strongly if they are not nearest neighbours in the sublattice, the local DOS can have a double-peak structure (see **Figure V.14**), which is analogous to the electronic level splitting into two for a pair of identical atoms. This may explain the double-peak structure of the Mn-induced Raman band resolved for higher crystal quality samples **[V.37, V.39]**.

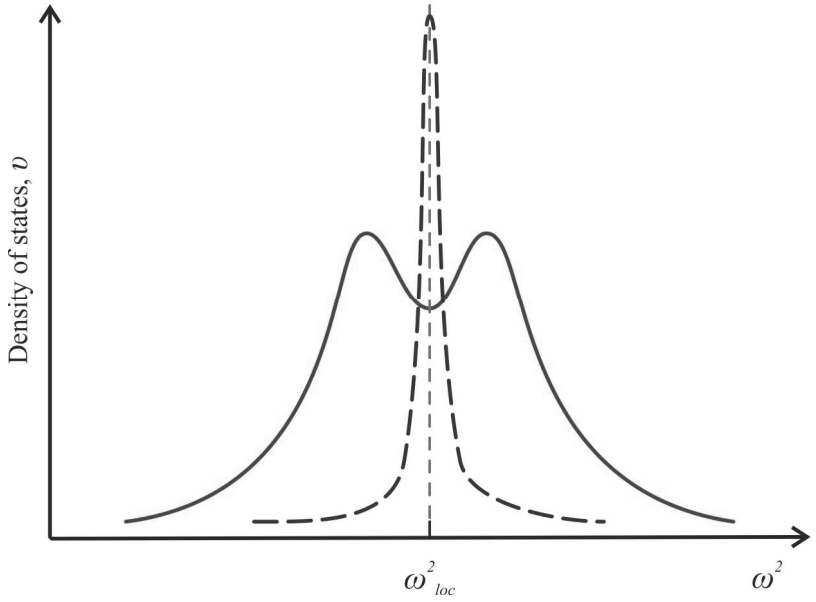

Figure V.14: Qualitative shape of the phonon DOS in the vicinity of a local impurity mode in the low concentration limit (dashed line) and at higher concentrations when pairs of impurity atoms start playing an important role (full line).

V.6 Resonant Raman Scattering Results: Multi-Phonon Peaks and Phonon-Assisted Absorption/Re-Emission Model

Resonant Raman scattering occurs when the excitation energy is higher than the energy gap of the semiconductor been studied. Usually it implies that the scattering probability is much higher and also the relative intensity of different modes changes in comparison with the case of non-resonant excitation (as it was discussed in **Chapter III**, the crystal symmetry dictated selection rules do not actually apply under strong resonance conditions). Moreover, multiple-phonon modes are frequently observed under resonant excitation.

Figure V.15a shows the resonant Raman scattering results obtained on a ZnO(sp):Mn(imp) and a ZnO(sp):Al(sp):Mn(imp)samples, as also in a undoped ZnO (sp) and **Figure 5.15b** shows, for comparison the non-resonant Raman spectra of the same samples. The energies of the incoming and inelastic-scattered (shifted up to 4000 cm^{-1}) photons match real electronic states in the material.

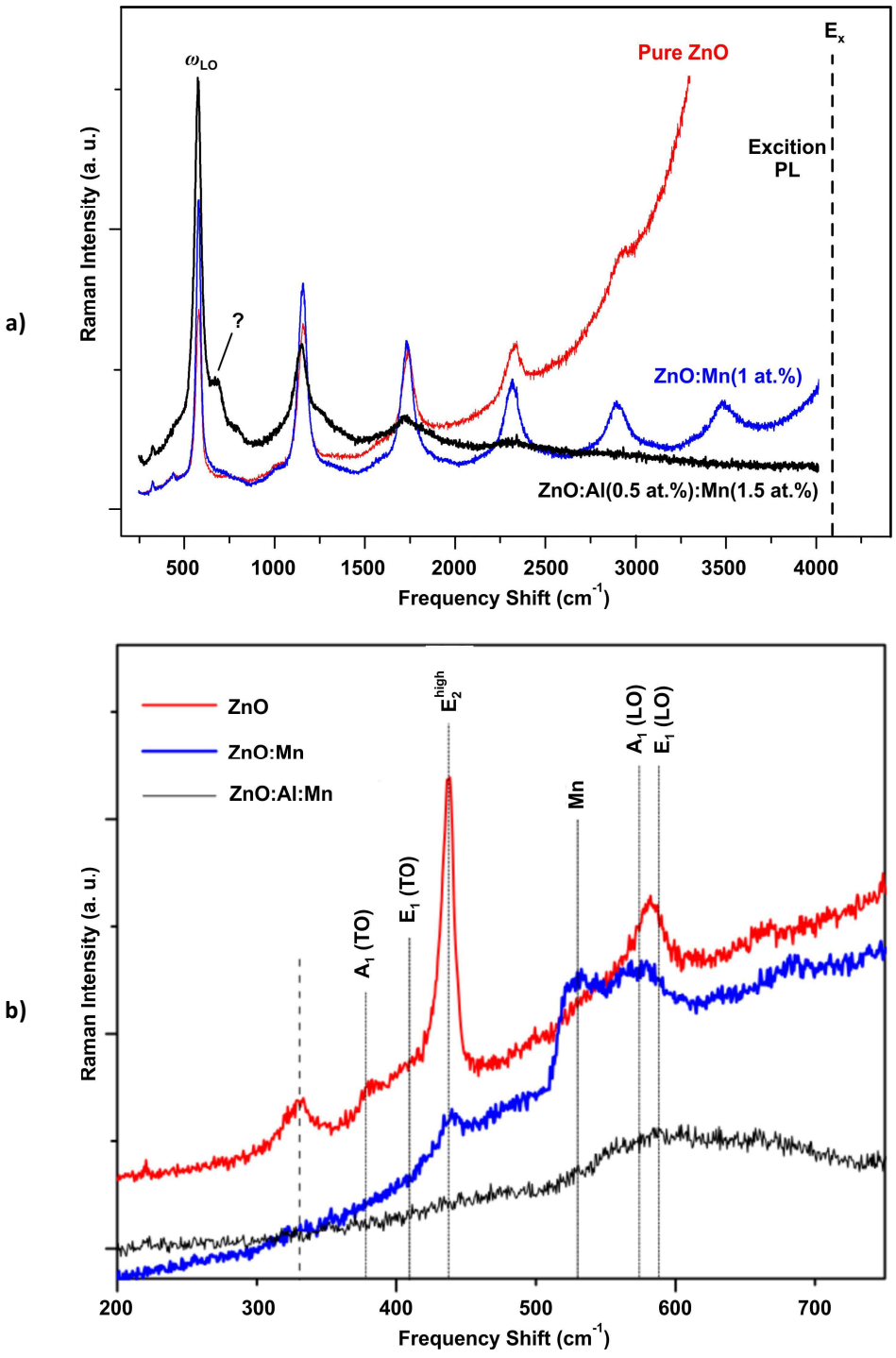

Figure V.15: a) Resonant Raman spectra of pure ZnO (#1), ZnO:Mn(#3) and ZnO:Mn:Al (#10) films. The increase in the signal from pure ZnO at higher frequency shift corresponds to exciton photoluminescence (PL). The vertical line denoted E_x shows the expected peak position of this PL band. b) Non-resonant Raman spectra of the same samples. The measurements were performed with Raman system 5 (see Section III.8.1) with the laser excitation 325 nm.

According to several previous studies **[V.53 – V.55]**, under resonant scattering conditions the Raman spectra of bulk ZnO-based materials consist of only LO phonon lines as the spectra shown in **Figure V.15a**. Although an exception is found for the ZnO:Al(sp):Mn(imp)[18] sample, where an extra mode, marked with '?', is seen.

From the resonant Raman spectra the measured shift of the one-phonon mode is ≈ 580 cm^{-1} and this values falls between the frequencies of the A_1 and E_1 LO phonons at $\vec{q} = 0$. As known **[V.56]**, for a small (finite) wavevector making an angle ϑ with the c-axis of a uniaxial crystal, the LO phonon mode is a mixture of the Brillouin zone centre A_1 and E_1 LO phonon modes, with the frequency given by :

$$\omega_{LO}^2(\vartheta) = \omega_{A_1}^2 \cos^2 \vartheta + \omega_{E_1}^2 \sin^2 \vartheta . \qquad \textbf{\{V.7\}}$$

The observed Raman resonant scattering (RRS) peak frequency corresponds to the maximum of:

$$\left\langle \frac{1}{\omega^2 - \omega_{LO}^2(\vartheta)} \right\rangle , \qquad \textbf{\{V.8\}}$$

where $\langle \ldots \rangle$ means an appropriate average over ϑ taking into account random orientations of the crystalline grains. The resonant enhancement of the (dipole-forbidden) LO-phonon scattering is associated with the Fröhlich electron–phonon interaction mechanism and corresponds to the participation of LO phonons with small but finite wavenumbers **[V.57]**.

The intensity and number of LO phonon lines observed in RRS spectra of different materials depend on several factors, but generally it is proportional to the strength of the exciton–phonon coupling which can be measured by the Huang–Rhys parameter (HRP). Based on the HRP value for ZnO **[V.58]**, it has been predicted that the number of multiple LO phonon lines in bulk ZnO crystals should be higher than that of CdS with 9 LO (n = 9) **[V.59, V.60]**. However, in most reported studies a smaller number of multi-LO-phonon lines has been observed, n = 4–8 for pure ZnO **[V.55, V.61]** and n = 3–5 for doped ZnO materials **[V.62, V.63]**. On the other hand, in a recent work **[V.54]** up to 11 replicas were resolved in the spectra of ZnO nanowires co-doped with two impurities.

[18] This mode seems to be related to the Al doping and is enhanced under resonance conditions. Its nature requires further investigation.

In the spectra of **Figure V.15**, the number of multi-phonon lines seen is also different for different samples, as the full width at half maximum (FWHM) value. In order to quantify the intensity of the *n*-LO lines in the RRS spectra, a fit using Lorentzians centred at the positions equal to $n\hbar\omega_{LO}$ was employed. For the undoped ZnO sample, the free exciton photoluminescence (PL) was subtracted[19] using a Lorentzian contour representing the free exciton photoluminescence (PL) band. The normalized (to the n=1 peak) area of each *n*-LO Lorentzian, considered as the intensity of the corresponding multi-phonon peak, is shown in **Figure V.16**.

As it can be seen from **Figure V.16**, doping of ZnO with (electrically inactive) Mn reduces the intensity of the n = 2 peak relatively to n = 1. This could be explained by a (small) variation of the exciton–phonon coupling strength in the presence of Mn, since Mn atoms deform the crystal lattice that could affect the properties of free excitons. However, it is seen that the Mn doping suppresses the free exciton PL, expected at a smaller Raman shift because of the increase of E_g. Six LO phonon replicas can be observed in our RRS spectrum of ZnO(sp):Mn(imp). The presence of (electrically active) aluminium (ZnO(sp):Mn(imp):Al(sp) samples) has a more drastic effect on the exciton properties comparing with ZnO:Mn, since a higher concentration of free carriers should destroy excitons because of the screening of the electron–hole interaction. Indeed, no exciton PL could be observed in this sample. Also, the number of multi-LO-phonon peaks and their intensity both decrease drastically. Clearly, the relative intensities of the *n*-LO and (*n*+1)-LO are not determined by the strength of the exciton–phonon coupling constant.

This puzzling situation was already realized in the 1970s and explained by the 'cascade' model **[V.64 – V.67]**. It has been shown that, as long as both the incident ($\hbar\Omega_1$) and scattered ($\hbar\Omega_S$) photon energies are larger than E_g, the multiple LO phonon 'resonance Raman effect', in fact, is a sequence of (phonon-assisted) indirect processes of light absorption and emission by excitons **[V.64]**.

[19] A Lorentzian contour was used, centered at the exciton energy, 3.31 eV at room temperature **[V.65]**, equivalent to the Raman shift of 4070 cm^{-1} with respect to the incident photon energy.

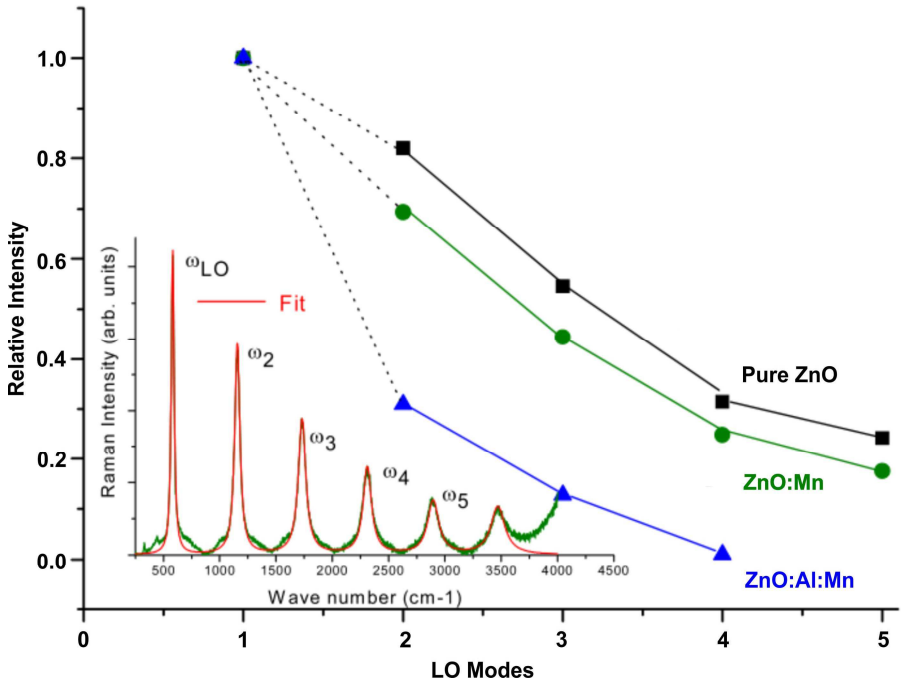

Figure V.16: Relative intensity of n-LO phonon lines in the RRS spectra of Figure V.15 (normalized to that of n = 1 peak for each sample). Lines are guides to the eye. Inset: RRS spectrum and corresponding fit for sample ZnO:Mn. Note that the mode frequencies ω_i (i = 2, 3, ...) are not exact multiples of ω_{LO}.

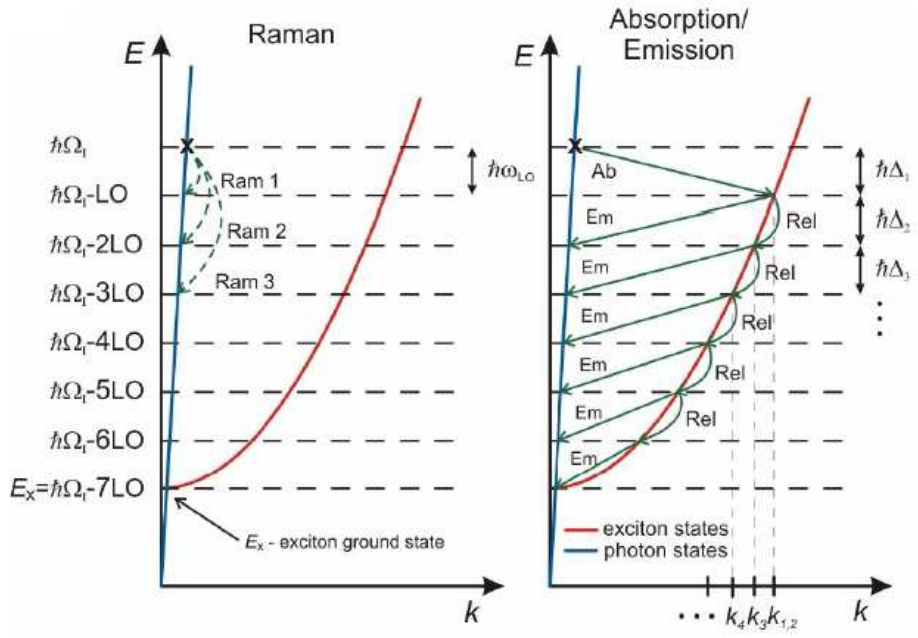

Figure V.17: Schematics of Raman (Ram 1–3, left panel) and indirect absorption (Ab)/emission (Em) processes (right panel) leading to multi-phonon replicas in the light emission/scattering spectra (adapted from [V.67]). The abbreviation Rel means relaxation. Values of the wavevector indicated in the right panel, k_i (i = 1, 2, ...) correspond to phonons interacting with the exciton in different states. Note that the spacings Δ_i (i = 1, 2, ...) shown in the right panel are not exactly equal to ω_{LO}.

According to the cascade model, the following sequence of elementary processes takes place:

(i) the creation of an exciton via absorption of the incident photon ($\hbar\Omega_1$),

(ii) the (non-radiative) relaxation of this exciton into lower energetic states with successive emission of LO phonons, and

(iii) the radiative recombination of the exciton with the emission of scattered phonons with energy $\hbar\Omega_S = \hbar\Omega_1 - n\hbar\omega_{LO}$ (n > 1), as schematically shown in **Figure V.17.**

In these experiments, $\hbar\Omega_1$ is approximately equal to ($E_x + 7\hbar\omega_{LO}$), where E_x = 3.31 eV is the ground state energy of free exciton. As illustrated in **Figure V.17**, the incident photon is absorbed into a virtual exciton state (marked by the cross). The 'true' n-th order Raman process (left panel) involving the simultaneous emission of n > 1 phonons is less efficient than the sequence of phonon-assisted absorption–emission (for n = 2) or absorption–relaxation– emission (for n > 2) processes, depicted in the right panel of **Figure V.17 [V.65]**.

The main argument behind the cascade model is that a process involving *simultaneous* emission of n phonons is described by a matrix element containing the exciton-phonon interaction rate to the n-th power. Since this rate, even in polar semiconductors, is not very high, the probability of such a process must decrease very rapidly with n. At the same time, the probability for the n-LO-phonon processes assumed in the cascade model can be written as **[V.57]**:

$$P_{ph}^{(n)} \propto \alpha_1 \left[\prod_{i=1}^{n-2} \tau_{rel} \Gamma_1\left(\vec{K}_i\right) \right]^{-1} \left(\tau_{rad} \Gamma_1\left(\vec{K}_{n-1}\right) \right)^{-1} \qquad \textbf{\{V.9\}}$$

where α_1 is the absorption coefficient for the LO-phonon-assisted creation of the excitons, τ_{rel} is the exciton relaxation time via emission of one LO phonon, K is the exciton centre of mass wavevector, $\Gamma_1\left(\vec{K}_i\right)$ is the damping of the exciton state with energy $E_1\left(\vec{K}_i\right)$, and τ_{rad} is the exciton lifetime corresponding to its LO-phonon-assisted radiative recombination. The relaxation time (i.e. the inverse of the LO-phonon emission probability) contains the same exciton-phonon interaction matrix element (squared) as the damping factor, $\Gamma_1\left(\vec{K}_i\right)$, so the exciton-phonon coupling constant cancels in the first bracket in **Equation {V.9}** and only enters the last factor. Consequently, the multiphonon cascade decreases only slowly with n. When the

excitons do not have enough energy to relax by LO phonon emission, the cascade process finish, i.e., the lowest scattered photon energy is $\hbar\Omega_S^{\min} \approx E_1\left(\vec{K} \approx 0\right)$.

Thus, according to the cascade model, only the first-order spectral peak corresponds to the 'true Raman process' (denoted by Ram1 in **Figure V.17**) and its cross-section (σ_1) is determined by the (Fröhlich) interaction between hot excitons and LO phonons with $\vec{q} \approx 0$. The other peaks represent the exciton PL emission processes assisted by absorption and emission of phonons. In particular, the second order process is physically different from the 1LO scattering, involves phonon absorption and emission (Ab + Em in **Figure V.17**) and its cross-section can be written as **[V.66]**:

$$\sigma_2 = A\sigma_{Abs}\left(\hbar\Omega_1\right)\times\left[\frac{W_{Em}\left(\hbar\Omega_1 - \hbar\omega_{LO}\right)}{W_{Nr}\left(\hbar\Omega_1 - \hbar\omega_{LO}\right)+W_{Em}\left(\hbar\Omega_1 - \hbar\omega_{LO}\right)}\right], \qquad \textbf{\{V.10\}}$$

where the constant A is of the order of unity, $\sigma_{Abs}\left(E\right)$ is the cross-section of the indirect photon absorption, $W_{Em}\left(E\right)$ is the probability of indirect annihilation of an exciton with kinetic energy E, accompanied by the emission of one LO phonon, and $W_{Nr} \approx \left(\tau_{rel}\right)^{-1}$ is the probability of all non-radiative processes involving the exciton (relaxation and dissociation). Comparing σ_2 /σ_1 for the three samples one can conclude that W_{Nr} for hot excitons must be much larger in the ZnO:Mn:Al sample, probably because of the high probability of the exciton dissociation in the presence of free carriers.

In analogy with the previous equation, one can write for the cross-section of the third-order process as:

$$\sigma_3 = \sigma_2\left[\frac{W_{Nr}\left(\hbar\Omega_1 - \hbar\omega_{LO}\right)}{W_{Em}\left(\hbar\Omega_1 - \hbar\omega_{LO}\right)}\right]\times\left[\frac{W_{Em}\left(\hbar\Omega_1 - 2\hbar\omega_{LO}\right)}{W_{Nr}\left(\hbar\Omega_1 - 2\hbar\omega_{LO}\right)+W_{Em}\left(\hbar\Omega_1 - 2\hbar\omega_{LO}\right)}\right]. \qquad \textbf{\{V.11\}}$$

Similar to the relative intensity of the 2LO line, the σ_3 /σ_2 ratio is also the lowest for the ZnO:Mn:Al sample, however, from **Figure V.16** we can conclude that σ_3 /σ_2 > σ_2 /σ_1 as it should be according to **Equation {V.11}.** For the sake of completeness, we note that this simple recurrent relation neglects (phonon-assisted) exciton transitions to higher energy states and becomes increasingly incorrect for larger *n*. If multi-phonon lines are observed for orders

$$n > n_{\max} = \left[\frac{\hbar\Omega_1 - E_x}{\hbar\omega_{LO}}\right], \qquad \textbf{\{V.12\}}$$

as is the case for some samples in **[V.54]**, they cannot be described by the cascade model assuming only free excitons.

From the fitting results presented in the inset of **Figure V.16**, it was verified that the separation between the consecutive "Raman peaks" is not exactly the same and not exactly equal to ω_{LO}. It is naturally explained by the cascade model because higher-order processes involve phonons with smaller wavevectors (see the right-hand side **Figure V.17**). Therefore it opens the possibility of determining the dispersion relation for phonons taking part in the cascade process. The quantities Δ_n shown in **Figure V.17** are the phonon frequencies and the corresponding values of the wavevector, k_n, can be calculated as explained below. For $n \geq 3$, we have $\Delta_n = \omega_n - \omega_{n-1}$, where ω_n are the shifts of the corresponding Raman peaks.

Since $\Delta_{1,2}$ cannot be measured (the first peak has a different nature!), it is taken:

$$\Delta_1 = \Delta_2 = \frac{\omega_2}{2} \text{ and } k_1 = k_2 , \qquad \textbf{\{V.13\}}$$

which is justified because the photon scanline in **Figure V.17** is almost vertical. The phonon frequencies Δ_n obtained for the pure ZnO sample are given in **Table V.6**. Note that the first Raman peak for the same sample is located at ω_{LO} = 581.6 cm^{-1}, *i.e.* $\omega_{LO} > \Delta_{1,2}, \Delta_3$ but at the same time $\omega_{LO} < \Delta_5$. It clearly indicates that the physical mechanisms responsible for the first- and higher-order peaks are different, in accordance with the cascade model.

Table V.6: Frequencies of the phonons taking place in the cascade process.

n	**1,2**	**3**	**4**	**5**
Δ_n (cm^{-1})	579.3	579.5	581.0	584.0

The corresponding values of the wavevector can be calculated from the following relation:

$$E_x + \frac{\hbar^2 k_n^2}{2M} = h\left(\Omega_1 - \sum_{i=1}^{n-1}\Delta_i\right), \quad (n \geq 2), \qquad \textbf{\{V.14\}}$$

where M is the free exciton mass (= 0 .9 m_0 for ZnO **[V.68]**).

Phonon dispersion curves for bulk ZnO have recently been measured using inelastic neutron scattering (INS) **[V.47]**. In **Figure V.18** is shown a comparasion of

these results, $\Delta_n(k_n)$, with the data of **Ref. [V.47]**. It should be pointed out that the INS measurements were performed at 10 K while the RRS data presented here correspond to room temperature. Within the Grüneisen model, the relative shift of the phonon frequencies with temperature can be estimated as

$$\frac{\delta\omega}{\omega} = -\overline{\gamma}\overline{\alpha}\,\delta T \qquad \textbf{\{V.15\}}$$

where $\overline{\gamma}$ and $\overline{\alpha}$ are the average Grüneisen parameter and average thermal expansion coefficient, respectively. With the data available from **[V.69]** it was obtained for $\delta\omega_{LO}$ less than 0.5 cm^{-1}, which is below our experimental precision.

From **Figure V.18** it can be seen that $\Delta_n(k_n)$ data fit quite well the LO phonon dispersion relation characteristic of the *xy* plane (E_1 type phonon modes). This is understandable because these polar phonons should interact most strongly with excitons, and their contribution to the total density of states is larger compared to A_1-type phonon modes.

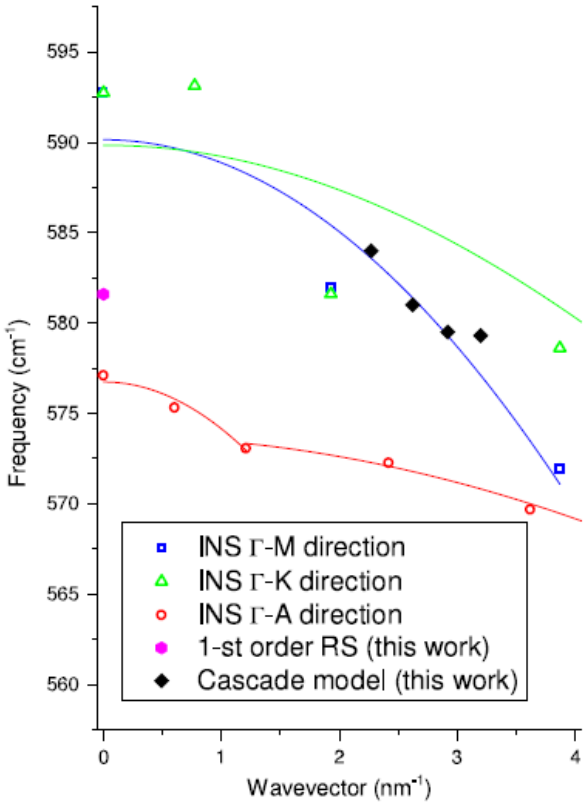

Figure V.18: ZnO LO phonon dispersion relations along Γ–M, Γ–K and Γ–A directions in the Brillouin zone and our ω_{LO} and $\Delta_n(k_n)$ data (full symbols). Open symbols represent the INS data from [V.47] rescaled to the units used here and curves are parabolic fits to these data (guides to the eye).

Conclusions

A set of ZnO films, either undoped or doped with Mn and also Al were produced and their structural, magnetic and electrical properties were characterised. Detailed Raman spectroscopy studies, employing both non-resonant and resonant excitation and focused on the changes introduced by doping with Mn and Al impurities were performed.

For undoped polycrystalline films, a strong LO-phonon band, not seen in the spectrum of crystalline MBE-grown ZnO layer, was found. The presence of this band can be understood by the enhancement of the "forbidden" Fröhlich-type scattering (Gogolin-Rashba mechanism and eventually phonon confinement, although the estimated average grain size, ≈ 20 nm, is too large to make the latter really important).

It has been shown that the doping of ZnO films with Al, by either co-sputtering or ion implantation yields strong *n*-type conductivity as demonstrated by the results of the electrical resistivity measurements. Contrary to the expectations, no evidence of phonon-plasmon coupling was found in these rather heavily doped samples, possibly because the plasmons are overdamped. The Raman spectra of these samples are similar for both doping methods and no evidence of improvement of the electrical properties of the material was detected by using ion implantation. Otherwise, Mn magnetic doping of ZnO films by co-sputtering or by ion implantation results in very resistive samples and the Raman spectra show the presence of Mn-related modes (520-530 cm^{-1}) whose intensity increases with the increase of the Mn content. The nature of this mode was discussed and model calculations and further qualitative arguments were presented in support of the opinion that this Raman feature originates from local vibrations of Mn atoms and their clusters (at higher concentrations), substituting Zn in the cationic sublattice of the ZnO crystal. This mode is Raman active because it falls into the gap of the optical phonon density of states of undoped ZnO crystal.

A large enhancement of the polar LO phonon mode in the first-order spectrum under resonant excitation has been observed, owing to the strong Fröhlich interaction between excitons and LO phonons. No enhancement of Mn-related Raman features in

the spectra of ZnO:Mn and ZnO:Mn:Al films was found, although a new feature, presumably related to Al doping, was detected in the RRS spectra. The intense multi-LO-phonon lines observed in the RRS spectra of all of our ZnO are caused by phonon-assisted emission and reabsorption of photons by hot excitons with appropriate energy, more efficient than the simultaneous emission of several phonons. This is confirmed, in particular, by the fact that the separation between the consecutive Raman peaks for $n > 2$ is different from the LO phonon frequency measured by the position of the first peak.

Bibliography

[V.1] D.A Minkov. *Method for determining the optical constants of a thin film on a transparent substrate.* J. Phys. D: Appl. Phys. **22**, 199, (1989).

[V.2] M. Shatnawi, A.M. Alsmadi, I. Bsoul, B. Salameh, M. Mathai, G. Alnawashi, Gassem M. Alzoubi, F. Al-Dweri, and M.S. Bawa'aneh. *Influence of Mn doping on the magnetic and optical properties of ZnO nanocrystalline particles.* Results in Physics **6**, 1064, (2016).

[V.3] M. Bououdina, K. Omri, M. El-hilo, A. El Amiri, O.M. Lemine, A. Alyamani, E.K. Hlil, H. Lassri, and L. El Mir. *Structural and magnetic properties of Mn-doped ZnO nanocrystals.* Physica **E 56**, 107, (2014).

[V.4] K. Jayanthi Sharda, and S. Chawla. *Synthesis of Mn doped ZnO nanoparticles with biocompatible capping*. Appl. Surf. Sci. **256**, 2630, (2010).

[V.5] J.I. Langford. *A rapid method for analysing the breadths of diffraction and spectral lines using the Voigt function.* J. Appl. Crystallogr. **11**, 10, (1978).

[V.6] Edited by Z.M. Jarzebzki, and R.B. Pamplin. *Oxide Semiconductors*. Pergamon Press, Oxford, UK, (1973).

[V.7] C. Klingshirn, J. Fallert, H. Zhou, J. Sartor, C. Thiele, F. Maler-Flaig, D. Schneider, and H. Kalt. *65 years of ZnO research – old and very recent results.* Phys. Status Solidi **B 247**, 1424, (2010).

[V.8] T. Dietl, H. Ohno; F. Matsukara, J. Gilbert, and D. Ferrand. *Zener Model Description of Ferromagnetism in Zinc-Blende Magnetic Semiconductors.* Science **287**, 1019, (2000).

[V.9] S. J. Pearton, D.P. Nprton; K. Ip. Y. W. Heo, and T. Steiner. *Recent progress in processing and properties of ZnO.* Prog. Mater. Sci. **50**, 293, (2005).

[V.10] J. R. Neal, A. J. Behan, R. M. Ibrahim; H. J. Blythe, M. Ziese; A. M. Fox, and G. A. Gehring. *Room-Temperature Magneto-Optics of Ferromagnetic Transition-Metal-Doped ZnO Thin Films.* Phys. Rev. Lett. **96**, 197208, (2006).

[V.11] H. Schmidt, M. Diaconu, H. Hochmuth, M. Lorenz, A. Setzer, P. Esquinazi, A. Pöppl, D. Spemann, K.-W. Nielsen, R. Gross, G. Wagner, and M. Grundmann. *Weak ferromagnetism in textured $Zn_{1-x}(TM)_xO$ thin films.* Superlattices Microstruct. **39**, 334, (2006).

[V.12] W. Shim, K. Lee. W. Lee, K. A. Jeon, S. Y. Lee, and M. H. Jung. *Evidence for carrier-induced ferromagnetic ordering in $Zn_{1-x}Mn_xO$ thin films: Anomalous Hall effect.* J. Appl. Phys. **101**, 123908, (2007).

[V.13] N. H. Hong, J. Sakai, and V. Brizé. *Observation of ferromagnetism at room temperature in ZnO thin films.* J. Phys.: Condens. Matter **19**, 036219, (2007).

[V.14] N. H. Hong, J. Sakai, N. Poirot, and V. Brizé. *Room-temperature ferromagnetism observed in undoped semiconducting and insulating oxide thin films.* Phys. Rev. **B 73**, 132404, (2006).

[V.15] B. B. Straumal, A. A. Mazilkin, S. G. Protasova, A. A. Myatiev, P. B. Straumal, G. Schutz, P. A. van Aken, E. Goering, and B. Baretzky. *Magnetization study of nanograined pure and Mn-doped ZnO films: Formation of a ferromagnetic grain-boundary foam.* Phys. Rev. **B 79**, 205206, (2009).

[V.16] F. F. Sizov, and Y. I. Ukhanov. The *Faraday and Voigt Magneto-Optic Effects Applied to Semiconductors*. Naukova Dumka, Kiev, (1979).

[V.17] M. Farle. *Ferromagnetic resonance of ultrathin metallic layers.* Rep. Prog. Phys. **61**, 755 (1998)

[V.18] J. Alaria, P. Turek, M. Bernard, M. Bouloudenine, A. Berbadj, N. Brihi; G. Schmerber, S. Colis, and A. Dinia. *No ferromagnetism in Mn doped ZnO semiconductors.* Chem. Phys. Lett. **415**, 337 (2005)

[V.19] Štefan Višňovský. *Optics in Magnetic Multilayers and Nanostructures*. CRC Press, Taylor & Francis, Boca Raton, USA, 1–61, (2006).

[V.20] A.I. Savchuk, V.I. Fediv, S.A. Savchuk, and A. Perrone. *Growth and characterization of ZnMnO thin films.* Superlattices Microstrucutes **38**, 421, (2005).

[V.21] P.I. Nikitin, and A.I. Savchuk. The Faraday effect in semimagnetic semiconductors. Sov. Phys. Usp **33**, 974, (1990).

[V.22] T. C. Damen, S. P. S. Porto, and B. Tell. *Raman effect in zinc oxide.* Phys. Rev. **142**, 570, (1966).

[V.23] U. Ozgur, Y.I. Alivov, C. Liu, A. Teke, M.A. Reshchikov, S. Dogan, V. Avrutin, S.J. Cho, and H. Morkoc. *A comprehensive review of ZnO materials and devices.* J. Appl. Phys. **98**, 041301, (2005).

[V.24] H. Zhou, L. Chen, V. Malik, C. Knies; D. M. Hofmann, K.P. Bhatti, S. Chaudhary, P.J. klar; W. Heimbrodt, C. Klingshirn, and H. Kalt. *Raman studies of ZnO:Co thin films.* Phys. Status Solidi **A 204**, 112, (2007).

[V.25] J.M. Calleja, and M. Cardona. *Resonant Raman scattering in ZnO.* Phys. Rev. **B 16**, 3753, (1977).

[V.26] F. Decremps, J. Pellicer-Porres, A. Marco Saitta, J.-C. Chervin, and A. Polian. *High-pressure Raman spectroscopy study of wurtzite ZnO.* Phys. Rev. **B 65**, 092101, (2002).

[V.27] J. Serrano, A.H. Romero, F.J. Manjón, R. Lauck, M. Cardona, and A. Rubio. *Pressure dependence of the lattice dynamics of ZnO: An ab initio approach.* Phys. Rev. **B 69**, 094306, (2004).

[V.28] R. Cuscó, E. Alarcon-Llado, J. Ibanez; L. Artus, J. Jimenez, B. Wang, and M.J. Callahan. *Temperature dependence of Raman scattering in ZnO.* Phys. Rev. **B 75**, 165202, (2007).

[V.29] M. F. Cerqueira, A. G. Rolo, T. Viseu, J. Ayres de Campos, T. de Lacerda-Arôso, F. Oliveira, M. I. Vasilevskiy, and E. Alves. *Raman study of doped-ZnO thin films grown by rf sputtering.* Phys. Status Solidi **C 7**, 2290, (2010).

[V.30] J. Merendez, and M. Cardona. *Interference effects: A key to understanding forbidden Raman scattering by LO phonons in GaAs.* Phys. Rev. **B 31**, 3696, (1985).

[V.31] M. F. Cerqueira, M. I. Vasilevskiy, F. Oliveira, A. G. Rolo, T. Viseu, J. Ayres de Campos, E. Alves, and R. Correia. *Resonant Raman scattering in ZnO:Mn and ZnO:Mn:Al thin films grown by RF sputtering.* J. Phys.: Condens. Matter **23**, 334205, (2011).

[V.32] A. A. Gogolinand, and E.I. Rashba. *Mechanism of strong resonant 1LO Raman scattering.* Solid State Commun. **19**, 1177, (1976).

[V.33] A. G. Rolo, and M. I. Vasilevskiy. *Raman spectroscopy of optical phonons confined in semiconductor quantum dots and nanocrystals.* J. Raman Spectrosc. **38**, 618, (2007).

[V.34] J. Gleize, E. Chikoidze, Y. Dumont, E. Rzepka, and O. Gorochov. *Resonant Raman scattering in Mn:ZnO dilute magnetic semiconductors.* Superlattices Microstruct. **42**, 242, (2007).

[V.35] A. El Manouni, F.J. Manjón, M. Mollar, B. Maríb, R. Gómez, M.C. López, and J.R. Ramos-Barrado. *Effect of aluminium doping on zinc oxide thin films grown by spray pyrolysis.* Superlattices Microstruct. **39**, 185, (2006).

[V.36] L.W. Yang, X.L. Wu, G.S. Huang, T. Qiu, and Y.M. Yang. *In situ synthesis of Mn-doped ZnO multileg nanostructures and Mn-related Raman vibration.* J. Appl. Phys. **97**, 014308, (2005).

[V.37] W. Gebicki; K. Osuch, C. Jastrzebski, Z. Golacki, and M. Godlewski. *Raman scattering study of ZnO:Ti and ZnO:Mn bulk crystals.* Superlattices Microstruct. **38**, 428, (2005).

[V.38] M. Schumm, M. Koerdel, S. Muller; H. Zutz, C. Ronning, J. Stehr, D.M. Hofman, and J. Geurts. *Structural impact of Mn implantation on ZnO.* New J. Phys. **10**, 043004, (2008).

[V.39] M. Jouanne, J.F. Morhange, W. Szuszkiewicz, Z. Golacki, and A. Mycielski. *Raman scattering on Mn or Co doped ZnO crystals Raman scattering on Mn or Co doped ZnO crystals.* Phys. Status Solidi C **3**, 1205, (2006).

[V.40] M. Schumm, M. Koerdel, s. Muller, C. Ronning, E. Dynowska, Z. Golacki, W. Szuszkiewicz, and J. Geurts. *Secondary phase segregation in heavily transition metal implanted ZnO.* J. Appl. Phys. **105**, 083525, (2009).

[V.41] X. Teng, W. Yu, L.Z.Y. Wu, W. Gao, and G. Fu. *Raman scattering characteristics of Mn-doped ZnO films.* Proc. International Conference on Electronics and Optoelectronics (ICEOE 2011), **3**, 195, (2011).

[V.42] Y.M. Hu, C.Y. Wang, S.S. Lee, T.C. Han, W.Y. Chou, and G.J. Chen. *Identification of Mn-related Raman modes in Mn-doped ZnO thin films.* J. Raman Spectrosc. **42**, 434, (2011).

[V.43] M. A. García, M.L. Ruiz-González, A. Quesada, J.L. Costa-Kramer, J.F. Fernández, S.J. Khatib, A. Wennberg, A.C. Caballero, M.S. Martín-González, M. Villegas, F. Briones, J.M. González-Calbet, and A. Hernando. *Interface Double-Exchange Ferromagnetism in the Mn-Zn-O System: New Class of Biphase Magnetism.* Phys. Rev. Lett. **94**, 217206, (2005).

[V.44] J. B. Eang, H.M. Zhong, Z.F. Li, and Wei Lu. *Raman study for E2 phonon of ZnO in $Zn_{1-x}Mn_xO$ nanoparticles.* J. Appl. Phys. **97**, 086105, (2005).

[V.45] A.A. Maradudin, E.W. Montroll and G.H. Weiss. *Theory of Lattice Dynamics in Harmonic Approximation*. Academic Press, New York, USA, (1963).

[V.46] J. Serrano, F.J. Manjón, A. H. Romero, A. Ivanov, M. Cardona, R. Lauck, A. Bosak, and M. Krisch. *Phonon dispersion relations of zinc oxide: Inelastic neutron scattering and ab initio calculations.* Phys. Rev. **B 81**, 174304, (2010).

[V.47] F. Cerdeira, T. A. Fjeldly, and M. Cardona. *Raman study of the interaction between localized vibrations and electronic excitations in boron-doped silicon.* Phys. Rev **B 9**, 4344, (1974).

[V.48] I.M. Lifshitz. *Energy Spectrum Structure and Quantum States of Disordered Condensed Systems*. Physics-Uspekhi **7**, 549, (1965).

[V.49] M. F. Cerqueira, T. Viseu, J. Ayres de Campos, A. G. Rolo, T. de Lacerda-Aroso, F. Oliveira, I. Bogdanovic-Radovic, E. Alves, and M. I. Vasilevskiy. *Raman study of insulating and conductive ZnO:(Al, Mn) thin films*. Phys. Status Solidi **A 212**, 2345, (2015).

[V.50] J. Serrano, F. Widulle, A.H. Romero, M. Cardona, R. Lauck, and A. Rubio. *Dependence of phonon widths on pressure and isotopic mass: ZnO.* Phys. Status Solidi **B 235**, 260, (2003).

[V.51] A.W. Hewat. *Lattice dynamics of ZnO and BeO.* Solid State Commun. **8**, 187, (1970).

[V.52] K. Thoma, B. Dorner, G. Duesing, and W. Wegener. *Lattice dynamics of ZnO.* Solid State Commun. **15**, 1111, (1974).

[V.53] V.V. Ursaki, I.M. Tiginyanu, V.V. Zalamai, E.V. Rusu, G.A. Emelchenko, V.M. Masalov, and E.N. Samarov. *Multiphonon resonant Raman scattering in ZnO crystals and nanostructured layers.* Phys. Rev. **B 70** 155204, (2004).

[V.54] T.L. Phan, R. Vincent, D. Cherns, N.X. Nghia, and V.V. Ursaki. *Raman scattering in Me-doped ZnO nanorods (Me = Mn, Co, Cu and Ni) prepared by thermal diffusion.* Nanotechnology **19** 475702, (2008).

[V.55] B. Kumar, H. Gong, S.Y. Chow, S. Tripathy, and Y. Hua. *Photoluminescence and multiphonon resonant Raman scattering in low-temperature grown ZnO nanostructures.* Appl. Phys. Lett. **89,** 071922, (2006).

[V.56] William Hayes, and Rodney Loudon. *Scattering of Light by Crystals*. Dover, New York, USA, (2004).

[V.57] Ed. by Manuel Cardona, and Gernot Güntherodt. *Light Scattering in Solids II* Topics Appl. Phys. **50**, Springer, Germany, 19-178, (1982).

[V.58] J. F. Scott. *UV resonant Raman scattering in ZnO.* Phys. Rev. **B 2,** 1209, (1970).

[V.59] R.C.C. Leite, J. C. Scott, and T. C. Damen. *Resonant Raman Effect in Semiconductors.* Phys. Rev. 188, 1285, (1969).

[V.60] M. V. Klein, and S. P. S. Porto. *Multiple-phonon resonant Raman scattering in CdS.* Phys. Rev. Lett. **22,**.782 (1969).

[V.61] V. V. Zalamai, V. V. Ursaki, E. V. Rusu, P. Arabadji, I. M. Tiginyanu, and L. Sirbu. *Photoluminescence and resonant Raman scattering in highly conductive ZnO layers.* Appl. Phys. Lett. **84**, 5168, (2004).

[V.62] R. B. Liu, A. L. Pan, H. M. Fan, F. F. Wang, Z. X. Shen, G. Z. Yang, S. S. Xie, and B. S. Zou. *Phonon-assisted stimulated emission in Mn-doped ZnO nanowires.* J. Phys.: Condens. Matter **19**, 136206, (2007).

[V.63] J.D. Ye, K.W. Teoh, X.W. Sun, G.Q. Lo, D.L. Kwong, H. Zhao, S.L. Gu, R. Zhang, Y.D. Zheng, S.A. Oh, X.H. Zhang, and S. Tripathy. *Effects of alloying and localized electronic states on the resonant Raman spectra of $Zn_{1-x}Mg_xO$ nanocrystals*. Appl. Phys. Lett. **91**, 091901, (2007).

[V.64] R.M. Martin, and C.M. Varma. *Cascade theory of inelastic scattering of light.* Phys. Rev. Lett. **26**, 1241, (1971).

[V.65] E. Gross, S. Permogorov, Ya Morozenko, and B. Kharlamov. *Hot-exciton luminescence in CdSe crystals.* Phys. Status Solidi **b 59**, 551, (1973).

[V.66] M.V. Klein. *Equivalence of resonance Raman scattering in solids with absorption followed by luminescence.* Phys. Rev. **B 8,** 919, (1973).

[V.67] C. Trallero-Giner, I.G. Lang, and S.T. Pavlov. *Theory of two-phonon resonance Raman scattering of light in ZnTe.* Sov. Phys. – Solid State **22**, 718 (1980).

[V.68] J. Fryar, E. McGlynn, M.O. Henry, and J-P Mosnier. *Study of exciton–polariton modes in nanocrystalline thin films of ZnO using reflectance spectroscopy.* Nanotechnology **16**, 2625, (2005).

[V.69] H. Iwananga, A. Kunishige, and S. Takeuchi. *Anisotropic thermal expansion in wurtzite-type crystals.* J. Mater. Sci. **35**, 2451, (2000).

Chapter VI

Conclusions and Outlook

This work focused on the Raman scattering spectroscopy study of two important semiconductor solid solutions (SSs), GeSn and ZnO:Mn. Both materials are of high interest because of their potential applications in multiple areas. The GeSn SSs can be used as active layers in IR light-emitting diodes and lasers, being compatible with silicon technology. Doped zinc oxide can be used as a transparent conductor, eventually replacing ITO in touchscreens and photovoltaics. Even though the fulfilment of the main promise of these materials, namely, direct band gap in the case of GeSn and room-temperature ferromagnetism in the case of ZnO:Mn, have not been convincingly demonstrated so far, the interest of researchers to these materials remains high worldwide. The studies performed in the framework of this PhD thesis contribute to the better understanding of these materials in what concerns their lattice dynamics influenced by dopant's incorporation and the related Raman scattering characteristics. A careful investigation by means of resonant and non-resonant Raman spectroscopies was performed, supported by theoretical modelling and discussed in detail in the thesis. It was accompanied by the comprehensive characterization of the materials and complementary studies using other techniques, such as the magneto-optic Faraday rotation spectroscopy.

GeSn layers and multilayer structures (GeSn/Si multiple quantum wells, MQWs) were grown by molecular beam epitaxy, with direct participation of the author of this thesis. Contrary to the results of earlier studies it was found that it is possible to overgrow ultra-thin layers of pure Sn with Ge and maintain their crystalline structure, which is a first step towards incorporating such nanostructures into devices. These studies showed that it is possible not only to incorporate Sn into the Ge lattice (in thin film form) but also to grow self-assembled GeSn dots. Moreover, it is possible to overgrow the GeSn dots with Si and, thus, incorporate them into Si-based devices. The

deposition of a few MLs of pure Sn and their subsequent overgrowth revealed a key strategy to producing nanostructures with a Sn content that is high enough to obtain a direct bandgap material. Among the techniques used for the characterization of the GeSn structures, those that provided most relevant information were RBS, XRD, TEM and AFM that yielded Sn contents and lattice constant values (and related to them strain components) along with the morphology and the crystalline quality of the structures.

Experimental Raman spectroscopy results for GeSn solutions, similar to the more studied SiGe system, reveal the fundamental Ge-Ge and Ge-Sn vibration modes but the Sn-Sn mode is very weak and cannot be unambiguously identified in the Raman spectra. Some of the previous studies tentatively assigned a weak feature with frequency similar to that of the intrinsic optical phonon mode of α-Sn to the "missing" Sn-Sn mode, while others (of the group of J. Menendez) attributed it to disorder-activated acoustic vibrations of Ge crystal. Numerical simulations using the semi-empirical Tersoff potentials, performed in the present work also do not show a Sn-Sn mode in the calculated Raman spectra. The reason is the small vibration amplitude of heavy tin atoms and the low probability of occurrence of clusters of several Sn atoms (that would support the Sn-Sn mode) in the solid solutions with small tin contents.

X-ray diffraction studies have shown that the Ge-Sn layers used in this work are almost fully relaxed, with the in-plane and out-of-plane strain tensor components not exceeding 0.30%, well below the values corresponding to the pseudomorpic strain. This conclusion is corroborated by the Raman spectroscopy results where the red shift of the Ge-Ge peak follows the composition dependence predicted theoretically, by both macroscopic (using bulk deformation potentials) and numerical (based on the semi-empirical potentials for lattice dynamics and the bond polrizabilty approximation for the Raman response) models.

Numerical calculations that were performed in this work also allowed for understanding the composition and strain effects on the bond length distribution in the Ge-Sn solid solutions. Calculated bond length dependence upon the Sn content has a three-mode behaviour, which represents the three types of bonds (Sn-Sn, Sn-Ge and Ge-Ge). Each of this bond lengths changes gradually with the composition but none follows Vegard's law. In fact, the latter represent a "virtual" bond length, average over

the three types of real bonds and not encountered as such in the solid solution crystal. In this sense, Vegard's law is meaningful only in the macroscopic sense, e.g. for the evaluation of the macroscopic strain components, and may be misleading in the microscopic sense.

The Al-doped ZnO thin films, fabricated by radio-frequency (RF) magnetron sputtering, are highly conductive and transparent in the visible and near IR range, which makes this material a good candidate for optoelectronic applications. The films are nanocrystalline, with the typical grain size of 20 nm and high interface-to-volume ratio that should facilitate the formation of point defects. In spite of these factors, favourable for the observation of room temperature ferromagnetism (which, according to the recent years literature, may not be exclusively related to the presence of magnetic Mn ions in the lattice), both the magnetic resonance and Faraday rotation studies revealed just paramagnetism of the studied ZnO:Mn material at room temperature, similar to the results of several previous studies. In fact, the experimental confirmation of the theoretical prediction made more than 15 years ago by T. Dietl remains a matter of controversy.[20] The present work's objectives did not include profound studies of the magnetism in ZnO:Mn..

The detailed Raman spectroscopy study of ZnO thin films performed in this work has been focused on the changes introduced by doping with Mn atoms. Yet, a considerable attention was paid to ZnO crystal phonons and resonant excitation effects in the Raman scattering in nominally undoped and also Al-doped samples. For undoped polycrystalline films, a strong LO-phonon band, not seen in the non-resonant Raman spectrum of a single-crystal MBE-grown ZnO layer has been found. The presence of this band can be understood by the enhancement of the "forbidden"

[20] According to the recent review [L. M. C. Pereira, *Experimentally evaluating the origin of dilute magnetism in nanomaterials*, J. Phys. D: Appl. Phys. **50**, 393002 (2017)], "…these remarkable magnetic phenomena have become one of the most controversial topics in magnetism. Various non-intrinsic sources of ferromagnetism (e.g. instrumental artifacts and magnetic contamination) are becoming well documented, and rarely are all of them taken into account when room-temperature ferromagnetism is reported." As for the calculated results of T. Dietl, they are now considered incorrect [A. Zunger, S. Lany, and H. Raebiger, *The quest for dilute ferromagnetism in semiconductors: Guides and misguides by theory*, Physics **3**, 53 (2010)].

Fröhlich type scattering under excitation resonance conditions. The intense *n*-LO-phonon lines (*n* >1) observed in the resonant Raman scattering (RRS) spectra of ZnO films, both pure and doped, appear because of the phonon-assisted emission of light by hot excitons with appropriate energy, more efficient than the simultaneous emission of several phonons (the so-called cascade model), so it may be called a pseudo-Raman effect. This interpretation is confirmed, in particular, by the fact that the separation between the consecutive Raman peaks for $n > 2$ is slightly different from the LO phonon frequency measured by the position of the first peak. Using the cascade model, the relation between the frequencies and wavevectors of phonons responsible for the higher-order peaks in the RRS spectrum of pure ZnO film was evaluated, which fits the known dispersion relation for E_1-type phonon modes in bulk ZnO quite well.

It has been found that ZnO films doped with Al by either co-sputtering or ion implantation (ZnO:Al) show a rather high n-type conductivity. However, no evidence of phonon–plasmon coupling in these rather heavily doped samples was found, possibly because the plasmons are overdamped. In contrast with ZnO:Al, Mn doping of the ZnO films (by co-sputtering or by ion implantation) results in very resistive samples. Their Raman spectra show the presence of Mn-related modes (520–530 cm^{-1}) whose intensity increases with the increase of Mn content. The nature of this mode was discussed and a simple model and arguments were presented in support of the opinion that this Raman feature originates from local vibrations of Mn atoms and their groups (at higher concentrations), substituting Zn in the cationic sublattice of the ZnO crystal. This mode is Raman active because it falls into the gap of the optical phonon density of states of undoped ZnO crystal. Furthermore, it was shown that it is possible to preserve the conductivity of the samples even when both Al and Mn atoms are incorporated into the ZnO lattice. It was achieved using conductive RF-sputtered ZnO:Al films implanted *a posteriori* with Mn ions. This can be an alternative method for the preparation of conductive and transparent ZnO-based films for different applications.

Contrary to the intrinsic LO phonon mode, no resonant enhancement of the Mn-related Raman features in the spectra of ZnO:Mn and ZnO:Mn:Al films was found. Doping with Mn and Al influences the RRS spectra in a different way and the

characteristic features of this influence have also been understood in the framework of the cascade model. In particular, it is suggested that the suppression of the higher-order LO phonon lines is caused by the dissociation of excitons in the heavily n-type doped ZnO because of the screening of the electron-hole interaction by free carriers.

To summarize, studies of the lattice dynamics of the two semiconductor solid solutions, SnGe and ZnO:Mn have been the main goal of this PhD work but also a number of related effects influencing the properties of these materials have been analysed. Arguments in favour of the occurrence of substitutional doping (Mn/Zn) in ZnO:Mn have been presented, based on the Raman spectroscopy results. A Mn atom inserted into the cationic sublattice of the ZnO crystal originates a local vibrational mode in the gap of the phonon density of states and yields a Raman feature at ≈ 530 cm^{-1}. In contrast, the Sn dopant substituting Ge produces just a resonant mode overlapping with the continuum of germanium crystal phonons and its impact on the Raman spectrum of the solid solution is negligible in the limit of low tin contents. The effect of Sn doping is much more clearly seen in the fundamental Ge-Ge phonon mode.

This insight may have no direct impact on the technological development of the studied materials but certainly contributes to the understanding of their characterization results where the Raman spectroscopy is a valuable tool, especially in combination with other techniques. In a hypothetical continuation of this project, future studies would be focused on a more detailed understanding of the effect of Sn on the growth kinetics of Sn/Ge quantum wells (QWs) and quantum dots (QDs), in particular, by investigating Sn/Ge QWs and QDs with higher Sn content, and on exploring the potential of such Sn/Ge nanostructures for optoelectronic device applications. There new phonon-related effects can arise.

Apendix A

Publications

Along the Ph.D time 11 publications were produced, of which, 8 papers were published in journals, 2 papers were published in conferences and 1 poster presented. Form these, 5 papers, 1 conference paper and 1 poster are of relevance for the work present in this thesis. The publications are list in the following chapters by chronological publication (recent to older) together with the respective abstract.

A1. Most Relevant Publications Related with Group IV Materials

"Photoluminescence from ultrathin Ge-rich multi-quantum wells observed up to room-temperature: experiments and modelling."

Authors: T. Wendav, I. A. Fisher, M. Virgilio, G. Capellini, F. Oliveira, M. F. Cerqueira, A. Benedetti, S. Chiussi, P. Zaumseil, B. Schwartz, K. Busch and J. Schulze.

Publication: Physical Review B (accepted)

Abstract: "Employing a low-temperature growth-mode, we fabricated ultrathin $Si_{1-x}Ge_x$/Si multiple quantum well (QW) structures with a well thickness of less than 1.5 nm and a Ge concentration above 60 % directly on a Si substrate. We identified an unusual temperature-dependent blueshift of the photoluminescence (PL) and an exceptionally low thermal quenching. We find that this behavior is related to the relative intensities of the no-phonon (NP) peak and a phonon-assisted replica that are the main contributors to the total PL signal. In order to investigate these aspects in more detail, we developed a strategy to calculate the PL spectrum employing a self-consistent multi-valley effective mass model in combination with second-order perturbation theory. According to our investigation, we find that while the phonon-assisted feature decreases with temperature, the NP feature shows a strong increase

in the recombination rate. Besides leading to the observed robustness against thermal quenching this also causes the blueshift of the total PL signal as has been observed."

"(Si)GeSn nanostructures for optoelectronic device applications."

Authors: I. A. Fischer, Filipe Oliveira, Alessandro Benedetti, Stefano Chiussi, Jörg Schulze.

Publication: 2016 39th International Convention on Information and Communication Technology, Electronics and Microelectronics (MIPRO), 30 May-3 June 2016

Abstract: "We present an overview of recent results on the fabrication of GeSn- and SiGeSn-nanostructures for optoelectronic device application."

"Fabrication of GeSn-multiple quantum wells by overgrowth of Sn on Ge by using molecular beam epitaxy."

Authors: Filipe Oliveira, I. A. Fischer, Alessandro Benedetti, P. Zaumseil, Maria F Cerqueira, M. I. Vasilevskiy, Stefan Stefanov, Stefano Chiussi and Jörg Schulze.

Publication: Applied Physics Letters 107(26):262102, December 2015

Abstract: "We report on the fabrication and structural characterization of epitaxially grown ultra-thin layers of Sn on Ge virtual substrates (Si buffer layer overgrown by a 50 nm thick Ge epilayer followed by an annealing step). Samples with 1 to 5 monolayers of Sn on Ge virtual substrates were grown using solid source molecular beam epitaxy and characterized by atomic force microscopy. We determined the critical thickness at which the transition from two-dimensional to three-dimensional growth occurs. This transition is due to the large lattice mismatch between Ge and Sn (≈ 14.7 %). By depositing Ge on top of Sn layers, which have thicknesses at or just below the critical thickness, we were able to fabricate ultra-narrow GeSn multi-quantum-well structures that are fully embedded in Ge. We report results on samples with one and ten GeSn wells separated by 5 and 10 nm thick Ge spacer layers that were characterized by high resolution transmission electron microscopy and X-ray diffraction. We discuss the structure and material intermixing observed in the samples."

"Multi-stacks of epitaxial GeSn self-assembled dots in Si: Structural analysis."

Authors: Filipe Oliveira, I. A. Fischer, Alessandro Benedetti, Maria F Cerqueira, Mikhail Vasilevskiy, Stefan Stefanov, Stefano Chiussi and Jörg Schulze.

Publication: Poster in Jornadas CFUM_2016, Braga, Portugal, 20-11-2015.

"Growth and characterization of SiGeSn quantum well photodiodes."

Authors: Inga A Fischer, Torsten Wendav, Lion Augel, Songchai Jitpakdeebodin, Filipe Oliveira, Alessandro Benedetti, Stefan Stefanov, Stefano Chiussi, Giovanni Capellini, Kurt Busch and Jörg Schulze.

Publication: Optics Express 23(19):25048, September 2015

Abstract: "We report on the fabrication and electro-optical characterization of SiGeSn multi-quantum well PIN diodes. Two types of PIN diodes, in which two and four quantum wells with well and barrier thicknesses of 10 nm each are sandwiched between B- and Sb-doped Ge-regions, were fabricated as single-mesa devices, using a low-temperature fabrication process. We discuss measurements of the diode characteristics, optical responsivity and room-temperature electroluminescence and compare with theoretical predictions from band structure calculations."

"Multi-stacks of epitaxial GeSn self-assembled dots in Si: Structural analysis."

Authors: Filipe Oliveira, I. A. Fischer, Alessandro Benedetti, Maria F Cerqueira, Mikhail Vasilevskiy, Stefan Stefanov, Stefano Chiussi and Jörg Schulze.

Publication: Journal of Applied Physics 117(12):125706, March 2015

Abstract: "We report on the growth and structural and morphologic characterization of stacked layers of self-assembled GeSn dots grown on Si (100) substrates by molecular beam epitaxy at low substrate temperature T = 350 °C. Samples consist of layers (from 1 up to 10) of $Ge_{0.96}Sn_{0.04}$ self-assembled dots separated by Si spacer layers, 10 nm thick. Their structural analysis was performed based on transmission electron microscopy, atomic force microscopy, and Raman scattering. We found that up to 4 stacks of dots could be grown with good dot layer homogeneity, making the GeSn dots interesting candidates for optoelectronic device applications."

“Epitaxial growth of strained and unstrained GeSn alloys up to 25 % Sn.”

Authors: Michael Oehme, Konrad Kostecki, M. Schmid, Filipe Oliveira, Erich Kasper and Jörg Schulze.

Publication: Thin Solid Films 557(1):169, April 2014

Abstract: “Strained and unstrainedGeSn layers on Si substrateswere grown with Sn contents up to 20% and 25%, respectively. All metastable layer structureswere fabricated bymeans of an ultra-lowtemperature molecular beamepitaxy process. The useful thickness of the metastable layers for a range of Sn contents, growth temperatures and two different strain values (unstrained, compressive strained) is explored. The epitaxial breakdown thickness which limits the useful thickness range decreases exponentially with increasing growth temperature and Sn concentration.”

A2. Most Relevant Publications Related with ZnO:Mn

“Raman study of insulating and conductive ZnO:(Al, Mn) thin films.”

Authors: Maria F Cerqueira, T. Viseu, Julia Tovar, Anabela Gomes Rolo, T. de Lacerda-Aroso, Filipe Oliveira, Iva Bogdanovic Radovic, E. Alves and Mikhail Vasilevskiy.

Publication: Physica Status Solidi (A) Applications and Materials 212(10), July 2015

Abstract: “Raman spectroscopy results obtained for undoped and Al- and/or Mn-doped ZnO thin films produced by RF-sputtering are reported. The effect of the doping method (either co-sputtering or ion implantation), the dopant type, and its concentration on the Raman-active vibrational modes in these films were studied in detail. The results are discussed with focus on the peak shifts and broadening, and on the doping-induced relaxation of the symmetry selection rules. A particular attention is paid to the 520–530 cm−1 Raman band observed in all Mn containing samples and a simple theoretical model and arguments are presented in support of its relation to the local (gap) phonon mode produced by Mn atoms substituting Zn in the cationic sublattice of the ZnO crystal.”

“Faraday effect in ZnO:Mn thin films.”

Authors: Filipe Oliveira, Maria F Cerqueira, Mikhail Vasilevskiy, T. Viseu, Nikolai A. Sobolev and M. C. Carmo.

Publication: AIP Conference Proceedings; Journal Volume: 1399; Journal Issue: 1; Conference: 30. international conference on the physics of semiconductors, Seoul (Korea, Republic of), 25-30 Jul 2010 (Publication date: 23-12-2011)

Abstract: “Undoped and Mn-doped ZnO transparent thin films were grown by RF magnetron co-sputtering. The films are nanocrystalline, with wurtzite-structure grains of a typical size of 20 nm, with a preferential orientation of the c-axis perpendicular to the surface. Although, according to the Raman spectroscopy data, Mn mostly substitutes Zn in the lattice sites, factor that is considered favourable for ferromagnetism in this material, the ZnO:Mn films are paramagnetic at room temperature as it follows from our Faraday effect (FE) measurements. The FE spectra show a significant influence of the Mn ions for photon energies sufficiently below the ZnO:Mn band gap but not in its vicinity.”

“Resonant Raman scattering in ZnO:Mn and ZnO:Mn:Al thin films grown by RF sputtering.”

Authors: Maria F Cerqueira, Mikhail Vasilevskiy, Filipe Oliveira, Anabela Gomes Rolo, T Viseu, Julia Tovar, E. Alves and M. R. Correia.

Publication: Journal of Physics Condensed Matter 23(33):334205, August 2011

Abstract: “Raman spectroscopy results obtained under visible (non-resonant) and UV (resonant) excitation for nanocrystalline ZnO, ZnO:Mn and ZnO:Mn:Al thin films grown by radio frequency magnetron sputtering are presented and compared. The origin of the multiple longitudinal optical (LO) phonon Raman peaks, strongly enhanced under resonance conditions, and the effects of the dopants on them are discussed in the framework of the 'cascade' model. It is suggested that the observed suppression of the higher-order LO phonon lines for ZnO:Mn:Al is caused by the dissociation of excitons in the heavily n-type doped material. On the basis of the cascade model interpretation of the higher-order Raman peaks in the resonant spectra, the LO phonon frequencies for wavevectors away from the point are evaluated and compared to previously published phonon dispersion curves.”

A3. Other Publications

"Ge-on-Si PIN-photodetectors with Al nanoantennas: The effect of nanoantenna size on light scattering into waveguide modes."

Authors: Inga A Fischer, Lion Augel, Timo Kropp, Songchai Jitpakdeebodin, Nuno Franz, Filipe Oliveira, Erlend Rolseth, Tobias W. W. Maß, Thomas Taubner and Jörg Schulze.

Publication: Applied Physics Letters 108(7):071108, February 2016

Abstract: "Metallic nanoantennas can be used to enhance the efficiency of optical device operation by re-distributing electromagnetic energy. Here, we investigate the effect of a random distribution of disc-shaped Al nanoantennas of different diameters deposited on Ge-on-Si PIN-photodetectors on the wavelength-dependent responsivity. We compare our experimental results to simulations and find that the largest responsivity enhancement is obtained for wavelengths that correspond to energies at or below the bandgap energy of Ge. We argue that this is the result of antenna-mediated scattering of light into waveguide modes within the Ge-on-Si PIN-photodetectors, which is effectively influenced by nanoantenna size, and we discuss a possible application of the concept for integrated biosensing."

Apendix B

Faraday Effect Details

B1. Magneto-Optic Effects

There are several different types of magneto-optic effects, some of them manifest in reflection while others in transmission. The magneto-optic effects can also be divided as linear or quadratic magneto-optic effects. The first ones are linear with the magnetization and consequently, they change sign upon the reversal of magnetization **[B.1]**. Examples these linear magneto-optic effect are the Faraday rotation effect, Kerr effect, magnetic circular dichroism, and Voigt effect. Quadratic magneto-optic effects states the quadratic proportionality between the angle of the rotation of the plane of polarization and the strength of the magnetic field **[B.2]**. Quadratic magnetic rotation of polarization of light (QMR effect) is the only known quadratic magneto-optic effect. This effect can be observed in the transverse geometry when the vector of the magnetic field strength is perpendicular to the direction of light propagation **[B.2]**. In semiconductors research, Faraday effect, Kerr effect and magnetic circular dichroism are the most used one.

B1.1. Faraday Rotation Effect

Faraday rotation effect (FE) or magnetic circular birefringence (MCB) belongs to the category of magneto-optic effects that take place in transmission configuration. In Farraday effect it is observed the rotation of the plane of polarization (angle) of an incident linearly polarized electromagnetic radiation wave when the magnetic field is oriented normal to the material's interface (see **Figure II.49**)

The refractive index can be different for left- and right-handed circularly polarized light, which causes a rotation of the plane of polarization and this rotation depends on a weighted average over all the transitions in the material. **[B.3]**

B1.2. Kerr Effect

Magneto-optic Kerr effect (MOKE) belongs to the category of magneto-optic effects that take place upon the reflection at surfaces and interfaces. Like in the Faraday effect, in Kerr effect is observed a rotation of the plane of polarization (angle) of the incident linearly polarized electromagnetic radiation wave. Kerr effect can be performed in three different geometries: polar, longitudinal and transversal (see **Table B1.1**).

In the polar geometry the magnetization and incident radiation are oriented normal to the interface incidence (see **Table B.1**). The MO longitudinal Kerr effect takes place when the magnetization is parallel both to the interface and the plane of incidence (see **Table B.1**). Again, upon reflection, a linearly polarized incident wave is transformed to an elliptically polarized one, with the major axis of the polarization ellipse rotated with respect to the incident azimuth. **[B.1]**

In magneto-optic transverse Kerr effect the magnetization lies in the plane of interface and normal to the plane of incidence (see **Table A.1**). Here, only the wave with its electric field vector polarized in the plane of incidence (TM wave) displays changes. These manifest themselves by transformations of both the amplitude and phase of the TM reflected wave linear (or more generally, odd) in magnetization. **[A.1]**

Table B.1: Definition of the MOKE geometries. [A.4]

Geometry	Mag. Field Orientation	Observable at normal incidence	Diagram
Polar	Parallel to the plane of incidence, normal to the sample surface	Yes	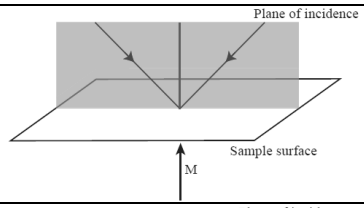
Longitudinal	Parallel to the plane of incidence and the sample surface	No	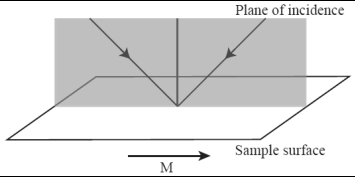
Transversal	Normal to the plane of incidence, parallel to the sample surface	No	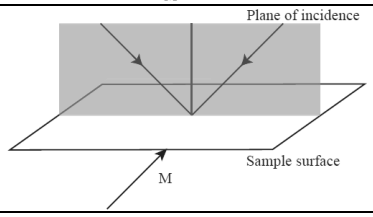

B1.3. Magnetic Circular Dichroism

Magnetic circular dichroism (MCD) can be measure in transmission or in reflection (this one is frequently used in magneto-optic spectroscopic ellipsometry). In the magnetic circular dichroism it is observed the difference in absorption for left- and right-circularly polarized light (RCP and LCP) at a particular frequency. This causes plane polarized light to become elliptically polarized. **[B.3]**

The Faraday rotation effect is very useful in applications because it is finite in spectral regions where the sample/medium/crystal is transparent. However, the magnetic circular dichroism is of most use for determining the nature of the magnetic states. Magnetic circular dichroism is only nonzero where the crystal is absorbing and the magnetic circular dichroism spectrum is often much sharper than the absorption spectrum and so it gives better energy resolution as well as information on the wave functions. **[B.3]**

Opaque samples are usually studied in reflection, and the largest signals can be obtained using the polar Kerr effect **[B.3].**

The reflected light (the polar Kerr effect) or transmitted light (the Faraday effect) becomes elliptically polarized to a slight degree with the major axis of the ellipse rotated with respect to the incident polarization. Subsequently, the rotation and ellipticity of the reflected light or transmitted light is measured (**Figure B.2**). The analysis of the magneto-optical activity of a substance is generally carried out in two stages. First, the measured quantities, that is, the Faraday or the Kerr rotation angle, θ_F or θ_k and ellipticity, ξ_F or ξ_K, are related to the dielectric tensor. In a second step, these functions are then interpreted in terms of crystal field states of magnetic ions or spin-polarized band-structure calculations.

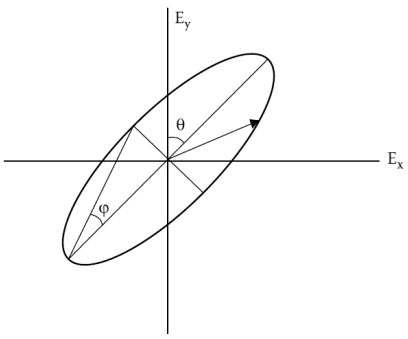

Figure B.2: The Faraday or Kerr rotation, θ, and ellipticity, $\xi = \tan\varphi$.

B2. Theory of Magneto-Optic Effects in Semiconductors

To understand the origin of magneto-optic effects it is not necessary to go into details of microscopic models describing the response of magnetic media to electromagnetic plane waves. This can be done from Maxwell equations assuming magnetization-dependent material tensors. However, microscopic models are necessary to understand the mechanisms responsible by these magnetic-optic effects. The must important mechanisms responsible by the magnetic-optic effects in semiconductors are the free electrons, inter-band transitions and excitons.

B2.1. Macroscopic Theory

B2.1.1. Magnetized Medium

In the optical region of electromagnetic spectrum, the medium can be described by complex conductivity or complex electric susceptibility tensors. Their form follows from symmetry arguments. In the case of an isotropic medium subjected to an applied uniform time-independent magnetic flux density field, *B*, the symmetry of the permittivity tensor is determined by the symmetry group of the axial vector *B* alone. A uniform magnetization, *M*, induced by *B* is parallel to *B* and displays the same symmetry. **[B.1]**

In the optic spectral region, magnetic susceptibility assumes very small values dependent on the radiation frequency. Then electric dipole approximation can be assumed and in most cases crystalline structure from the medium can be ignored. This leads to the simplest form of the material tensor in a magnetic medium. **[B.1]**

Complex electric susceptibility tensor is related with the complex dielectric tensor by $\varepsilon = 1 + 4\pi\chi$ (in the CGS units system). In a cubic symmetry crystalline medium with a magnetization *M* parallel to *z*-axis, the complex dielectric tensor assumes the form **[B.1, B.5]**:

$$\hat{\varepsilon} = \begin{pmatrix} \varepsilon_{xx} & \varepsilon_{xy} & 0 \\ -\varepsilon_{xy} & \varepsilon_{xx} & 0 \\ 0 & 0 & \varepsilon_{zz} \end{pmatrix} \qquad \textbf{\{B.1\}}$$

The effect of magnetization reversal on the tensor elements is obtained form the symmetry operation of reflection in the planes containing the principal axis. As result, the diagonal and off-diagonal elements of the complex dielectric function are even and odd functions of the magnetization, respectively **[B.1]**:

$$\varepsilon_{ij}(M) = \varepsilon_{ji}(-M). \qquad \textbf{\{B.2\}}$$

B2.1.2. Complex Refractive Index

For an isotropic medium, $\varepsilon_{xx} = \varepsilon_{yy} = \varepsilon_{zz} \equiv \hat{\varepsilon}(\omega)$ and $\hat{\varepsilon}(\omega)$ is a complex function of frequency with $\mathrm{Im}(\hat{\varepsilon}) > 0$. It can be written in the form:

$$\hat{\varepsilon}(\omega) = \varepsilon_{\infty} + i\frac{4\pi\hat{\sigma}}{\omega} \qquad \textbf{\{B.3\}}$$

where $\hat{\sigma} = \sigma_{\mathrm{Re}} + i\sigma_{\mathrm{Im}}$ is the complex conductivity index defined by

$$\hat{n}^2 \equiv (\eta + i\kappa)^2 = \hat{\varepsilon}(\omega) \qquad \textbf{\{B.4\}}$$

From **Equations {B1.3}** and **{B1.4}** it follows that

$$\eta^2 - \kappa^2 = \varepsilon_{\infty} - \frac{4\pi}{\omega}\sigma_{\mathrm{Im}} \qquad \textbf{\{B.5\}}$$

$$2\eta\kappa = \frac{4\pi}{\omega}\sigma_{\mathrm{Re}}. \qquad \textbf{\{B.6\}}$$

The same medium in magnetic field is described by the dielectric tensor **{B.1}** with $\varepsilon_{xx} = \varepsilon_{yy} \neq \varepsilon_{zz}\left(z \parallel \vec{B} \parallel \vec{M}\right)$. For an electromagnetic wave propagating in the medium along *z* (parallel to the magnetization), the wave equation yields:

$$\begin{pmatrix} k^2 E_x \\ k^2 E_y \\ 0 \end{pmatrix} = \frac{\omega^2}{c^2}\begin{pmatrix} \varepsilon_{xx} & \varepsilon_{xy} & 0 \\ -\varepsilon_{xy} & \varepsilon_{xx} & 0 \\ 0 & 0 & \varepsilon_{zz} \end{pmatrix}\begin{pmatrix} E_x \\ E_y \\ E_z \end{pmatrix} \qquad \textbf{\{B.7\}}$$

where *k* is the wavevector and $E_{x,y,z}$ are the components of the electric field ($\vec{E}$). The compatibility condition of the system of linear **Equations {B1.7}** reads:

$$\varepsilon_{zz}\left[N_z^4 - 2\varepsilon_{xx}N_z^2 + \left(\varepsilon_{xx}^2 + \varepsilon_{xy}^2\right)\right] = 0 \qquad \textbf{\{B.8a\}}$$

$$N_z \equiv kc/\omega. \qquad \textbf{\{B.8b\}}$$

Equation {B1.8} has the following solutions (eigenmodes):

(i) $\varepsilon_{zz} = 0$

(ii) $N_z^2 = \varepsilon_{xx} \pm i\varepsilon_{xy}$

The first solution corresponds to a longitudinal wave ($E_z \neq 0$) while the other two describe circular polarized waves, characterized by different refractive indices,

$$\eta_{\pm} = \sqrt{\varepsilon_{xx} \pm i\varepsilon_{xy}} \qquad \textbf{\{B.9\}}$$

corresponding to the left hand (LH, +) and right hand (RH, –) polarized waves.

B2.1.3. Faraday Effect

Let's consider a slab of thickness *d* with *z* axis perpendicular to its surfaces. A linear polarized (along *x*) wave with amplitude *E* impinges on one of the surfaces (*z* = 0). It can be decomposed into a pair of LH and RH circular polarized waves with amplitudes:

$$\vec{E}_{\pm} = \frac{1}{2} E_0 \left(\vec{e}_x \pm \vec{e}_y\right). \qquad \textbf{\{B.10\}}$$

The phases of the LH and RH waves inside the slab are:

$$\varphi_{\pm} = \omega\left(\eta_{\pm}\frac{z}{c} - t\right) \qquad \textbf{\{B.11\}}$$

Inside the slab the *x* and *y* component of the electric field are:

$$E_x = \vec{e}_x\left\{\vec{E}_+ \exp(i\varphi_+) + \vec{E}_- \exp(i\varphi_-)\right\} = E_0 \exp\left[i(\varphi_+ + \varphi_-)\right]\cos\left(\frac{\varphi_+ - \varphi_-}{2}\right) \qquad \textbf{\{B.12a\}}$$

$$E_y = \vec{e}_y\left\{\vec{E}_- \exp(i\varphi_-) - \vec{E}_+ \exp(i\varphi_+)\right\} = E_0 \exp\left[i(\varphi_+ + \varphi_-)\right]\sin\left(\frac{\varphi_- - \varphi_+}{2}\right) \qquad \textbf{\{B.12b\}}$$

When the wave leaves the slab ($z = d$), its polarized is rotated by an angle θ_F,

$$tg(\theta_F) = \frac{\mathrm{Re}\,E_y(d)}{\mathrm{Re}\,E_x(d)} = tg\left(\frac{\varphi_- - \varphi_+}{2}\right) \qquad \textbf{\{B.13a\}}$$

or

$$\theta_F = \frac{\omega}{2c}(\eta_- - \eta_+)d\,. \qquad \textbf{\{B.13b\}}$$

This is the Faraday rotation effect: the Faraday angle is proportional to the difference between η_- and η_+. If this difference is small, one can also write:

$$\theta_F \approx \frac{\omega d}{2c}\frac{\left(\eta_-^2-\eta_+^2\right)}{2\eta} = -\frac{\omega d}{2\eta c} i\varepsilon_{xy} = \frac{2\pi d}{\eta c}\sigma_{xy}. \qquad \textbf{\{B.14\}}$$

It is clear from **Equation {B.14}** that the Faraday rotation is linear in magnetization of the medium.

A more general consideration, suitable for multilayer media and taking into account multiple reflections at surfaces and interfaces, uses transfer matrices obtained by solving the wave equation for each layer and applying appropriate boundary conditions. Of course, the knowledge of the dielectric tensor **{B.1}** for each medium is required.

B2.2. Microscopic Models of Magneto-Optic Effects

B3.2.1. Becquerel Model

The simplest model explaining microscopically the Faraday rotation effect was proposed by H. Becquerel for a dielectric material with diamagnetic properties, magnetic causes Larmour precession of electrons orbital of the atoms, with the following precession frequency:

$$\omega_L = \frac{eB}{2m_0 c} \qquad \textbf{\{B.15\}}$$

The precession affects the dielectric response of the atoms to circular polarized light,

$$\eta_\pm = \eta \mp \omega_L \frac{d\eta}{d\omega}. \qquad \textbf{\{B.16\}}$$

B2.2.2. Lorentz Model

In this model, the material is envisaged as an assembly of a large number of polarized atoms, each of which is small (in comparison to the wavelength of light) and close to its neighbours. When a light wave is incident on such a medium, each atom can be thought of as a classical forced oscillator, being driven by a time-varying electric field, $E(t)$, which here is assumed to be applied in the *z*-axis direction. The force

exerted on an electron of charge *q* by the $E(t)$ field of the harmonic wave at frequency, *ω*, is of the form:

$$F_E = eE_0 \exp(-i\omega t). \quad \textbf{\{B.17\}}$$

Newton's second law provides the equation of motion:

$$eE_0 \exp(-i\omega t) = m_e \frac{d^2 z}{dt^2} + m_e \gamma \frac{dz}{dt} + m_e \omega_0^2 z\,. \quad \textbf{\{B.18\}}$$

where γ is the damping constant and ω_0 is the natural frequency. The solution of equation **{B.18}** is:

$$z(t) = \frac{q_e / m_e}{\omega_0^2 - \omega^2 - i\gamma\omega} E_0 \exp(-i\omega t). \quad \textbf{\{B.19\}}$$

It can be interpreted as the relative displacement between the negative cloud and the positive nucleus. Without a driving force, the oscillator will vibrate at its resonant frequency, ω_0. The dipole moment is equal to the product of the charge *q* and its displacement, and if there are *N* contributing electrons per unit volume, the electric polarization, *P* (*i.e.*, the density of dipole moments) is:

$$P = ezN = \frac{q^2 / m_e}{\omega_0^2 - \omega^2 - i\gamma\omega} NE\,. \quad \textbf{\{B.20\}}$$

The dielectric function is:

$$\varepsilon_{xx}(\omega) = 1 + \frac{4\pi P(t)}{E(t)} = 1 + \frac{4\pi e^2 / m_e}{\omega_0^2 - \omega^2 - i\gamma\omega} N\,. \quad \textbf{\{B.21\}}$$

The quantum mechanical expression is obtained from this classical result by assuming that there are *N* atoms/molecules per unit volume, and that each oscillator has a range of natural frequencies ω_{0j}, each with oscillator strength f_j. In this case:

$$\varepsilon_{xx}(\omega) = 1 + 4\pi N \frac{e^2}{m_e} \sum_i \frac{f_j}{\omega_0^2 - \omega^2 - i\gamma_j \omega}\,. \quad \textbf{\{B.22\}}$$

For electric dipole transitions, the off-diagonal elements are given by a sum over all initial states, *i*, and final states, *j*:

$$\varepsilon_{xy} = 1 + 2\pi N \frac{e}{m_e} \left[\sum_{ij} \frac{f_{ij+}}{\omega_{ij+}^2 - \omega^2 - i\gamma_{ij}\omega} - \sum_{ij} \frac{f_{ij-}}{\omega_{ij-}^2 - \omega^2 - i\gamma_{ij}\omega} \right] \quad \textbf{\{B.23\}}$$

where $f_{ij\pm}$ are the oscillator strengths for transitions caused by RCP and LCP light. **[B.5]**

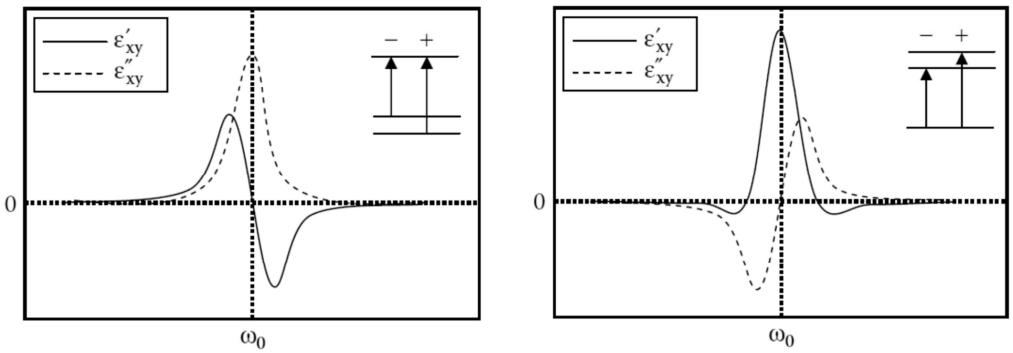

Figure B.3: ε'_{xy} and ε''_{xy} behaviour as a function of frequency of a) paramagnetic and b) diamagnetic line shapes. Inside: Energy level scheme and transitions involved. [B.3]

According to **Equation {B.23}**, there are two reasons why there might be a magnetic-optic response. First, the two oscillator strengths may be different in the presence of magnetic field, $f_{ij+} \neq f_{ij-}$ because of different populations, but $\omega_{ij+} \approx \omega_{ij-}$. (This means that the splitting in the ground state is large compared with the thermal energy so that a population difference occurs, but small compared with the optical linewidths or experimental resolution.) In this case, both the real and imaginary components of ε_{xy} have the same frequency dependence as a normal oscillator, but the magnitude is reduced because of the difference in populations. This gives the so called paramagnetic line shape, in which the imaginary part has a peak and the real part shows a dispersive shape as shown in **Figure B.3a**. Since a paramagnetic signal depends on population differences, it is temperature dependent. **[B.3]**

The second reason why it is possible to obtain a signal is because the two absorption frequencies are different due to splitting in either the ground state or excited state, or in both states, so $\omega_{ij+} \neq \omega_{ij-}$, but the oscillator strengths are the same, $f_{ij+} = f_{ij-}$ (see **Figure B.4**). The subtraction of the two absorption spectra results in a dispersive feature in the resulting spectrum (see **Figure B.3b**). Using the Kramers–Kronig analysis, it is expected a peak in the real part, which is confirmed by calculations **[B.5]**. The line shape in this case is called diamagnetic **[B.3]**.

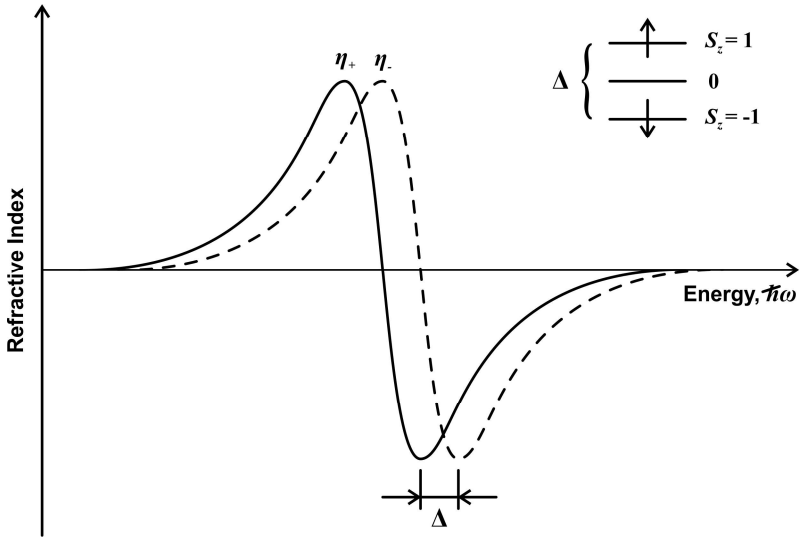

Figure B.4: Refractive index for two circular polarizations. Δ is the magnetic field induced spectral shift between excitons with spin up and spin down (total spin is 1, S = 1).

It should be noted that it is not possible to have a population difference without having some energy splitting between the states of the ground state manifold, and so this separation is in part idealized. Nevertheless, the paramagnetic lineshape can be observed when the spectral resolution is too broad to detect splitting that causes the population differences **[B.3]**.

If there is a purely diamagnetic effect arising from a splitting of the levels of either the ground or the excited state, then ε''_{xy} is a purely dispersive feature that has equal weights in its positive and negative parts. If the transition is stronger for one polarization than for the other, then this usually indicates unequal populations of two states with different orbital momentum quantum numbers. This can be in the ground state in which the transition is stronger than in the state with the higher population, or in the excited state, in which case the transition to the state with a higher population has a reduced strength **[B.3]**.

B2.2.3. Drude Model

Free electron response to electromagnetic wave, important for metals and doped semiconductors, can be described by Drude model. It is equivalent to putting $\omega_0 = 0$ in equations **{B.21} – {B.23}** *i. e.*:

$$\varepsilon_{xx}(\omega) = 1 - \frac{\omega_\rho^2}{\omega^2 + i\gamma_\rho \omega} \qquad \textbf{\{B.24a\}}$$

where

$$\omega_\rho = \sqrt{\frac{4\pi N e^2}{m_e}} \qquad \textbf{\{B.24b\}}$$

is the plasma frequency (N now denotes the free electrons concentration) and $\gamma_\rho = \tau_\rho^{-1}$, τ_ρ is the momentum relaxation time. **Equation {B.24}** can be generalized to include "background" dielectric constant of the material by replacing 1 by ε_∞.

The conductivity tensor components, according to Drude model are **[A.6]**:

$$\sigma_{xx} = \frac{e^2 N \tau_\rho}{m_e} \frac{1 + i\omega\tau_\rho}{\left(1 + i\omega\tau_\rho\right)^2 + \left(\omega_c \tau_\rho\right)^2} \qquad \textbf{\{B.25a\}}$$

$$\sigma_{xy} = \frac{e^2 N \tau_\rho}{m_e} \frac{\omega_c \tau_\rho}{\left(1 + i\omega\tau_\rho\right)^2 + \left(\omega_c \tau_\rho\right)^2} \qquad \textbf{\{B.25b\}}$$

where $\omega_c = eB/m_e c$ is the cyclotron frequency. The corresponding dielectric tensor is given by **Equation {B.4}**. **Equation {B.14}** together with **Equation {B.25b}** provides the spectral dependence of the Faraday effect within this model.

B2.2.4. Interband Transitions

Interband transitions determine the dielectric functions of typical semiconductors in the optical range. For a cubic semiconductor with direct band gap and allowed dipole transitions the imaginary part of $\hat{\varepsilon}(\omega)$ is given by:

$$\operatorname{Im}\hat{\varepsilon}(\omega) = \left(\frac{2\pi e}{m_0 \omega}\right)^2 \left(\frac{2}{3} D^2\right) g_i(\omega) \qquad \textbf{\{B.26\}}$$

where m_0 is the free electron mass, *D* is the so called Kane's matrix element of the moment operator between the conduction and valence band and

$$g_j(\omega) = \begin{cases} \dfrac{\sqrt{2}\left(\mu^*\right)^{3/2}}{\pi^2 \hbar^3} \sqrt{\hbar\omega - E_g} & ; \quad \omega \geq \dfrac{E_g}{\hbar} \\ 0 & ; \quad \omega < \dfrac{E_g}{\hbar} \end{cases} \qquad \textbf{\{B.27\}}$$

is the joint density of states. In equation **{B.27}** $\mu^* = m_e m_h / \left(m_e + m_h\right)$; m_e and m_h are the electron and hole effective masses, respectively, and E_g is the energy band gap. The real part of $\hat{\varepsilon}$ can be found through the Kramers-Kronig relation.

Magnetic field produces Landau quantization of the electronic energies and also splitting of the Landau levels owing to the Zeeman effect. Transitions between electron and hole states with opposite spin projections are linked to circular polarized right as required by the angular momentum conservation ($\Delta m = \pm 1$ for LH and RH polarized light, respectively). The transition energies are given by

$$E_n^{\pm} = E_g + \left(n + \frac{1}{2}\right)\left(\hbar\omega_c^e + \hbar\omega_c^h\right) \pm \hbar\gamma \qquad \textbf{\{B.28\}}$$

where *n* = 0,1,2,…; $\hbar\omega_c^{e,h}$ are the cyclotron frequency for electrons and holes and γ is the Zeeman splitting (proportional to the magnetic field, likewise ω_c).

Based on equation **{B.28}** the calculation of the dielectric tensor can be performed in the same way as equation **{B.27}** (for *B* = 0).

For $\gamma << \omega_c$ and $\omega z\, E_g/\hbar$ one can obtain **[A.7]**

$$\eta_- - \eta_+ = \frac{Const.}{\omega^2}\gamma\left[\frac{1}{\sqrt{E_g - \hbar\omega}} - \frac{1}{\sqrt{E_g + \hbar\omega}} + \frac{\hbar\omega}{E_g^{3/2}}\right]; \qquad \textbf{\{B.29a\}}$$

$$Const. \propto \left(m_h - m_e\right) \qquad \textbf{\{B.29b\}}$$

Then the Faraday angle, θ_F , as a function of frequency can be obtained by applying **Equation {B.13b}.** The sign of θ_F is usually positive for photon energies below the band gap, the range where **Equation {B.29}** is valid (because typically $m_h > m_e$).

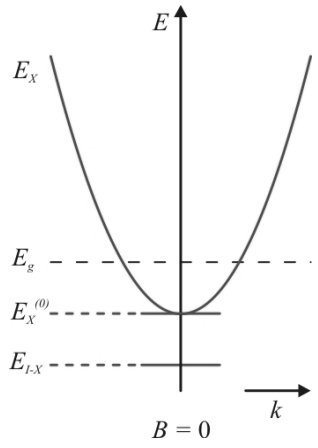

Figure B.5: Diagram showing the Wannier-Mott exciton energy without external magnetic field applied. $E_{I\text{-}X}$ is a localized state in energy and moment.

B2.2.5. Excitons

The absorption of a photon by an inter-band transition in a semiconductor creates an electron in the conduction band and a hole in the valence band. These particles attract each other through their mutual Coulomb interaction, and in the right conditions, a bound between the electron and hole can be formed, forming a Wannier-Mott exciton. At room temperature, the exciton effect on the optical properties of semiconductor is usually small because of thermal decay of the excitons. However it becomes important at low temperatures.

The energy of the exciton, E_X, (similar to hydrogen atom) and the kinetic energy of the free movement of its centre of mass, are given by:

$$E_X = E_X^{(n)} + \frac{\hbar^2 k^2}{2M} \quad ; \quad M = m_e + m_h$$
$$E_X^{(n)} = E_g - \frac{e^2}{\varepsilon_0 \varepsilon_R a_x}\frac{1}{n^2} \quad ; \quad a_X = \frac{\varepsilon \hbar^2}{\mu e^2} \quad ; \quad n = 0,1,2,... \qquad \textbf{\{B.30\}}$$

where a_X is the exciton Bohr radius and ε_0 is the static dielectric constant.

The dielectric function **{B.27}** is modified by the exciton effect. For $\hbar\omega > E_g$, $\mathrm{Im}\,\hat{\varepsilon}$ should be multiplied by the following function:

$$f_x(x) = \frac{2\pi}{\sqrt{x}\left(1 - \exp\left(-2\pi x^{-1/2}\right)\right)} \qquad \textbf{\{B.31\}}$$

where $x = \hbar\omega / E_g$ (notice that $\mathrm{Im}\,\hat{\varepsilon}$ now takes a finite value at $\hbar\omega = E_g$). Below the gap, resonance transitions appear at energies $E_x^{(n)}$ given by equation **{B.30}**. These transitions can contribute to the Faraday rotation.

Some type of crystal defects, like impurities or vacancies, can act like traps, creating a local potential well. When trapped, the exciton energy with the superposition of the potential well results in the lowering of the excitonic energy. This compensates the free movement energy forming an impurity-exciton complex with discrete energy levels, $E_{I\text{-}X}$ (see **Figure B.5**).

The application of a magnetic field perturbs the excitons by exerting forces to the charged particles. In the language of Quantum Mechanics, it means splitting of the exciton energy levels. They can be classified according to the "magnetic quantum number", which determines the *z*-projection ($z//B$) of the total momentum,

$\vec{J} = \vec{L} + \vec{S}$, where $\vec{L}$ and $\vec{S}$ are the orbital momentum and the spin of the exciton. The ground state exciton total angular momentum can be 0 or 1 if the spins of the electron and the hole are anti-parallel or parallel to each other. The last case will result in a triplet state split by the magnetic field (see **Figure B.6**).

The spectral dependence of the Faraday effect caused by bound excitons can be evaluated as **[B.8]**:

$$\eta_- - \eta_+ \approx Const \frac{E_X E}{\left(E_X - E\right)^2} \left(1 + \frac{\Delta_{LT}}{E_X - E}\right)^{1/2} \qquad \textbf{\{B.31\}}$$

where $E_X = E_X^{(1)}$ is the ground state energy, Δ_{LT} is the longitudinal–transverse splitting energy.

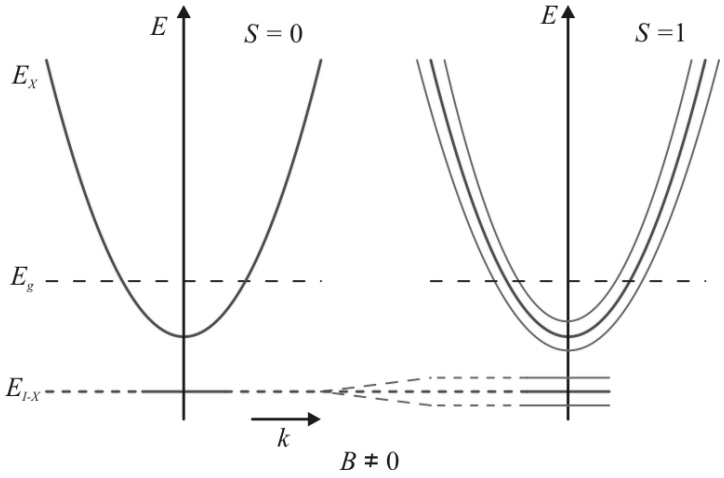

Figure B.6: Wannier-Mott exciton energy with an external magnetic field applied. Left: case the total spin magnetic moment of the exciton is zero; Right: case the total spin magnetic moment of the exciton is one. $E_{I\text{-}X}$ is a localized state in energy and moment.

Bibliography

[B.1] Štefan Višňovský. *Optics in Magnetic Multilayers and Nanostructures*. CRC Press, Taylor & Francis, Boca Raton, USA, 1–61, (2006)

[B.2] N. F. Kharchenko, A. V. Bibik, and V. V. Eremenko. *Quadratic magnetic rotation of the polarization plane of light in the antiferromagnet CoF_2*. Pis'ma Zh. Eksp. Teor. Fiz. **42**, 447 (1985)

[B.3] Edited by Y. B. Xu, and S. M. Thompson. *Spintronic Materials and Techonogy*. Series in Materials Science and Engineering, Taylor & Francis, Boca Raton, USA, 1-35 (2007)

[B.4] Theodore C. Oakberg. *Magneto-Optic Kerr Effect, Hinds Instruments*. Photoelastic modulators – Application note (www.hindinstruments.com);

[B.5] Frederic J. Kahn, P. S. Pershan, and J. P. Remeika. *Ultraviolet Magneto-Optical Properties of Single-Crystal Orthoferrites, Garnets, and Others Ferric Oxide Compounds*. Physical Review **186**, 891, (1969)

[B.6] Mikhail I. Vasilevskiy, and Isabel Calado Ferreira. *Física dos Semicondutores – Fundamentos, Aplicações e Nanoestruturas*. Almedina, Coimbra, Portugal, 181-186, (2005)

[B.7] I. M. Boswarva, R. E. Howard, and A. B. Lidiard. *Faraday effect in semiconductors*. Proceeddings of The Royal Socialty London **A 269**, 125, (1962);

[B.8] P. I. Nikitin, and A. I. Savchuk. The Faraday effecting semi-magnetic semiconductors. Soviet Physics Uspekhi **33**, 975, (1990)

Appendix C

Raman Peak Shift Owing to Strain

Isomorphic strain related to lattice mismatch between a film and a substrate can be described by the theory analogous to that of thermal expansion induced deformations. Non-zero stress components are given by (*e.g.* **[C.1]**):

$$\sigma_{xx} = \sigma_{yy} = -\frac{Y}{1-\upsilon}\theta \qquad \textbf{\{C.1\}}$$

where

$$\theta = \frac{a_{Sn-Ge}(x) - a_{Ge}}{a_{Ge}} = 0.147x \qquad \textbf{\{C.2\}}$$

and $a_{Sn-Ge}(x)$ is the lattice constant of uniform Sn-Ge alloy with Sn content x. In Equation **{C.1}**, Y and υ are the Young modulus and Poisson coefficient, respectively.

Applying the generalized Hooke's law:

$$\varepsilon_{ik} = \frac{1}{Y}\left[(1-\upsilon)\sigma_{ik} - \upsilon \mathrm{Tr}\hat{\sigma}\,\delta_{ik}\right] \qquad \textbf{\{C.3\}}$$

one obtains:

$$\varepsilon_{xx} = \varepsilon_{yy} = -\theta\,, \qquad \textbf{\{C.4a\}}$$

$$\varepsilon_{zz} = \frac{2\upsilon}{1-\upsilon}\theta\,. \qquad \textbf{\{C.4b\}}$$

Here the isotropic approximation is used:

$$Y = \frac{(C_{11}+2C_{12})(C_{11}-2C_{12})}{C_{11}+C_{12}}, \qquad \textbf{\{C.5\}}$$

$$\upsilon = \frac{C_{12}}{C_{11}+C_{12}}. \qquad \textbf{\{C.6\}}$$

Therefore one has:

$$\frac{\varepsilon_{\perp}}{\varepsilon_{\parallel}} = -\frac{2\upsilon}{1-\upsilon} = -2\frac{C_{12}}{C_{11}}\,. \qquad \textbf{\{C.7\}}$$

The second equality uses cubic crystal elastic constants instead of the Poisson coefficient used for isotropic media and corresponds to **Equation {IV.3}**.

The frequencies of optical phonons in the presence of elastic strain are given by the following secular equation **[C.2]**

$$\begin{vmatrix} p\varepsilon_{xx}+q\left(\varepsilon_{yy}+\varepsilon_{zz}\right)-\lambda & 2r\varepsilon_{xy} & 2r\varepsilon_{xz} \\ 2r\varepsilon_{xy} & p\varepsilon_{yy}+q\left(\varepsilon_{xx}+\varepsilon_{zz}\right)-\lambda & 2r\varepsilon_{yx} \\ 2r\varepsilon_{xz} & 2r\varepsilon_{yx} & p\varepsilon_{zzx}+q\left(\varepsilon_{xx}+\varepsilon_{yy}\right)-\lambda \end{vmatrix}=0 \qquad \{C.8\}$$

where

$$\lambda=\Omega^2-\omega_0^2 \qquad \{C.9\}$$

with $\omega_0(\Omega)$ denoting unshifted (shifted) optical phonon frequency and p, q and r are deformation potentials introduced in **Ref. [C.2]**. Thus, strain-induced shift is given by

$$\Omega-\omega_0\approx\frac{\lambda}{2\omega_0}, \qquad \{C.10\}$$

where λ is obtained by solving **Equation {C.8}**.

A simple example is hydrostatic strain/stress:

$$\varepsilon_{xx}=\varepsilon_{yy}=\varepsilon_{zz}=\varepsilon \qquad \{C.11\}$$

with

$$\lambda=(p+2q)\varepsilon=-\gamma\varepsilon\omega_0^2 \qquad \{C.12\}$$

$$\Omega-\omega_0=-\gamma\varepsilon\omega_0 \qquad \{C.13\}$$

where γ is called Grüneisen parameter, $\gamma=-(p+2q)/6\omega_0^2$. So, one has blue shift ($\Omega-\omega_0>0$) for compression ($\varepsilon<0$) and red shift for expansion ($\varepsilon>0$).

For isomorphic strain with x, y and z axes along the principal axes [(001), *etc*] all non-diagonal components ε_{ij} are equal to zero and one has from **Equation {C.8}**:

$$\left(\lambda-(p+q)\varepsilon_{\parallel}-q\varepsilon_{\perp}\right)^2\left(\lambda-2q\varepsilon_{\parallel}-p\varepsilon_{\perp}\right)=0 \qquad \{C.14\}$$

So, two solutions exist:

$$\lambda_1=(p+q)\varepsilon_{\parallel}+q\varepsilon_{\perp} \qquad \{C.15\}$$

(double-degenerated) and

$$\lambda_2=2q\varepsilon_{\parallel}+p\varepsilon_{\perp}\ . \qquad \{C.16\}$$

Parameters $\gamma = -(p+2q)/(6\omega_0^2)$ and $\beta = (p-q)/2\omega_0^2$ have been determined in **[C.2]**; for Ge: $\beta \approx 0.23$ and $\gamma \approx 1$ (average of two values).

Expressing p and q in terms of β and γ:

$$\frac{q}{2\omega_0^2} = -\frac{1}{3}(3\gamma + \beta) \qquad \textbf{\{C.17a\}}$$

$$\frac{p}{2\omega_0^2} = \frac{1}{3}(2\beta - 3\gamma) \qquad \textbf{\{C.17b\}}$$

one obtains:

$$\frac{\Omega_1 - \omega_0}{\omega_0} = -\frac{1}{3}(6\gamma - \beta)\varepsilon_{\parallel} - \frac{1}{3}(\beta + 3\gamma)\varepsilon_{\perp} \qquad \textbf{\{C.18\}}$$

$$\frac{\Omega_2 - \omega_0}{\omega_0} = -\frac{2}{3}(3\gamma + \beta)\varepsilon_{\parallel} - \frac{1}{3}(3\gamma - 2\beta)\varepsilon_{\perp} \qquad \textbf{\{C.19\}}$$

With strain components **{C.4}**, the singlet phonon mode **{C.16}** corresponds to the displacement vector along *z*, while the doublet mode **{C.17}** corresponds to the displacement vector within the *x*-*y* plane. If the Raman scattering experiment was performed in a backscattering geometry with the scattering vector $\Delta\vec{k}$ || (001), then the singlet mode corresponds to LO phonon and the doublet to the two TO phonon modes. According to selection rules for the (001) surface of a diamond crystal, scattering is precisely due to LO phonons **[C.3]** ($z(xy)\bar{z}$ configuration). Therefore we should use Equation **{C.19}** to evaluate the strain-induced shift.

According to **Figure IV.8**, for x = 0.043, $\varepsilon_{\parallel} \approx$ -0.09 % and $\varepsilon_{\perp} \approx$ 0.06 %. Then $\Delta\omega_{strain} = \Omega_2 - \omega_0 \approx 0.0097\omega_0 \approx 2.93\text{cm}^{-1}$ for sample #12 in **Table IV.7**.

Taking $\upsilon \approx\sim 0.27$ **[C.4]** (so that $\varepsilon_{\perp} \approx -2/3\,\varepsilon_{\parallel}$), θ from **Equation {C.2}** and β and γ given above:

$$\Delta\omega_{strain} = \Omega_2 - \omega_0 \approx 67.1x \text{ [cm}^{-1}\text{]},$$

essentially coinciding with that presented in **[C.3]**.

Bibliography

[C.1] S. V. Khazanova, and M. I. Vasilevskiy. Modelling of the composition segregation effect during epitaxial growth of InGaAs quantum well heterostructures. Semiconductor Science and Technology 25, 085008, (2010).

[C.2] F. Cerdeira, C. J.Buchenauer, F. H. Pollak, and M. Cardona. *Stress-induced shifts of first-order Raman frequencies of diamond-and zinc-blende-type semiconductors.* Phys. Rev. **B 5**, 580, (1972).

[C.3] William Hayes, and Rodney Loudon. *Scattering of Light by Crystals*. Dover, New York, USA, (2004).

[C.4] http://www.ioffe.ru/SVA/NSM/Semicond/ (September, 28, 2017)

[C.5] O. Gurdal, P. Desjardins, J. R. A. Carlsson, N. Taylor, H. H. Radamson, J.-E. Sundgren, and J. E. Greene. *Low-temperature growth and critical epitaxial thicknesses of fully strained metastable* $Ge_{1-x}Sn_x$ *(x*δ*0.26) alloys on Ge(001) 2x1*. Journal of Applied Physics **83**, 162, (1998).